Temporally and Spatially Resolved Characterization of Martensitic Transformation Induced in AISI 347 Steel by Thermo-Mechanical Fatigue Loads

DISSERTATION

zur Erlangung des Grades
des Doktors der Ingenieurwissenschaften
der Naturwissenschaftlich-Technischen Fakultät
der Universität des Saarlandes

von

Viktor Lyamkin

Saarbrücken
2023

Tag des Kolloquiums:	13.02.2024
Dekan:	Prof. Dr. Ludger Santen
Berichterstatter:	Prof. Dr.-Ing. Christian Boller
	Prof. Dr.-Ing. Peter Starke
	Prof. Dr. Tetsuya Uchimoto
Vorsitz:	Prof. Dr. mont. Christian Motz
Akad. Mitarbeiter:	Dr.-Ing. Christoph Pauly

Acknowledgments

I would like to thank Christian Boller for giving me the opportunity to work at the Chair of Non-Destructive Testing and Quality Assurance at Saarland University. Thank you for your trust and scientific freedom, which helped me to move forward as an independent researcher. This would not have been possible without the initial support of Peter Starke in the organization of the laboratory and a constant attention to the financial support of the projects.

Special thanks go to Christoph Pauly, to whom I am in debt for many hours of electron microscopy and microstructural analysis. Thank you for your patience and invaluable support. Equally valuable help with the vibrating sample magnetometer was provided by Micha Gratz, who was very kind to do the magnetization measurements. I would also like to thank Gerd Dobmann for providing valuable scientific information and comments.

A big thank you goes to Sascha Power, who helped me with an infinite number of problems, most notably the programming of the TMF rig. Thank you for your constantly positive attitude and your friendship. I would like to thank Sascha Schneider and his team at the central workshop of the NT Faculty for the nearly one hundred parts that have been machined. Thank you all for a great job. I would also like to thank my colleagues Haoran Wu, Ruth Acosta, Aadhik Asokkumar, and Nora Kleser for their help and for making my scientific life a little warmer. I am very grateful to my good friends Yevgeniya Lugovtsova and Tatiana Mishurova who made all the difference in difficult times.

Last but not least, the two three-year projects on which this work is based received financial support from the German Federal Ministry for the Environment, Nature Conservation, Nuclear Safety and Consumer Protection.

Abstract

This work focuses on the kinetics behind the phase transformation process from γ austenite to α' martensite under isothermal and thermo-mechanical fatigue (TMF) conditions. The test conditions were set to simulate those at the start-up and cool-down of a nuclear powerplant. The formation of deformation-induced martensite is inhibited at elevated temperatures, making it difficult to measure and analyze. By implementing novel magnetic measurement techniques, dynamics of α' martensite formation were observed for the first time under TMF load and elevated temperatures. Based on the obtained experimental data, a mathematical relationship was established between the rate of $\gamma \rightarrow \alpha'$ phase transformation, temperature, and strain amplitude. In addition, α' martensite start temperature and the lower accumulated strain limit were determined experimentally for a low-cycle fatigue regime. A relationship was also found between α' martensite morphology, strain amplitude, and magnetic properties of the steel.

Kurzfassung

Diese Arbeit konzentriert sich auf die Kinetik des Phasenumwandlungsprozesses von γ-Austenit zu α'-Martensit unter isothermen und thermomechanischen Ermüdungsbedingungen. Die Prüfbedingungen wurden so gewählt, dass sie die Bedingungen beim Anfahren und Abkühlen eines Kernkraftwerks simulieren. Die Bildung von verformungsinduziertem Martensit wird bei hohen Temperaturen gehemmt, was die Messung und Analyse erschwert. Durch den Einsatz neuartiger magnetischer Messtechniken konnte erstmals die Dynamik der Martensitbildung unter thermomechanische Belastung und bei erhöhten Temperaturen beobachtet werden. Auf der Grundlage der gewonnenen experimentellen Daten wurde eine mathematische Beziehung zwischen der Geschwindigkeit der Phasenumwandlung, der Temperatur und der Dehnungsamplitude hergestellt. Darüber hinaus wurden die α'-Martensit-Starttemperatur und die untere Grenze der akkumulierten Dehnung experimentell in einem niedrigzyklischen Ermüdungsmodus bestimmt. Es wurde auch eine Korrelation zwischen der α'-Martensitmorphologie, der Dehnungsamplitude und den magnetischen Eigenschaften des Stahls festgestellt.

Contents

Symbols and Abbreviations

Greek

α'	Deformation-induced martensite
γ	Austenite
ε	Strain, hcp martensite
ε_{max}	Maximum strain within one fatigue cycle
ε_{min}	Minimum strain within one fatigue cycle
ε_{at}	Total strain amplitude
ε_{ap}	Plastic strain amplitude
ε_{am}	Mechanical strain amplitude
ε_{atm}	Thermal strain amplitude
ε_{mech}	Mechanical strain
ε_t	Total strain that includes thermal and mechanical strains
ε_{therm}	Thermal strain
λ	Cumulative plastic strain
μ_r	Relative magnetic permeability (μ in cgs system)
μ_{rst}	Relative permeability of the standard calibration sample
μ_{mfi}	Output calibrated to relative magnetic permeability
ν	Poisson's ratio
ξ	α' martensite volume fraction
ξ_{fm}	Ferromagnetic volume fraction
$\tilde{\xi}_{fm}$	Ferromagnetic volume fraction compensated for the change in d_w
ξ_s	α' martensite saturation fraction
σ	Stress
σ_a	Stress amplitude
σ_m	Mean stress
σ_{max}	Maximum stress within a given cycle
σ_{min}	Minimum stress within a given cycle
τ_s	Equivalent shear stress
χ	Magnetic susceptibility
Ω	Cumulative strain energy density

Latin

C_{Fe}	Ferrite calibration factor
$\tilde{C}_{Fe}$	Ferrite calibration factor compensated for the change in d_w
d_w	Working distance
E	Young's modulus
F	Force
F_{air}	Force measurement without the sample, or simply "in air"
F_{ast}	Force measurement of a fully austenitic sample
F_{st}	Force measurement of a standard calibration sample
G	Chemical free energy, shear modulus

G_{mech}	Mechanical (external) contribution to the free energy
G_{min}	Minimum energy required for $\gamma \rightarrow \alpha'$ transformation
G_{therm}	Thermal contribution to the free energy
H	Enthalpy, applied magnetic field
H_c	Coercivity or coercive force
h_s	Noise amplitude with the sample
h_b	Noise amplitude without the sample
k_s	Austenite stability coefficient
L	Mean free distance
M	Magnetization
M_d	Highest temperature at which deformation-induced martensite can occur
M_{d30}	Temperature at which 50 % martensite is formed at 30 % deformation
M_{rs}	Saturation remanence
M_s	Saturation magnetization
M_s	Martensite start temperature
$M_{s,\sigma}$	Stress-induced start temperature of martensite
m	Magnetic moment
m_s	Mean output value with the sample
m_b	Mean output value without the sample
N	Number of fatigue cycles
N_f	Number of fatigue cycles to failure
N_p	Number of cycles to reach peak phase transformation rate
R	Electrical resistance, load ratio
R_0	Initial electrical resistance
R^2	Coefficient of statistical determination in a regression model
$R_{\mu r}$	Resolution expressed in terms of relative magnetic permeability
R_{Fe}	Resolution expressed in terms of ferrite volume fraction
R_z	Roughness by the difference between the tallest peak and the deepest valley
T_0	Temperature at which α' and γ chemical free energies are equal
T_c	Temperature at the center of the specimen
T_{ch}	High temperature of a TMF cycle at the center of the specimen
T_{cl}	Low temperature of a TMF cycle at the center of the specimen
t_{step}	Duration of a “step” in a strain or load increase test
V_γ	γ austenite volume fraction
W	Strain energy density

Abbreviations

AC	Alternating Current
AFM	Atomic Force Microscopy
AISI	American Iron and Steel Institute
ASTM	American Society for Testing and Materials
bcc	body-centered cubic
BCM	Balanced Core Magnetometer

bct	body-centered tetragonal
CAT	Constant Amplitude Test
cgs	centimeter–gram–second system of units
DSA	Dynamic Strain Aging
EBSD	Electron Backscatter Diffraction
EDM	Electric Discharge Machining
EDS	Energy Dispersive X-ray Spectroscopy
fcc	face-centered cubic
Fe%	Ferrite volume fraction in %
FIB	Focused Ion Beam
FN	Ferrite Number
GMR	Giant Magneto-Resistance
GND	Geometrically Necessary Dislocations
HCF	High Cycle Fatigue
hcp	hexagonal close-packed
IP	In-Phase
IPF	Inverse Pole Figure
ISO	Isothermal, International Organization for Standardization
KAM	Kernel Average Misorientation
LAM	Local Average Misorientation
LC	Load Cell
LCF	Low Cycle Fatigue
LIT	Load Increase Test
LR	Linear Range
MFI	Magnetic Force Imaging
MFM	Magnetic Force Microscopy
NDT	Non-Destructive Testing
OECD	Organization of Economic Cooperation and Development
OP	Out-of-Phase
OPDE	OECD piping failure data exchange
OP-S	Oxide Polishing (colloidal silica suspension)
OR	Orientation Relationship
PID	Proportional, Integral, Derivative (controller)
PRIAS	Pattern Region of Interest Analysis System
SEM	Scanning Electron Microscopy
SIT	Strain Increase Test
SNR	Signal-to-Noise Ratio
SQUID	Superconductive Quantum Interference Device
TMF	Thermo-Mechanical Fatigue
TRIP	Transformation Induced Plasticity
UMB	Uniaxial Magnetic Balance
VHCF	Very High Cycle Fatigue
VSM	Vibrating Sample Magnetometer

List of Figures

List of Tables

Part I
Introduction

“It is a capital mistake to theorize before one has data.”

Arthur Conan Doyle

1 Problem Definition and Scope

Over the past decades, numerous piping failures have been reported in nuclear power plants worldwide. In the OPDE[1] database [1] there are about 3600 cases of piping failures. Many piping elements and other components in a nuclear power plant have to be highly corrosion-resistant and are therefore made of austenitic stainless steel. Of particular interest is the pressurizer surge line that connects the pressurizer vessel with the hot-leg piping and the reactor pressurizer spray line system. During each heat-up of the plant hot water in the surge line rides on a layer of cold water. This causes only the upper part of the pipe to expand, resulting in a cyclically repeated stress gradient and low-cycle fatigue of the material [2]. Another example where thermo-mechanical fatigue (TMF) occurs is the spray line system. The spray line system has the objective of reducing the pressure by spraying cold water into the steam to force condensation of water and therefore pressure reduction [2].

Metastable austenitic stainless steels, such as AISI 347 (X6CrNiNb18-10, 1.4550), can undergo a phase transformation from paramagnetic γ austenite into ferromagnetic α' martensite in two ways: when cooled down to martensite start temperature M_s or by mechanical deformation. The higher the temperature, the more (accumulated) mechanical deformation is required for $\gamma \rightarrow \alpha'$ transition to occur. It would have been easy to deduct the remaining fatigue life from the amount of α' martensite if nuclear power plant components did not have to operate at elevated temperatures. For AISI 347, the formation of α' martensite is significantly reduced above 100 °C, and it is generally accepted that no phase transformation takes place at the temperatures of a pressurized water reactor of about 320 °C. However, there is experimental evidence [3] that $\gamma \rightarrow \alpha'$ transformation still occurs at this temperature, but in extremely small quantities.

The evaluation of early fatigue damage and, therefore, the remaining life of austenitic steel components remains to be of significant practical relevance. Despite extensive research into the fatigue behavior of austenitic stainless steels, a number of questions remain unanswered:

- *What are the dynamics of $\gamma \rightarrow \alpha'$ transformation at elevated temperatures in a low-cycle fatigue regime?*

- *What is the lower accumulated strain limit for the phase transformation, below which no phase transformation should occur at a given temperature?*

[1] OPDE stands for "OECD piping failure data exchange", where OPDE is the Organization of Economic Cooperation and Development.

- *Can deformation-induced martensite morphology be different in low-cycle fatigue and high-cycle fatigue?*
- *How do the magnetic properties of austenitic stainless steel change after TMF loading, similar to that of the start-stop cycle of a powerplant?*
- *Where does the $\gamma \rightarrow \alpha'$ transformation localize within the material at elevated temperatures and under TMF?*

The scope of this thesis is not the direct evaluation of fatigue life under TMF conditions, but rather the investigation of the physical mechanisms that can further lead to the non-destructive evaluation of fatigue damage at elevated temperatures. The $\gamma \rightarrow \alpha'$ transformation is one of such mechanisms, that requires further experimental evaluation. For this purpose, specialized experimental instrumentation based on the principle of magnetic force measurement has been developed and is described in section 5. This specialized equipment allowed for high-sensitivity *in-situ* measurement of deformation-induced martensite at elevated temperatures and TMF loads, which had not been done before. In addition, a handheld prototype for magnetic evaluation of α' martensite content and morphology (balanced core magnetometer, section 5.4) has been developed and tested in laboratory conditions. To quantitatively describe the localization of $\gamma \rightarrow \alpha'$ transformation in fatigue specimens, the magnetic force imaging (MFI) technique has been developed and is described in section 5.1. Using newly developed experimental tools, this work aims to establish a clear relationship between $\gamma \rightarrow \alpha'$ transformation rate, strain amplitude, and temperature under low-cycle fatigue conditions in a spatially resolved manner.

2 Martensitic Phase Transformation

To many material scientists, and especially to metallurgists, martensitic phase transformation is of particular interest. In the past few decades, a considerable effort went towards studying of this phenomenon, which gave rise to many advances in steel manufacturing including transformation-induced plasticity (TRIP) steels [5]. Cohen, Olson, and Clapp in 1979 defined martensitic transformation as part of a wider displacive (diffusionless) transformations [4]. In this classification (see Fig. 1), martensitic transformation belongs to the group of lattice-distortive transformations, which occur when lattice distortions dom-

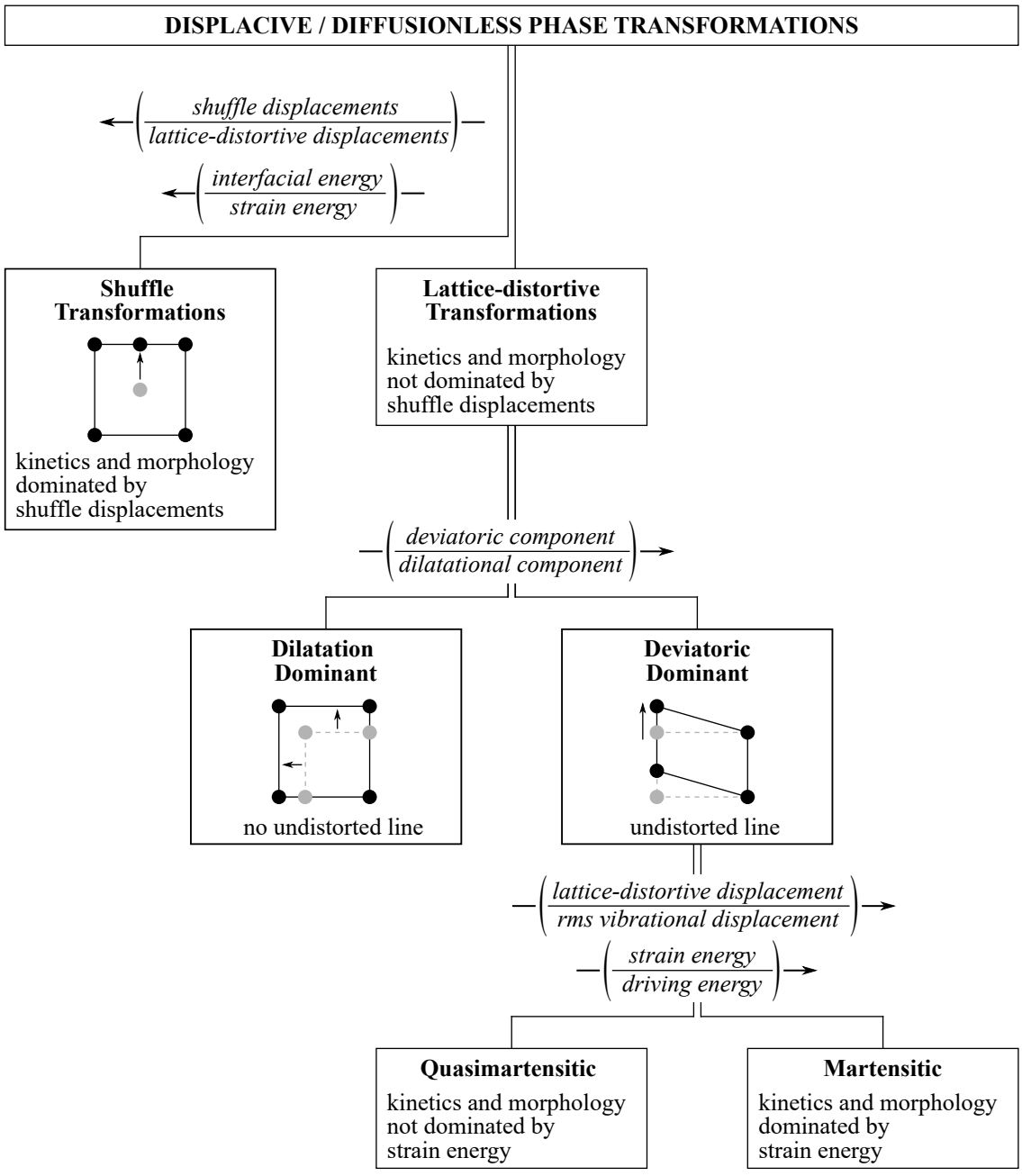

Fig. 1. Classification of the diffusionless phase transformations as proposed by Cohen, Olson, and Clapp [4].

inate shuffle displacements and strain energy exceed interfacial (surface) energy.

Since the introduction of this classification scheme, it has been suggested by Olson that nucleation is an important characteristic of martensitic phase transformation [6]. With this regard, a specific definition of martensitic transformation can be given as "*shear dominant, lattice distortive, diffusionless transformation occurring by nucleation and growth*" [6]. It was later suggested to use the shape change of the product crystals as an experimental test for the displacive martensitic mechanism [7, 8].

2.1 Crystallography and orientation relationships

Experimental research showed three possibilities for phase transformation [9]:

1. γ austenite $\rightarrow$ α' martensite
2. γ austenite $\rightarrow$ ε martensite
3. γ austenite $\rightarrow$ ε martensite $\rightarrow$ α' martensite

Direct $\gamma \rightarrow \alpha'$ transformation can be described in a simplified manner by a model introduced by Bain (B) [10]. Bain showed that the body-centered tetragonal (bct) structure of α' martensite is already contained in the face-centered cubic (fcc) lattice of austenite (see Fig. 2a). The model shows how a simple distortion allows fcc lattice to be transformed into a body-centered cubic (bcc) lattice: an intermediate tetragonal lattice is constructed from the fcc lattice by choosing $1/2[110]_\gamma$, $1/2[\bar{1}10]_\gamma$, and $1/2[001]_\gamma$ to be a new reference frame. In order to obtain the bct lattice $[110]_\gamma$ and $[\bar{1}10]_\gamma$ vectors expand by 12.6 % and $[001]_\gamma$ contracts by 20.3 % [12].

The Bain distortion suffers from several intrinsic problems:

- the resulting orientation relationship (OR) between α' and the parent phase is by more than 10° from the experimental ORs [12].
- martensite transformation is a shear process, but the shear plane, assumed to be the habit plane, is not in agreement with experimentally observed ORs [13].

A different model was proposed by Kurdjumow and Sachs (K-S) in 1930 [14]. It relates the compact planes of the γ phase $\{111\}_\gamma \parallel \{110\}_\alpha$ to those of the α' phase and the compact directions of the planes $\langle 110\rangle_\gamma \parallel \langle 111\rangle_\alpha$. The martensite lattice is formed from the fcc parent lattice by shear on $\{111\}_\gamma$ planes along $\langle 110\rangle_\gamma$ directions. Consequentially, planes and directions that remain

parallel within the fcc lattice are the ones that form slip systems. The number of possible martensite variants can be calculated using the four planes of the family $\{111\}_\gamma$ and three directions $\langle 110\rangle_\gamma$ corresponding to each of these planes. Since both $\langle 110\rangle_\gamma$ directions and their opposites can be chosen, 24 variants are possible in this model [15].

A very similar model was proposed later by Nishiyama in 1934 [16]. In this model, planes are parallel as in the K-S model but with the direction $[10\bar{1}]_\gamma$ parallel to $[100]_\alpha$. In this case, the shear occurs on $\{111\}_\gamma$ planes along $\langle 112\rangle_\gamma$ directions. One year later the same relationship was published by Wassermann. This OR is therefore known as Nishiyama-Wassermann (N-W) [15]. K-S and N-W are the most common ORs in Ni-based austenitic steels. Sandoval

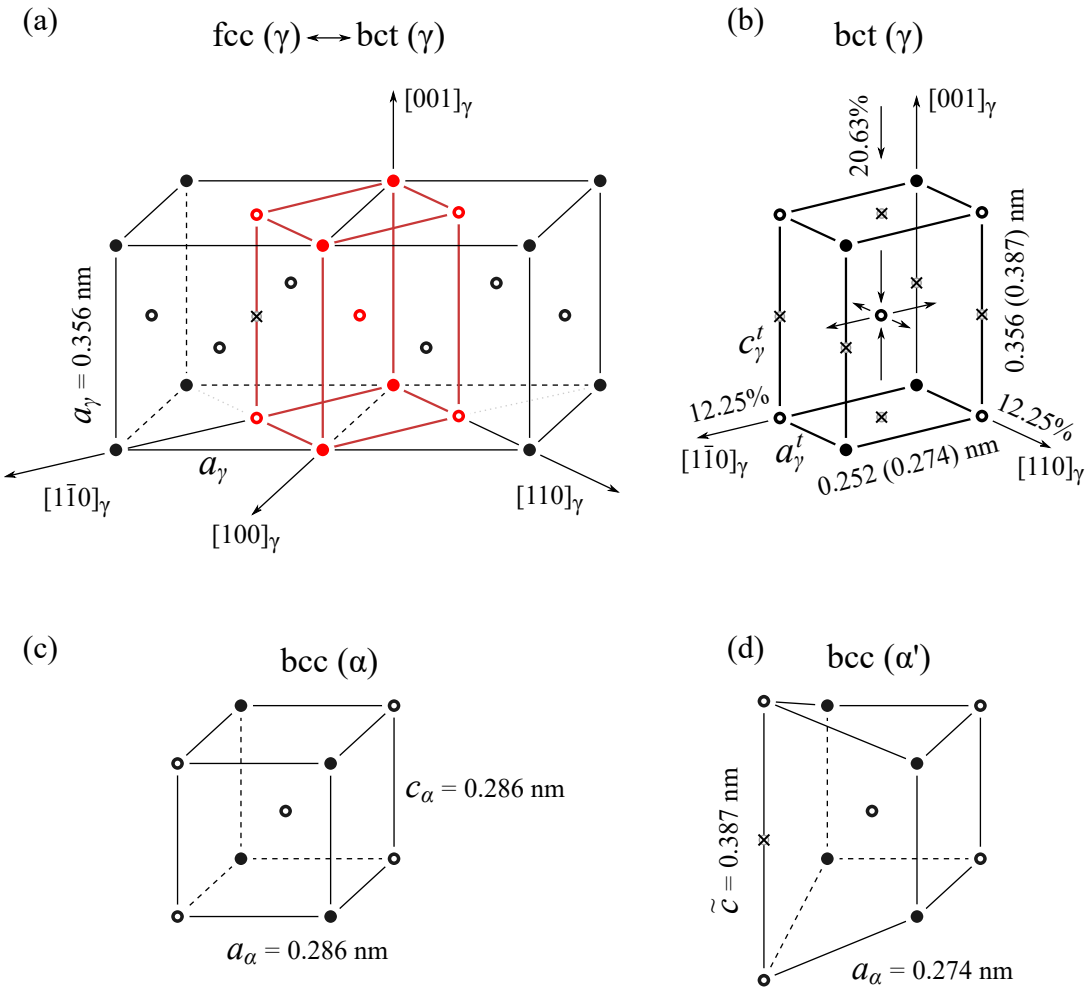

Fig. 2. Schematic illustration of crystal lattices in iron: a) bct lattice of γ-iron in two unit fcc unit cells. b) bct lattice of γ-iron. Parameters are given for carbon-free iron and with carbon in brackets. c) bcc lattice of pure iron after $\gamma \rightarrow \alpha$ transformation. d) distorted bcc lattice having a carbon atom cube edge $\tilde{c}$. Modified after Lobodyuk et al. [11].

et al. [17] showed with atomistic calculations that the N-W distortion is more energetically favorable for the $\gamma \rightarrow \alpha'$ transformation when compared to Bain.

There have been other models to explain the $\gamma \rightarrow \alpha'$ phase transformation process. Pitsch (P) [18] established and OR in Fe-N alloys using transmission electron microscopy. This relationship is typically observed between ferrite, perlite, and cementite in steels [19]. This OR relates $\{0\bar{1}1\}_\alpha$ planes being parallel to $\{001\}_\gamma$ and $\langle 111\rangle_\gamma$ directions parallel to $\langle 110\rangle_\gamma$. Bogers and Burgers [20] proposed a double-shear mechanism for the $\gamma \rightarrow \alpha$ transformation. This model shows relationships between the phases, depending on the misfit dislocations generated at interfaces to release misfit strains [21].

For most steels, K-S and N-W models can predict the orientations of the product phases, but as was pointed out by Greninger and Troiano (G-T) [13], the calculated habit planes do not correspond to those measured experimentally. G-T came up with a two-homogeneous-shear mechanism in $\gamma \rightarrow \alpha$ transformation. The first step corresponds to the macroscopically observed change in shape, while the second one is responsible for the changes in the crystal structure without macroscopic consequences. The G-T model shows crystallographic relationships between granular bainite and austenite. The development of the G-T model led to the phenomenological theory of martensitic transformation [22–25].

More recent studies suggested a two-step mechanism for $\gamma \rightarrow \alpha'$ transformation with an intermediate hexagonal close-packed (hcp) ε phase: $\gamma \rightarrow \varepsilon \rightarrow \alpha'$. Cayron et al. suggested [26] that the α' martensite is the result of a shear followed by deformation on the $\{111\}_\gamma$ planes. Although the intermediate ε phase was only observed in FeMnC and FeCrNi alloys [27–30], it might be possible that the ε phase is unstable in other systems and quickly transforms to α' martensite. Later Cayron [12] proposed a new one-step model based on Pitsch distortion.

The ORs described here can also be represented by the minimum rotation around an invariant line or the Euler angles with three rotations (φ_1, Ψ, φ_2) required to bring the product and the parent phases into coincidence. A summary of all ORs is given in Table 1.

While α' martensite in pure iron may have a bcc lattice, in steel alloys it is very often a bct structure. The original evidence for α' martensite tetragonality came from the splitting of (002) and (200) X-ray diffraction peaks [31–33]. It was established that the parameter a of the martensitic lattice (α', 0.285 nm) is always smaller than that of ferrite (α, 0.286 nm). With an increase in carbon content from 0.8 % to 1.2 % the c parameter of martensite (see Fig. 2) increased from 0.291 to 0.302 [11]. The observed tetragonality was theoretically explained by a statistical theory of the ordering of carbon in one preferred sub-

Table 1
Summary of the orientation relationships (ORs) related to martensitic phase transformations. B, K-S, P, N-W, and G-T represent Bain, Kurdjumow-Sachs, Pitsch, Nishiyama-Wassermann and Greninger-Troiano ORs, respectively. Data from Vallejos et al. [15].

OR	Planes	Directions	Transformation Euler angles ($\gamma \rightarrow \alpha$)			No. of martensite variants
			φ_1 (°)	Ψ (°)	φ_2 (°)	
B	$\{010\}_\gamma \parallel \{010\}_\alpha$	$\langle 001\rangle_\gamma \parallel \langle 001\rangle_\alpha$	0	45	0	3
K-S	$\{111\}_\gamma \parallel \{110\}_\alpha$	$\langle 1\bar{1}0\rangle_\gamma \parallel \langle 1\bar{1}1\rangle_\alpha$	5.77	48.2	5.77	24
P	$\{001\}_\gamma \parallel \{\bar{1}01\}_\alpha$	$\langle 110\rangle_\gamma \parallel \langle 111\rangle_\alpha$	9.74	45	0	12
N-W	$\{111\}_\gamma \parallel \{110\}_\alpha$	$\langle 0\bar{1}1\rangle_\gamma \parallel \langle 001\rangle_\alpha$	0	45	9.74	12
G-T	$\{111\}_\gamma \sim 1^\circ \{110\}_\alpha$	$\langle 121\rangle_\gamma \sim 2^\circ \langle 110\rangle_\alpha$	2.7	46.6	7.5	24

lattice, out of the three possible sublattices of octahedral interstices [34, 35].

When C atoms are located at the middle of the cube edge of the bct austenite lattice (see Fig. 2d), the distance between the corresponding two Fe atoms increases. Due to the diffusionless nature of $\gamma \rightarrow \alpha'$ transformation, it is possible to have only one C atom along the cube edge. This results in the remaining three cube edges changing their length to a lesser extent. Lobodyuk et al. [11] therefore suggested that such a structure should be named *pseudo-tetragonal*.

2.2 Thermodynamics of $\gamma \rightarrow \alpha'$ transformation

The crystal lattice changes described above can be induced either thermally or by applying mechanical stress [36]. When the chemical free energy of austenite is equal to that of martensite, they are in thermodynamic equilibrium at T_0, as shown in Fig. 3a, based on a diagram by Vöhringer and Macherauch [37]. At temperatures above T_0 austenite is the more energetically favorable phase, while below T_0 α' martensite is more favorable. As temperature decreases, the transition from γ to α' does not happen immediately. It is necessary to undercool austenite to the martensite start temperature M_s to initiate the thermal $\gamma \rightarrow \alpha'$ transition. This delay is due to the existence of non-chemical energy barriers such as interfacial and elastic energy [40]. This leads to the conclusion that a critical driving force is required to initiate the martensitic transformation. This critical force corresponds to the chemical free energy difference ΔG_{min} between undeformed austenite and α' martensite at M_s temperature, where the transformation occurs without any additional external energy.

Patel and Cohen [41] studied the influence of applied stress on the $\gamma \rightarrow \alpha'$ transformation. They have shown that chemical free energy can be influenced

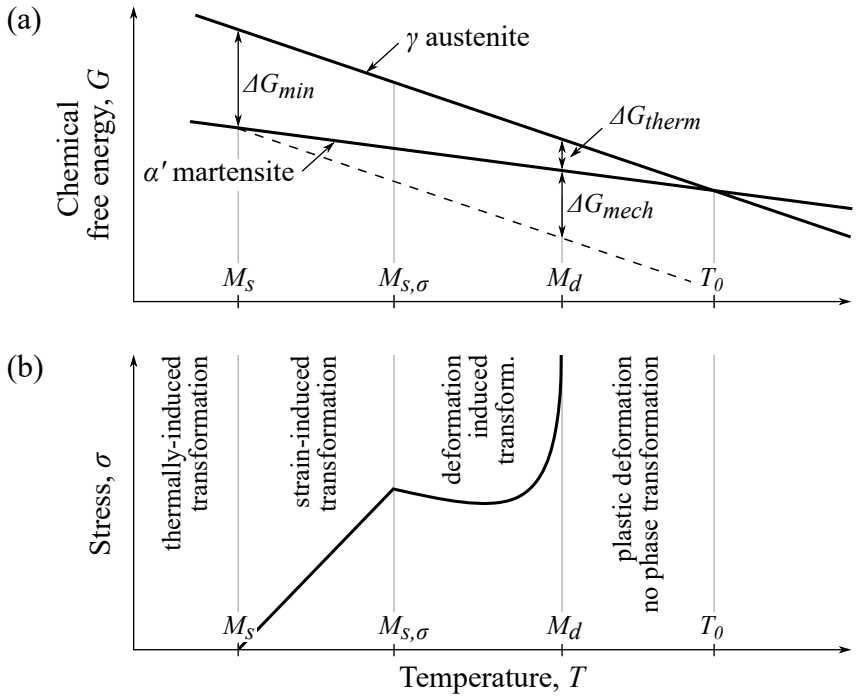

Fig. 3. Schematic illustration of the factors affecting $\gamma \rightarrow \alpha'$ transformation: a) chemical free energy required to initiate $\gamma \rightarrow \alpha'$ transformation according to Vöhringer and Macherauch [37]; b) applied stress necessary for $\gamma \rightarrow \alpha'$ transformation according to Olson and Cohen [38]. Modified after [39].

mechanically. As the stress increases, the mechanically induced free energy ΔG_{mech} also increases so less thermal free energy ΔG_{therm} needs to be induced to reach the critical amount of free energy ΔG_{min}. Such condition when the transition from γ to α' is favorable can be written as Eq. (1):

$$(\Delta G_{therm} + \Delta G_{mech}) \geq \Delta G_{min} \tag{1}$$

This can be illustrated by Fig. 3b, which goes back to the research of Olson and Cohen [38]. In the temperature range $M_s \leq T \leq M_d$, a distinction can be made between stress-induced and deformation-induced martensite formation [39]. Bolling and Richman [42] showed that there is a temperature $M_{s,\sigma}$ up to which stress-induced martensite formation occurs only due to elastic deformation. Above $M_{s,\sigma}$ the applied stress must exceed the yield strength to initiate the phase transformation [39].

The martensite deformation temperature M_d is the highest temperature at which the martensitic phase transformation can still occur, even though between T_0 and M_d free energy of α' martensite is below that of γ austenite. From a purely thermodynamic point of view, the $\gamma \rightarrow \alpha'$ transformation is still possible here, but the required critical free energy ΔG_{min} can no longer be applied since the stress required to reach ΔG_{mech} increases exponentially [39].

The formation of α' martensite was measured experimentally at various

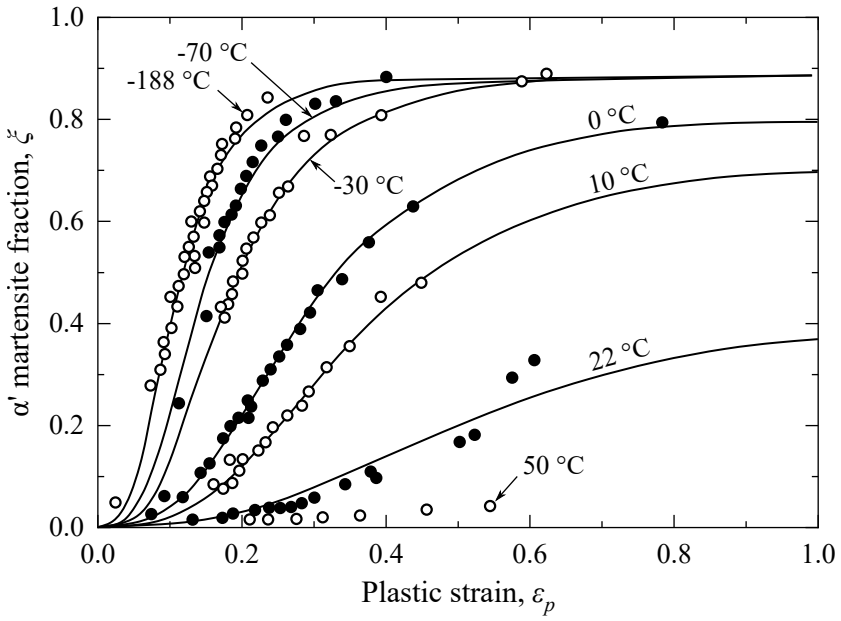

Fig. 4. Content of α' martensite mathematically fitted by Olson and Cohen (solid lines) on experimental data of Angel (dots) for 304 stainless steel [43].

temperatures by Angel [36] and is shown in Fig. 4. This information was then used by Olson and Cohen, and others to generate mathematical models for the kinetics of $\gamma \rightarrow \alpha'$ transformation. These models are described in more detail in section 2.4.

2.3 Factors affecting austenite stability

2.3.1 Chemical composition

The meaning behind austenite stability from a thermodynamic point of view can be understood directly from Fig. 3. The higher ΔG_{min} and the lower the M_s temperature, the more stable austenite will be. Austenite stability can be divided into thermal stability and mechanical stability, based on the driving force (cooling or stress) [44]. Alloying elements greatly affect the stacking fault energy and, consequently, the stability of austenite [45]. Depending on the size of the alloying atoms, they may occupy interstitial or substitutional positions in Fe lattice. The stabilization can be achieved by alloying with Ni, N, C, and Mn, as it increases the difference of chemical free energy between austenite and martensite. It can be mathematically formulated as Eq. (2) [46]:

$$\Delta G^{\gamma \rightarrow \alpha'} = (1 - x) \cdot \Delta G_{Fe}^{\gamma \rightarrow \alpha'} + x \cdot \Delta H^{\gamma \rightarrow \alpha'} \tag{2}$$

where x is the element content and ΔH is the change in enthalpy. Martensite start temperature M_s can be used to evaluate the effect of chemical composition on austenite stability. Izumiyama et al. [47] experimentally investigated

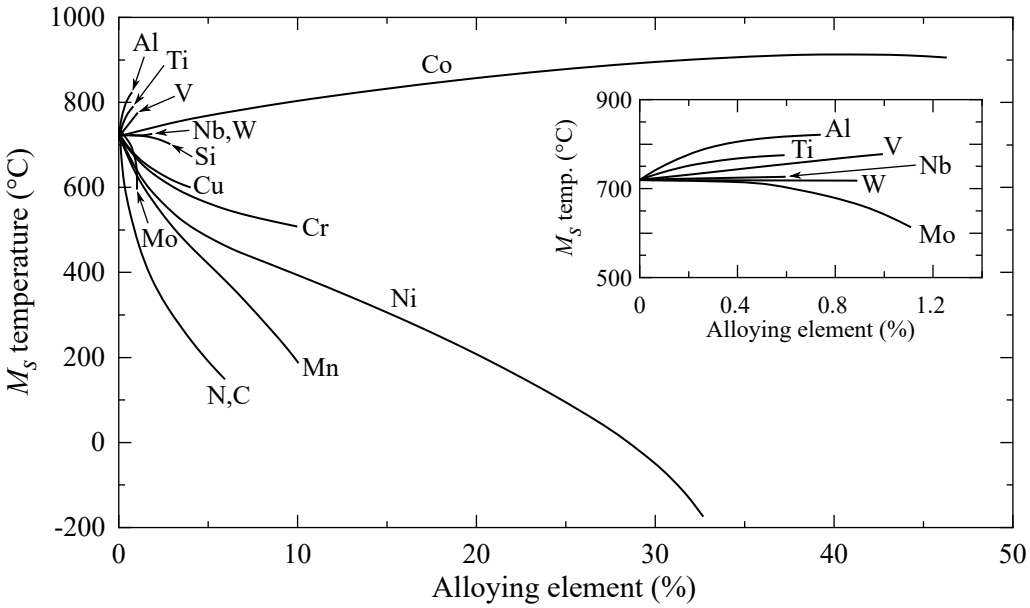

Fig. 5. Effect of alloying elements on M_s temperature of iron. Data after Izumiyama et al. [47].

the influence of alloying elements on M_s temperature in binary systems (iron plus alloying element, without additional carbon). The results are presented in Fig. 5. Many equations have been developed to predict the M_s temperature based on the chemical composition [48–51]. Original formulation by Eichelmann and Hull [52], as cited in [39], is shown in Eq. (3):

$$M_s(°C) = 1350 - 1665(C + N) - 28Si - 33Mn - 42Cr - 61Ni \quad (3)$$

Another commonly used determination of M_s in Eq. (4) was provided by Andrews [53]:

$$M_s(°C) = 539 - 423C - 30.4Mn - 17.7Ni - 12.1Cr - 7.5Mo \quad (4)$$

where the element contents are in wt. %. From these equations it is evident that carbon stabilizes austenite. However, it was found that the stability of austenite in 18 % Cr and 8 % Ni steel is higher with N rather than with C [54]. The addition of Ni and Cr, key elements of austenitic stainless steel, decreases M_s temperature and enhances austenite stability [27, 55]. Mn is a more cost-effective alternative to Ni and also increases the stability of austenite. The effect of Al is not shown in Eq. (4) but can be calculated as +30 °C/wt.% [56]. Consequently, it is generally undesirable to have any amount of Al in austenitic steel, as it reduces austenite stability. Hydrogen was found to have little effect on austenite stability, despite the well-known embrittlement effect of hydrogen [57].

Since it is difficult to determine the M_d temperature experimentally, An-

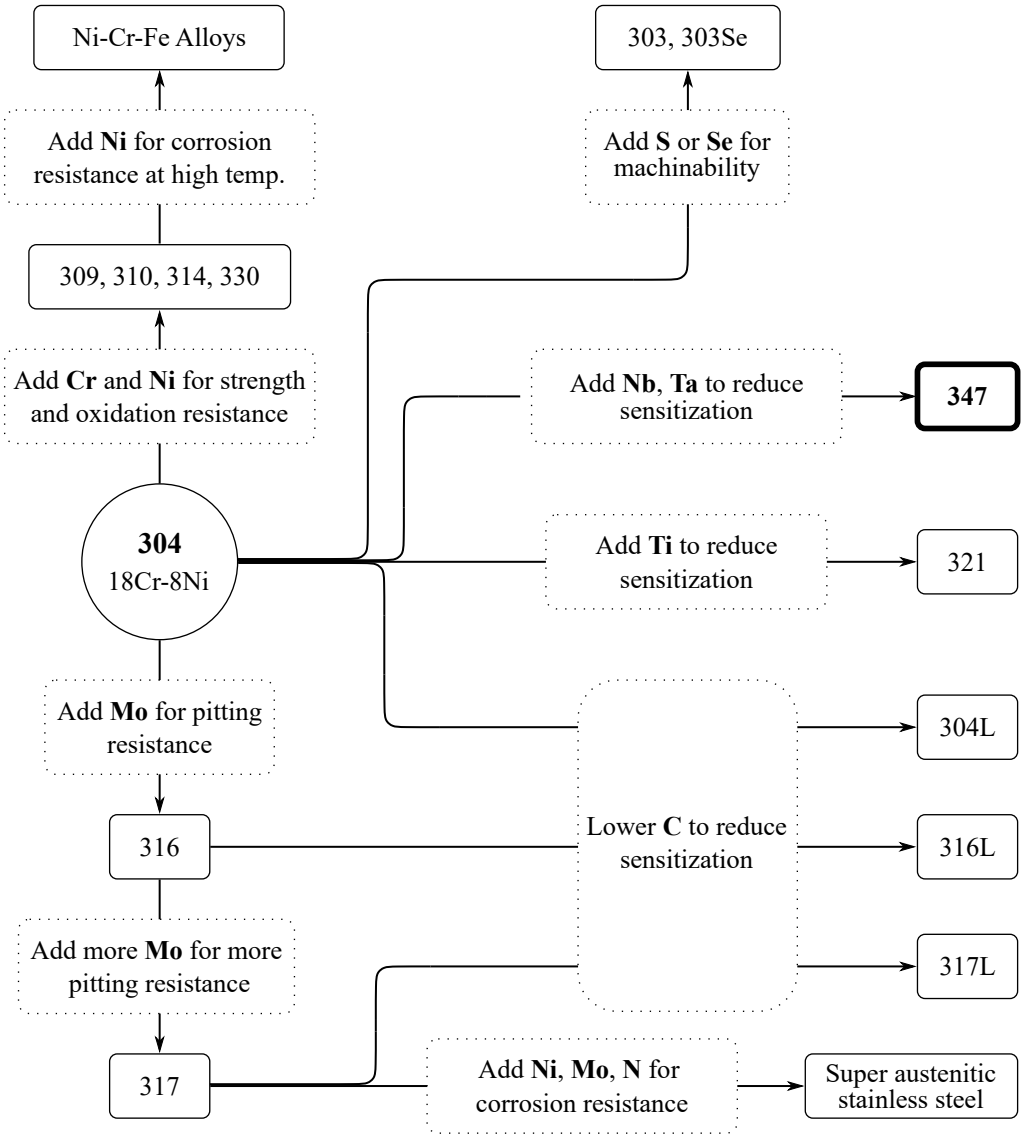

Fig. 6. Relationship between alloying elements in 300 series austenitic stainless steels. Modified after [58].

gel [36], as cited in [39], introduced the M_{d30} temperature at which 50 % α' martensite is formed at 30 % plastic deformation:

$$M_{d30}(°C) = 413 - 462(\mathrm{C} + \mathrm{N}) - 9.2\mathrm{Si} - 8.1\mathrm{Mn} - 13.7\mathrm{Cr} - 9.5\mathrm{Ni} - 18.5\mathrm{Mo} \quad (5)$$

While M_s temperature reflects the *thermal stability* of austenite, M_{d30} reflects *mechanical stability*. A lower M_{d30} temperature, similar to M_s, indicates higher austenite stability. The role of alloying elements in 300 series austenitic stainless steel is further explained in Fig. 6.

2.3.2 Grain size

As a general rule, the smaller the grain size, the greater the stability of the austenite during quenching [59, 60] as well as the plastic deformation [61].

Grain refinement has been used to retain austenite at room temperature without stabilizing alloying elements [62]. The following empirical equation (6) can be used to interpret austenite stability as a function of grain size in terms of M_s temperature [63]:

$$M_s(°C) = M_{s0} - A_{xc} - BV_\gamma^{-\frac{1}{3}} \tag{6}$$

where V_γ represents austenite grain volume, M_{s0} is martensite start temperature determined by chemical composition excluding carbon. A = 423 wt.%/°C according to Andrews equation (4), B is a fitting parameter that can be determined experimentally.

2.3.3 Dislocations

Dislocations play an important role in the nucleation and growth of α' martensite and therefore should also affect the austenite stability. However, there is no general consensus on how the dislocations affect austenite stability. The dissociation of dislocations into partial dislocations could lead to a bcc structure that could serve as a martensite embryo [38], as cited in [44]. The dislocation loops generated at the embryo/austenite interface can glide to extend the interface and facilitate embryo growth [46]. In other words, in terms of nucleation and growth, the dislocations could support the martensitic transformation. At the same time in austenite grains with large plastic deformation presence of dislocation debris was reported to cause mechanical stabilization [64]. It is, therefore, reasonable to assume that dislocations can also act as barriers to martensite growth [65, 66]. The critical strain after which mechanical stabilization occurs can be derived in Eq. (7) by equating the chemical driving force ΔG to the force resisting the glide of the interface [65]:

$$b\Delta G = \frac{1}{8\pi(1-\nu)} G b^{3/2} \left(\frac{\varepsilon}{L}\right)^{1/2} + \tau_s b \tag{7}$$

where ε is the plastic strain, G is the shear modulus, b are Burgers vectors, ν is the Poisson's ratio, τ_s is the equivalent shear stress, and L is mean free distance.

The dual role of dislocations in $\gamma \rightarrow \alpha'$ transformation may be explained by the number of dislocations [67, 68]. The presence of a large number of dislocations suppresses the nucleation, leading to the higher austenite stability, while a small amount of dislocations facilitates nucleation. Recent work by He et al. [69] showed that small deformation increases the M_s temperature, while large deformation decreases M_s. Small deformation leads to geometrically necessary dislocations (GND) close to the grain boundaries [70]. GND near the

austenite grain boundary increase the potency of the martensite embryo which leads to an increase in the M_s temperature [69]. Large deformation leads to intense dislocation formation inside the austenite grain. The arrangement of the dislocations is then such that subgrains are formed. The presence of subgrains consequently inhibits the growth of martensite lath [69].

2.3.4 Morphology

For various steel grades, the dependence of austenite stability on its morphology was often reported in the literature [71–75]. The morphology of austenite is quite often dictated by the presence of other phases, including α' martensite. In general, the blocky/globular austenite is less stable during plastic deformation compared to the film/lath austenite [76, 77]. However, the effect of morphology on austenite stability is often overshadowed by the contribution of other factors. This is due to the fact that austenite grains of different morphology have different microstructural features, including grain size and chemical composition.

2.3.5 Stress state and loading direction

The $\gamma \rightarrow \alpha'$ transformation has usually been studied under the uniaxial stress state conditions of a tensile test. However, the response of austenite to a different stress state is not necessarily the same and should be considered. Uniaxial tensile stress facilitates phase transformation more when compared to uniaxial compressive stress [41]. This is because the uniaxial compressive stress can be decomposed into normal stress, which resists deformation, and shear stress, which facilitates the transformation [41]. Hydrostatic pressure greatly suppresses the $\gamma \rightarrow \alpha'$ transformation as also opposes the expansion of martensite necessary for the transformation [78]. The shear stress state when examined against uniaxial tensile stress in TRIP steel appeared to promote the transformation [79]. From these observations, it can be concluded that the different stress state interacts with different components of transformation strain, which leads to different amounts of mechanical interaction energy [41]. This mechanical interaction energy can be formulated in Eq. (8) as a change of chemical free energy to account for the effect of stress state on the austenite stability [41]:

$$G_{mech} = \frac{1}{2}\gamma_0\sigma_1 \sin 2\theta \pm \frac{1}{2}\epsilon_0\sigma_1(1+\cos 2\theta) \tag{8}$$

where γ_0 is the shear component, θ is angle between the specimen axis and the normal to any potential habit plane, σ_1 is the absolute value of the applied stress (tension or compression), and ϵ_0 is the dilatational component.

An analytical model was derived by Todinov et al. [80] to explain the change in the M_s temperature in a complex stress state. They found that M_s is independent of the intermediate principal stress and is mainly affected by the minimum and the maximum principal stresses. A simplified relationship between the mechanical interaction energy and uniaxial tensile stress for a uniaxial tensile test can be described as $\Delta G_{mech} = 0.86\sigma$ [44].

The amount of transformed martensite during biaxial tension was found to be twice that of uniaxial tension at the same effective strain, which may be due to the higher number of shear band intersections formed during biaxial tension [81, 82].

The effect of initial grain orientation on austenite stability is difficult to observe in a polycrystalline material. However, some understanding can be gained from the deformation of a single crystal. Nimaga et al. found the critical compressive stress for initiating martensitic transformation in [100] and [110] micropillars to be 483 MPa and 700 MPa, respectively [83]. The underlying mechanism for this difference was ascribed to the stress required to induce the deformation twins, which were found only in [100] micropillars. Since the intersection of the deformation twins can become a nucleation site for martensite, it can also lower the critical stress for martensitic transformation in [100] micropillars [83].

2.3.6 Strain rate

There are two major effects to consider when looking at strain rate effects: adiabatic heating and martensite nucleation. High plastic deformation generates a lot of heat, and the higher the strain rate, the less time the material has to dissipate the heat. Since the amount of heating is proportional to the plastic deformation, adiabatic heating is limited when the deformation is mostly elastic. When the plastic work is substantial, a rise in the temperature may inhibit the transformation following the mechanism described earlier in section 2.2. Hecker et al. [81] found that in 304 stainless steel, the amount of α' martensite formed at the high strain rate (10^3 s^{-1}) was nearly identical to that formed at the low strain rate (10^{-3} s^{-1}), but only up to 20 % elongation. Above 20 % strain, the high-strain rate test resulted in nearly three times less amount of α' martensite due to the increased adiabatic heating. On the other hand, there is evidence that in TRIP steel, a larger amount of martensite can be formed when the strain rate is over 1 $s^{-1}$and strain amplitude does not exceed 10 % [84].

2.3.7 Magnetic field

The application of a magnetic field can affect the transformation of paramagnetic austenite to ferromagnetic α' martensite [85–87]. Herbert [88], as cited in [44], was the first to discover this effect by observing the increased hardness of martensite with the application of an external magnetic field. Later, Sadovsky et al. [89, 90] demonstrated that the M_s temperature in a Fe-Ni-Cr-C system increases with the application of a magnetic field. In other words, experimental data indicate that the $\gamma \rightarrow \alpha'$ transformation is accelerated by the magnetic field. However, there appears to be a critical magnitude of magnetic field below which no $\gamma \rightarrow \alpha'$ transformation is observed [91]. In Fe-Ni and Fe-Ni-C systems, the critical magnetic field appears to be in the order of 10 MA/m (125.6 kOe, 12.6 T) [92]. Once the critical magnetic filed was achieved, the fraction of the transformed martensite appeared to be unaffected by the magnetic field [92].

2.4 Models for phase transformation kinetics

2.4.1 Static strain models

Over the past few decades, several models have been proposed to describe the kinetics of $\gamma \rightarrow \alpha'$ transformation. Most models have been developed on a semi-experimental basis after tensile testing and are listed in Table 2. As a result of such an approach, considerable variance in the mathematical formulation can be found in the literature. Ludwigson et al. [94] and Angel et al. [93] described the kinetics of $\gamma \rightarrow \alpha'$ transformation as a function of strain with empirical Eq. (9). The exponent p is an autocatalytic constant that reflects the mechanism of accelerated phase transformation from the generation of additional α' martensite nuclei. The constant k_s indicates austenite stability. A more stable retained austenite would have a lower k_s value and the other way around.

Matsumura et al. [96] used an equation originally proposed by Burke et al. [95] to formulate a similar model for strain-induced transformation kinetics. Their equation was modified by Tsuchida [97] to obtain Eq. (10) and can be named as BMT model. Similarly to the LBA model, BMT takes into account autocatalysis via the exponent p. Alternative formulation for $\gamma \rightarrow \alpha'$ transformation kinetics was proposed by Sugimoto et al. [98], where the rate of transformation is proportional to the remaining fraction of retained austenite and can be expressed as Eq. (11). Pychmintsev et al. [99] suggested a modification of the Sugimoto model by taking into account hydrostatic pressure.

Previous models of $\gamma \rightarrow \alpha'$ transformation did not take into account the

microstructural phenomena and, therefore, only described the macroscopic consequences of the transformation process. Olson and Cohen (OC) [43], as cited in [102], decided to correct this and formulated a physical model in which shear band intersections are considered to behave as effective strain-induced nucleation sites. These shear bands can be mechanical stacking faults, twins, or ε martensite plates which fraction is related to the strain. The rate of shear band formation in the OC model, Eq. (13), is governed by a temperature-dependent function α, related to the intrinsic stacking-fault energy. The value

Table 2
Summary of different models for static strain-induced martensite transformation kinetics.

Model	Equation	
Ludwigson–Berger–Angel (LBA) [93, 94] V_γ initial austenite fraction ε conventional strain k_s austenite stability constant p autocatalytic strain exponent	$\xi = V_\gamma \cdot \left(1 + \frac{1}{e^{k_s \cdot \varepsilon^p}}\right)^{-1}$	(9)
Burke–Matsumura–Tsuchida (BMT) [95–97]	$\xi = V_\gamma \cdot \left(1 + \frac{p}{k_s \cdot \varepsilon^p \cdot V_\gamma}\right)^{-1}$	(10)
Sugimoto [98]	$\xi = V_\gamma \cdot \left(1 - e^{-k_s \cdot \varepsilon}\right)$	(11)
Pychmintsev [99] β_h hydrostatic pressure sensitivity P_h hydrostatic pressure during tensile test	$\xi = V_\gamma \cdot \left(1 - e^{-\varepsilon(k_s - \beta_h \cdot P_h)}\right)$	(12)
Olson–Cohen (OC) [43] α martensitic nucleation rate β possibility of a martensite embryo at the shear bands n fixed exponent	$\xi = V_\gamma \cdot \left(1 - e^{-\beta(1-e^{-\alpha\varepsilon})^n}\right)$	(13)
Gerberich [100] A constant for a given set of test conditions	$\xi = V_\gamma \cdot A\sqrt{\varepsilon}$	(14)
Guimarães [101] k_G stability of retained austenite Z measure of tiraxiliy	$\xi = V_\gamma \cdot \left(1 - e^{-k_G \varepsilon^Z}\right)$	(15)
Shin, Ha and Chang (SHC) [40] β stability of retained austenite ε_0 critical inelastic strain ξ_s martensite saturation fraction n speed of nucleation sites forming	$\xi = \xi_s \left[1 - e^{-\beta(\varepsilon - \varepsilon_0)^n}\right]$	(16)

of the parameter α increases when the stacking-fault energy decreases. This means α is both temperature and composition dependent. In the OC model, β is another temperature-dependent function indicating the probability for shear-band intersections to form α' nuclei. The exponent n is a constant. It relates to the number of shear band intersections per unit volume of austenite. High n values indicate that the number of shear band intersections is initially low and increases rapidly with strain [102]. A strain-induced martensite nucleation model equivalent to the OC model was also developed by Gerberich et al. [100] and Guimarães et al. [101].

Inspired by the OC model, several researchers have developed further constitutive models. Tomita and Iwamoto [103] based on the OC implemented a finite-element method taking into account the latent heat induced by martensitic transformation. Stringfellow et al. [104] reformulated the OC model in a generalized rate form so that the extent of martensite nucleation is a function not only of plastic strain and temperature but also of the triaxial stress state. Finally, Shin et al. [40] formulated Eq. (16) where the parameter β denotes the stability of retained austenite as a function of chemical composition and loading temperature. Shin pointed out that M_d temperature can be determined indirectly from the relationship between the stability parameter β and the test temperature.

The amount of deformation-induced martensite ξ as a function of strain can be generally outlined in Fig. 7. Three phases can be identified: accelerated (I), constant (II), and decelerated (III) rate of phase transformation [105].

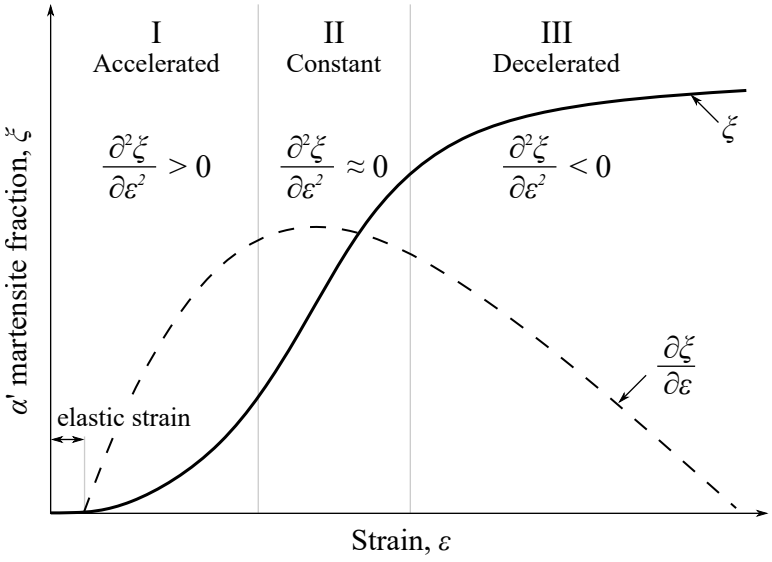

Fig. 7. Content of α' martensite as a function of strain in an isothermal tensile test.

2.4.2 Cyclic strain models

Unlike static tensile loading, cyclic loading introduces repeated elastic deformation. This leads to a deviation in the $\gamma \rightarrow \alpha'$ kinetics from Fig. 7. Depending on the temperature, chemical composition, and strain amplitude, the phase transformation rate can vary from linear to extremely sigmoidal with a clear martensite saturation threshold. For 300 series steel in the low-cycle fatigue (LCF) regime, it is common to observe a behavior similar to that shown in Fig. 8. The accelerated period (I) is present but occupies a much shorter period of time than the decelerated period (III). The end of the test is typically followed by a short but impactful crack propagation period where the rate of phase transformation increases again due to changes in the stress state until complete specimen failure.

On the basis of extensive experimental data, Smaga, Walther, and Eifler [106] developed a model for the description of plasticity-induced martensite formation in metastable austenite under cyclic loading. This model was done on the basis of plastic-strain-controlled fatigue tests where cumulative plastic strain λ is a major input parameter that can be calculated as Eq. (17):

$$\lambda = 4 \cdot \sum_{i=1}^{N_i} \varepsilon_{ap} \tag{17}$$

It was observed [106] that the strain energy density W, which essentially is the area of the hysteresis, shifted to higher values with increased plastic strain amplitude ε_{ap} for identical λ values. This signified that the cumulative strain energy density Ω in Eq. (18) is another parameter influencing the martensite

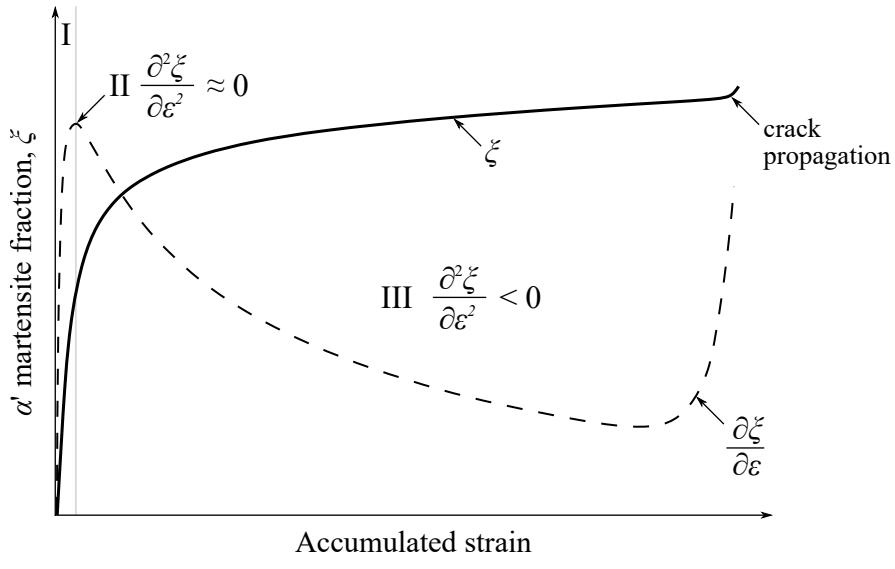

Fig. 8. Content of α' martensite as a function of accumulated strain in a constant amplitude total strain controlled isothermal fatigue test.

transformation.

$$\Omega = \sum_{i=1}^{N_i} W \tag{18}$$

With this in mind, the rate of cyclic martensite transformation $^{d\xi}/_{dt}$ can be described as a function of cumulative plastic strain λ and the cumulative strain energy density Ω:

$$\frac{d\xi}{dt} = (\xi_s - \xi) \cdot a \cdot \Omega \frac{d\lambda}{dt} \tag{19}$$

where ξ – measured martensite fraction, ξ_s – martensite saturation (maximum) fraction, and a is a fit parameter. The difference between the measured and saturation fractions $\xi_s - \xi$ describes the rate of martensite formation. Solving the differential equation (19) with the boundary conditions $\xi_0 = 0$ and $\lambda_0 = 0$ at the start of cyclic loading, Eq. (20) can be derived, representing the martensite formation under cyclic load.

$$\xi = \xi_s \cdot \left(1 - e^{-a \cdot \Omega \cdot \lambda}\right) \tag{20}$$

The relation between the cumulative plastic strain and the cumulative strain energy density can be described with a power law:

$$\Omega = b \cdot \lambda^c \tag{21}$$

where b – load amplitude coefficient, c – material constant. Substituting Ω in Eq. (20) by using Eq. (21) with $\alpha = a \cdot b$ and $n = c + 1$, the expression for martensite fraction ξ can be written as Eq. (22):

$$\xi = \xi_s \cdot \left(1 - e^{-\alpha \cdot \lambda^n}\right) \tag{22}$$

Prior to the work of Smaga, Kaleta, and Zietek [107] proposed the introduction of a martensitic transformation cyclic limit, which would be a critical point for the $\gamma \rightarrow \alpha'$ transformation. Later, Krupp [108] as cited by [109] suggested a similar approach toward the estimation of α' martensite fraction in the LCF regime, which can be formulated by Eq. (23):

$$\xi = 1 - e^{\left(-\frac{N}{\tau}\right)^n} \tag{23}$$

with parameter τ proportional to plastic strain amplitude and n is a test conditions specific fit parameter. Mroz and Zietek [110] would later derive constitutive equations for an elastoplastic model making use of irreversible thermodynamics with internal parameters. Similarly to previous models, they also described the martensite volume fraction as a function of accumulated strain. Chen et al. [111] published a cyclic plasticity model for martensite transfor-

mation, where they studied the uniaxial ratcheting[2] behavior of 304 austenitic stainless steel at 110 K. Under the assumption of the von Mises yield criterion and normal plasticity flow rule, they developed a numerical algorithm of plastic strain with the proposed model to implement the finite element calculation of the model.

[2]Ratcheting is a cyclic creep caused by unsymmetric stress cycles.

3 Fatigue Parameters and Terminology

Much of the literature defines fatigue in terms of crack propagation due to cyclic loading. However, this does not cover all aspects of cyclic loading and fatigue. By considering the changes in the material at the pre-crack stage, a more comprehensive definition of fatigue can be given: *an undesirable change in mechanical and electrochemical properties due to cyclic loading that can further lead to crack initiation and eventual failure of a component.*

Much progress has been made in fatigue testing since Albert Wilhelm published the first paper on fatigue in 1837. Modern servo-hydraulic fatigue machines allow better control of stress and strain while recording the response of the material at high resolution. Recently, many non-destructive techniques have been introduced to improve material characterization beyond stress-strain measurement. These include infrared measurements, eddy current, magnetic sensing, and digital image correlation, to name a few. With this large number of variables in fatigue testing, it is important to define what parameters constitute a fatigue test. The following are the parameters that should be selected from each section to define a single fatigue test. The methods used in this work are underlined.

3.1 Control parameter

A control parameter is a change in a physical value (stress, strain, temperature) that follows a predetermined by the test program variation over time. The most common control parameters include the following:

Total strain When the fatigue test is controlled directly by the extensometer readout, it is called a total strain controlled test. Fig. 9a illustrates the applied strain function with a triangular waveform of constant amplitude. Stress, in this case, is not controlled and may gradually increase or decrease in accordance with changes in the microstructure. Such material response is known as cyclic hardening and cyclic softening (see Fig. 9b and c). Regardless of the control parameter, total strain amplitude is defined by Eq. (24):

$$\varepsilon_{at} = \frac{1}{2}\left(\varepsilon_{max} - \varepsilon_{min}\right) \tag{24}$$

Plastic strain If the elastic portion is subtracted from the total strain, such tests would be plastic strain controlled. To obtain plastic strain, it is necessary to analyze a stress-strain hysteresis loop, which is shown schematically in Fig. 10. From the hysteresis in Fig. 10, it is clear that plastic strain can-

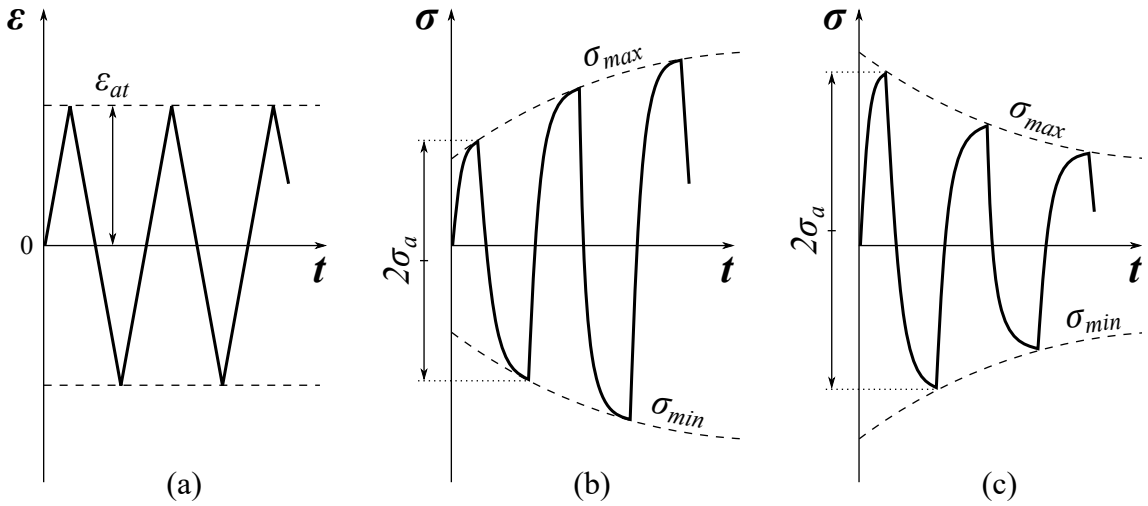

Fig. 9. Constant amplitude total strain controlled fatigue test with a triangular input waveform: a) control waveform; b) cyclic hardening response; c) cyclic softening response.

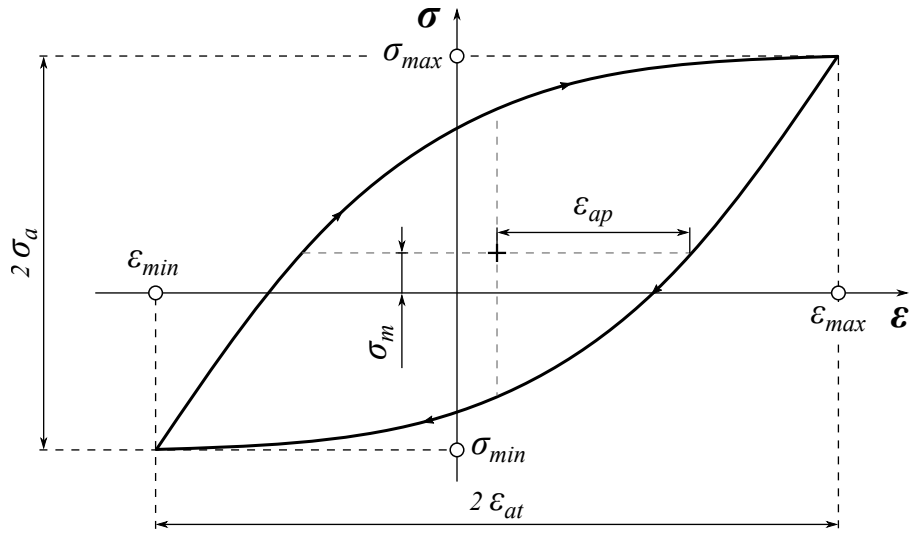

ε	strain	σ	stress
ε_{max}	maximum strain	σ_{max}	maximum stress
ε_{min}	minimum strain	σ_{min}	minimum stress
ε_{ap}	plastic strain amplitude	σ_m	mean stress
ε_{at}	total strain amplitude	σ_a	stress amplitude

Fig. 10. Schematic representation of an isothermal stress-strain hysteresis loop.

not be measured directly but can only be calculated from simultaneous stress and strain measurements. This makes it more difficult to control, and if strain is primarily elastic, the control error can be significant. Nevertheless, there are reasons to perform plastic strain controlled fatigue testing. Since many microstructural changes in the material are proportional to the plastic strain, plastic strain control allows for easier analysis of plastic deformation since the accumulated plastic strain in this case is an arithmetic sum of the number of cycles.

Stress One of the more common methods of conducting a fatigue test is to control the force applied to the specimen, which is measured by a force sensor (load cell). Stress-controlled tests are not only easier to perform, but also provide direct information on the number of cycles to failure for a given load, which may be preferable to strain in practical applications. In stress-controlled testing, strain and temperature become the material response. Cyclic softening results in increased strain amplitude and cyclic hardening results in decreased total strain amplitude, which is the opposite of the stress response in Fig. 9. Stress-controlled tests are typically performed in the elastic deformation range. Regardless of the control parameter, the stress amplitude is defined by Eq. (25), while mean stress in defined by Eq. (26), which can also be explained by Fig. 10.

$$\sigma_a = \frac{1}{2}\left(\sigma_{max} - \sigma_{min}\right) \tag{25}$$

$$\sigma_m = \frac{1}{2}\left(\sigma_{max} + \sigma_{min}\right) \tag{26}$$

Temperature It is possible to perform a simple thermo-mechanical test simply by controlling the change in temperature. When the fatigue specimen is constrained from changing its dimensions, thermal expansion can generate large stresses in the material. In this case, stress and strain simultaneously become the response of the material. This is undesirable because it creates ambiguity in the failure mechanisms. In other words, such tests simulate only specific loading conditions that do make sense in some applications. In a more comprehensive approach, the temperature change is superimposed on strain or stress control, as described in section 3.5.

3.2 Strain rate and waveform

The strain rate is determined by the frequency of the applied load and its waveform. Common waveforms include sine, triangle, and trapezoid. The triangular waveform has the advantage of applying strain at a constant rate. It can only be used at low frequencies because it has a very sharp change in direction. At higher frequencies, and especially in resonant systems, the sine wave is a more practical option. The sine wave has a larger fraction of time at the extremes compared to the triangle waveform. This can be significant when material creep occurs, such as at elevated temperatures. The creep-specific studies typically use a trapezoidal waveform with a long dwell time.

3.3 Amplitude variation

Depending on the objective of the fatigue test, the amplitude of the control parameter may vary accordingly. The most common variations are listed below.

Constant Constant amplitude test (CAT) signifies no variation in the amplitude of the control parameter. CATs are the standard tests for investigating fatigue life and other material failure-related parameters specified in ISO 12106 and ASTM E606. Constant amplitude testing requires a large number of fatigue tests to gain an understanding of material performance at both low and high stress levels. Fig. 9a illustrates a constant amplitude total strain controlled test.

Step increase In a step increase test, the amplitude of the control parameter remains constant over a given time period t_{step}. Each time t_{step} elapses, the amplitude is increased by a fixed amount, making "steps". Depending on the type of control, such a test may be called a Strain Increase Test (SIT) or a Load Increase Test (LIT). Step increase tests are performed to gain an understanding of the initial elastic behavior of the material with subsequent large plastic deformation within a single fatigue test. When a SIT is performed under constant strain rate conditions, as shown in Fig. 11, the test frequency would have to decrease with each step to accommodate the increased strain amplitude.

Complex / random load In many applications, structures are subjected to random loads. It is possible to design an application-specific load sequence that simulates real-life conditions. Commonly used are block tests, where the sequence of two different amplitudes is repeated continuously. Typically, the high amplitude block would have a shorter duration and the low amplitude block would have a longer duration. Although there are advantages to applying

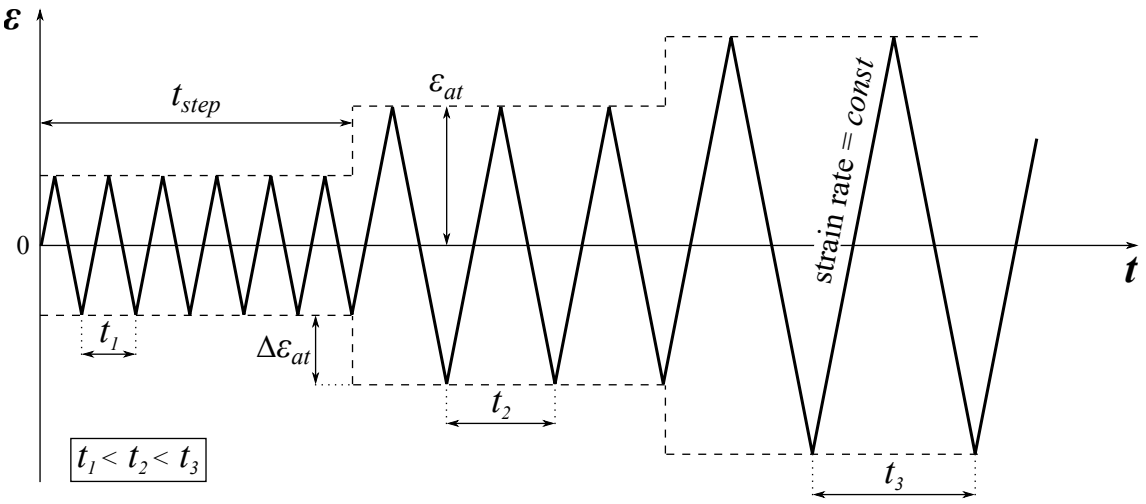

Fig. 11. Strain increase test (SIT) with a constant strain rate triangular waveform.

the load in an application-specific manner, analyzing and interpreting such data can be challenging.

3.4 Compression-tension ratio

Depending on the objective of the fatigue test, the maximum and minimum amplitudes of the control parameter can be either symmetrical or skewed to one side. In a stress-controlled test, the ratio R between compression and tension amplitudes, known as the stress ratio, can be determined as follows:

$$R = \frac{\sigma_{min}}{\sigma_{max}} \tag{27}$$

While any R value can be set for a fatigue test, there are three common ratios:

Fully reversed ($R = -1$) If the positive (tension) load is equal to the negative (compression) load, the fatigue test is completely reversed. Note that the ratio R is only valid for the control parameter. If the strain is controlled, there may be a shift in the mean stress (see Fig. 10). If stress is controlled, the same can be true for the strain amplitude.

Compression-compression ($R = -\infty$) If the applied load remains negative (compressive) with a maximum value of zero, such a test can be called a fully unloaded compression-compression test.

Tension-tension ($R = 0$) If the applied load is only positive (tensile) with the lowest value being zero, such a test can be called a fully unloaded tension-tension test.

3.5 Specimen temperature

Depending on how the specimen temperature changes during the fatigue test, three categories can be distinguished:

Ambient Such fatigue tests are performed without any external heating or cooling of the fatigue specimen. The specimen temperature may still increase due to the adiabatic self-heating of the fatigue specimen.

Isothermal If the temperature of the fatigue specimen remains constant during the test, the test is said to be isothermal. It can be performed at any temperature, including ambient, elevated, or cryogenic, as long as that temperature is constant. Adiabatic heating of the specimen should be compensated in this case.

Thermo-mechanical When the temperature of the fatigue specimen follows a predetermined time variation, such a test is said to be a thermo-mechanical fatigue (TMF) test. Typically, the temperature variation frequency is the same as the applied strain to simulate stresses due to thermal expansion. The difference between the strain waveform and the temperature waveform can be expressed in terms of phase angle. If maximum temperature occurs at maximum (tensile) strain, the phase angle is 0° and such a test is an in-phase (IP) TMF test. If maximum temperature occurs at minimum (compressive) strain, the phase angle is 180° and such a test is out-of-phase (OP). In TMF testing, the thermal expansion of the specimen can be comparable to or greater than the applied strain. For this reason, a distinction should be made between mechanical strain ε_{mech} and thermal strain ε_{therm}. Total strain ε_t can be represented as a sum of thermal and mechanical strains:

$$\varepsilon_t = \varepsilon_{therm} + \varepsilon_{mech} \tag{28}$$

where thermal strain ε_{therm} can be also calculated with the thermal expansion coefficient as a function of temperature.

Following parameters are given specifically for the TMF setup described in section 5.3 on page 67. The temperature of the specimen was measured at the center of the gauge length and denoted as T_c. The highest temperature reached at the center of the gauge length is denoted as T_{ch}, and the lowest temperature is denoted as T_{cl}. The low temperature T_{cl} was used here as the zero thermal strain point, i.e. when $T = T_{cl} \rightarrow \varepsilon_{therm} = 0$. Note that the maximum temperature of the specimen $T_{max} = T_{ch}$ but the minimum temperature $T_{min} < T_{cl}$. This is due to the fact that the shoulders of the specimen remain close to T_{cl} and,

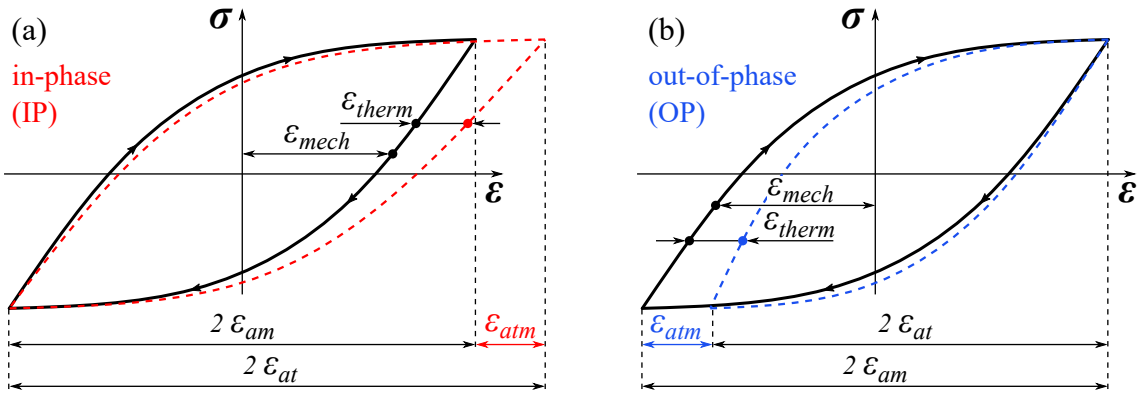

Fig. 12. Thermo-mechanical stress-strain hysteresis loops: a) in-phase, b) out-of-phase, where ε_{therm} – thermal strain, ε_{mech} – mechanical strain, ε_{am} – mechanical strain amplitude, ε_{atm} – thermal strain amplitude.

when additionally cooled with compressed air, can become colder than the gauge length. Since the thermal load was always applied relative to T_{cl}, the mechanical strain amplitude ε_{am} in the case of an IP test (see Fig. 12a) can be defined by Eq. (29):

$$\text{IP} \rightarrow \varepsilon_{am} = \frac{1}{2}\left[(\varepsilon_{max} - \varepsilon_{atm}) - \varepsilon_{min}\right] \tag{29}$$

and in the case of an OP test by Eq. (30), which is also illustrated by Fig. 12b:

$$\text{OP} \rightarrow \varepsilon_{am} = \frac{1}{2}\left[\varepsilon_{max} - (\varepsilon_{min} - \varepsilon_{atm})\right] \tag{30}$$

where ε_{max} and ε_{min} are the maximum and the minimum total strain, respectively.

3.6 Load magnitude / number of cycles

The relationship between applied load and the number of cycles to failure is the fundamental parameter of fatigue testing. It is described by the σ_a-N_f (or simply S-N) curve, also known as the Wöhler curve, after August Wöhler (1819 – 1914). This curve shows how many cycles N_f it would take for a fatigue specimen to fail at a given stress amplitude σ_a. In the case of a strain-controlled fatigue test, this curve is substituted by the ε_{at}-N_f curve. Logically, high stress equals a low number of cycles to failure and low stress equals a high number of cycles to failure. Based on this principle, fatigue tests can be divided into three categories:

Low-cycle fatigue (LCF) Materials subjected to extreme thermal and mechanical stresses are typically tested in the LCF regime, where the number of cycles to failure does not exceed 10^4. Such fatigue tests are typically performed

on servo-hydraulic machines. With a typical test frequency of 1 to 5 Hz, it is relatively easy to implement more accurate means of strain measurement. For this reason, strain-controlled tests are common in LCF.

High-cycle fatigue (HCF) The typical number of cycles to failure in HCF testing can exceed 10^6 and is performed specifically to determine high cycle fatigue strength. HCF testing is still possible on servo-hydraulic fatigue machines capable of at least 5 Hz frequency. However, even if the fatigue system is capable of much higher frequency, the self-heating of the fatigue specimen may be the limiting factor.

Very high cycle fatigue (VHCF) VHCF tests exceed the HCF range by approximately two orders of magnitude and can exceed 10^8 cycles. The performance of the material in the VHCF regime must be investigated when the material is subjected to vibrational loading. In VHCF, the fatigue specimen is typically vibrated at its own resonant frequency by a piezoelectric or electromagnetic actuator. Cooling of the specimen should often be provided to avoid excessive self-heating of the specimen.

3.7 Failure criteria

The definition of what constitutes a specimen failure in fatigue testing directly affects the *S-N* curve. Complete specimen rupture is the most obvious way to define specimen failure. However, under some test conditions, especially in strain-controlled tests, there may be a significant number of cycles between crack initiation and complete rupture. In this case, a decision can be made to define failure when the tensile load has been reduced by a certain percentage compared to the compressive load (assuming the strain is fully reversed). In this work, specimen rupture was considered as the failure criterion.

4 Analytical Methods for Martensite Measurement

4.1 Magnetic parameters related to α' martensite

As described before in section 2, deformation-induced martensite forms a distorted bcc or bct lattice and it is generally considered to be ferromagnetic. In ferromagnets below Curie temperature, spins spontaneously align due to exchange forces [112]. This means α' martensite is magnetized to saturation even in the absence of an external magnetic field. Martensitic grains are then divided into smaller magnetic domains, which directions of magnetization are such that the specimen as a whole has no net magnetization. This phenomenon of ferromagnetism leads to the formation of a hysteresis loop when subjected to an external magnetic field, as demonstrated by Fig. 13.

It is important to keep in mind that ferromagnets are always magnetized to saturation and change the net magnetization primarily by domain wall movement. In the case of α' martensite, ferromagnetic grains can be separated by significant distance from each other in a paramagnetic fcc matrix. When a ferromagnetic grain is small enough, it may turn into a single-domain grain, with magnetization along the easy crystal axis. In case the grain is smaller than 10 nm, it may have thermal vibrations with the same order of magnetite as its magnetic energy [113, 115]. Such grains do not have a stable remnant magnetization, as they continually undergo thermal reorientation. Fig. 14 shows

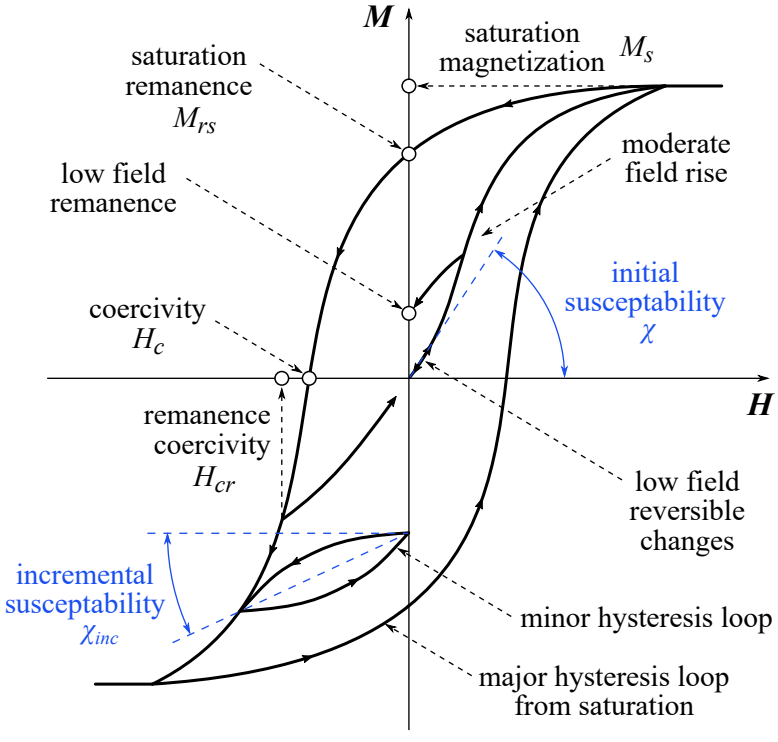

Fig. 13. Schematic representation of a magnetic M-H hysteresis loop and the initial magnetization curve. Modified after Thompson [113], Sung, and Rudowicz [114].

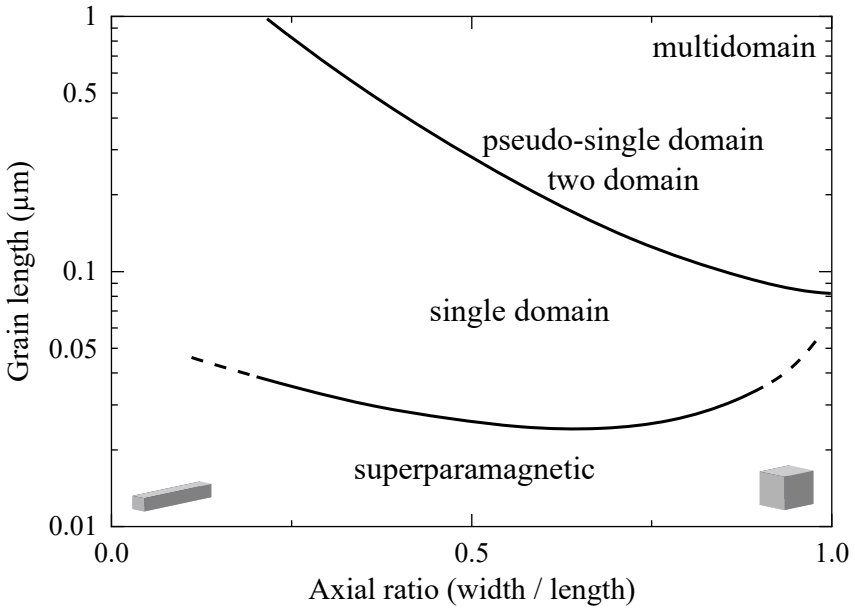

Fig. 14. The division between multidomain, stable single-domain and superparamagnetic grains in magnetite as a function of grain length to width ratio. Data after Butler and Banerjee in [113].

critical sizes for magnetite[3], as an example.

There are three forms of magnetic anisotropy applicable to α' in γ austenite. One arises from the crystal lattice structure, i.e., crystals have different magnetic properties in different orientations. This can be well illustrated by magnetization curves for single crystals of iron in Fig. 15. Single crystal of bcc iron is harder to magnetize in the body diagonal direction, although saturation magnetization remains the same for all directions. A second form of anisotropy is connected with the shape, size, and overall distribution of α' grains. Considering that α' martensite commonly has a lath or lenticular (lens) shape [117, 118] demagnetizing field[4] would oppose the magnetization in the short dimension more than in the long dimension. Due to this effect, the easiest to magnetize is a needle-shaped grain along its axis. A third form of anisotropy is induced by mechanical stress through the phenomenon of magnetostriction. The magnetostriction coefficient for iron is negative, meaning the magnetization direction will be perpendicular to the principal stress direction. For a single crystal of iron, this coefficient is in order of 10^{-10} Oe^{-1} at room temperature [120, 121].

[3]Magnetite is an oxide of iron ($Fe^{2+}Fe_2^{3+}O_4$) with ferrimagnetic properties. It is not directly comparable with α' martensite, but rather an example of how size affects magnetic properties.

[4]Demagnetizing field is a field in the opposite to magnetization direction, created by magnetic poles where magnetization goes from a positive value inside the object to zero immediately outside. It strongly depends on shape and orientation of the object in the magnetic field [119].

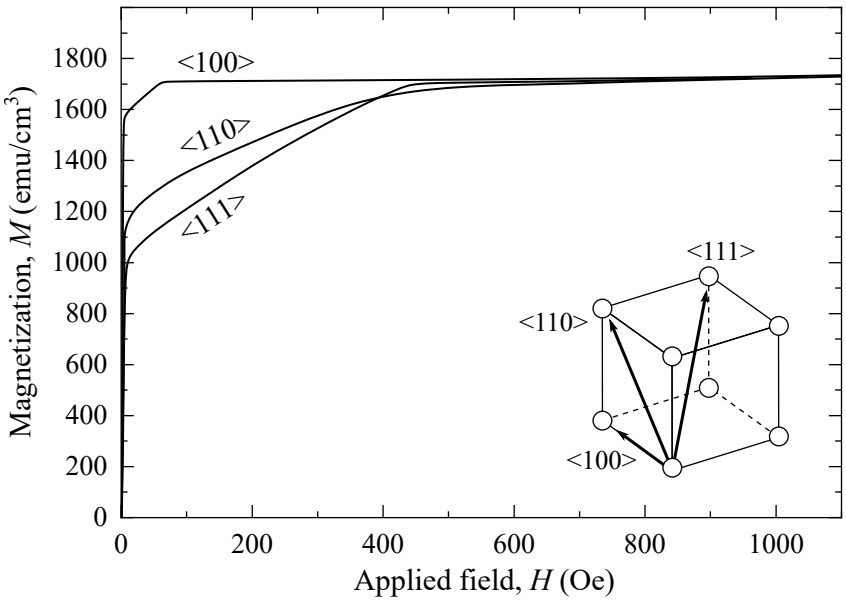

Fig. 15. Magnetization curves for a single crystal of iron. Adopted from [112, 116].

4.2 Magnetic methods

The ever-popular instrument for the measurement of α' martensite in fatigue testing is the Feritscope, produced by Fischer [122]. It can be found in many studies involving mechanical deformation and $\gamma \rightarrow \alpha'$ phase transformation [39, 123–136]. Feritscope was developed primarily for testing welds and supposed to be calibrated on a set of δ ferrite standard samples. Talonen et al. [137] pointed out that this calibration is not always accurate for α' martensite. When compared with X-ray diffraction, Feritscope had on average 1.766 times lower values, meaning the ferrite (%) could be converted to α' martensite (%) by multiplying the ferrite reading by 1.766 [137].

If the amount of deformation-induced martensite is fairly small (below 0.5 %), which is often the case at elevated temperatures, the magnetic contribution of austenite can no longer be neglected. Zhao et al. [138] demonstrated the differences in ferromagnetic and paramagnetic responses to an applied magnetic field. Their work showed that the contribution of austenite to magnetization should be taken into consideration when the volume fraction of α' martensite is low.

When it comes to very low quantities of α' martensite, magnetic methods usually have an advantage over diffraction methods. One of the popular instruments to analyze feebly magnetic materials is a vibrating sample magnetometer (VSM). The volume fraction of martensite can be calculated as a ratio of the saturation magnetization of the test specimen to the specimen with a pure martensitic structure. The saturation magnetization of pure α' martensite can be expected to be in the range of 143 – 157 emu/g [139–142]. Magnetization of the material in a pure austenitic state should be then subtracted from

the calculation.

There have been attempts to utilize magnetic flux sensors, such as GMR or Hall effect sensors in the vicinity of the sample without any external magnetic field[5] applied [2, 143–145]. For example, Nebel and Eifler [146] used a superconducting quantum interference device (SQUID) to measure the remanent magnetization of fatigue specimens *ex-situ*. However, this approach does not qualify as a quantitative method and can only indicate a change in magnetic flux around the specimen. A much more reliable way of estimating the quantity of ferromagnetic phase in austenite is to measure the magnetization and orient magnetic dipole moments in one direction using an external magnetic field, i.e., to measure magnetic susceptibility.

Some of the common methods that utilize this principle are listed in Table 3, with appropriate references to more detailed information. The disadvantage of magnetic measurements comes down to a nontrivial calculation of the martensite fraction and, in many cases, it requires calibration. Magnetic methods are also at a disadvantage when the amount of α' martensite exceeds that of austenite. In this case, it becomes more difficult to give an accurate volume fraction of the two phases due to a diminishing change in magnetization.

4.3 Metallographic and diffraction methods

Commonly used in material science methods to characterize a crystalline structure, such as X-ray diffraction and electron backscatter diffraction (EBSD), are quite dependent on the quality of surface preparation. Juuti et al. demonstrated that for surface preparation of metastable austenite, most α' martensite is induced by mechanical polishing, with focused ion beam (FIB) milling being slightly better, and electropolishing being the best in terms of deformation-free surface preparation [176].

The problem lies in the depth of information of metallographic methods. For EBSD, it can be around 50 nm [177, 178], which is comparable with laboratory X-ray diffraction (Cu Kα) [179]. The shallow information depth is less of a concern for synchrotron X-ray diffraction, where the depth of information can exceed 100 μm [179, 180]. Neutron diffraction is the least affected by the surface preparation as the neutrons can penetrate deep inside the material.

Microscopy-based methods, which include EBSD, rely on counting the surface area of each phase to estimate the volume fraction. This is already an approximation that only works under the assumption that the distribution of two phases in the volume is somewhat homogeneous. Furthermore, when the

[5] Earth magnetic field has very little effect due to high coercivity of the material and in this context can be neglected.

Table 3
Common methods suitable for low quantity α' martensite measurements. Size refers to the maximum sample size that can be used for the given technique.

Method			Sensitivity	Size
Induction method (alternating field)	Moving sample	Vibrating sample magnetometer [147]	• • • • [a]	•
		Spinner magnetometer [148]	• • •	• •
		Extraction magnetometer [149, 150]	• • •	• •
	Stationary sample	Balanced a.c. bridge (e.g., Kappabridge) [151]	• • •	• •
		Alternating current method (single pick-up coil) [152]	• [b]	• • •
		Satmagan[c] [153]	• • •	• •
		Feritscope[d] [122, 154] and eddy current systems [155]	• •	• • • •
Force method (static field)	Force on the sample	Curie-Cheneveau balance [156]	• • •	• •
		Gouy balance [157]	• • •	• •
		Faraday balance [158]	• • •	• •
		Horizontal translation balance [159]	• • •	•
		Variable field translation balance[e] [160]	• • • •	•
	Force on the magnet	Pull-force measurement (e.g., Magne-Gage) [161]	• •	• • • •
		Magnetic indicators (e.g., Severn Gage) [162]	•	• • • •
		Evans (Johnson-Matthey) balance [163]	• • •	• •
		Rankine balance [164]	• • •	• •
		Davis balance [165]	• • •	• •
		Magnetic Force Imaging ([166], sec. 5.1)	• • •	• • •
		Uniaxial force balance ([167], sec. 5.2)	• • •	• • • •
		Balanced core magnetometer (sec. 5.4)	• •	• • • •
Metallographic methods	Point / area counting	Scanning electron microscopy + EBSD [168, 169]	• •	• •
		Light microscopy [137]	•	• • •
		Chemical etching / ferrofluid + microscopy [137]	• •	• • •
		Magneto-optical Kerr effect microscopy [170]	• •	• • •
		Atomic / magnetic force microscopy [171]	• [f]	• •
	Peak height	X-ray diffraction [172]	• •	• • •
		Synchrotron X-ray diffraction [173]	• • •	• •
		Neutron diffraction [174]	• • [g]	• • •

a The pickup coil can be coupled with superconducting quantum interference device (SQUID) [175] to increase sensitivity even further.
b Primarily used to obtain *B*-*H* curves in soft magnetic materials.
c Essentially, a commercially available version of the Gouy balance with a torsion beam.
d Commercially available low-frequency eddy current hand-held instrument
e Uses a combination of static and alternating magnetic fields.
f Limited by scanning speed.
g Generally more reliable than X-ray due to much larger gauge volume, but neutron sources typically inferior in brilliance to synchrotron sources.

amount of α' is very small, a much higher magnification is needed to observe it, while a much smaller surface area is examined. This leads to a further decrease in the statistical significance of the measurement.

Chemical etching can greatly improve the detectability of α' martensite in austenite. The etching solution proposed by San Martin et al. [181], which is based on the work of Lichtenegger and Blöch, can be used to reveal prior austenite grain boundaries while providing contrast between the two phases. There is a big variety of etching techniques that can be chosen based on what should be revealed in the microstructure. A good overview of imaging phases in steels was provided by Vander Voort and Manilova [182].

One big advantage of metallographic and diffraction methods over magnetic methods is a more straight-forward interpretation of the data. For that reason, magnetic measurements should be complimented with diffraction or microscopic analysis. Some of the most common methods are listed in Table 3 with relative sensitivity and sample size provided for comparison.

Part II

Experimental Results and Methods

"An experiment is a question which science poses to Nature, and a measurement is the recording of Nature's answer. But before an experiment can be performed, it must be formulated. Before the result of a measurement can be used, it must be interpreted."

Max Planck

5 Original Experimental Instrumentation

This chapter gives a fundamental description of the instrumentation that has been developed to analyze the $\gamma \rightarrow \alpha'$ transformation process. A thorough characterization would require information about where and how fast the transformation takes place. To answer the first part of this question, Magnetic Force Imaging (MFI) was developed. As described in more detail in section 5.1, it allowed quantitative visualization of the distribution of the smallest amount of martensite in the material. What MFI could not do was characterize the dynamics of the phase transformation.

Two additional instruments were developed for dynamic characterization: a special thermo-mechanical fatigue (TMF) rig and *in-situ* magnetic measurement equipment. The TMF setup had to provide unobstructed access to the fatigue specimen during the test and have no significant electromagnetic interference. This TMF rig is described in section 5.3. The magnetic instrument had to read fractions of a percent of the martensite volume in a very hostile environment for precision measurement, where the temperature changes more than 300 °C in a few seconds, compressed air cools below ambient temperature, and the heating current of several hundred amperes inevitably generates a strong magnetic field. This issue was resolved with uniaxial magnetic balance (UMB), described in section 5.2.

An experimental force-based magnetometer was constructed to further analyze the magnetic properties of the material. The signals obtained showed the possibility of estimating the coercive force of weakly magnetic materials in a handheld format. Such a device is further described in section 5.4. To the best of the author's knowledge, the magnetic devices described in this chapter are not directly analogous to any of the existing methods. Patent information can be found in Appendix B.

5.1 Magnetic Force Imaging (MFI)

MFI was developed to answer the question of where the $\gamma \rightarrow \alpha'$ phase transformation occurs and to quantify the amount of deformation-induced martensite. The scale required for this in fatigue testing is tens of millimeters. The common technique used at this scale is chemical etching and optical microscopy [182]. A wide variety of etching techniques are available, including solutions capable of revealing the prior austenite grain [181]. However, etching is not really able to differentiate small differences in α'-martensite volume fraction [136]. Magnetic methods, on the other hand, can be extremely sensitive to the presence of a ferromagnetic phase in paramagnetic materials.

Some similar to MFI magnetic methods include Feritscope [122], Kerr effect and magneto-optical sensors [183, 184], Gouy, Faraday-Curie magnetic balances [113], Satmagan [153], pull-force measurement [185], magnetic force microscopy (MFM) [171, 186], scanning Hall probe microscopy [187]. A good comparison of some of these methods was given by Talonen et al. [137]. A more in-depth overview of existing magnetic methods can be found in section 4.2.

The working principle of MFI is similar to that of magnetic force microscopy (MFM), which is essentially atomic force microscopy (AFM) with a magnetic tip. The main difference between MFI and MFM is the size of the magnetic tip and therefore the induced magnetization in the material. The MFM magnetic tip does not generate a sufficient magnetic field to cause significant reorientation of magnetic moments in the material [188]. In this sense, the principle of MFM analysis is closer to scanning Hall probe microscopy, which maps the magnetic stray field on the surface. The MFI magnetic tip, on the other hand, generates a field strong enough to reorient magnetic domains in the material (see Fig. 16).

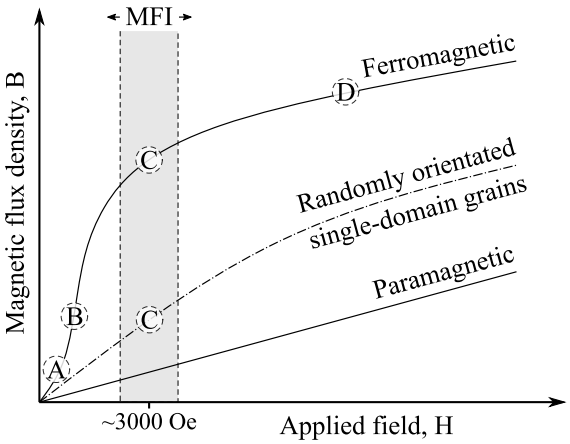

Fig. 16. A simplified explanation of different magnetic states that can be analyzed with MFI: A) initial permeability; B) maximum permeability; C) MFI range, where relative permeability is estimated; D) saturation magnetization.

5.1.1 MFI working principle

The MFI method measures the force interaction between a NdFeB magnetic tip (see Fig. 17) and the surface of a specimen. The magnetic tip is mounted on a ferromagnetic rod and attached to a sensitive force sensor (load cell). The force acting on this magnetic tip is the result of the interaction between the magnetic tip and the dominant ferromagnetic part in the material together with the weak paramagnetic part.

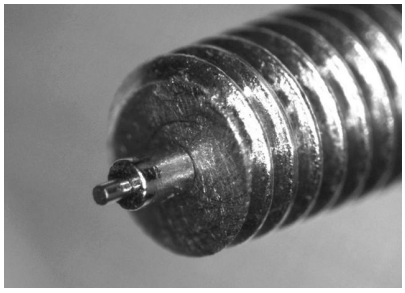

Fig. 17. NdFeB magnetic tip used for MFI, 0.3 mm in diameter.

By using magnetic tips with different field strengths, different effects can be achieved. A weak magnetic tip is unable to sufficiently magnetize the material (that is, to align most mag-

netic moments within the effective interaction volume in one direction [157]), and therefore, results obtained mainly represent stray fields on the surface, as with MFM. A strong magnetic field generated by the NdFeB tip used in this work is capable of locally magnetizing the material to a (near) saturation state. In this case, the measured force is directly related to the magnetic permeability of the material and, as such, can be calibrated to the ferrite fraction [137, 189, 190].

The imaging process is realized by consequent line scanning in XY (linear) or ΩY (rotary) coordinates (Fig. 18 and Fig. 19) in constant speed mode. Scanning starts with a fast trace line, where no data are acquired. The purpose is to pre-magnetize the material for the retrace line, where the force response is measured. After the retrace is complete, the Y-stage moves the sensor to the next line. As a result, data are obtained only in one direction of the scanning. The typical spatial resolution of a scan is 0.05 mm. Lateral resolution is strictly limited by the magnetic tip diameter and dependent on the working distance.

The minimum feature size detectable by MFI is not strictly limited by the diameter of the magnetic tip. As long as the force response exceeds the noise level, the magnetic feature can be visualized. Micron-sized ferromagnetic particles can typically be detected in single quantities on a non-magnetic substrate. Stainless steel in a fully austenitic state can also be measured despite a very weak force response of the fcc lattice.

The depth at which most MFI information is obtained is highly dependent on the material, the working distance, the gradient and the strength of the magnetic field generated by the tip. As a rule of thumb, it can be said that the depth of MFI information is equal to half the diameter of the magnetic tip. For the magnetic tip used in this work, this would be 150 μm. This depth significantly exceeds that of many other metallographic analysis methods. For example, it is only around 50 nm for electron backscatter diffraction (EBSD) [177, 178].

5.1.2 Calibration to ferrite vol. fraction and permeability

For the correct interpretation of MFI data, it is important to note that the values of volume fraction are given for δ ferrite and not α' martensite. Metallographic investigations with EBSD showed no significant difference between α' martensite content and MFI reading, calibrated to δ ferrite below 20 % vol.. This is also in agreement with the calibration curves presented by Fava et al. [133]. For MFI readings above 20 %, a calibration factor of 1.7 is recommended to convert ferrite fraction to α' volume fraction [133].

Although calibration to volume fraction provides a quick evaluation cri-

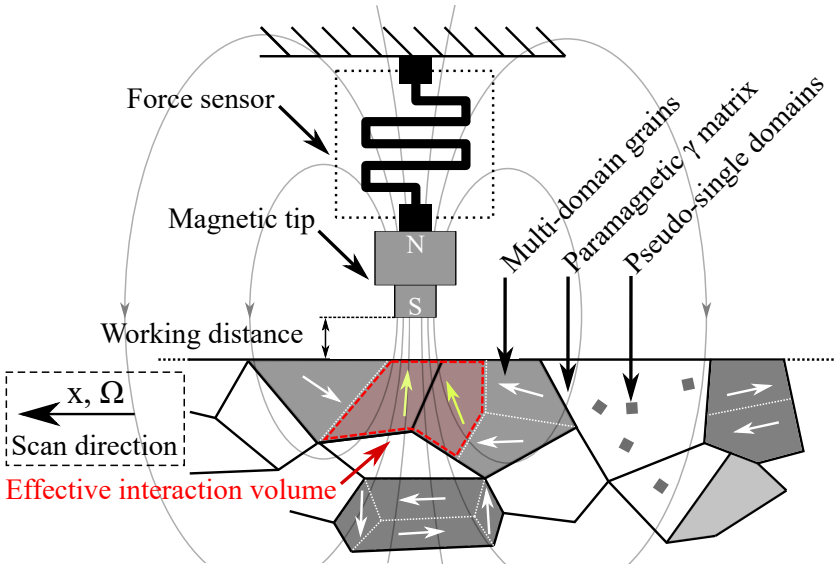

Fig. 18. Schematic illustration of the magnetic force imaging principle. Filled areas show ferromagnetic grains in an otherwise paramagnetic austenitic matrix. Effective interaction volume illustrates the depth of information obtained with MFI.

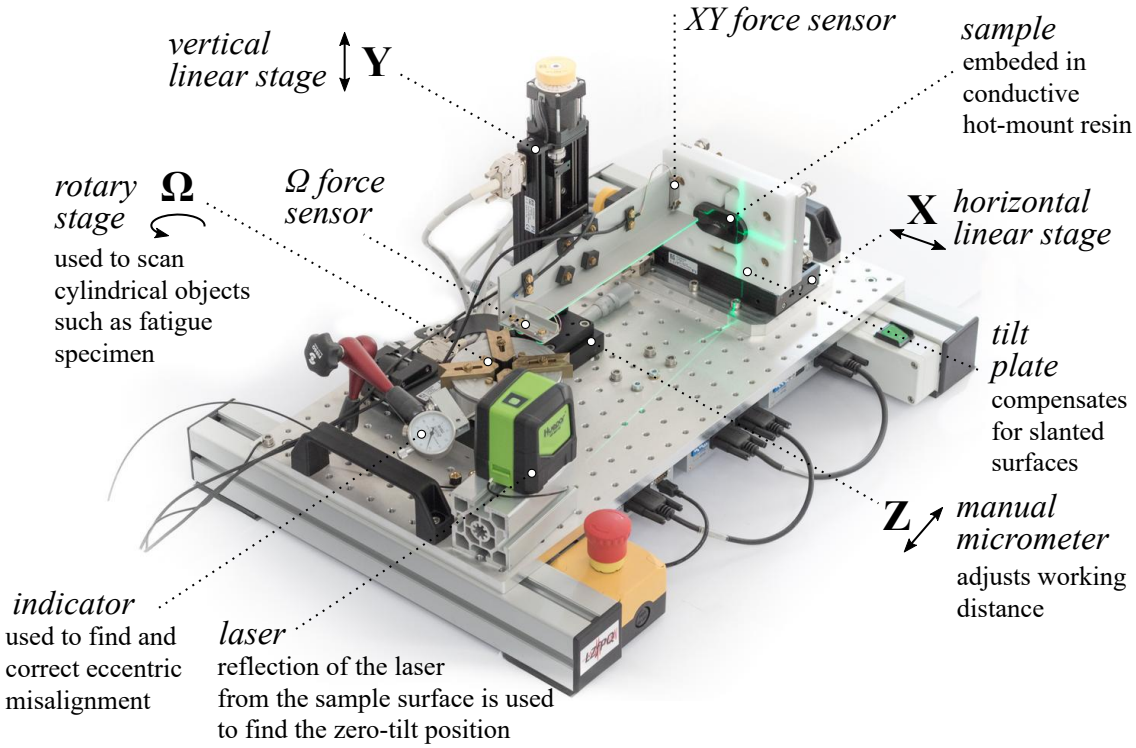

Fig. 19. Experimental setup for magnetic force imaging. Rotary and planar configurations share one Y linear stage. The sample orientation is always vertical. Reflection of the laser from the polished surface of the sample is used to determine and adjust the tilt of the specimen.

terion, from a physical point of view, MFI shows density rather than a given volume fraction. Correct interpretation, therefore, depends on the size of a feature in the scan. The larger the feature, the more accurate the interpretation of the signal as a volume fraction. For smaller features, especially below 0.7 mm, the volume fraction is averaged over the effective interaction volume. This and other influences on MFI measurements are discussed further in section 8.1 on page 144.

Calibration to ferrite volume fraction To convert the force-response measurement of MFI to ferrite volume fraction, Eq. (31) can be used:

$$\xi_{mfi} = (F_i - F_{air} - F_{ast}) \cdot C_{Fe} \tag{31}$$

where ξ_{mfi} – MFI output calibrated to ferrite volume fraction; F_i – force response to the sample under investigation; F_{air} – force measurement without the sample, i.e. "in the air"; F_{ast} – force response from a fully austenitic sample; C_{Fe} – calibration factor, obtained from standard ferrite samples with a known amount of ferrite.

Since the force response of a fully austenitic sample F_{ast} does not equal zero, it is therefore subtracted to give an accurate reading below 3 Fe%. The fully austenitic sample was made out of annealed X6CrNiTi18-10S steel. The sample for calibration was cut with electric discharge machining (EDM) to the size of 20×20×10 mm. Electro-chemical polishing was then used to remove the erosion mark after EDM. After scanning with MFI, this sample showed a very homogeneous surface with relative magnetic permeability of $\mu_r = 1.002$.

The remaining three standard ferrite samples were acquired from Helmut Fischer GmbH. The ferrite content of these samples was determined by comparative measurement against primary standards owned by Helmut Fischer. The comparison of the ferrite number (FN) was made by means of an instrument using the magnetic induction method, which was calibrated according to ANSI/AWS A4.2M: 2006. Ferrite volume fraction, as a secondary value, was determined by means of a microscopic examination using the point count method. These samples serve as primary calibration standards in this work and are summarized in Table 4. The manufacturer specified the uncertainty only for the ferrite number.

A linear fit with aforementioned standard samples determines the calibration factor C_{Fe}. The result of the measurement for $d_w = 10$ μm is shown in Fig. 20a. The calibration factor has to be specific for each working distance and was determined in the range from 10 to 50 μm. Fig. 20b shows the relationship between the calibration factor and working distance. The relationship

Table 4
Primary calibration standards.

No	Microstructure	Ferrite vol. fraction	Ferrite number (FN)	Uncertainty
1	γ-austenite	0 %	n/a	n/a
2	δ-ferrite, γ-austenite	0.64 %	0.51	± 0.6 FN
3	δ-ferrite, γ-austenite	1.78 %	1.32	± 0.6 FN
4	δ-ferrite, γ-austenite	11.6 %	10.7	± 0.8 FN

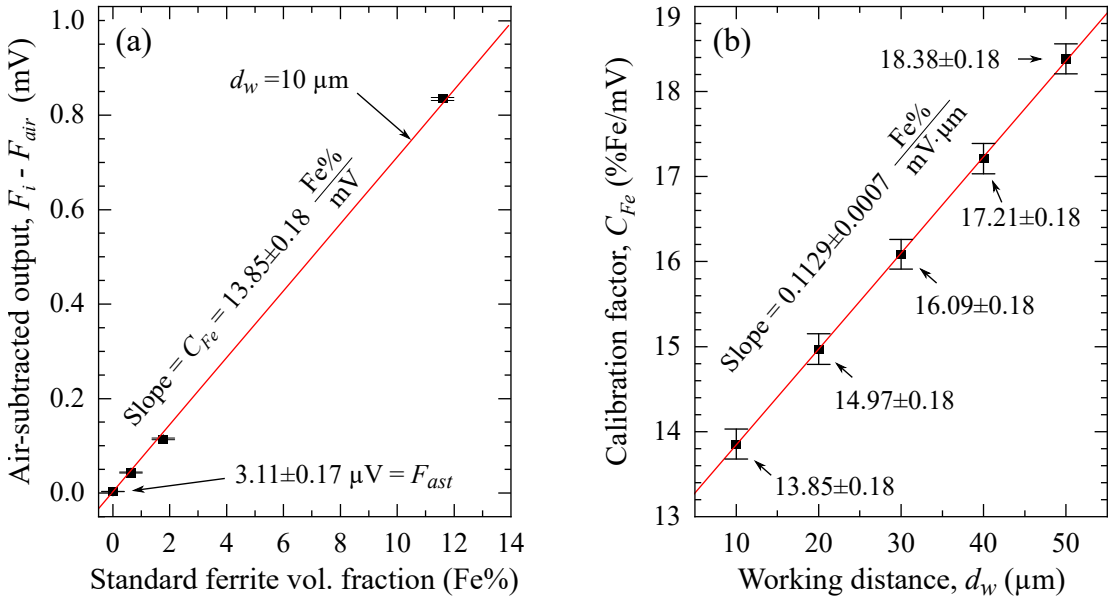

Fig. 20. MFI calibration curves: a) MFI signal from different standard calibration samples; b) calibration factor for different working distances.

appeared to be very linear in the range from 0 to 12 Fe%. The calibration beyond 12 Fe% has not been done due to difficulties measuring the working distance. With the next closest calibration sample, 51 Fe%, it was not possible to accurately measure the working distance because it was not possible to move the magnetic tip away from the surface without overloading the force sensor.

Calibration to relative permeability Magnetic force reading of MFI can be converted to relative magnetic permeability with Eq. (32):

$$\mu_{mfi} = (\mu_{rst} - 1) \cdot \frac{F_i - F_{air}}{F_{st}} + 1 \tag{32}$$

where μ_{mfi} – MFI output calibrated to relative magnetic permeability; μ_{rst} – relative permeability of the standard calibration sample; F_i – force response of the sample under investigation; F_{air} – force measurement without the sample, i.e., "in the air"; F_{st} – force response from the standard calibration sample.

A carbonyl iron powder sample with relative magnetic permeability of

1.37 was used for the calibration. This sample has been produced by Stefan Mayer Instruments GmbH & Co. KG by mixing the carbonyl iron powder and epoxy resin with an approximate mass ratio of 2:5.

5.2 Uniaxial Magnetic Balance (UMB)

The UMB was specifically designed for *in-situ* monitoring of $\gamma \rightarrow \alpha'$ phase transformation in austenitic stainless steel during fatigue testing. The UMB is based on the principle of measuring the mutual force of attraction between a sample and two axially aligned magnets. Each magnet is attached to a separate force (or displacement) sensor for independent and simultaneous readout. When the specimen is placed between the magnets, its magnetic properties will affect the interaction force between the magnets, and therefore the force response can be related to the magnetic properties of the material under test. Since this additional change in force interaction due to the presence of the test object can be significantly smaller than the attraction force between the magnets, the latter force must be compensated for. This is accomplished by introducing a balancing mechanism into the system. The purpose of such a mechanism is to ensure that the magnets are pulled apart with the same force as they are attracted, or in other words, to bring them into a balanced state. This configuration makes it possible to achieve high sensitivity, which is directly proportional to the magnetic field strength generated by the magnets.

5.2.1 UMB working principle

As Fig. 21 illustrates, the attractive forces between the magnets *M1* and *M2* are balanced by the ferromagnetic "ballasts" *B1* and *B2* of which the distance to

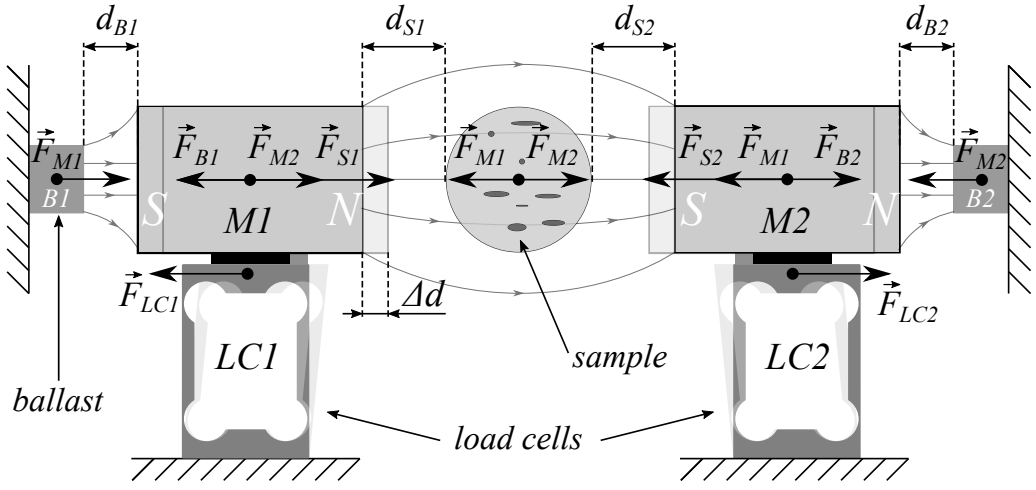

Fig. 21. Schematic drawing illustrating the principle of the uniaxial magnetic balance (UMB).

the magnets d_{B1} and d_{B2} can be adjusted to set the system in balance, such that F_{LC1} and F_{LC2} are equal zero and condition (33) is fulfilled:

$$\vec{F}_{M1} + \vec{F}_{B1} + \vec{F}_{M2} + \vec{F}_{B2} + \vec{F}_{LC1} + \vec{F}_{S1} + \vec{F}_{LC2} + \vec{F}_{S2} = 0 \tag{33}$$

Assuming a perfect axial alignment, equations can be further written in a simple scalar form. In a case where no sample is present, a set of equations (34) can be written. When the sample is inserted into the opening between the magnets (Eq. 35), additional forces F_{S1} and F_{S2} cause the deflection Δd of the load cells, which is directly related to the magnetic permeability of the material.

$$\begin{cases} F_{LC1} & = 0 \\ F_{M2} - F_{B1} & = 0 \end{cases} \qquad \begin{cases} F_{LC2} & = 0 \\ F_{M1} - F_{B2} & = 0 \end{cases} \tag{34}$$

$$\begin{cases} F_{LC1} & = F_{M2} + F_{S1} - F_{B1} \\ F_{M2} - F_{B1} & = \beta_1 \end{cases} \qquad \begin{cases} F_{LC2} & = F_{M1} + F_{S2} - F_{B2} \\ F_{M1} - F_{B2} & = \beta_2 \end{cases} \tag{35}$$

The deflection of load cells causes the ballast distances d_{B1} and d_{B2} to increase, which results in decreased F_{B1} and F_{B2} and, overall, a higher attraction force between the magnets. This additional force gained is denoted by coefficients β_1 and β_2. This additional force is what makes UMB much more sensitive compared to a single magnet pull force measurement.

The resulting force, measured by both load cells, can be written as (36):

$$\begin{cases} F_{LC1} & = F_{S1} + \beta_1 \\ F_{LC2} & = F_{S2} + \beta_2 \end{cases} \tag{36}$$

Independent force readout from each load cell also allows compensating for the little movement of the specimen during fatigue testing. The final UMB output F is calculated as a mean output of the two load cells (37):

$$F = \frac{F_{LC1} + F_{LC2}}{2} \tag{37}$$

There have been three versions of UMB manufactured with different features and characteristics. Essential parameters of each version are summarized in Table 5 on page 65. The first prototype of the instrument UMB-1 used cylindrical NdFeB magnets 5 mm in diameter and 25 mm in length, spaced 10 mm apart. UMB-1 has been successfully used for several room temperature fatigue tests. UMB-2 version had much larger NdFeB magnets with dimensions of 14×7×25 mm separated by a 15 mm distance. UMB-2 has been primarily used

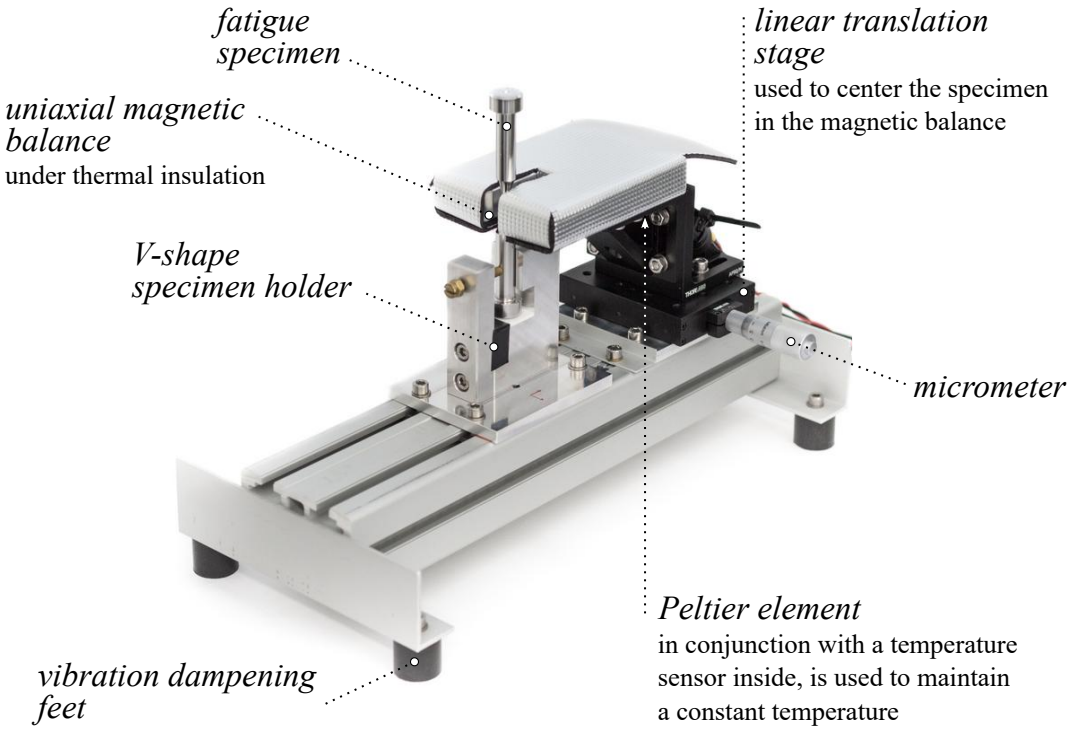

Fig. 22. Uniaxial magnetic balance (UMB) on the *ex-situ* stand for fatigue specimen characterization.

on an *ex-situ* stand Fig. (22) to characterize the initial amount of α' martensite. The exceptionally high sensitivity of UMB-2 did not allow it to be used in thermo-mechanical fatigue testing, where strong magnetic fields are present. A third version, the UMB-3, was designed to withstand the heating current of the TMF setup, which can typically reach 500 A.

UMB-3 was fitted with smaller magnets 12×5×2 mm in size, separated by 15 mm distance, similar to UMB-2. Since alternating current was used for the heating in the TMF setup, it was sufficient to mount a heavy mass together with the magnets to prevent excessive vibrations. Magnets were placed inside machined tungsten blocks similar to the size of the magnets in UMB-2 so that the same housing could be used. UMB-2 and UMB-3 had an internal voltage reference, temperature sensor, and magnetic sensor built in into the aluminum housing. An internal temperature sensor was used together with an external Peltier element to maintain a constant temperature during TMF testing. Typical temperature stability was ± 5 mK or better. The configuration of UMB-3 for *in-situ* TMF testing is illustrated in Fig. 26 on page 68. All UMB versions used 200 g capacity aluminum shear beam load cells placed inside a fully enclosed aluminum housing. Additional thermal insulation was applied over the aluminum housing for better thermal stability.

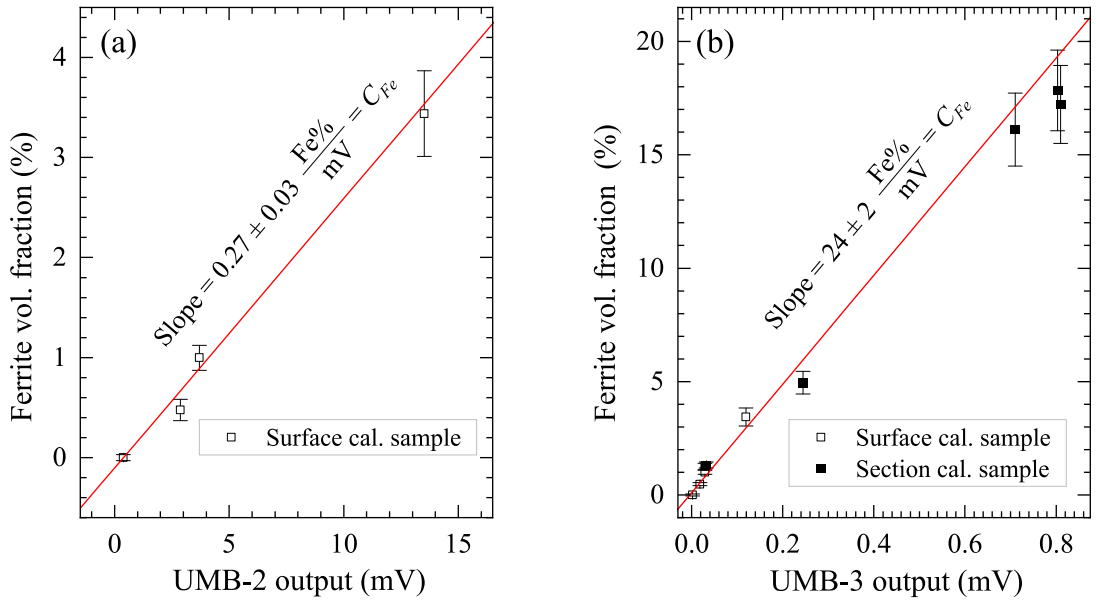

Fig. 23. UMB-2 (a) and UMB-3 (b) calibration curves. Surface calibration samples were measured with MFI on the surface, whereas section samples were measured after cutting the specimen along the rotation axis.

5.2.2 Calibration to ferrite volume fraction

UMB output has been calibrated to ferrite volume fraction on secondary standards, obtained from primary standards from Table 4 on page 59 by means of MFI. Since UMB measurements are sensitive to the volume and geometry of the test material, fatigue specimens were used to transfer ferrite content information from the primary standards. Nine fatigue specimens have been analyzed with MFI after a different amount of accumulated strain from fatigue loading. Five of them have been cut along the rotation axis and measurements have been taken on the inner surface to make sure the deformation-induced martensite is measured throughout the entire volume. The cutting process removes a significant amount of the material and therefore UMB measurement could only be done once prior to cutting. The calibration curves for UMB-2 and UMB-3 are shown in Fig. 23. Although the secondary standards contain α' martensite instead of δ ferrite, they still define ferrite volume fraction, which is inherited from the primary standards.

As it has been mentioned in the previous section, magnetic permeability of pure austenite is much higher compared to air, and therefore, zero ferrite reference cannot be measured in air. A fully annealed X6CrNiTi18-10S steel rod 6 mm in diameter and 85 mm in length was used as a fully austenitic reference. It was cut with EDM and electropolished to remove erosion from the surface. MFI was used to confirm the absence of ferromagnetic phases in the material. A linear fit across all calibration samples appeared to be sufficient to characterize the UMB output in terms of ferrite volume fraction (see Fig. 23). Final output

of UMB calibrated to ferrite volume fraction in Fe% can be written as

$$\xi_{umb} = (F_i - F_{air} - F_{ast}) \cdot C_{Fe} \tag{38}$$

where ξ_{umb} – UMB output calibrated to ferrite volume fraction; F_i – force response to the sample under investigation; F_{air} – force measurement without the sample, i.e. "in the air"; F_{ast} – UMB force response to a fully austenitic sample; C_{Fe} – calibration factor, obtained from standard ferrite samples with a known amount of ferrite.

Calibration factors C_{Fe} for UMB-2 and UMB-3 can be found in Fig. 23. Calibration was done in the linear range, which spans from zero to up to 20 Fe%. Further increase in the amount of ferromagnetic phases results in reduced UMB output. This means readings above 20 Fe% are likely to be underestimated. Within the scope of this work, it was not necessary to perform calibration above 20 Fe%. Accumulated error on the measurements was higher for specimens with higher ferrite reading. This is due to the fact that deformation-induced martensite, which was introduced by cyclic loading, forms inhomogeneously within the specimen volume. A very common occurrence is the formation of α' martensite in bands that follow the axial direction of the specimen.

5.2.3 Resolution, repeatability and accuracy

The signal-to-noise ratio (SNR) was determined by placing the sample in and out of the UMB twice and measuring the signal and noise amplitudes. The signal amplitude was determined as mean output with the sample m_s minus mean output without the sample m_b. The results of the measurements are presented in Fig. 24. To calculate SNR Eq. (39) was used:

$$\mathrm{SNR} = \frac{m_s - m_b}{\sqrt{h_s^2 + h_b^2}} \tag{39}$$

where m_s – mean output with the sample; m_b – mean output without the sample; h_s – noise amplitude with the sample; h_b – noise amplitude without the sample.

Fig. 24a shows the result of a measurement on a cylinder made of 99.99 % pure bismuth, 6 mm in diameter and 50 mm in length. Bismuth is a highly diamagnetic material with typical relative permeability of $\mu_r = 0.999834$ or $(\mu_r - 1) = -1.66 \cdot 10^{-4}$ [191]. Therefore the signal acquired with this sample is negative. For UMB-3, the bismuth sample was indistinguishable from noise (Fig. 24c). Increasing the diameter of the sample also increases the sensitivity of UMB. However, the specifications here were made for the same diameter

as fatigue specimens. Identical measurements of a fully austenitic sample are presented in Fig. 24b and d. The sample was a cylinder 6 mm in diameter and 85 mm in length. Relative permeability of this sample was measured with MFI and was estimated to be $\mu_r = 1.002$. Knowing the permeability, resolution $R_{\mu r}$ can be determined in terms of volumetric susceptibility with Eq. (40):

$$R_{\mu r} = \frac{\mu_r - 1}{SNR} \tag{40}$$

Resolution R_{Fe} in terms of ferrite fraction was defined as a double noise amplitude multiplied by the calibration factor C_{Fe} by Eq. (41) and the results of all calculations were summarized in Table5.

$$R_{Fe} = 2 \cdot C_{Fe} \sqrt{h_b^2 + h_s^2} \tag{41}$$

Long-term stability is essential for *in situ* monitoring during fatigue tests, which

Table 5
Comparison of different versions of the uniaxial magnetic balance. Aperture refers here to the opening between the magnets, where the sample is placed. This is also the largest possible diameter of the sample that can be measured.

	UMB-1	**UMB-2**	**UMB-3**
Application	*R*oom temp. tests	Initial Fe% measurement	Elevated temp. and TMF tests
SNR austenite cylinder, ⌀ 6 mm	n/a	89	7
Resolution ⌀ 6 mm cylinder, $(\mu_r - 1)$/SNR	n/a	$2 \cdot 10^{-5}$	$3 \cdot 10^{-4}$
Resolution ⌀ 6 mm cylinder, ferrite	n/a	23 ± 7 ppm (0.0023 %)	216 ± 9 ppm (0.022 %)
Accuracy % from ferrite reading	n/a	± 10 %	± 10 %
Temperature drift with PID stabilization	n/a	0.01 Fe%/K	0.1 Fe%/K
Aperture	10 mm	15 mm	15 mm
Magnetic field center of the aperture	120 mT	180 mT	50 mT
Magnetic field edge of the aperture	280 mT	450 mT	200 mT
Magnet shape	Cylinder	Rectangular cuboid	Rectangular cuboid
Magnet dimensions	⌀ 5×25 mm	14×7×25 mm	12×5×2 mm
Magnetization direction	axial	in the longest dimension	in the shortest dimension

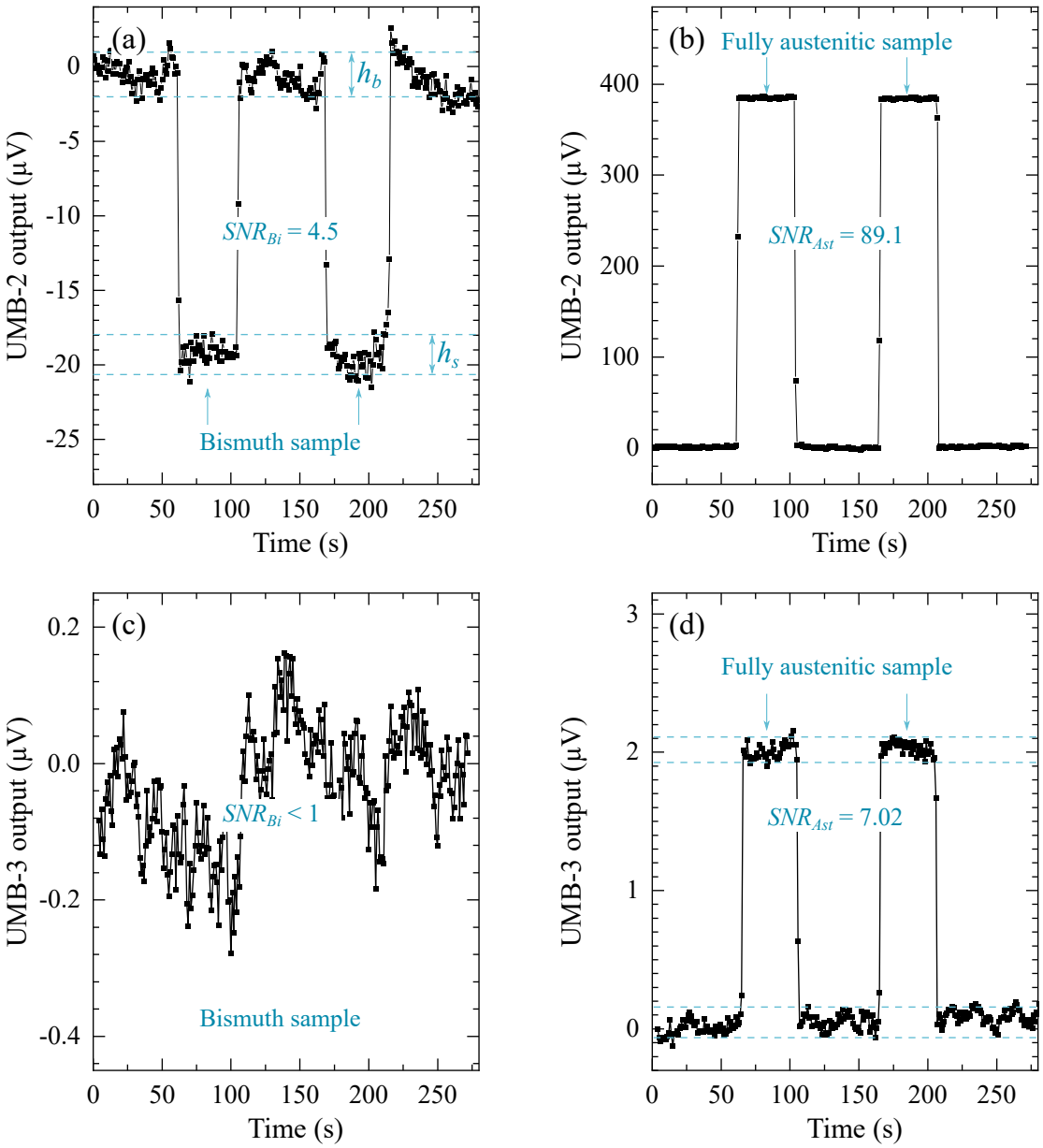

Fig. 24. Determination of the signal-to-noise ratio for: a) diamagnetic bismuth sample with UMB-2; b) fully austenitic sample with UMB-2; c) bismuth sample with UMB-3; d) fully austenitic sample with UMB-3.

can last several days. Temperature control with a PID algorithm greatly improved the drift of the signal over time. However, it does not eliminate it completely since the equipment responsible for temperature stabilization is itself under the influence of temperature fluctuations.

The accuracy of UMB measurements is greatly influenced by calibration. Since Helmut Fischer GmbH, the manufacturer of primary standards, does not specify the accuracy in terms of ferrite volume fraction, but rather in ferrite number, it is not possible to directly transfer the uncertainty of the measurement. However, judging from the fitting error in Fig. 23 on page 63, accuracy can be estimated to be around 10 % from the ferrite reading.

5.3 Thermo-mechanical fatigue testing rig

The thermo-mechanical (TMF) testing setup was built around a commercial 20 kN Shimadzu Servopulser servo-hydraulic fatigue testing machine. The decision was made to avoid induction coils and to achieve heating by passing 50 Hz alternating current directly through the sample. An induction coil would not only take up valuable space around the specimen, but would also cause significant interference with *in-situ* magnetic measurements. The resulting TMF configuration was capable of performing tests on the standard fatigue specimen geometry.

The current injection was realized with special gold-plated clamps (see Fig. 26), which grip the specimen laterally and maintain good electrical contact under axial load. Current injection clamps were connected directly to the secondary winding of the high-current transformer via 500 mm^2 copper busbars. The high current transformer was manufactured with 8 taps on the primary winding, which were used to adjust the voltage, as shown in Fig. 25. A solid-state tap changer allowed switching between taps with no moving mechanical parts to wear out. The input to the tap changer can be adjusted with a variable autotransformer to achieve a wide range of temperatures. The system was designed for 800 A continuous current and up to 1000 °C maximum specimen temperature.

A heat shield, machined from a single copper block, was used to protect the UMB from extreme temperature changes. The heat shield geometry follows the shape of the fatigue specimen and allows unobstructed access for the uniaxial magnetic balance. To maintain stable temperature, the grips and the heat shield were continuously water-cooled with 15 °C water. More detailed

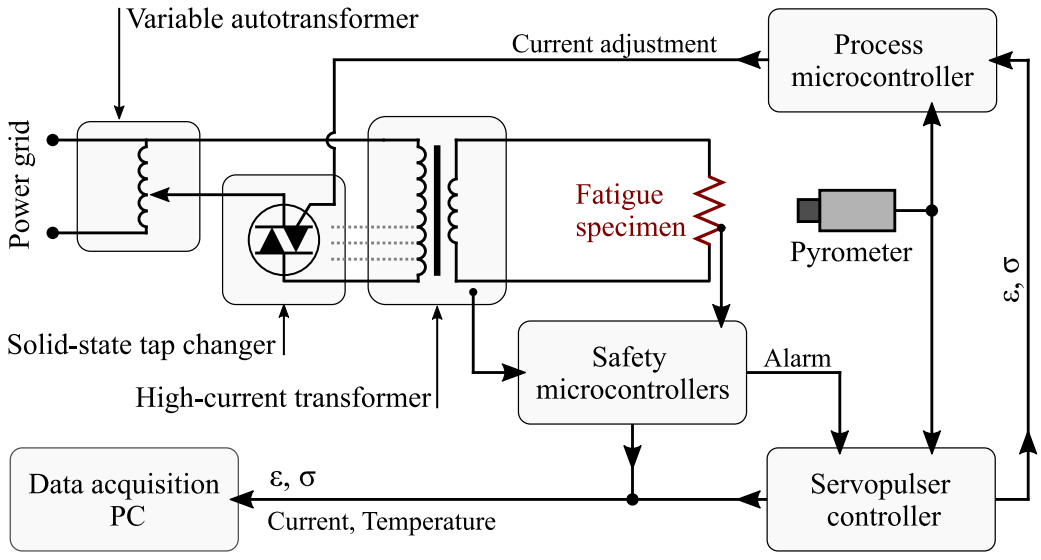

Fig. 25. A schematic drawing of the various elements that make up the TMF setup.

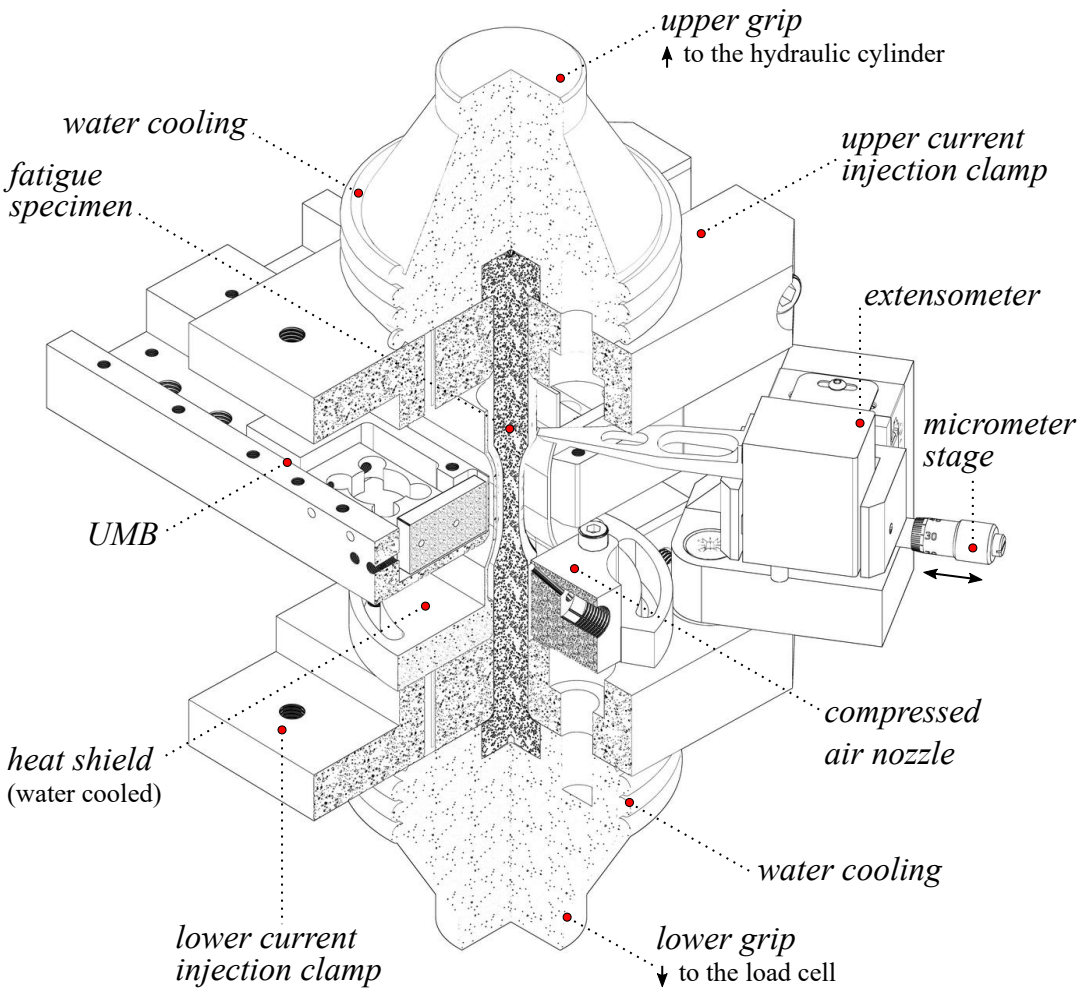

Fig. 26. Three-quarter section view of the thermo-mechanical fatigue rig. A fatigue specimen can be recognized at the center by dark gray color. Around the specimen is a heat shield, from the left side of which UMB is depicted without the front cover.

technical drawings of the heat shield and other parts of the TMF are provided in Appendix A.

CellaTemp PA 10 pyrometer with a thermopile sensor from Keller HCW GmbH was used to measure the temperature of the fatigue specimen. The pyrometer was placed at a distance of 155 mm from the pyrometer lens to the specimen surface (see Fig. 30). At this distance, the field of view of the pyrometer is 3.23 mm in diameter, which is quite acceptable for 6 mm in diameter specimens. The measuring range of this pyrometer spans from 0 to 1000 °C, which corresponds to a wavelength of 14 to 8 μm. While the pyrometer was connected to the temperature control circuit, two additional infrared cameras, such as Micro-Epsilon TIM450, were used to monitor the temperature distribution along the specimen.

The cooling phase of the TMF tests was assisted by compressed air, regulated to a pressure of 3 bar. Fig. 27 shows the compressed air nozzle that splits the air flow into three directions: two going around the fatigue specimen and one directed directly at the center. The air nozzle was mounted on the heat

shield so that the air bends around the bottom of the specimen and then flows upward. This causes the air around the specimen to expand, which also causes some adiabatic cooling.

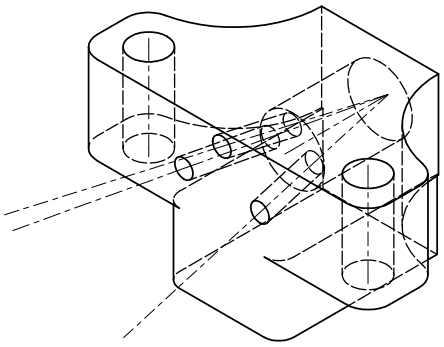

Fig. 27. Compressed air nozzle used in the cooling phase of TMF tests.

Fig. 30 shows how the uniaxial magnetic balance was mounted. The UMB is first placed away from the specimen, where the output of the two load cells is zeroed. The UMB is then moved to the measurement position, where the fatigue specimen is exactly in between the magnets of the UMB. The balance aperture fits around the heat shield, leaving a sufficient air gap. The alignment is then adjusted with the micrometer stage until the signals from the two load cells are equal. This assures that the distances d_{S1} and d_{S2} are equal (see Fig. 21 on page 60).

The extensometer was adapted to high temperatures by extending one blade to a length of 50 mm while holding another blade in a fixture attached to a miniature linear stage. The linear stage was then bolted to the lower current injection clump. This unconventional design was chosen to allow unobstructed magnetic and thermal measurements. The housing of the extensometer is essentially the bottom plate, as they are rigidly connected. Therefore, adding a lower blade while the housing is mounted in the fixture would have created opposing strains in the extensometer and negatively affected the linearity of the strain measurement. Since the current injection clumps were firmly attached to the fatigue specimen by lateral compression, the mechanical hysteresis in the strain measurement was also reduced. Another reason for not placing the extensometer blades at the gauge length of the specimen is that it would interfere with the magnetic measurements with the UMB. While ceramic blades could be placed closer to the center of the fatigue specimen, they would most likely slip during the cooling phase when compressed air cools the specimen. In such a configuration, calibration is required to compensate for the strain differences between the gauge length and the TMF extensometer readout.

5.3.1 Extensometer calibration

The same extensometer, but with 12 mm spacing between the blades, was used to calibrate the output of the TMF configuration to the actual strain in fatigue specimens. Two tests with a cyclic load of ±2 kN were performed with each extensometer. The results of the measurements are shown in Fig. 28. Both

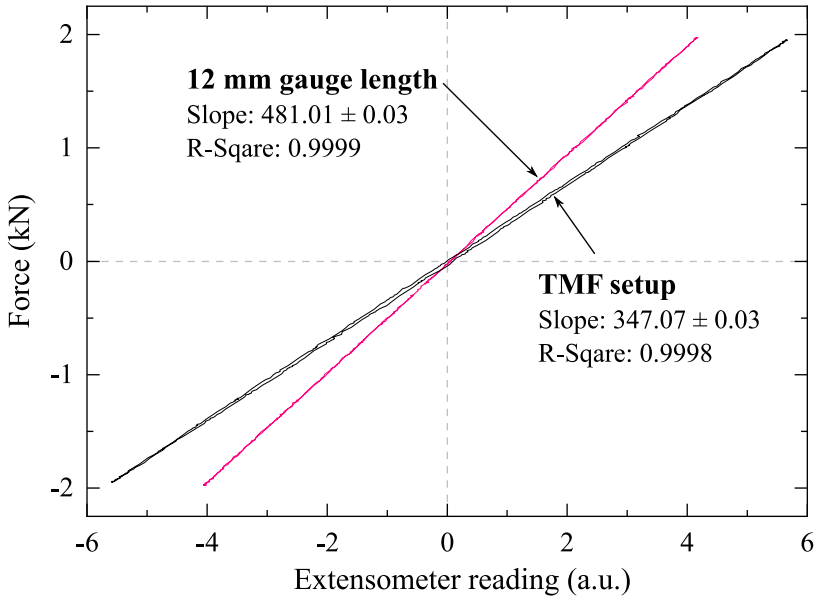

Fig. 28. Comparison of strain measurements of 12 mm gauge length extensometer and the TMF extensometer.

measurements were performed in the TMF setup, with the specimen mounted in the current injection clamps.

The results showed a linear response of the TMF extensometer with a small opening in the hysteresis. Ideally, calibration should be performed at a higher force amplitude, but this would cause strain hardening of austenitic specimens and invalidate the calibration. The ratio between the slopes in Fig. 28 was calculated to be 1.386. The readings from the 12 mm extensometer configuration are in microns, while the readings from the TMF configuration are an arbitrary value due to the lever-like action of the extension blade.

5.3.2 Zero-force calibration

To perform strain-controlled TMF tests, it is important to know how much the specimen expands and contacts as the temperature changes. To estimate this thermal strain, a zero-force test was performed. The servo-hydraulic part of the machine was set to maintain the force at zero kN while the specimen was subjected to a thermal cycle. The extensometer recorded the thermal deformation, i.e. the thermal strain.

The results of the test are shown in Fig. 29. The test was performed at average heating rates of 35 °C/s and 65 °C/s. Radial stresses due to a fast heating rate are not a significant concern here because the entire volume in the gauge length of the specimen is heated simultaneously by passing the current through at 50 Hz. At this frequency, the skin effect is negligible, and very fast heating rates can be realized.

Thermal strain hysteresis in Fig. 29b shows how the offset for the thermal

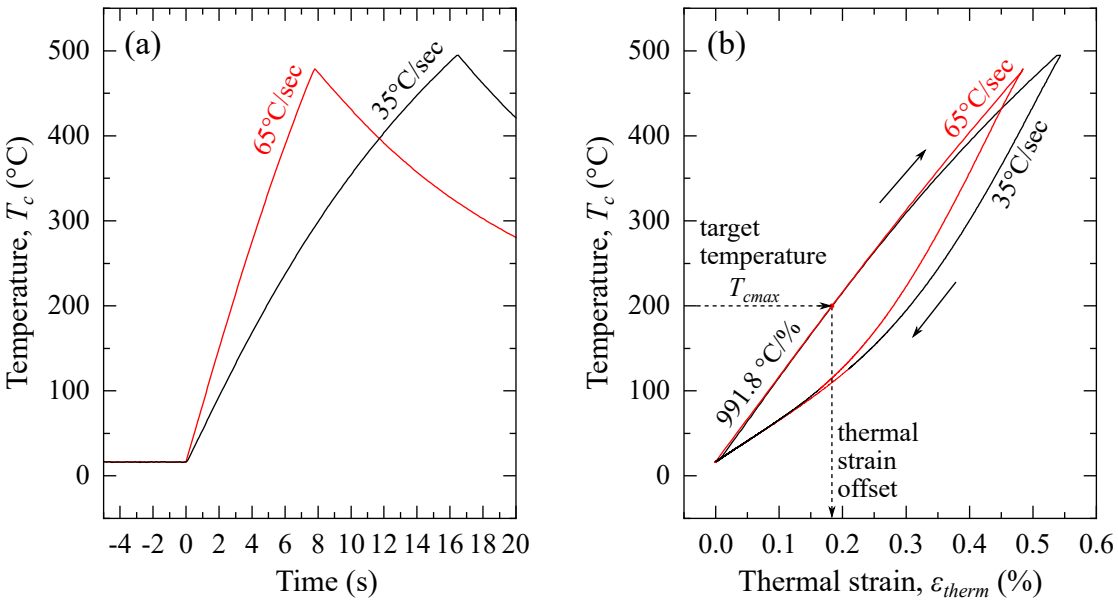

Fig. 29. Zero-force test for two different heating rates: a) specimen temperature as a function of time; b) thermal strain hysteresis. Thermal offset is determined from the upper part of the hysteresis.

expansion was calculated. The initial part of the heating cycle was very linear because, at such a high heating rate, heat does not have time to spread from the gauge length to the shoulders of the specimen. In the cooling cycle, compressed air was not used to cool the specimen. The coefficient of thermal expansion for the given combination of geometry and heat distribution was calculated to be 991.8 °C for the thermal strain of 1 %.

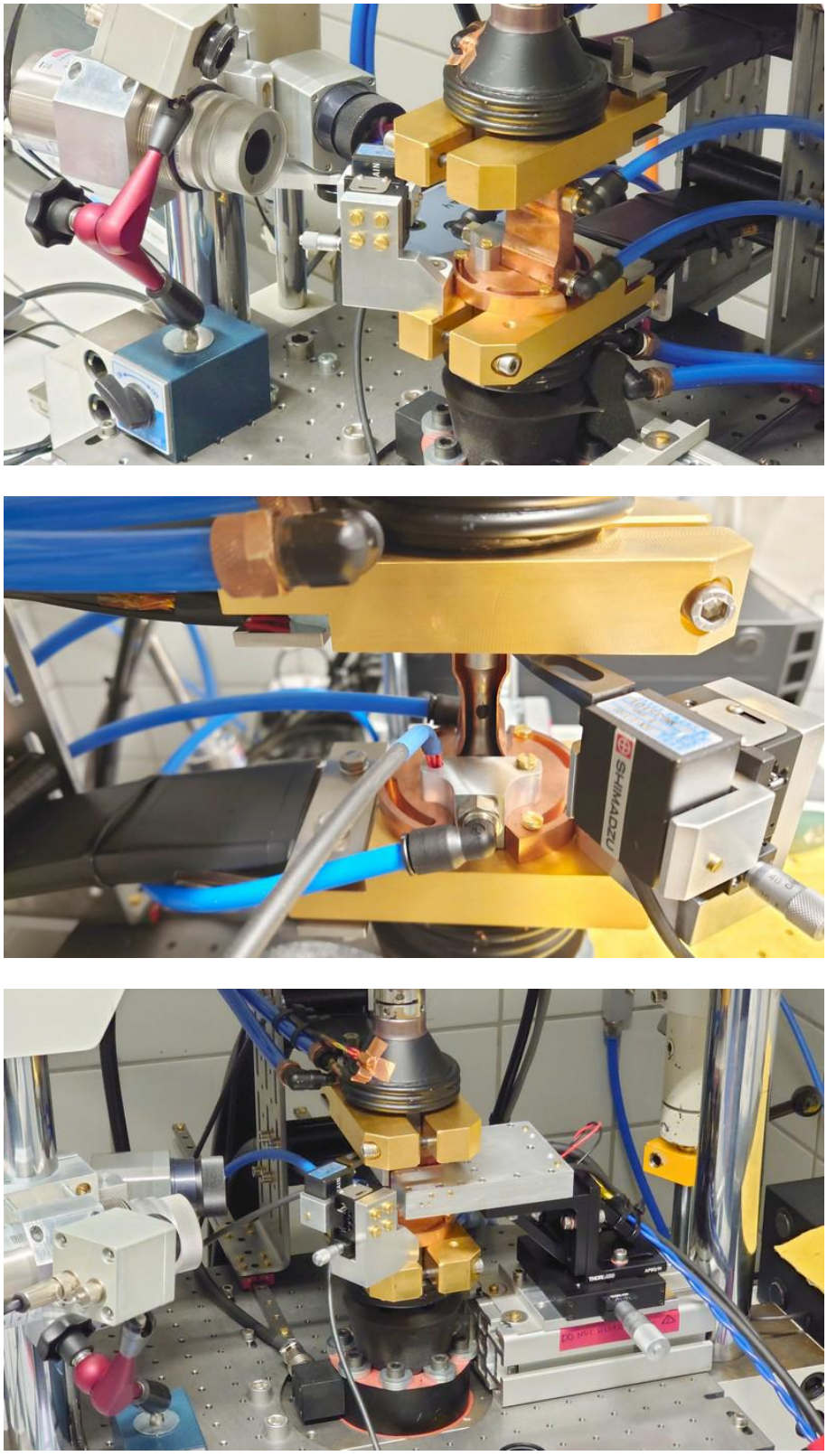

Fig. 30. Views of the fatigue specimen mounted in the servo-hydraulic thermo-mechanical setup. The specimen is covered by the water-cooled copper heat shield. The uniaxial magnetic balance is inserted over the heat shield.

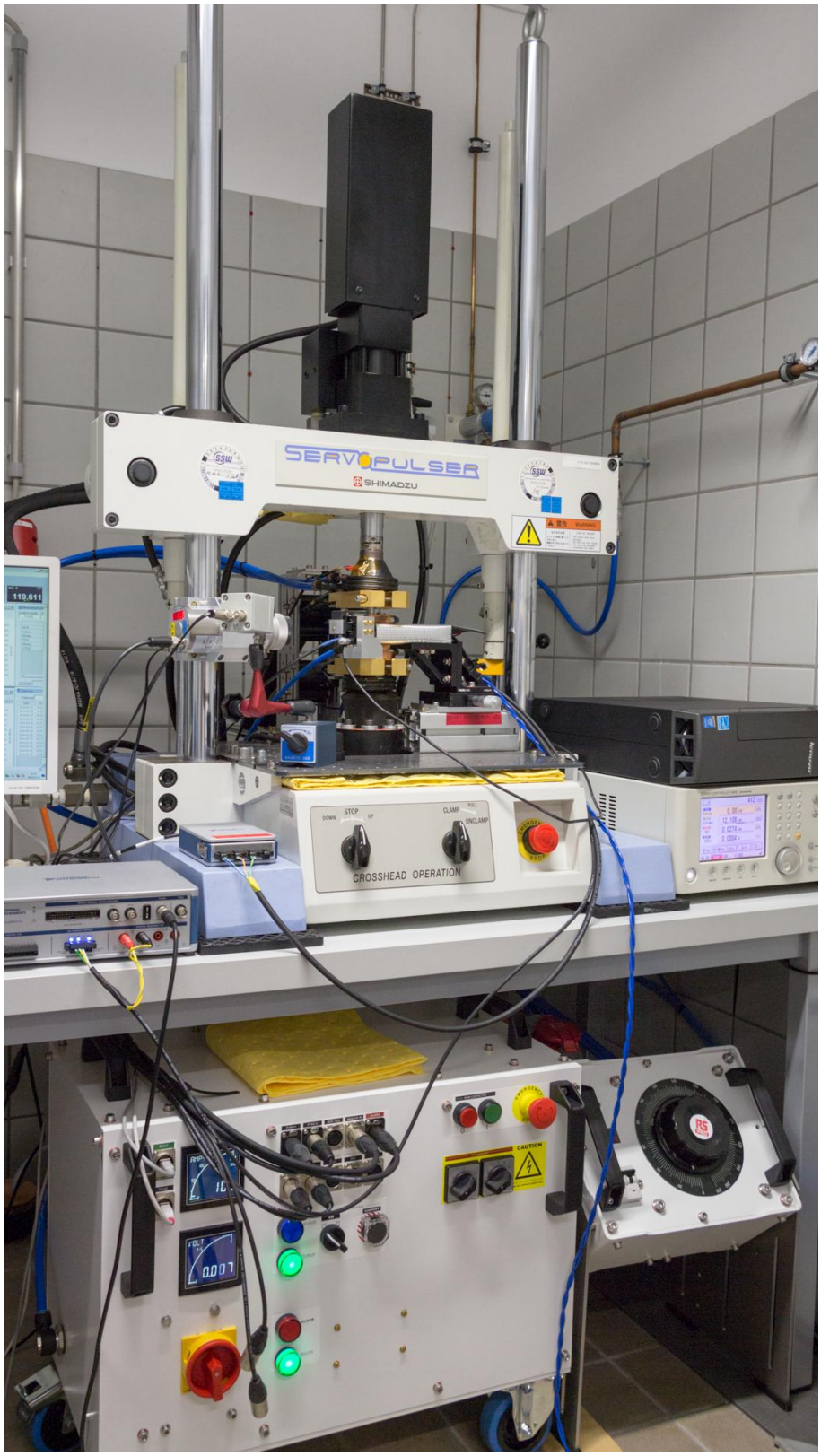

Fig. 31. A photograph of the thermo-mechanical power unit (at the bottom) and Shimadzu Servopulser servo-hydraulic fatigue testing machine with mounted uniaxial magnetic balance.

5.4 Balanced Core Magnetometer (BCM)

The BCM is an instrument developed for non-contact measurement of the magnetic properties of weakly ferromagnetic materials such as austenitic stainless steels. It uses the principle of magnetic force measurement between a ferromagnetic core and a sample. The magnetization of the core, and thus the magnetic field generated, can be controlled by an external magnetic field provided by a field coil. As a result, a force-magnetization curve can be obtained where the field strength is compared to the force interaction between the magnetic core and the test material.

5.4.1 BCM working principle

As shown in Fig. 32 and 33, the device consists of a field coil, a magnetic core, and a force transducer. The magnetic core is positioned in the center of the field coil, such that the net forces acting between the coil and the core are equal or close to zero:

$$\vec{F}_{a1} + \vec{F}_{a2} + \vec{F}_{r1} + \vec{F}_{r2} = 0 \tag{42}$$

where $\vec{F}_{a1}$ and $\vec{F}_{a2}$ are the axial forces, $\vec{F}_{r1}$ and $\vec{F}_{r1}$ are the radial forces reflecting the axial and radial alignment of the core. When the magnetic core is aligned within the field coil, the balance condition (42) is fulfilled, meaning no force response will be detected when the field coil is energized without a specimen.

When the specimen is placed near the magnetic core, an additional force towards the specimen $\vec{F}_{sp}$ is generated proportionally to the magnetic field produced by the magnetic core and the field coil. Because the coil and the core are not rigidly connected, forces acting on the specimen can be separated

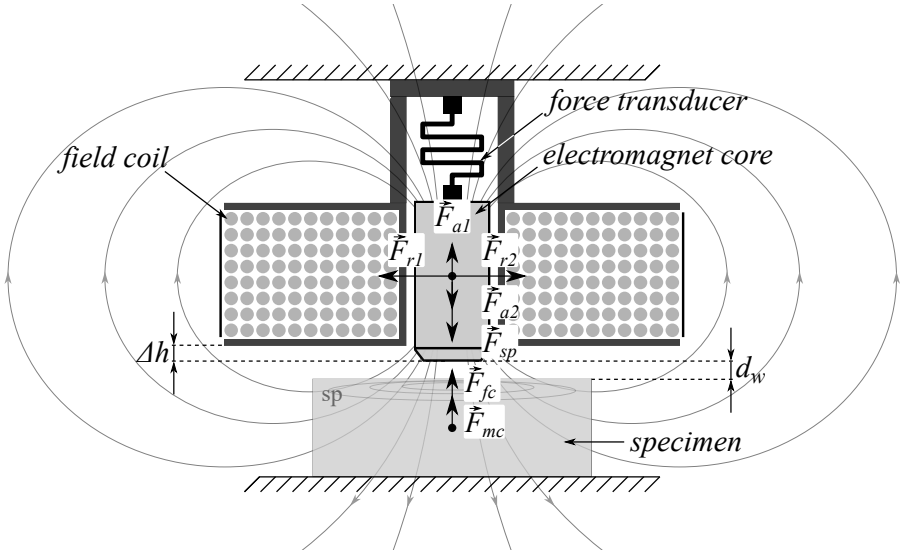

Fig. 32. Working principle of the balanced core magnetometer (BCM).

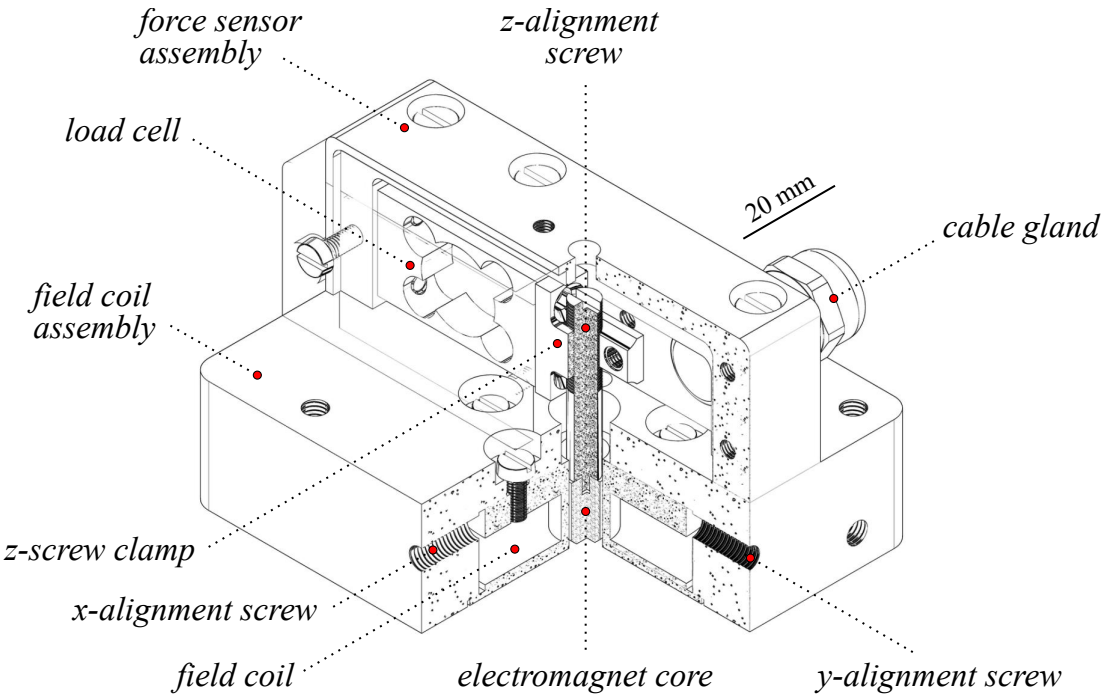

Fig. 33. Balanced core magnetometer design in a handheld format (core section view).

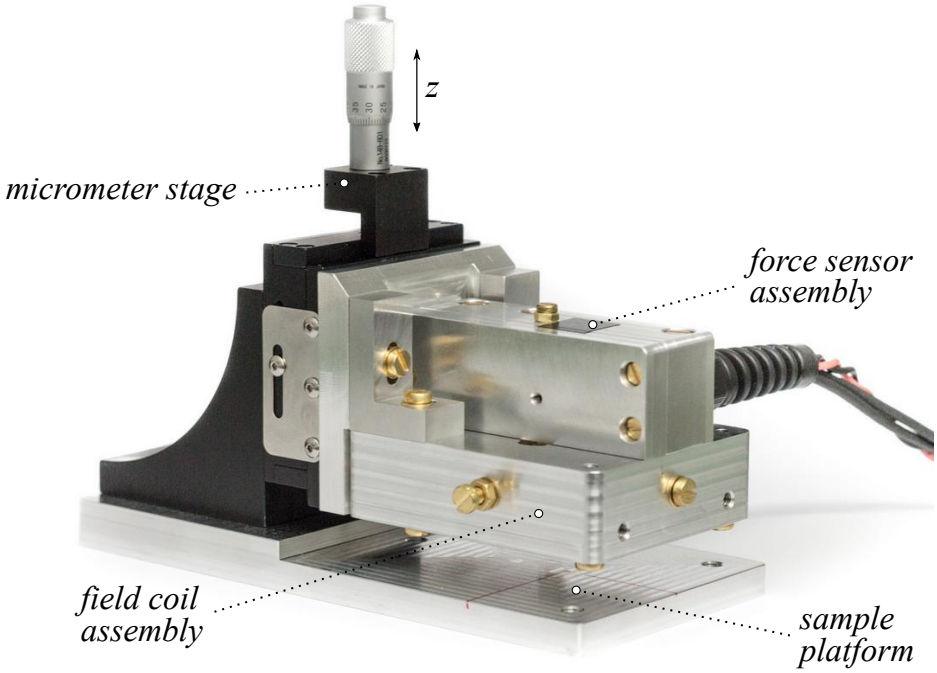

Fig. 34. A photograph of the BCM prototype, mounted on a vertical micrometer stage.

into the field coil force $\vec{F}_{fc}$ and the magnetic core force $\vec{F}_{mc}$. Only $\vec{F}_{mc}$ and $\vec{F}_{fc}$ are measured as a material response to the magnetic field. The advantage of having the magnetic core mechanically separated from the coil is a significant reduction in the load applied to the force transducer. The field coil is the heaviest component of the system, which size and weight are very difficult to reduce due to restrictions of heat dissipation and maximization of the energy density. The magnetic core, on the other hand, can be made as lightweight as required. When the force transducer is only attached to the magnetic core, a much higher sensitivity in the force measurement can be achieved.

As an example, Fig. 35 shows typical curves that can be obtained with the balanced core magnetometer. Excitation in V refers to the voltage applied to the field coil. Response in mV reflects the force measured by the force transducer. Data in Fig. 35 were obtained on 347 austenitic stainless steel specimen after a constant amplitude fatigue test with 0.16 % total strain amplitude.

The measurement procedure to acquire the magnetization force curves starts with adjusting the working distance d_w to the desired value. It can be decreased for higher sensitivity or increased if forces exceed the measurement range. When the working distance is set, the current in the coil is increased stepwise such that the force response is measured when the current is constant. The prototype with a mechanical micrometer stage for working distance adjustment is shown in Fig. 34. A force-magnetization curve obtained on a standard relative permeability sample with $\mu_r = 1.37$ is shown in Fig. 37, which can be used as a calibration curve for relative permeability.

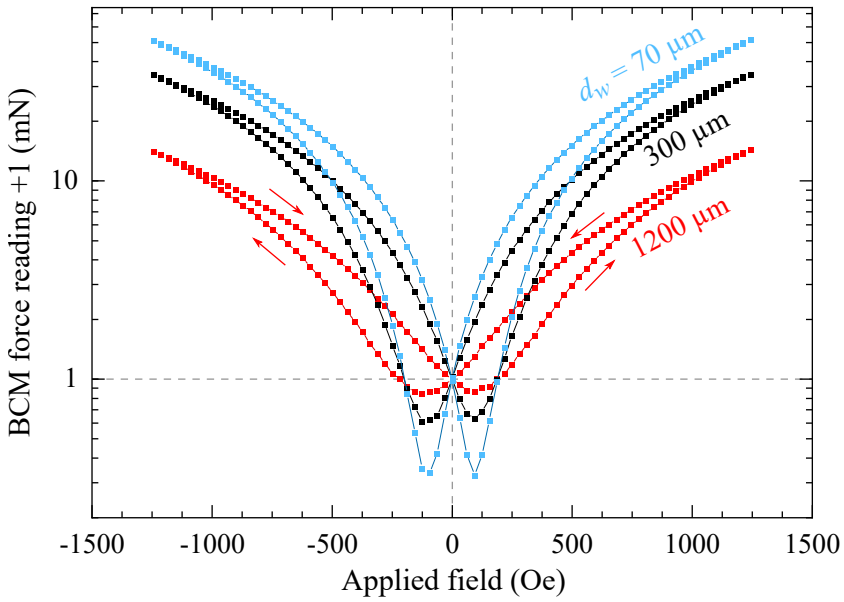

Fig. 35. Typical force-magnetization curves that can be obtained with BCM. Each V-shaped curve was obtained on a fatigue specimen after constant amplitude fatigue testing with 0.16 % total strain amplitude. The difference between each curve is the working distance.

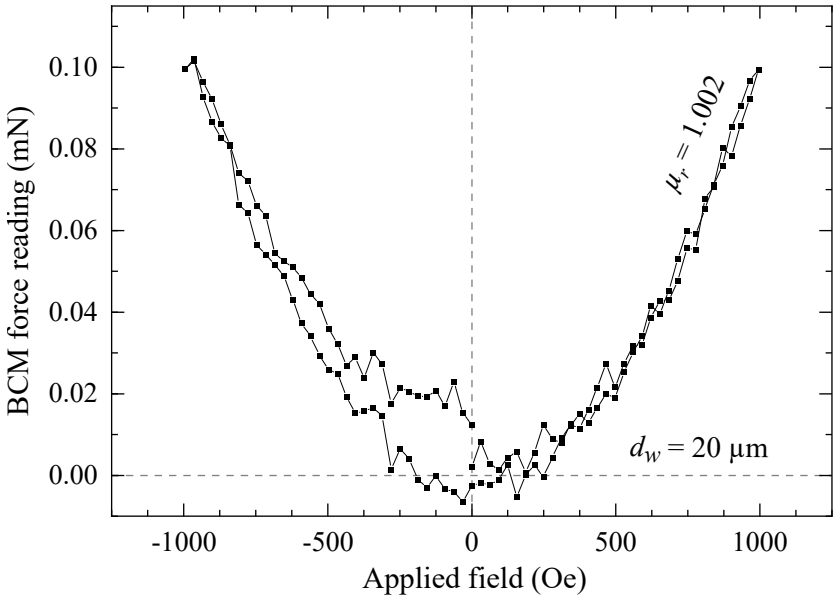

Fig. 36. A balanced core magnetometer measurement of the fully austenitic sample. Approximate relative permeability of the sample μ_r = 1.002. Working distance: 20 μm, Integration time: 10 seconds per point.

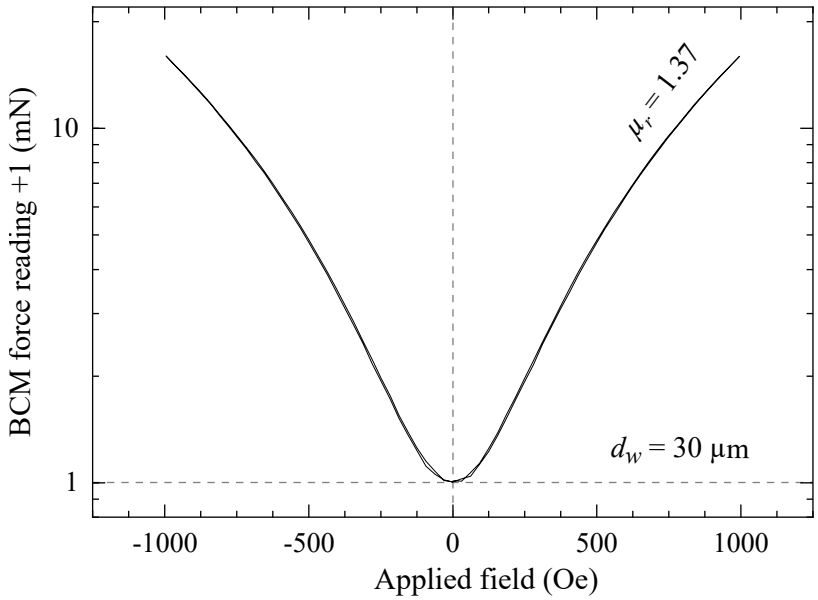

Fig. 37. A force-magnetization curve obtained on a standard sample with relative magnetic permeability μ_r = 1.37. Standard calibration sample, made of carbonyl iron powder shows very little to no coercivity. Individual points are not shown to make the hysteresis opening more

5.4.2 Measurement characteristics

To test the performance of BCM, fatigue specimens obtained after the fatigue tests described in section 7.2 were measured with the BCM and a vibrating sample magnetometer (VSM). The results are shown in Fig. 38. The (a-c-e) column represents the BCM measurement, while the (b-d-e) column was acquired with the VSM. Fig. 38a and b show a fatigue sample after a large number of cycles, which resulted in deformation-induced martensite with high coercivity. At the same time, Fig. 38e and f shows a much lower coercivity which was the result of a lower number of fatigue cycles. The opening in the force-magnetization curve was directly proportional to the opening in the magnetic hysteresis acquired by the VSM.

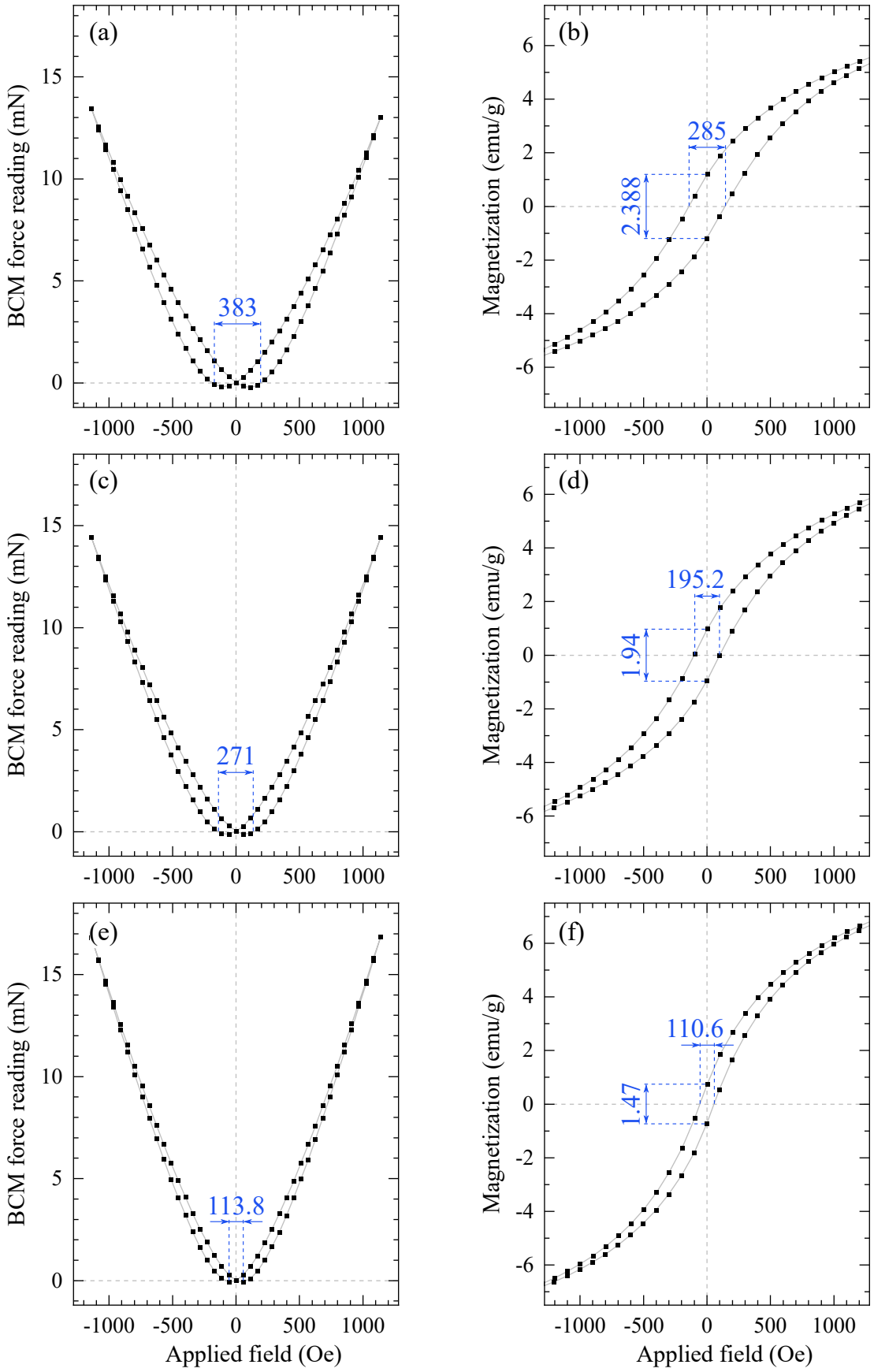

Fig. 38. Comparison of balanced core magnetometer (BCM) with vibrating sample magnetometer (VSM): (a), (c), and (e) are the BCM measurements, while (b), (d), and (f) are the VSM measurements of the same samples.

6 Material and Geometry

This work focuses on the study of the austenitic stainless steel AISI 347 (1.4550, X6CrNiNb18-10). The unique aspect of this steel is the addition of niobium, which has a higher affinity for carbon than chromium. This prevents the formation of chromium carbides and results in improved resistance to intergranular corrosion. This steel is also considered metastable and undergoes deformation-induced phase transformation from paramagnetic γ austenite to ferromagnetic α' martensite under plastic deformation at room temperature. This change from a paramagnetic to the ferromagnetic state is what has been largely exploited in this work to analyze the phase transformation kinetics. The analysis begins with the material, where one of the first factors influencing the kinetics of $\gamma \rightarrow \alpha'$ transformation is the manufacturing process and the resulting microstructural and chemical (in)homogeneity.

6.1 Steel production process and chemical composition

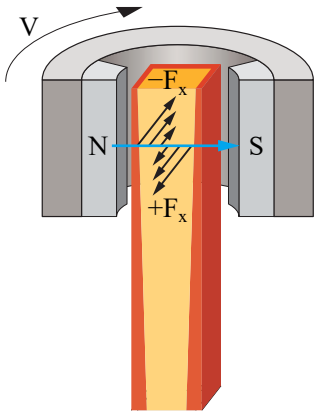

Fig. 39. Schematic illustration of an electromagnetic stirrer for billet casters [192].

The raw material was manufactured through continuous casting to a square cross-section using an electromagnetic stirring device (see Fig. 39) alongside the continuous casting height, followed by hot rolling to change the cross-section from a square to a circular shape with a diameter of 31.2 mm. The semi-finished bars then went through a heat treatment in a furnace at a temperature of 1058 °C. Table 6 provides the chemical composition of the material, of which two batches were acquired. Based on the content of Table 6, equivalent Cr and Ni content was calculated in accordance to Eq. (43) and (44) [193] and a region on the Schaeffler diagram was plotted in Fig. 40.

Table 6
Chemical composition of the 347 steel (wt%) with Fe as balance, including calculated martensite start temperature (M_s) and temperature, at which 50 % martensite is formed under 30 % strain (M_{d30}) in °C.

Batch	C	Si	Mn	Ni	Cr	S	P	Nb	M_s	M_{d30}
A	0.025	0.401	0.577	10.064	18.147	0.0011	0.024	0.402	-97.97	48.87
B	0.051	0.409	0.714	9.121	17.165	0.003	0.029	0.547	-47.24	58.08
Norm.	≤0.08	≤1.00	≤2.00	9 – 12	17 – 19	≤0.015	≤0.045	≤1.00	–	–

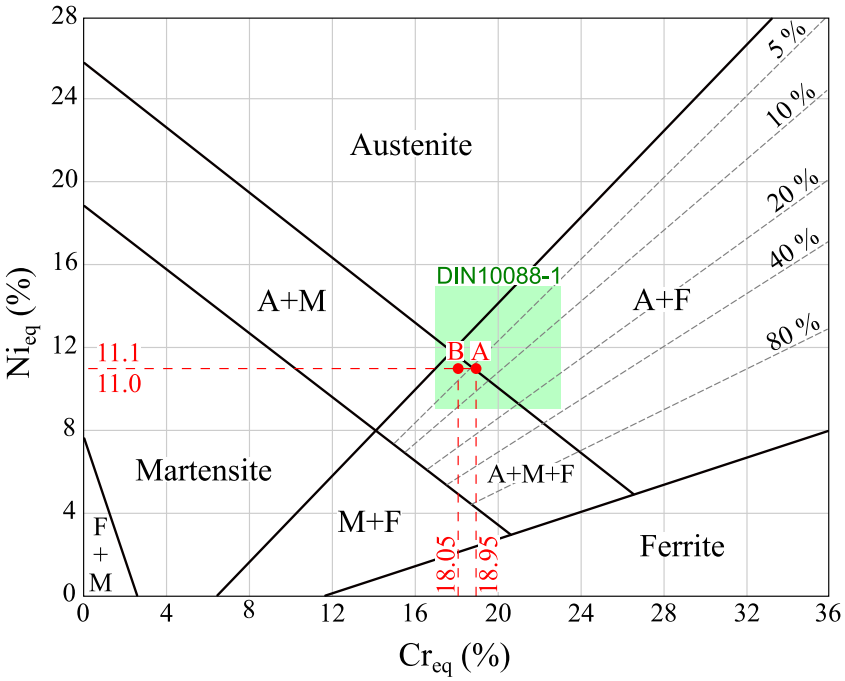

Fig. 40. Schaeffler diagram with the marked position of 347 austenitic stainless steel batches A and B. Modified after [193].

$$\mathrm{Ni_{eq}} = \mathrm{Ni} + 30\mathrm{C} + 0.5\mathrm{Mn} \tag{43}$$

$$\mathrm{Cr_{eq}} = \mathrm{Cr} + \mathrm{Mo} + 1.5\mathrm{Si} + 0.5\mathrm{Nb} + 2\mathrm{Ti} \tag{44}$$

Additionally, in Table 6, martensite start temperature M_s and M_d temperature, at which 50 % martensite is formed under 30 % strain, were calculated according to Eq. (4) and Eq. (5) on page 28.

6.2 Fatigue specimen geometry

Fatigue specimens were machined at Demgen Werkzeugbau GmbH from 30 mm bars to the geometry presented in Fig. 41. All fatigue specimens from Batch A were mechanically polished, which resulted in a very good surface roughness with R_z values in the range of 0.05 to 0.1 μm. However, mechanical polishing created a thin layer of deformation-induced martensite on the surface. Magnetic measurements showed a higher concentration of α' martensite on the polished surface when compared to the only machined surface. In fact, no additional α' martensite could be found on the machined surfaces of Batch A. Taking this into consideration, the Batch B specimens were only electro-chemically polished by Poligrat GmbH. This resulted in very little to no machining-induced martensite transformation. The drawback was an increased surface roughness.

Roughness measurements were performed on Mahr Perthometer PGK 120 and presented in Fig. 42. In the case of Batch A, the roughness calculation was

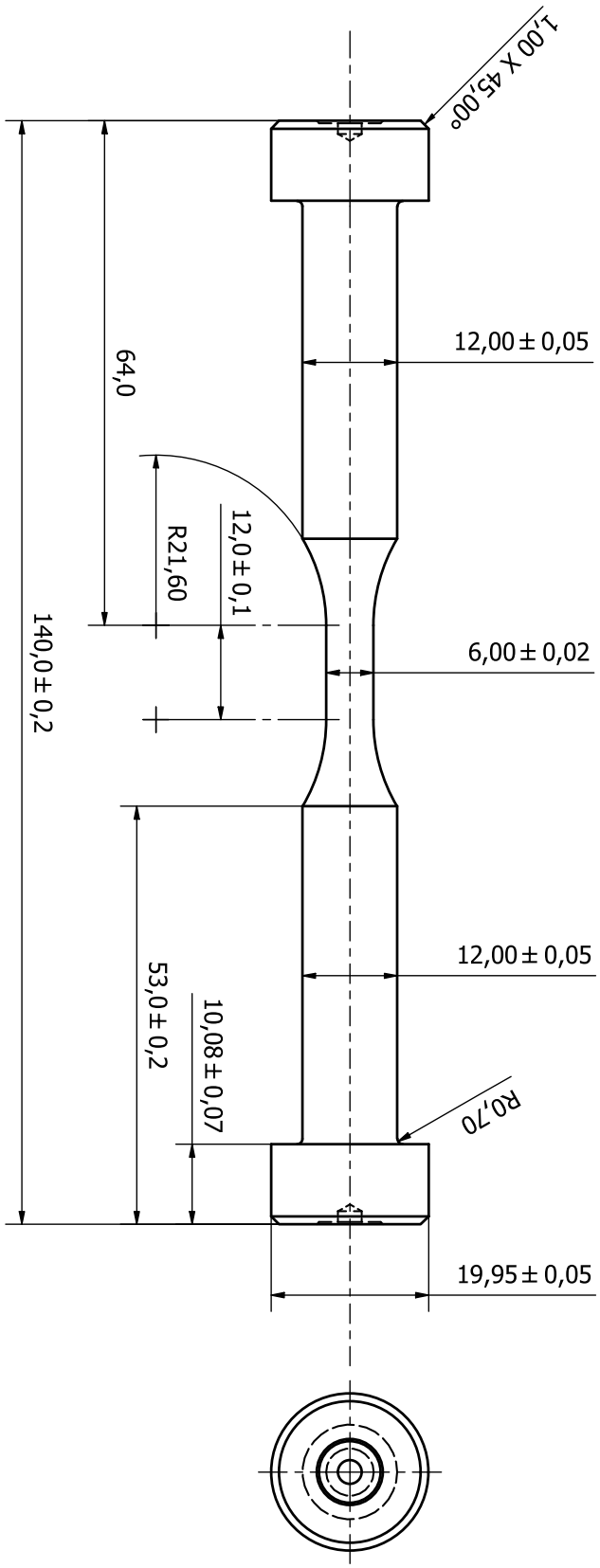

Fig. 41. Fatigue specimen geometry used in this work.

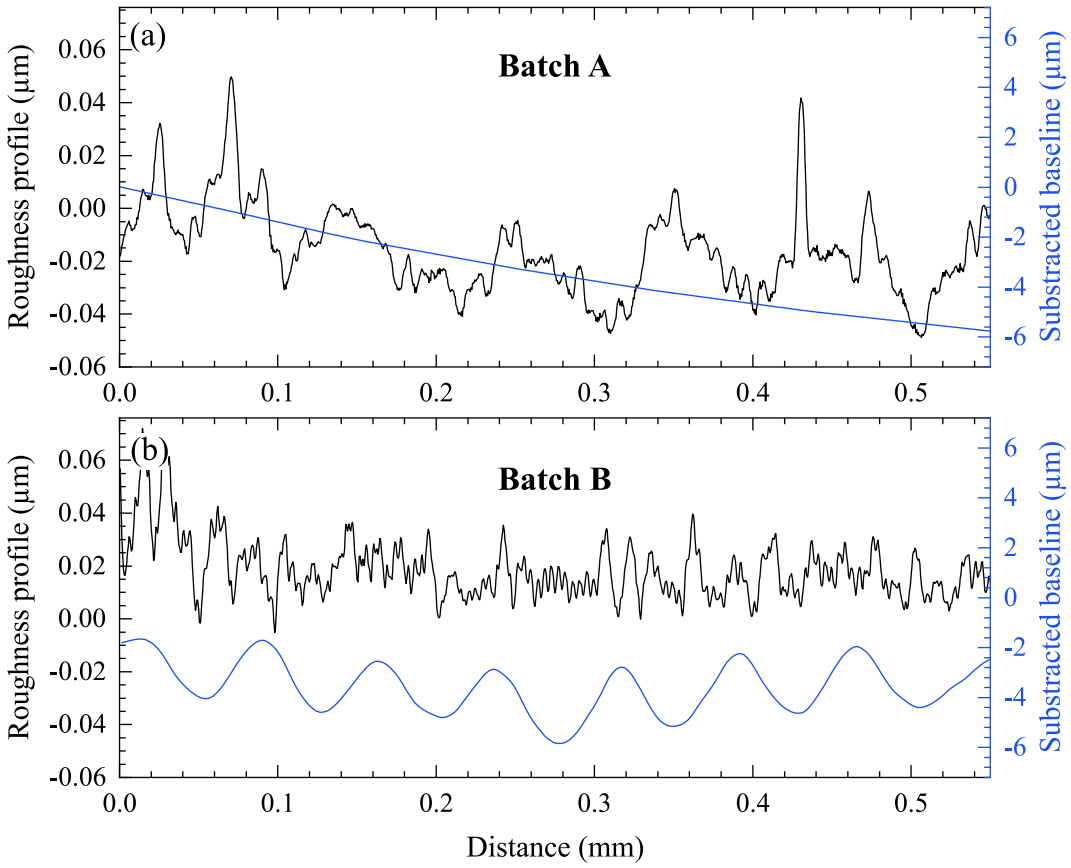

Fig. 42. Roughness profiles of fatigue specimens measured at the center of the gauge length: a) Batch A; b) Batch B.

relatively straightforward. In the case of Batch B, electropolishing produced a very smooth surface but did not remove the waviness from turning. If calculated according to the standard, this waviness should not be subtracted and results in R_z value of about 2 μm, even though the sharp changes in the topography have been removed.

6.3 Metallographic investigation

The microstructure in the initial condition was investigated with electron backscatter diffraction (EBSD) and energy dispersive X-ray spectroscopy (EDS). The results showed slight differences in chemical composition and grain size along the diameter of the bar while not having any significant texture. These variances form band structures along the casting (longitudinal) direction. The most notable difference was found in Cr and Ni content (see Fig. 43), where a higher amount of Ni also correlated with smaller grain size. EDS was done qualitatively, without a calibration that is needed to provide quantitative analysis. Given that a 24-hour integration time was required to obtain the EDS map in Fig. 43, differences in Cr and Ni content are not likely to significantly deviate from Table 6. Similarly to band-structured deviations in Cr and Ni con-

tent, Nb carbides were found to agglomerate in longitudinal bands as well. Fig. 44 shows an EDS map of a cluster with Nb carbides. These carbides could be identified by the simultaneous increased in carbon and niobium contents. Chromium, on the other hand, did not appear to bond with carbon.

Band structures could also be identified with a local average misorientation (LAM) map from the EBSD scan in Fig. 45. This material was found to be extremely sensitive to surface preparation. Considering that the depth of information in EBSD may not exceed 50 nm [177, 178], deformation-free surface preparation is essential for EBSD analysis of such material. After mechanical polishing with 6 μm, 3 μm, and 1 μm diamond suspension followed by 0.04 μm colloidal silica suspension (OP-S), the EBSD phase map contained more than 30 % bcc/bct lattice, which would also form longitudinal band structures. This result did not agree with magnetic measurements. Only when OP-S polishing was followed by 30 seconds of electropolishing in A3 electrolyte, did the phase map (see Fig. 45c) have the bcc/bct fraction below 1 %, which is in agreement with MFI measurements. The mean grain size was around 17 μm with the full distribution shown in Fig. 46.

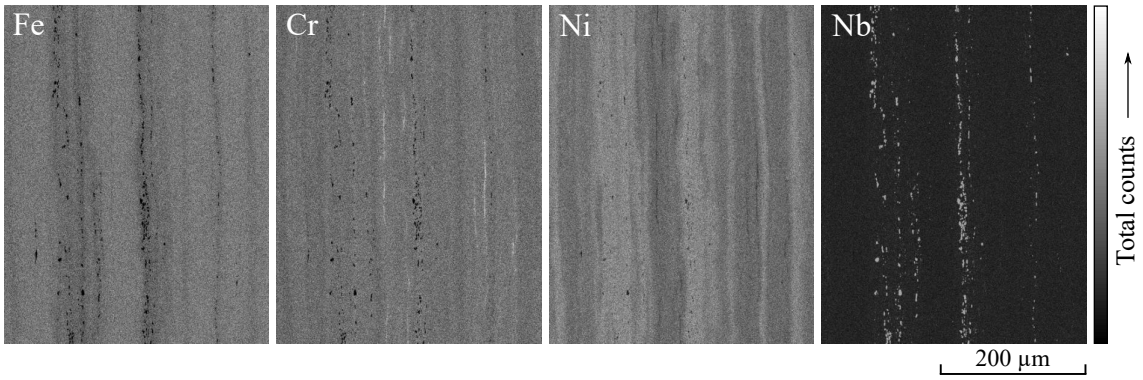

Fig. 43. Energy dispersive X-ray spectroscopy (EDS) of 347 Batch B, acquired from the center of longitudinally sectioned fatigue specimen. Final surface preparation: electropolishing.

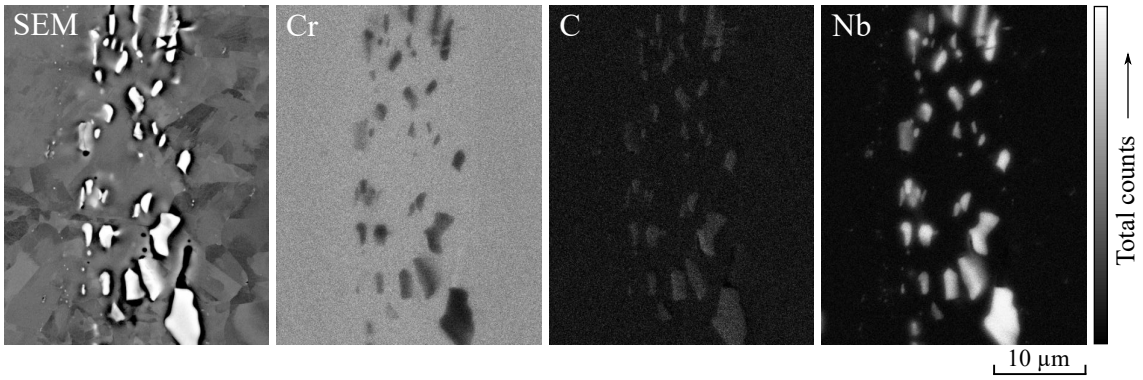

Fig. 44. An agglomeration of Nb carbides imaged with energy dispersive X-ray spectroscopy (EDS), acquired from the center of longitudinally sectioned fatigue specimen. Final surface preparation: electropolishing.

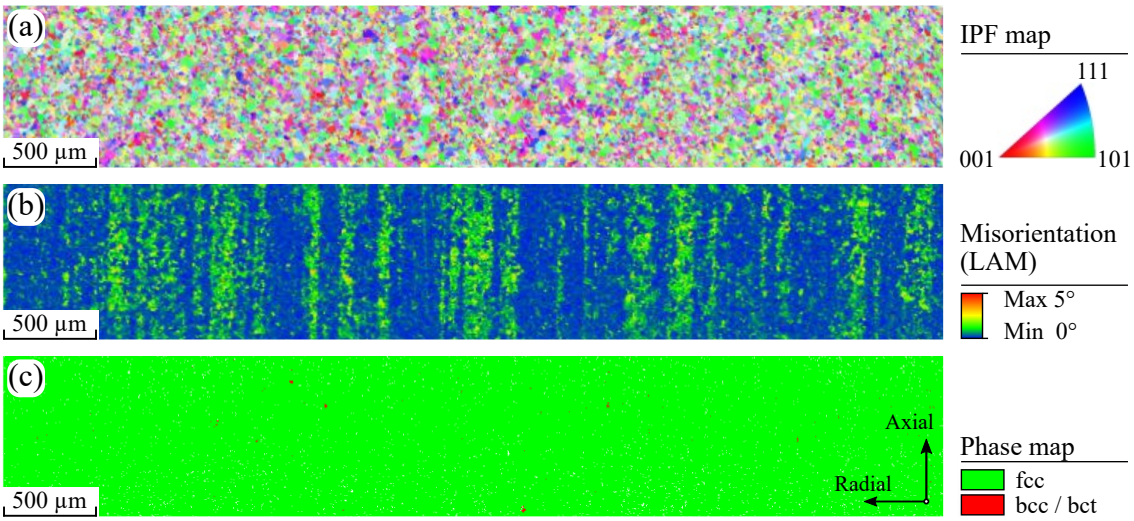

Fig. 45. A large area EBSD scan of a sample from Batch A: a) inverse pole figure; b) local average misorientation (LAM) map; c) phase map. Final surface preparation: electropolishing.

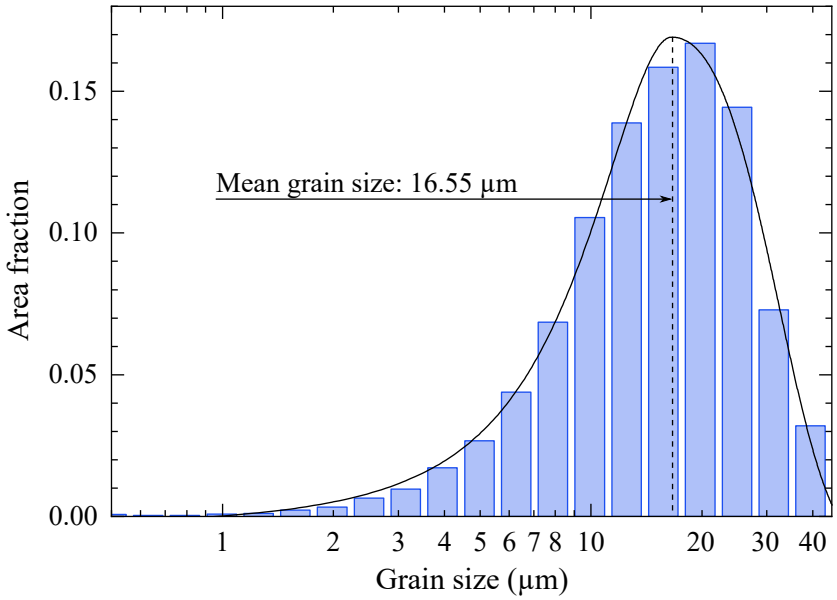

Fig. 46. Grain size (diameter) from a Batch B sample, acquired from the center of a longitudinally sectioned fatigue specimen.

6.4 Local magnetic properties

Magnetic force imaging (MFI, section 5.1) was used to map the density of ferromagnetic phases, such as α'-martensite and δ-ferrite. In Fig. 48, transverse sections of 30 mm diameter stock bars from batches A and B were scanned at a working distance of 20 μm. The austenite component was subtracted according to the calibration curve in Fig. 20 on page 59. Batch A showed overall lower quantities of ferromagnetic phase ξ_{fm}. Within a 3 mm radius from the center, Batch A had ξ_{fm} of 0.15 Fe%, whereas it was 0.34 Fe% for Batch B. In both batches there was a small decrease in ξ_{fm} at the center, but it was more pronounced for Batch B. Initial rectangular shape of continuous casting,

also known as the “stirring mark”, could be identified by increased ξ_{fm} values. Between the outer edge and the stirring mark there appeared to be pure austenite, with ξ_{fm} reading of 0.05 %, which is likely to be caused by shading from a much more ferromagnetic outer edge.

Longitudinal band structure that was identified with EDS and EBSD was also found with MFI. In Fig. 49, longitudinal and transverse sections were combined with a rotary scan of the outer bar surface. As a result, a 3D section was reconstructed to demonstrate the distribution of the ferromagnetic phases in the material. The stirring mark from Fig. 48 can be observed to extend in the longitudinal (axial) direction, forming the previously identified band structure. The spiral on the outer surface of the bar corresponds to the turning process, intended to reduce the diameter to the final dimension of 30 mm.

Uniaxial magnetic balance UMB-2 (section 5.2) was used to measure the ferromagnetic content in machined fatigue specimens before fatigue testing. In Fig. 47, the distribution of ξ_{fm} was plotted as density for each fatigue specimen. Most fatigue specimens from Batch A had ξ_{fm} values between 0.2 and 0.3 Fe%, with a small group of specimens with ξ_{fm} values between 0.4 and 0.5 Fe%. Fatigue specimens from Batch B were in the range from 0.75 Fe% to 0.95 Fe% with only three specimens above this range, which is likely to be caused by less careful machining.

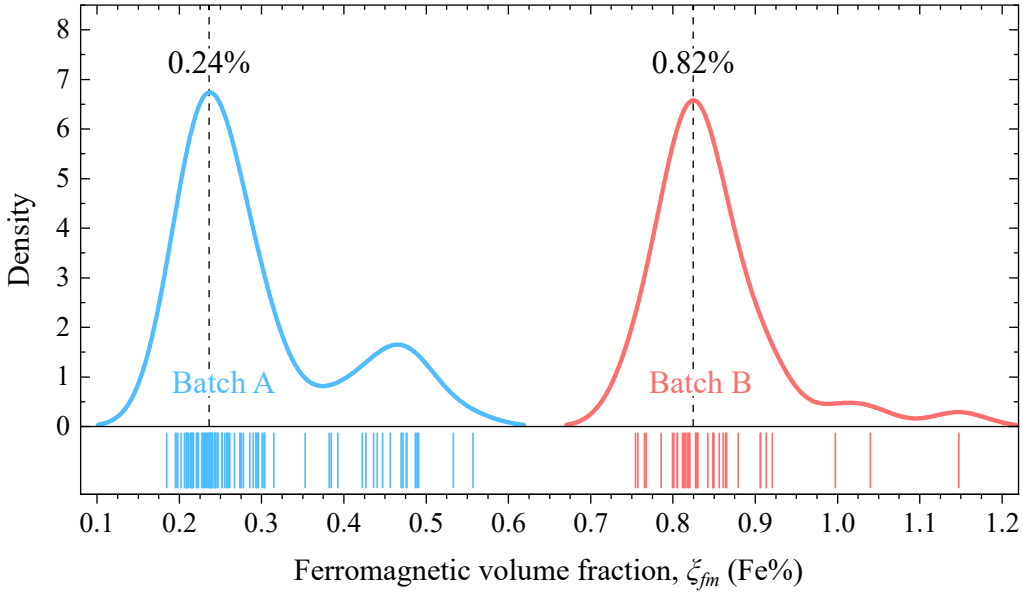

Fig. 47. Density of ferromagnetic volume fraction distribution in fatigue specimens from Batch A and B.

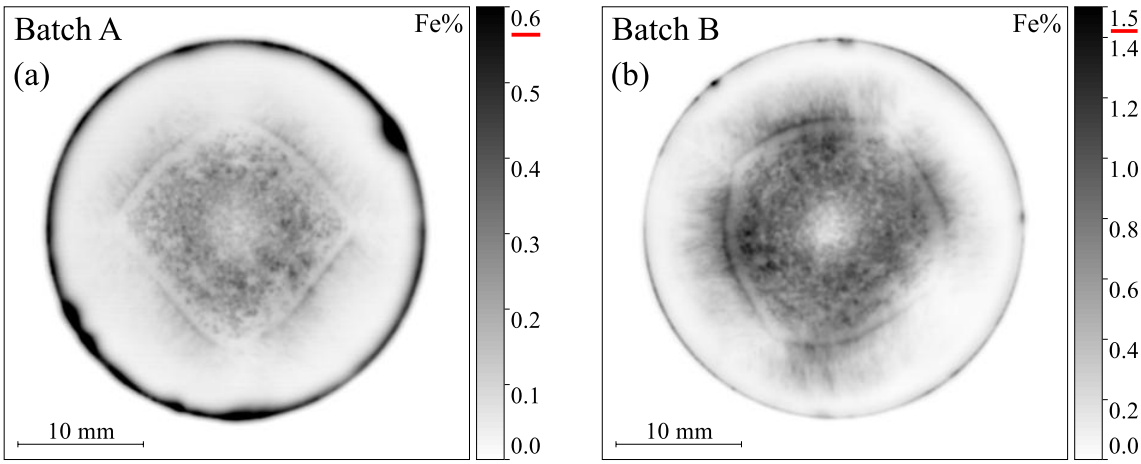

Fig. 48. Magnetic force imaging (MFI) ferromagnetic volume density map of the stock material: a) transverse section of 347 Batch A, 0.15 Fe% at the center; b) transverse section of 347 Batch B, 0.34 Fe% at the center. Final surface preparation: 1 μm diamond suspension polishing.

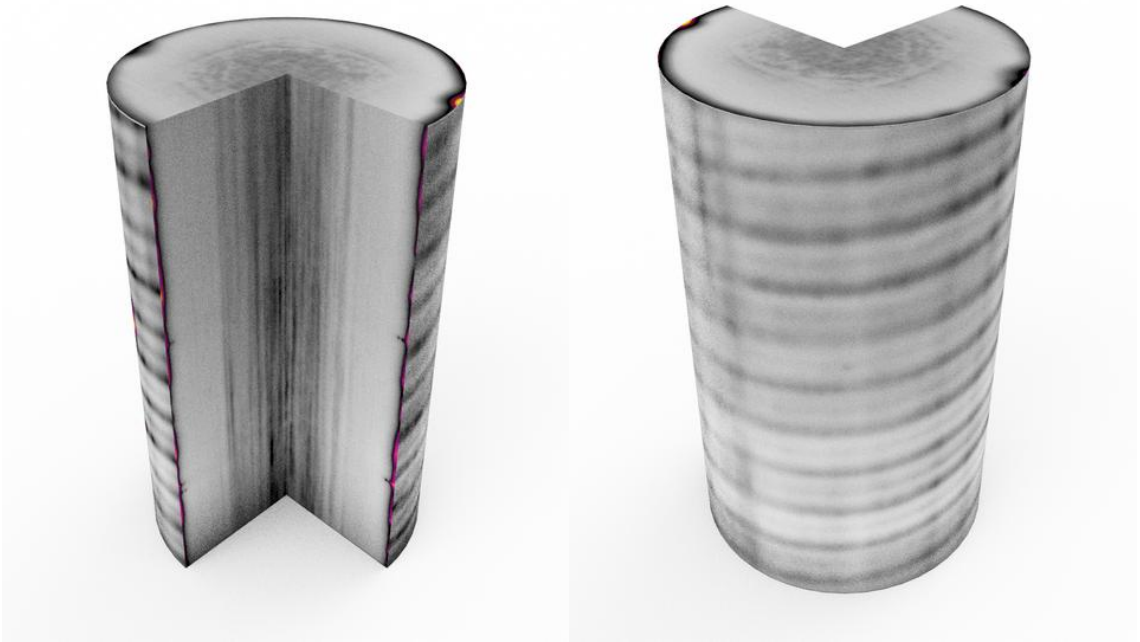

Fig. 49. Combined transverse, longitudinal, and rotary MFI scans indicating ferromagnetic volume density of the 347 Batch A stock material.

7 Experimental Results

7.1 Lower accumulated strain limit for phase transformation

strain	strain rate	stress	temperature	α' volume
variable	constant	variable	variable	variable

One of the less explored areas in $\gamma \rightarrow \alpha'$ transformation process is the combination of elevated temperatures with fairly low strain amplitudes. The combination of a highly inhibited $\gamma \rightarrow \alpha'$ process with the difficulty of measuring magnetic properties at elevated temperatures inside a fatigue machine creates very unfavorable conditions for the experimental evaluation. Using a uniaxial magnetic balance (UMB, section 5.2 on page 60) it became possible to detect small fractions of deformation-induced martensite *in situ* at elevated temperatures during a full-scale fatigue test.

A strain increase test with a constant strain rate was chosen to evaluate the dynamics of $\gamma \rightarrow \alpha'$ transformation process at HCF to VHCF strain amplitudes with a transition to the LCF regime. Initial changes in the microstructure were also observed with an electrical resistance measurement. The location and growth dynamics of α' were captured *post-mortem* by means of magnetic force imaging.

7.1.1 Strain increase test parameters

A strain increase test (SIT) is a total strain controlled fatigue test that starts at a low strain amplitude which increases gradually in fixed intervals, called steps. Within one step total strain amplitude remains constant (see section 3.3 on page 41 for more information). All SITs in this work have been performed with identical parameters, shown in Table 7. A constant strain rate of $0.004\,s^{-1}$ in a triangular waveform was chosen to avoid excessive heat generation at lower temperatures. The duration of a single step was equal to 120 minutes. Every 120 minutes, total strain amplitude was increased by 0.01 %, starting from 0.05 %. The consequence of having a fixed strain rate is the variable number of cycles within each step, as shown in Table 7.

7.1.2 Influence of temperature on low-strain phase transformation

A series of five strain increase fatigue tests was performed in accordance with the parameters in section 7.1.1. Each fatigue test was performed using the same setup described in section 5.3 on page 67, the only variable being temperature. The temperature was examined from ambient 17 °C to 240 °C with

Table 7
Strain amplitudes for strain increase tests (SITs). The duration of each step is 120 minutes. Strain rate 0.004 s^{-1}

Step	Total strain amp. ε_{at}, %	Frequency f, Hz	Cycles per step N_{step}	Step	Total strain amp. ε_{at}, %	Frequency f, Hz	Cycles per step N_{step}
1	0.05	2.000	14400	17	0.21	0.476	3429
2	0.06	1.667	12000	18	0.22	0.455	3273
3	0.07	1.429	10286	19	0.23	0.435	3130
4	0.08	1.250	9000	20	0.24	0.417	3000
5	0.09	1.111	8000	21	0.25	0.400	2880
6	0.10	1.000	7200	22	0.26	0.385	2769
7	0.11	0.909	6545	23	0.27	0.370	2667
8	0.12	0.833	6000	24	0.28	0.357	2571
9	0.13	0.769	5538	25	0.29	0.345	2483
10	0.14	0.714	5143	26	0.30	0.333	2400
11	0.15	0.667	4800	27	0.31	0.323	2323
12	0.16	0.625	4500	28	0.32	0.313	2250
13	0.17	0.588	4235	29	0.33	0.303	2182
14	0.18	0.556	4000	30	0.34	0.294	2118
15	0.19	0.526	3789	31	0.35	0.286	2057
16	0.20	0.500	3600	32	0.36	0.278	2000

no more than ±2 °C variation within the full duration of the test. The temperature was set 120 minutes prior to the start of the test to allow the temperature differences between UMB and the specimen to settle. Fatigue specimens here belong to Batch A (see section 6 on page 80 for more information). Uniaxial magnetic balance UMB-3 was used for α' volume fraction measurement (see section 5.2 for more information).

Fig. 50 combines the results from all five SITs but separates them by mean stress, stress amplitude, strain amplitude, and ferromagnetic volume fraction calibrated to ferrite volume fraction. Additionally, plastic strain amplitude was plotted in Fig. 50b, together with the total strain amplitude taken from the ambient temperature test, which is valid for all five tests.

The plastic strain amplitude was consistently higher at elevated temperatures. The test at 240 °C showed twice the plastic strain compared to the ambient temperature test. An indication of cyclic hardening can be identified here as the plastic strain amplitude drops within a single step after ε_{at} = 0.15 %. Such behavior could be observed only up to 160 °C. The test performed at 240 °C showed no significant change in plastic strain amplitude within one step. Logically, the lowest stress amplitudes could also be found at 240 °C. From stress amplitudes, signs of cyclic softening could be observed for all temperatures, except 17 °C in the range $0.11 \leq \varepsilon_{at} \leq 0.16$ (%). After step number 16 at ε_{at} = 0.20 %, cyclic hardening could be observed even at 240 °C by increased stress amplitude within a single step. Cyclic relaxation at 80 °C and above

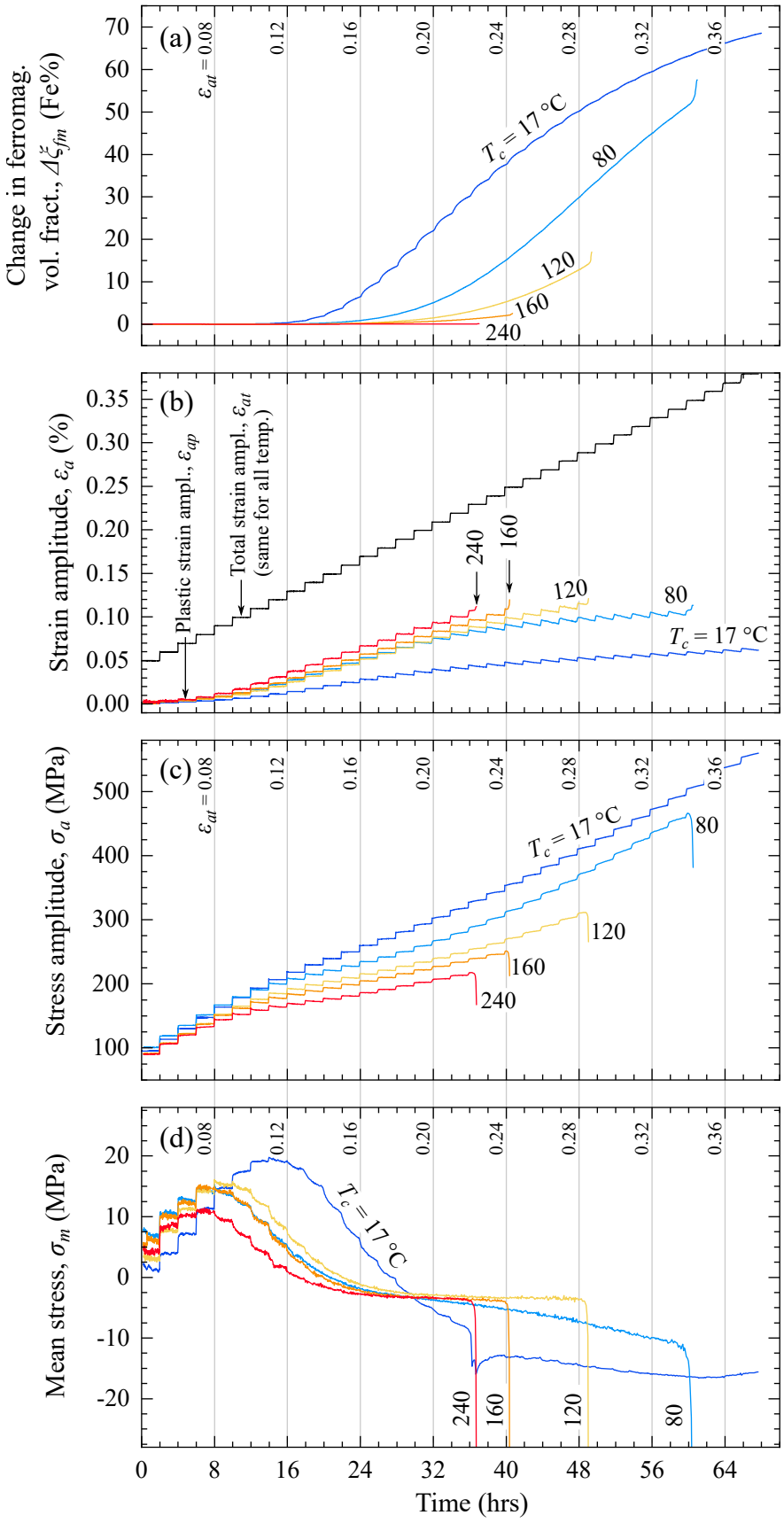

Fig. 50. Strain increase fatigue tests at various temperatures: a) fraction of α' martensite in Fe% with subtracted initial values; b) total strain amplitude, valid for all temperatures and plastic strain amplitudes; c) stress amplitude response of the material; d) mean stress. Material: 347 Batch A.

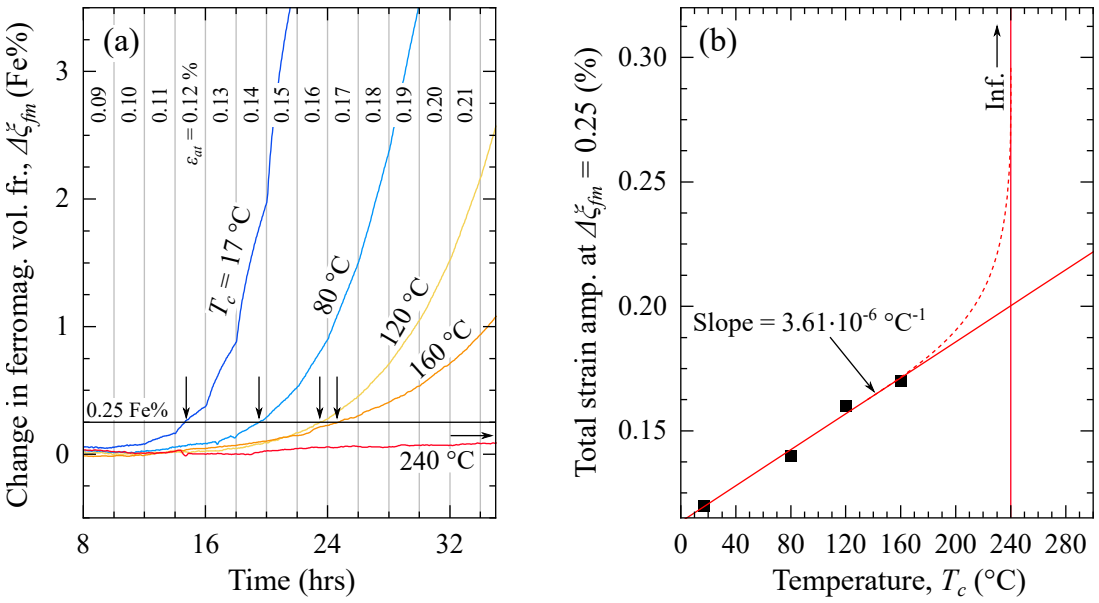

Fig. 51. Evolution of α' martensite in a SIT as a function of temperature: a) initial values from Fig. 50a of α' volume fraction in Fe% with subtracted initial values; b) total strain amplitude, at which 0.25 Fe% was reached at different temperatures. Material: 347 Batch B.

could be observed after step 4, ε_{at} = 0.08 %, by a decreasing mean stress (see Fig. 50d). As for the test at 17 °C, mean stress starts to decrease after step 7, ε_{at} = 0.11 %.

Since cyclic hardening is a result of an increased volume of the much stiffer α' phase, this behavior is reflected well by magnetic measurements in Fig. 50a. From these measurements, the temperature influence on $\gamma \rightarrow \alpha'$ phase transformation could be observed even better. At 17 °C, an arc-shaped component in the signal could be identified. The troughs of the arc correspond with the start and the end of individual steps. This is not a unique phenomenon. Such behavior has been observed in at least 5 other SITs at ambient temperature (not shown here). At elevated temperatures, this irregularity in the rate of phase transformation was not observed.

Fig. 51a provides a better look at strain amplitudes at which the formation of α' had started. For the ambient temperature test at 17 °C, the total strain amplitude at which phase transformation took place was found to be as low as ε_{at} = 0.10 %. It most likely initiated even earlier, but SNR and drift of the signal do not allow for a definitive verdict. Coincidentally, this is when the mean stress relaxation at 17 °C started. At elevated temperatures, first detection of phase transformation occurred much later. To avoid false positive detection of initial phase transformation, a threshold of 0.25 Fe% was chosen to plot the total strain amplitude required to initiate $\gamma \rightarrow \alpha'$ transformation against temperature. The result is shown in Fig. 51b. The obtained curve is a quick evaluation of how strain energy is balanced with thermal energy and the limit

at which strain can no longer overcome thermal energy. Since SIT at 240 °C resulted in specimen failure before 0.25 Fe% was reached, a vertical line was plotted at 240 °C to signify the possibility of M_d being reached. All other SITs crossed the 0.25 Fe% line in a manner that can be described as a linear function with a slope of $3.61 \cdot 10^{-6}$ °C^{-1}.

7.1.3 Changes in the material detected with electrical resistance

Electrical resistance (or conductivity) measurements are often considered sensitive to the changes in the microstructure [194–198]. Dislocation movement can already trigger changes in the electrical resistance of the material. There are two factors that highly affect electrical resistance measurements: temperature and thermoelectric voltages. A fatigue process inherently generates heat, which is proportional to plastic deformation. This means in a strain increase test, even if the strain rate is constant throughout the test, the temperature of the specimen will inevitably rise. To address this issue, a hold time of 60 minutes after each step has been introduced to the SIT program. All other parameters remained unchanged and correspond to Table 7.

Electrical resistance was measured with the 4-wire Kelvin method. Two copper-plated steel wires were spot-welded to the gauge length, while another two were welded to the shafts of the specimen. The fatigue specimen was taken from Batch A. A constant current of 1 Ampere was applied to the shafts, while voltage drop at the gauge length was measured. The signal was acquired with a National Instruments NI9238 module capable of 24 bit ADC resolution over ±500 mV range. The temperature was measured with an LM35 temperature sensor, when combined with 24-bit ADC, capable of 1 mK resolution. A 3 mm radius was milled on the side of the sensor package to match the curvature of the fatigue specimen. A plastic clip was then used to press the temperature sensor together with the applied thermal compound to the center of the fatigue specimen.

The DAQ was programmed to take a mean average of the applied current and the voltage drop over a 3-second period. These values were then measured again for another 3 seconds but with no current applied. The voltage drop values with no current applied were then subtracted from the values with the current applied. This was done to compensate for thermoelectric voltages generated at various junctions.

Unprocessed data from the test is shown in Fig. 52. After every 120-minute step, there was a 60-minute hold time to stabilize the temperature. After 100 hours, there was a larger break for machine maintenance. In further calculations, a mean value of the last 15 minutes of the hold time was plotted

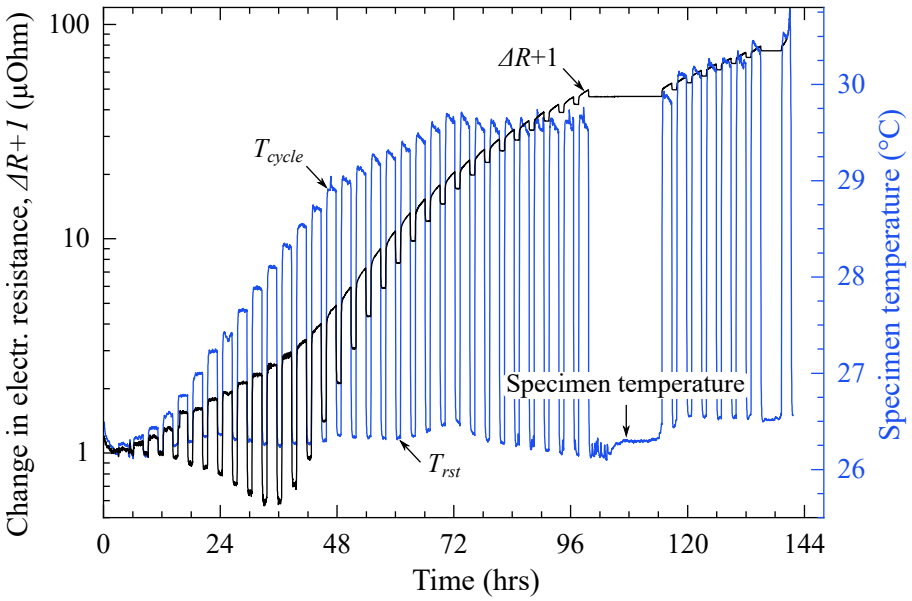

Fig. 52. Electrical resistance measured in a strain increase fatigue test at 26 °*C* ambient temperature. Initial electrical resistance was subtracted while 1 μOhm was added to display negative values in the logarithmic scale. Material: 347 Batch A.

against total strain amplitude in Fig. 53. In both diagrams 1 μOhm was added to be able to show negative values on logarithmic scale.

From Fig. 52 one can observe that the initial cyclic deformation of the material leads to a decrease in electrical resistance. After careful examination of temperature data, this drop in electrical resistance appears to be due to microstructural changes in the material and does not correlate with the temperature of the specimen. The very first decrease in electrical resistance could be found in step 5, where total strain amplitude equals 0.09 %. Coincidentally, this is where the first relaxation of mean stress happens (see Fig. 50). At step 6, ε_{at} = 0.10 %, and step 7, ε_{at} = 0.11 %, first sign of deformation-induced transformation could be detected by magnetic measurements (see Fig. 51).

After step 11, ε_{at} = 0.15 %, electrical resistance stopped decreasing and changed to a positive slope. At this point, phase transformation at room temperature produced over 3 Fe% of α' martensite and triggered phase transformation at 80 °C. By the end of the test, the electrical resistance of the specimen increased by nearly 80 μOhm. Considering initial electrical resistance R_0 = 687.5 μOhm, the change equals to 12 % total increase in electrical resistance. The maximum decrease in electrical resistance was equal to 0.35 μOhm.

7.1.4 Localization of initial phase transformation

Fatigue testing is always performed on a finite-size piece of material with a specific geometry. The typical shape of fatigue specimens is intended to create a homogeneous uniaxial stress-state. This is a simplification that works better

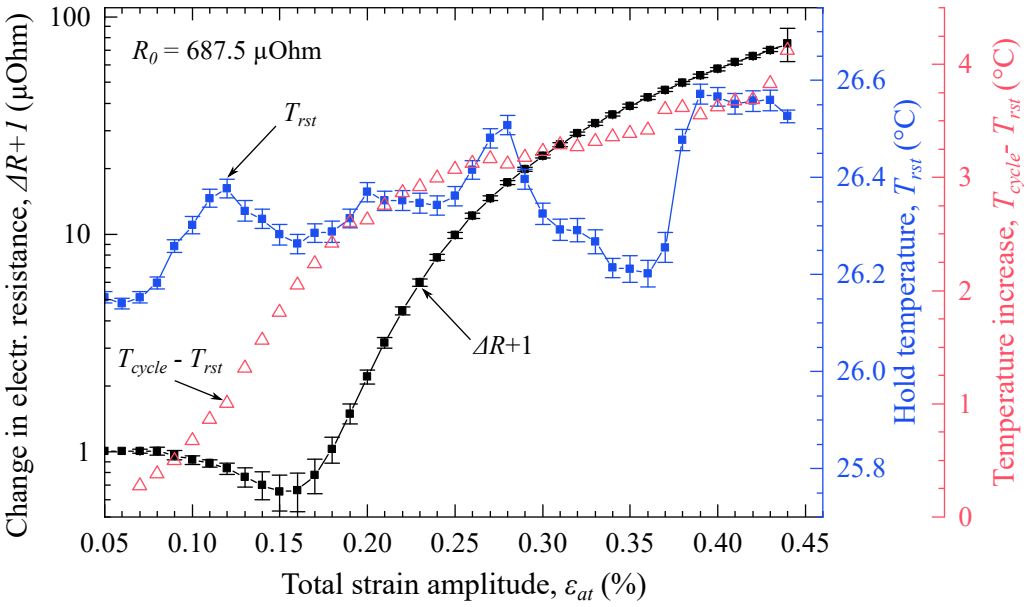

Fig. 53. Electrical resistance as a function of strain amplitude in a SIT. Only mean average at the end of the rest period is plotted. Error bars show the scatter of values recorded during the hold period. Initial electrical resistance R_0 was subtracted while 1 μOhm was added to display negative values in logarithmic scale. Material: 347 Batch A.

in homogeneous materials and less so in a metastable multi-phase steel. It is, therefore, essential to know what happens within the volume of the fatigue specimen gauge length.

To see where in the specimen $\gamma \rightarrow \alpha'$ transformation originates, four SITs at ambient temperature were interrupted after steps 6, 10, 13, and 15. Fatigue specimens were then cut in half with electric discharge machining, ground and polished. The specimen temperature for all interrupted tests was 25 °C, slightly higher when compared to the 17 °C test in Fig. 50. The reason for that is grip cooling was supplied with 25 °C water instead of chilled to 15 °C. This, however, did not affect the overall temperature stability during the tests.

The distribution of deformation-induced martensite was analyzed with magnetic force imaging (MFI, section 5.1 on page 54), calibrated to relative magnetic permeability. MFI can be interpreted here as the density of deformation-induced martensite. It has already been shown in section 6 that the material in the initial condition contains a small quantity of a ferromagnetic phase, around 0.15 Fe% for Batch A. This ferromagnetic phase was found to be α' that formed in longitudinal bands, following the variation in γ grain size. What can be seen in Fig. 54 after step 6 (ε_{at} = 0.10 %, N = 60886) is essentially identical to the initial condition distribution of α'-martensite. An increase in permeability along the outer surface of the gauge length corresponds to the α'-martensite generated by mechanical polishing of the Batch A fatigue specimens.

The first significant indication of the deformation-induced martensite from

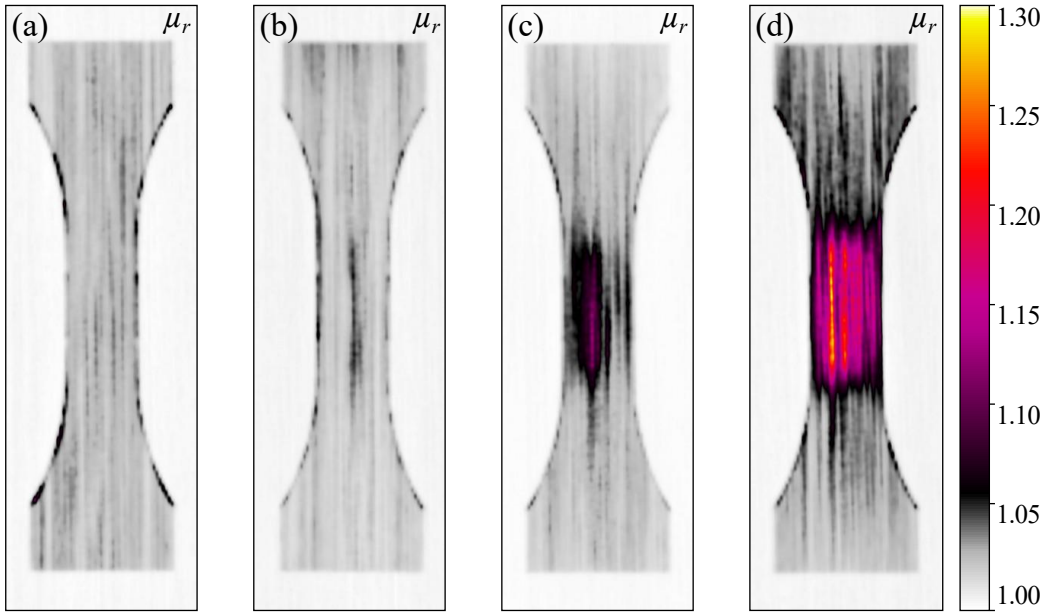

Fig. 54. MFI relative magnetic permeability maps at different stages of a strain increase test at 25 °*C*: a) after step 6, which reaches a total strain amplitude of 0.10 %; b) after step 10 (0.14 %); c) after step 13 (0.17 %); d) after step 15 (0.19 %). Final surface preparation: 3 μm diamond suspension polish. Material: 347 Batch A. $d_w = 50\,\mu$m.

fatigue loading could be found after step 10 (ε_{at} = 0.14 %, N = 84112). Here, α' martensite formed at the center of the gauge length, in a thin, under 1 mm in width band. In the following steps, this band grew in width, as illustrated by Fig. 54c, made after step 13 (ε_{at} = 0.17 %, N = 97648). Here the vertical α' bands start to exceed the gauge length and go into the increased diameter regions of the specimen. By step 15 (ε_{at} = 0.19 %, N = 105437), the distribution of α' becomes more homogeneous withing the gauge length, and further propagation of α' could be seen away from the center of the specimen.

7.2 Martensite morphology and magnetic properties

strain	strain rate	stress	temperature	α' volume
variable	variable	variable	ambient	**constant**

Previously, in section 7.1, we saw how α'-martensite volume fraction predictably increases with accumulated plastic strain. If we were to analyze the magnetic B-H curve at different accumulated strain levels at ambient temperature, e.g., from Fig. 54, we would see a gradual increase in saturation magnetization and relative permeability. This has been demonstrated by many studies, e.g., in [127, 128, 132, 137, 190, 199]. On the other hand, the role of *coercivity*[6] H_c (coercive force, coercive field) was not exhaustively investigated. There are studies that report an increase in coercivity along with an increase in plastic deformation [142, 190, 201], while a completely opposite behavior has also been reported [139–141, 202].

Since the volume of α' is directly proportional to plastic deformation, and magnetic moment m is directly proportional to the volume of the analyzed material, there is a non-causal[7] relationship between H_c and plastic deformation. When normalized to the volume fraction of α', coercivity is likely to decrease with plastic strain [203]. Under repeated cyclic strain conditions it is possible to achieve identical α' volume with different strain amplitudes. From an NDT perspective, this also creates an ambiguity in the determination of remaining fatigue life by α' volume fraction. Coercivity, on the other hand, is not directly linked to the amount of α' martensite but rather to the ability of domain walls to move and interact with other domains. As such, H_c can be potentially used as supplementary information to permeability and saturation magnetization, which reflect the quantity of α' phase in γ austenite.

This section presents differences observed in the magnetization behavior of fatigue specimens with equal α' martensite volume fractions obtained with different strain amplitudes.

7.2.1 Fatigue tests resulting in equal volume fraction of α' martensite

Five fatigue tests have been performed at ambient temperature (25 °C) in a total-strain-controlled regime with fully reversed (R = −1) strain. The strain had a sinusoidal function with a fixed frequency of 5 Hz. The parameters of the test are presented in Table 8. Although all tests were done at ambient

[6] Coercivity here refers to the field required to reduce magnetization M from the remnant magnetization to zero [114], as opposed to the field required to reduce the magnetic induction B to zero. When using the B-H curve, lower values of H_c can be expected [200].

[7] Relationship that is evident between the two variables but is not completely the result of one variable directly affecting the other.

temperature, due to fixed frequency, tests at higher strain amplitude had higher self-heating. The temperature at the gauge length center was recorded with Micro-Epsilon TIM450 thermal camera with 40 mK sensitivity.

In-situ data on ferromagnetic volume fraction were obtained with uniaxial magnetic balance UMB-1 (see section 5.2 on page 60). As shown in Fig. 55a, the highest rate of phase transformation corresponds to the highest strain amplitude ε_{at} = 0.220 % (specimen A). When compared to the lowest strain amplitude in specimen E, specimen A required 71 times fewer cycles to achieve a similar ≈ 5.5 % martensite volume fraction. Specimens B and D were the last to test and were interrupted at slightly different $\Delta\xi_{fm}$ values to negate the positive correlation of strain amplitude with α' volume fraction for specimens A, C, and E (see Table 8).

The initial temperature for all specimens was equal 25 °C, but due to self-heating they reached peak temperature at around $N \approx 3 \cdot 10^3$, as illustrated by Fig. 55b. The peak temperature corresponds to the maximum of plastic deformation, which can be deducted from the troughs in stress amplitude in Fig. 55c, where cyclic softening can be observed in the first 10^3 – 10^4 cycles. Although this rise in temperature may have decreased the rate of $\gamma \rightarrow \alpha'$ transformation, it clearly was not sufficient to prevent it.

Since none of the specimens were fatigued to failure, the strain to number of cycles to failure (the ε_{at}-N_f curve) in Fig. 56 can be used to estimate the remaining fatigue life and usage factor. The number of cycles to failure N_f and corresponding usage factor N/N_f were calculated in accordance with Eq. 45 [204]:

$$ln(N_f) = a_{\varepsilon n} - b_{\varepsilon n} \cdot ln(\varepsilon_{at} - c_{\varepsilon n}) \tag{45}$$

where $a_{\varepsilon n}$ = 5.42 ±0.09; $b_{\varepsilon n}$ = 2.6 ±0.3; $c_{\varepsilon n}$ = 0.15 ±0.03. Parameters a, b, and c were fitted to the ε_{at}-N_f data (Fig. 56) from the same material batch and specimen geometry, excluding runouts. Tests in the ε_{at}-N_f database were performed at a constant strain rate of 0.004 s^{-1}at ambient temperature and minimal self-heating. Calculated usage factors are listed in Table 8. Fatigue

Table 8
Fatigue test parameters of the five specimens that were fatigued until the target α' volume fraction has been reached.

Sp.	Tot. str. amp. ε_{at}, %	No of cycles N	Avg. strain rate $4f \cdot \varepsilon_{at}$, s^{-1}	Usage fact. N/N_f	Sat. mag. M_s, emu/g	α′vol. fract. $\frac{M_s}{157.1}$, %
A	0.220	29,370.	0.044	0.08	9.35	5.95
B	0.203	125,002.	0.040	0.13	7.91	5.04
C	0.185	289,074.	0.037	0.08	8.73	5.56
D	0.175	485,323.	0.035	0.03	8.28	5.27
E	0.165	2,098,542.	0.033	0.01	8.36	5.32

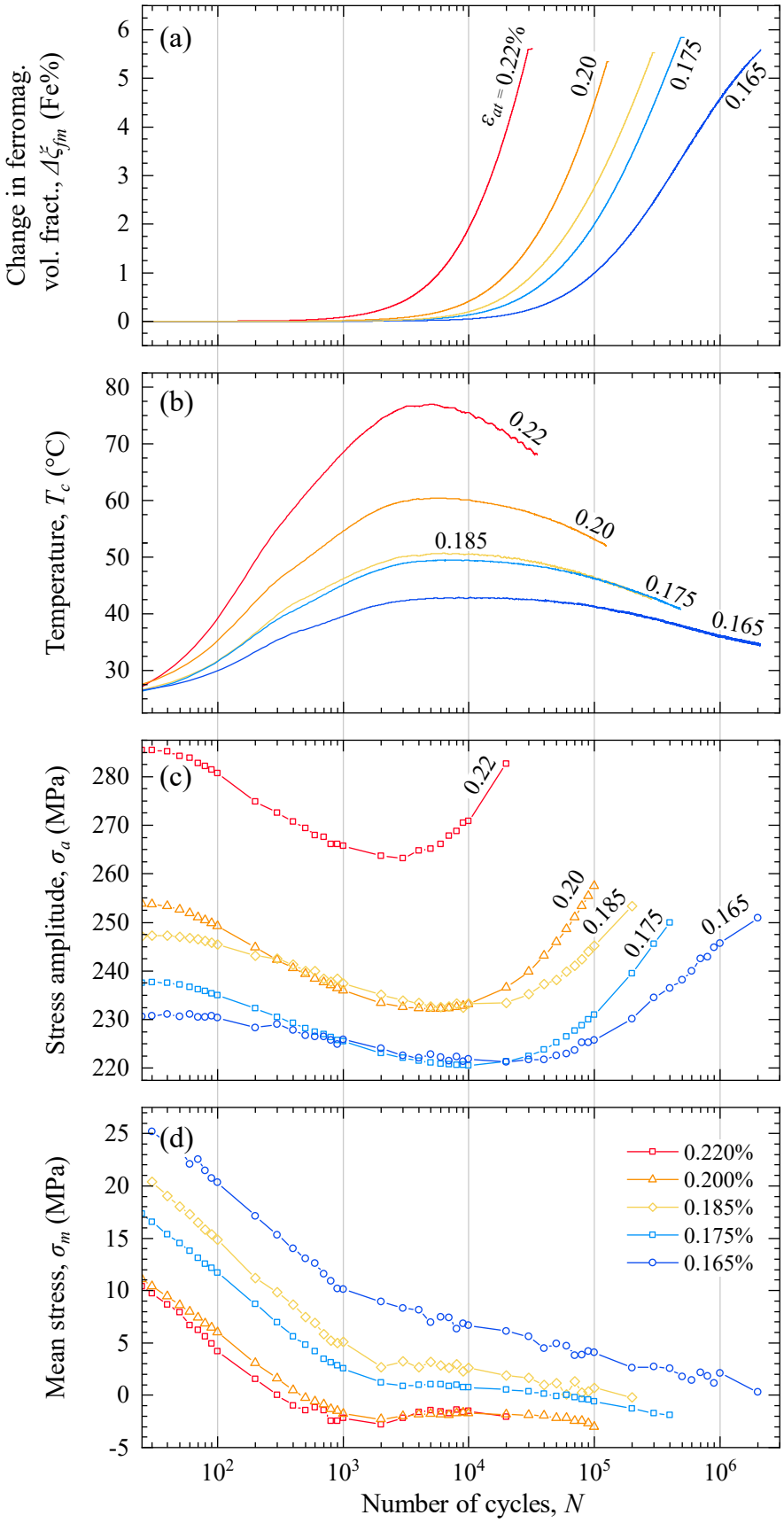

Fig. 55. Constant strain amplitude tests, interrupted at equal martensite vol. fraction: a) fraction of martensite in Fe% with subtracted initial values; b) temperature in the center of gauge length; c) stress amplitude response of the material; d) mean stress. Material: 347 Batch A.

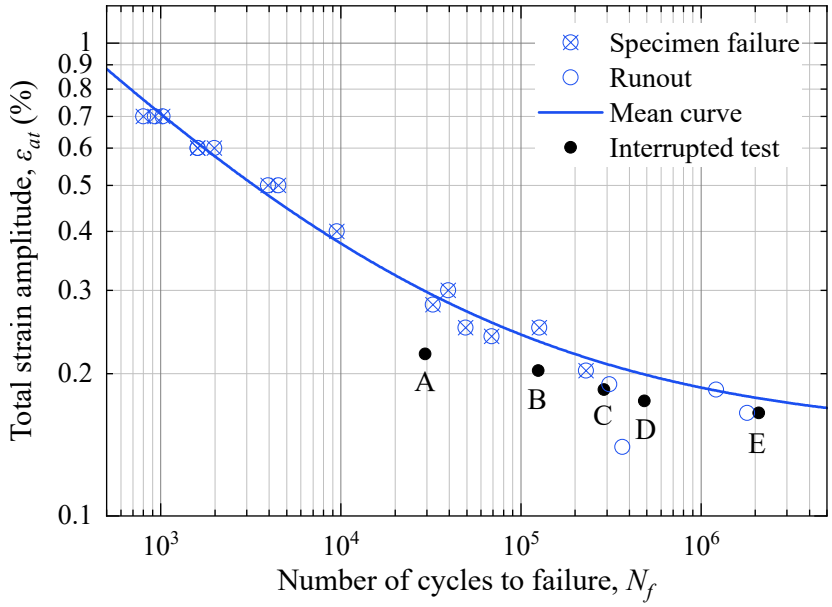

Fig. 56. ε_{at}-N_f curve generated during the material Batch A fatigue life investigations at ambient temperature. Interrupted tests with equal martensite volume fraction are shown by solid dots.

data for AISI 347, which is presented in Fig. 56, is comparable to the data obtained by other institutions, such as MPA Stuttgart, Technical University of Darmstadt, IWM Freiburg, and AREVA [205, 206].

7.2.2 Variations in coercivity with strain amplitude

After samples A through E were fatigued to similar α' volume fraction, a vibrating sample magnetometer (VSM) was used to obtain M-H magnetization curves[8]. Since the entire fatigue specimen is too large for VSM analysis, central part of the fatigue specimen with a height of 2.97 ± 0.01 (mm) and diameter of 5.94 ± 0.02 (mm) was cut out with electric discharge machining. Each cut-out sample had a mass of 0.65 ± 0.01 (g). Hysteresis loops were then obtained in a constant field mode within the range of ±7 kOe and the orientation of the magnetic field along the axial direction of the fatigue specimen.

The magnetization curves[9] for all five samples are shown in Fig. 57. The magnetization at the highest applied field of 7 kOe did not level off completely, as it would in case of full saturation. However, further increase of applied field is very unlikely to significantly increase saturation magnetization M_s, which was calculated as magnetization in emu/g at 7 kOe. M_s values were also consistent to UMB measurements, when converted to Fe%. M_s values are summarized in Table 8. To convert M_s values into α' volume fraction, Eq. (46),

[8] M-H curve is similar, but not the same as B-H curve. Magnetization M is an intrinsic magnetic field of the material, whereas magnetic induction B includes applied field H and magnetization M. The defining relationship is $B = \mu_0(H + M)$ in SI units, or $B = H + 4\pi M$ in cgs units.

[9] Measurements were done in cgs units and also presented as such to avoid rounding errors.

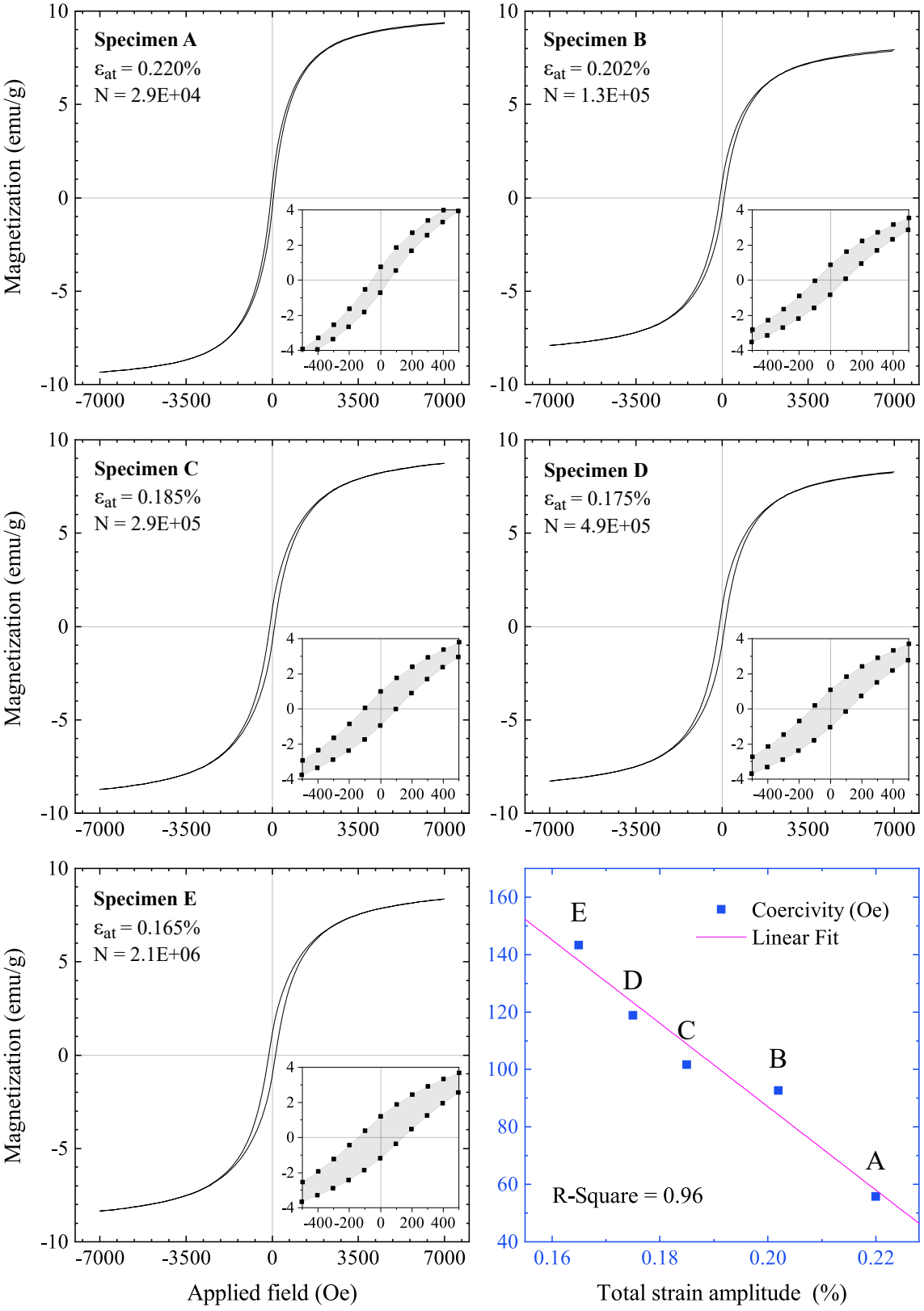

Fig. 57. Vibrating sample magnetometer (VSM) magnetization curves and corresponding coercivity values for specimen A–E. Material: 347 Batch A.

was used, taking 157.1 emu/g as an intrinsic saturation magnetization of the martensitic phase, suggested by Tavares and Mumtaz [139, 141, 207]:

$$\xi = \frac{M_s}{157.1} \tag{46}$$

where ξ is α' martensite volume fraction.

The highest saturation magnetization was measured in specimen A with $M_s = 9.35$ emu/g. The lowest saturation magnetization corresponds to specimen B with $M_s = 7.91$ emu/g, with a difference in martensite volume fraction in the range of 1 %, according to Eq. (46). A gradual increase in the width of the M-H hysteresis with decreasing strain amplitude can be seen in Fig. 57. Differences in martensite volume fraction did not seem to correlate to or have an influence on the coercive field. From plotted total strain amplitude against coercivity in Fig. 57, a linear trend can be observed with the highest coercivity in specimen E and the lowest in specimen A.

7.2.3 Distribution of martensite in the gauge volume

Magnetic force imaging (MFI, section 5.1 on page 54) was implemented to see how the deformation-induced martensite distributed after fatigue loading. The samples from VSM measurements (Fig. 58 right side) were analyzed with MFI, as well as the remaining half of the gauge length, cut in the axial direction (Fig. 58 left side). The imaging was done by sequential line-scanning at a 50 μm working distance.

Overall, a consistent transition from inhomogeneous α' band-like structures to more homogeneously scattered α' martensite can be observed from Fig. 58. High strain amplitude (specimen A, $\varepsilon_{at} = 0.22$ %) resulted in dominant α' bands at the center of the specimen. At the same time, α' appears to be homogeneously distributed along the transverse section of the specimen at low strain amplitude (specimen E, $\varepsilon_{at} = 0.165$ %). The highest and the lowest values of relative permeability are indicated on the colormap scale. The colormap was adjusted to cover the full range of each individual figure. Observed by means of MFI, the α' distribution was consistent with microstructural investigations.

7.2.4 Correlation to microstructural changes

Changes in the magnetization behavior are quite often linked to the microstructure. Microstructural observations with SEM (see Fig. 59 and 60) showed that higher strain amplitude results in coarser martensite. Low strain amplitude and a high number of cycles produced martensite with a much finer structure

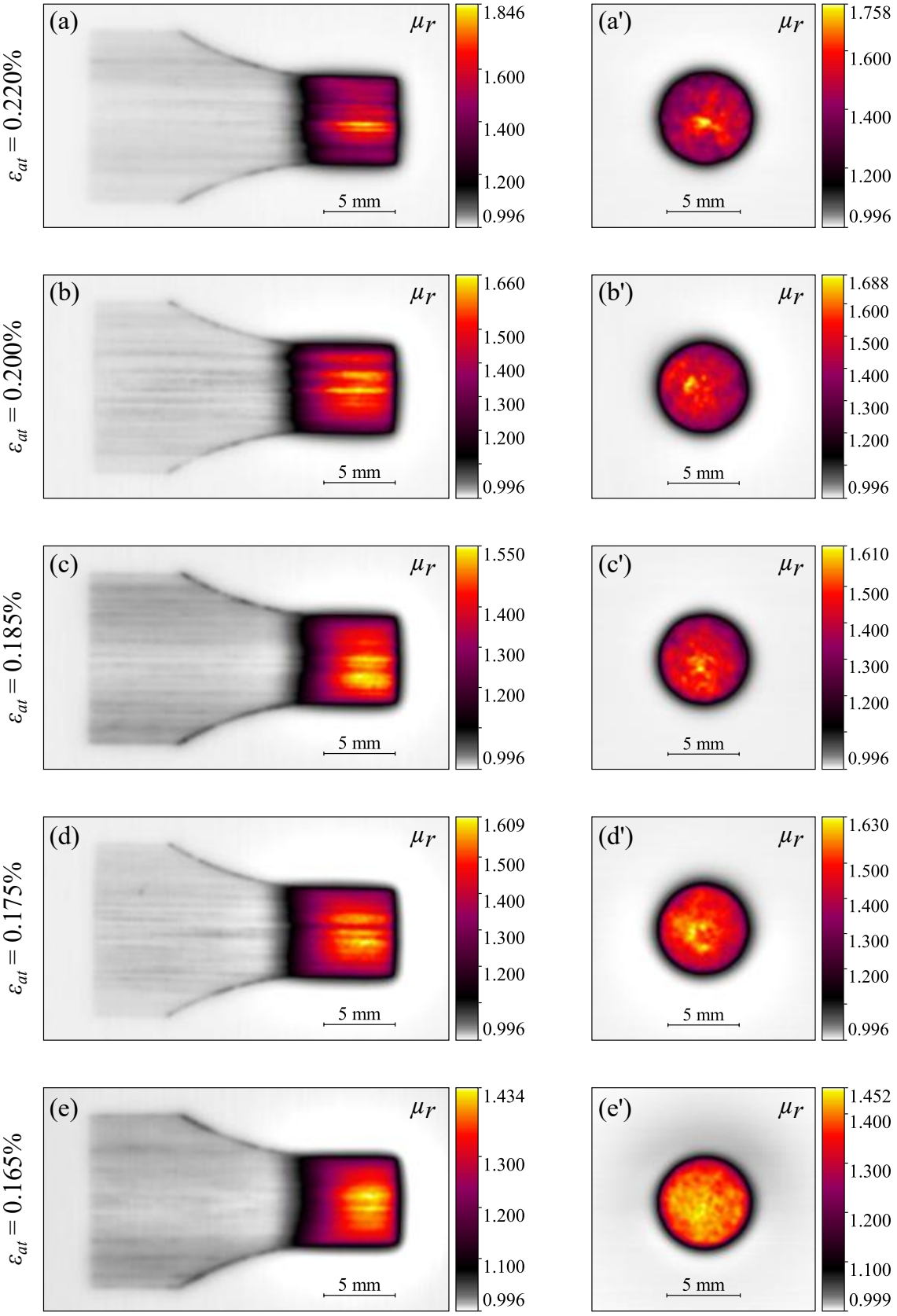

Fig. 58. Magnetic force imaging (MFI) of the samples cut out from fatigue specimens A – E. The MFI output is calibrated to relative magnetic permeability. Higher μ_r values can be interpreted as a higher density of α' martensite. Material: 347 Batch A.

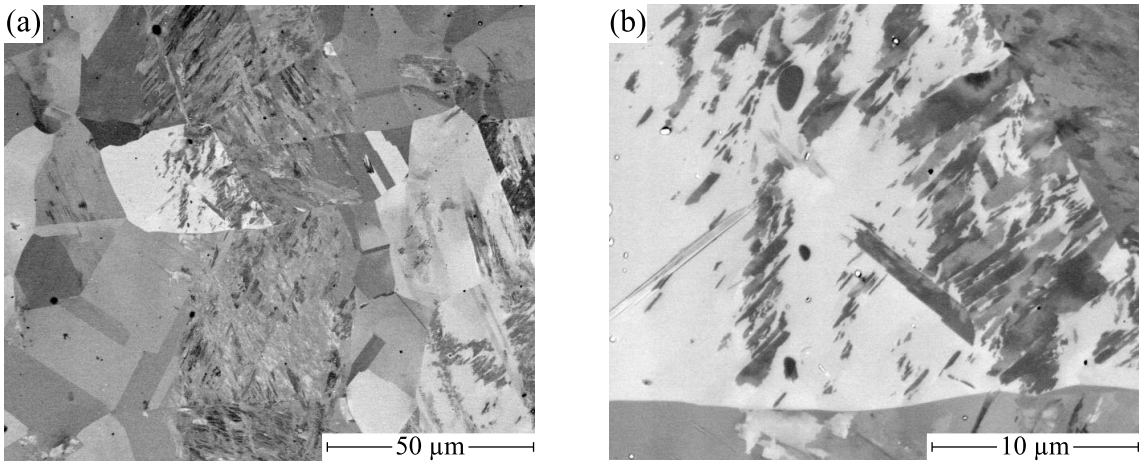

Fig. 59. Backscatter contrast SEM image of sample A (ε_{at} = 0.22%, $N = 2.9 \cdot 10^4$). Final surface preparation: 1 μm diamond suspension followed by electropolishing.

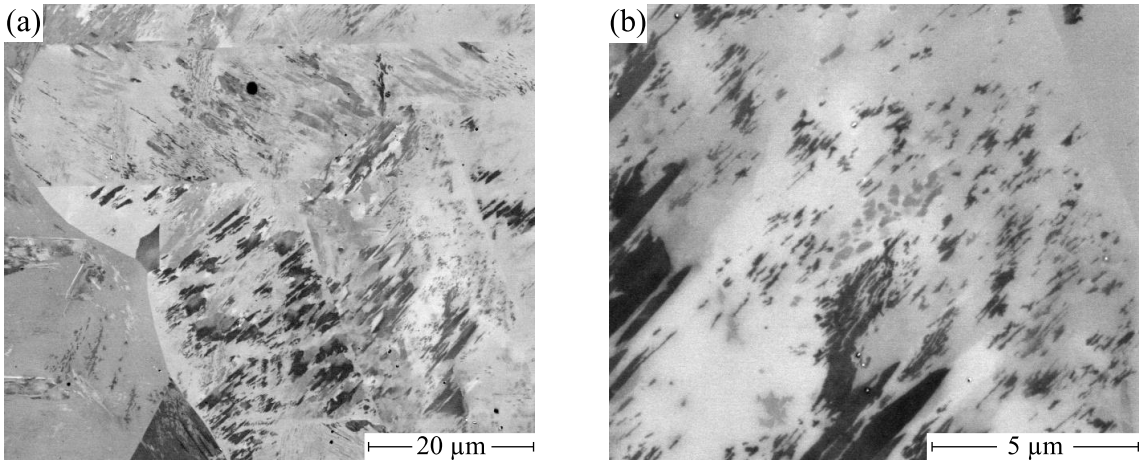

Fig. 60. Backscatter contrast SEM image of sample E (ε_{at} = 0.165%, $N = 2.1 \cdot 10^6$). Final surface preparation: 1 μm diamond suspension followed by electropolishing.

and grain size down to the nanometer range. Some of the martensitic needles were found to be as small as 70 x 500 (nm) for specimen E.

While Fig. 57 shows a linear relationship between coercivity H_c and strain amplitude ε_{at}, coercivity does not necessarily have a linear function with grain (or particle) size. Due to thermal effects, particles smaller than 6 – 10 nm start to exhibit superparamagnetic properties with H_c very close to zero at room temperature [208]. From this state, H_c linearly increases with particle (grain) size until the transition from a single magnetic domain to a multi-domain is reached. After this point, at about 80 nm for Fe_3O_4 particles at 300 K [209], H_c starts to decrease with the particle size. Since deformation-induced α' martensite typically has a very small width-to-length ratio, it is easier for such needle geometry to maintain a single-domain structure [113].

Pole figures of neighboring austenite / martensite grains were extracted from an EBSD scan (not shown here) in order to investigate the presence of orientation relationships (OR).

Three typical OR were considered:

- Nishiyama-Wassermann (N-W) $(111)_{fcc} \parallel (011)_{bcc}$ $[11\bar{2}]_{fcc} \parallel [01\bar{1}]_{bcc}$
- Kurdjumov-Sachs (K-S). $(111)_{fcc} \parallel (011)_{bcc}$ $[10\bar{1}]_{fcc} \parallel [11\bar{1}]_{bcc}$
- Bain $(001)_{fcc} \parallel (011)_{bcc}$ $[100]_{fcc} \parallel [110]_{bcc}$

Note that the planes are identical for N-W and K-S. An OR was found in all cases, being either N-W or K-S. However, when comparing the individual pole figures, it was impossible to distinguish between N-W and K-S. The reason for that is the limited angular resolution of the EBSD method, together with the transformation-induced orientation spread in the martensite phase. Similar OR were found in both specimens A and E. A representative example of pole figures is shown in Fig. 61. Parallel planes and directions are highlighted. It is also possible that both OR are present in the same grain [210].

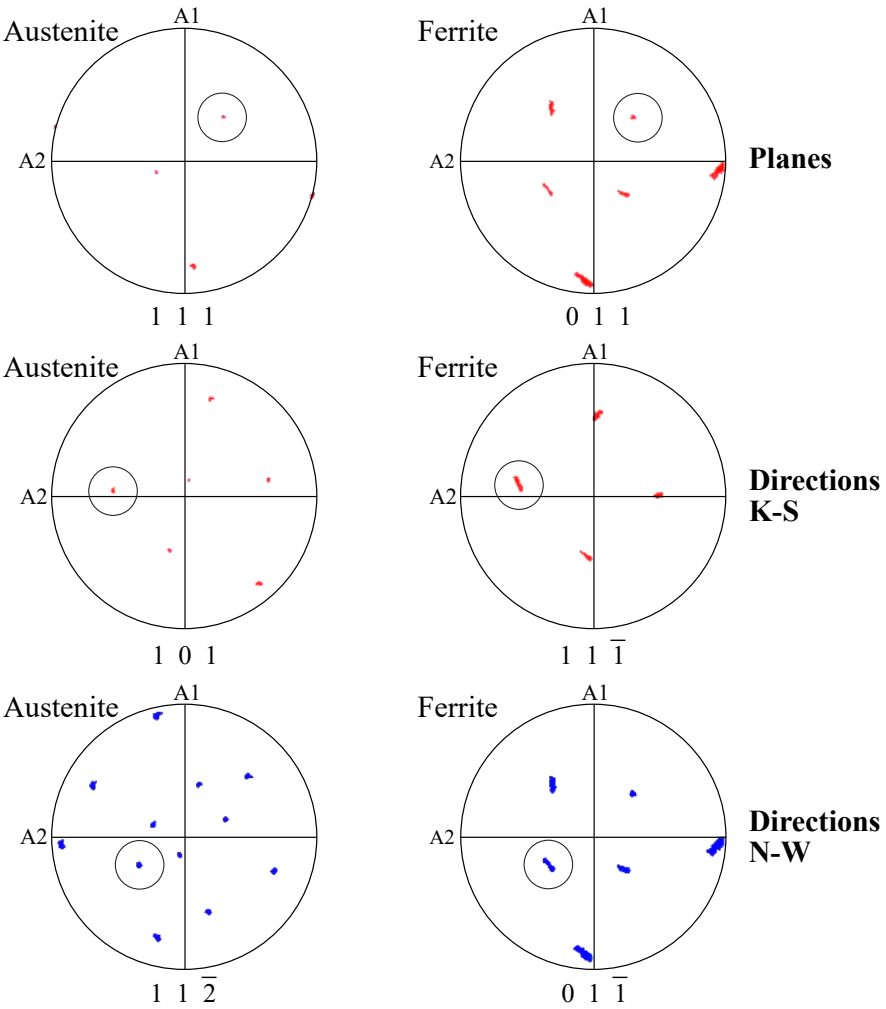

Fig. 61. Pole figures of neighboring austenite and martensite grains in specimen A. Coinciding lattice planes are encircled. The first row compares $(011)_F$ and $(111)_A$ for both N-W and K-S OR. The second and third rows compare directions of the K-S and N-W relationship, respectively. Spots in ferrite pole figures are blurred due to transformation induced orientation spread which makes the determination of the OR ambiguous.

7.3 Influence of strain on phase transformation kinetics

strain	strain rate	stress	temperature	α' volume
variable	constant	variable	ambient	variable

In the previous section, we observed the kinetics of $\gamma \rightarrow \alpha'$ transformation at different strain amplitudes at a fixed frequency. In this section, a larger number of constant strain amplitude fatigue tests is presented to further demonstrate the relationship between the total strain amplitude and evolution of α' martensite at ambient temperature. The parameters for fatigue testing here are similar to those of a single step in a strain increase test in section 7.1, i.e., total strain amplitude and strain rate were constant for the entire duration of the test.

A constant strain rate of $0.004\,s^{-1}$ with a triangular waveform was used to avoid self-heating of fatigue specimens. The resulting variation of temperature for all tests did not exceed $\pm 2\,°C$. Tests were done in a total strain controlled regime with fully reversed strain. Fatigue specimens belong to the material Batch A (see section 6 on page 80 for more information, including initial α' martensite volume fractions). The evolution of α' martensite volume fraction was measured with uniaxial magnetic balance UMB-1 (section 5.2). As before, the change in ferromagnetic volume fraction here indicates the volume of α' martensite, expressed as a percentage of ferrite (Fe%), since the calibration was done on δ ferrite samples. Volume fractions of α' and δ estimated by the UMB should have very little difference up to 20 % and can therefore be used interchangeably in this range. It can be further assumed that the change in ferromagnetic volume fraction $\Delta\xi_{fe}$ caused only by $\gamma \rightarrow \alpha'$ transformation.

Evolution of α' volume at different total strain amplitude ε_{at} is shown in Fig. 62a, covering the range $0.14 < \varepsilon_{at} < 1.00$ (%). A value of 0.04 Fe% has been added to the data to avoid negative values in the logarithmic scale, which is essential to properly display high and low values together. For $\varepsilon_{at} = 1$ % and 0.7 %, phase transformation could be observed already within the very first fatigue cycle. At 10 cycles, phase transformation could be detected down to $\varepsilon_{at} = 0.3$ %. Lower strain amplitude took a significantly longer time to accumulate enough deformation: for $\varepsilon_{at} = 0.14$ % first α' phase could be detected only by 10^4 cycles.

7.3.1 Transition from accelerated to decelerated rate

The rate of phase transformation is demonstrated in Fig. 62b by calculating the first derivative from plot (a). For the first 10 cycles, the derivative is not quite reliable due to the small number of data points. As the density of the

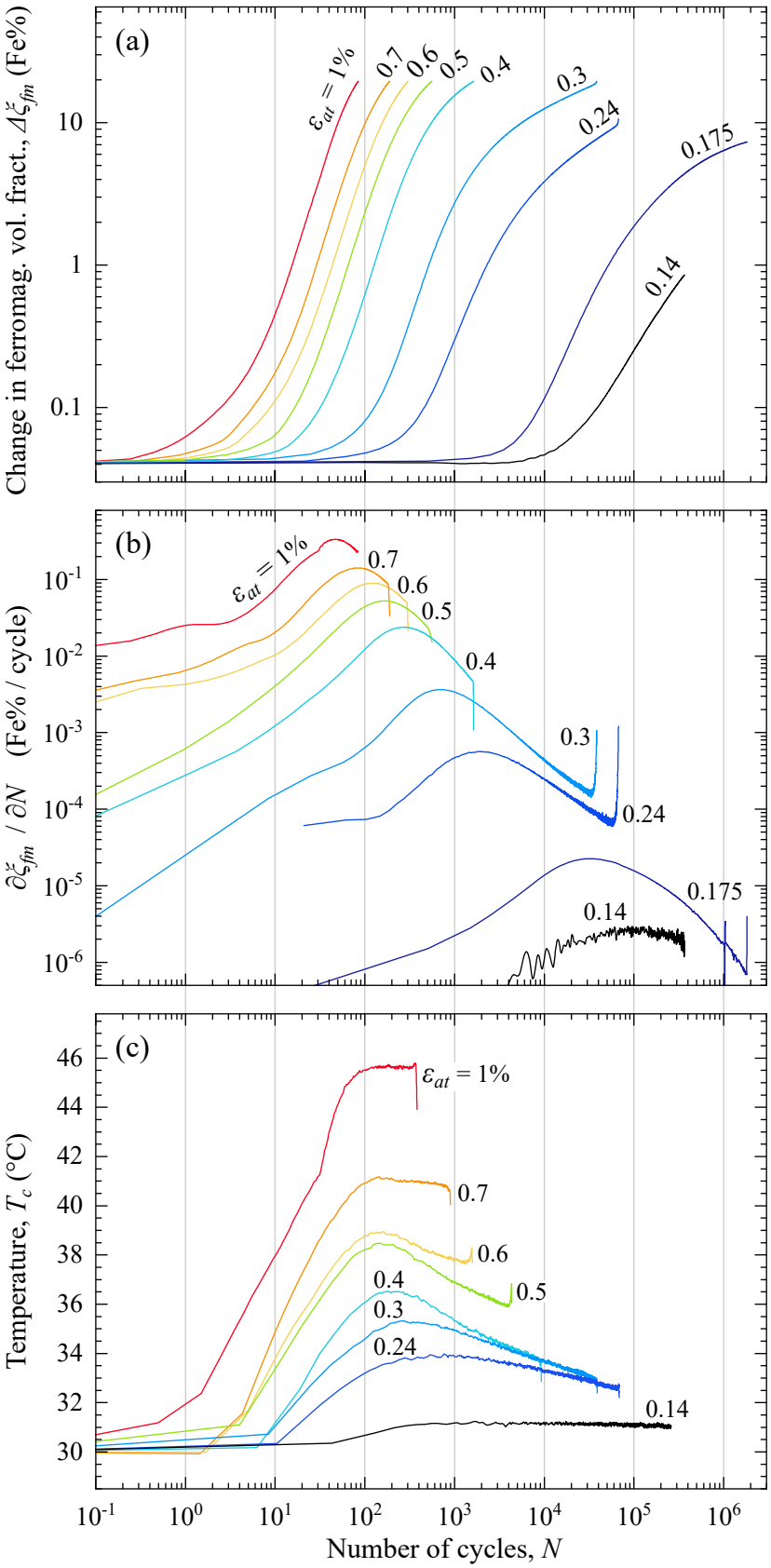

Fig. 62. Evolution of α' martensite during constant strain amplitude fatigue tests at ambient temperature: a) change in ferromagnetic volume fraction in Fe%; b) rate of phase transformation in Fe% per cycle; c) temperature at the center of the gauge length. A value of 0.04 Fe% has been added to avoid negative values in logarithmic scale. Acquired with UMB-1, which had a limit of 20 Fe%. Material: 347 Batch A.

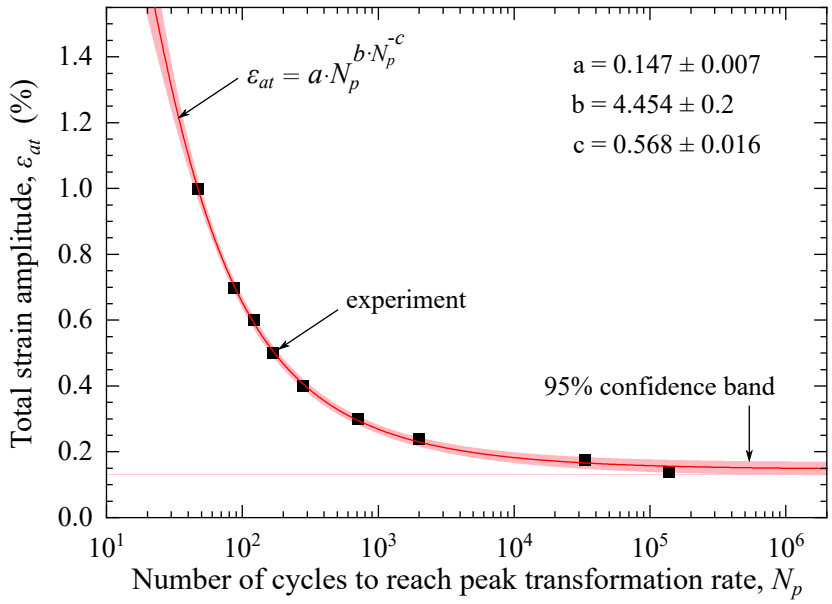

Fig. 63. Number of cycles required to reach the peak phase transformation rate for a given total strain amplitude.

data points increased, a bell-shaped function could be reliably identified for all fatigue tests. Before the peak in the derivative, the phase transformation rate is accelerated, while after it is decelerated. The very top of the peak corresponds to the most constant phase transformation rate. The peak position of the phase transformation rate appeared to also have a clear mathematical relation to the number of cycles. To further analyze the trend, the peak position was calculated for all strain amplitudes and plotted in Fig. 63. A modified Freundlich equation (47), which originally describes the relationship between the amount of gas adsorbed by a solid at a particular temperature, was able to fit the experimental data with R^2 value of 0.998.

$$\varepsilon_{at} = a \cdot N_p^{b \cdot N_p^{-c}} \tag{47}$$

where ε_{at} – total strain amplitude (%); N_p – number of cycles to reach peak phase transformation rate; a, b, c – fit parameters.

7.3.2 Linearly approximated rate of phase transformation: LR1 and LR2

Formation of α'-martensite under constant total strain fatigue loading essentially follows a sigmoidal function, which is more visually apparent in a linear scale in Fig. 64, which shows the same data as Fig. 62a. To describe the phase transformation as a sigmoidal function, at least 3 variables would be required: an amplitude constant and two transition constants. Applying a temperature function for all three constants would generate 8-dimensional data which is not ideal for visualization. A much better approach is to define two linear ranges

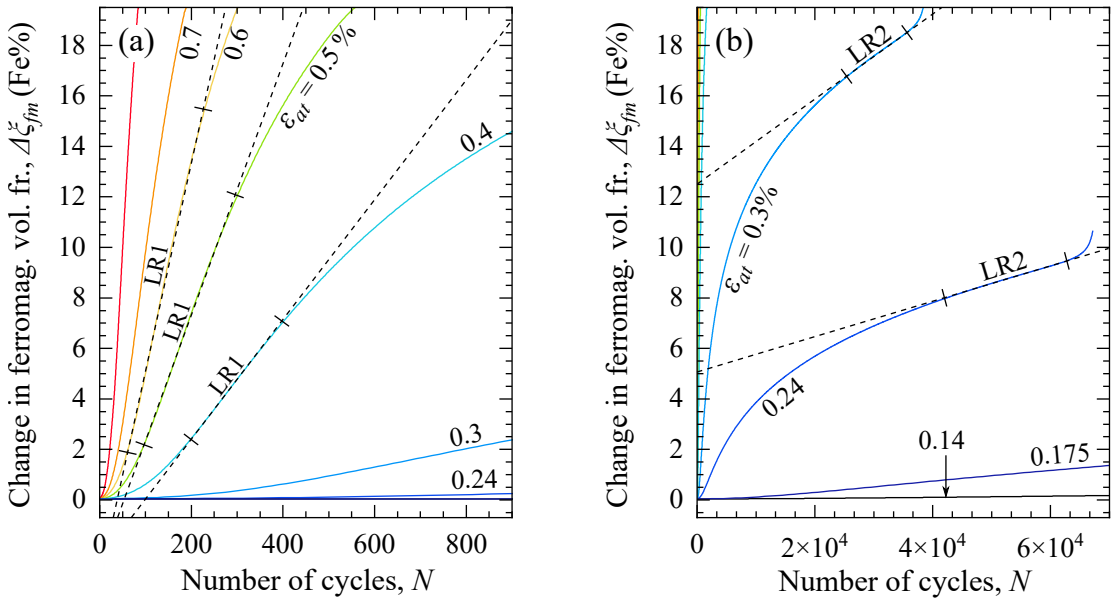

Fig. 64. Explanation of linear ranges LR1 and LR2 in the development of α', as indicated by ferromagnetic volume fraction in Fe%: a) from 0 to 900 cycles; b) from 0 to 70000 cycles. Acquired with UMB-1. Material: 347 Batch B.

LR1 and LR2, where each can be described with only one constant. LR1 is the phase transformation rate, before the accelerated rate changes to a decelerated (see Fig. 64a). In other words, LR1 signifies the fastest transformation rate and LR2 – the slowest. As demonstrated in Fig. 64b, LR2 is measured at the end of deceleration phase, but before the crack propagation stage, where the rate of transformation increases again.

In fatigue tests performed at ambient temperature, the LR1 portion increased with strain amplitude, and at ε_{at} = 1 % almost the entire duration of the test could be described as linear. On the other hand, at strain amplitudes below 0.3 %, LR2 was found to hold the larger portion of the curve. When plotted together, the slopes of LR1 and LR2 show the possible range of the rate of phase transformation at a given strain amplitude, as shown in Fig. 65. Both curves can again be descried with the modified Freundlich equation (48), similarly to equation (47):

$$\frac{\partial \xi_{fm}}{\partial N}(\varepsilon_{at}) = a \cdot \varepsilon_{at}^{b \cdot \varepsilon_{at}^{-c}} \tag{48}$$

where ξ_{fm} – ferromagnetic volume fraction (Fe%); N – number of fatigue cycles; $\partial\xi_{fm}/\partial N$ – rate of $\gamma \rightarrow \alpha'$ transformation (Fe% / cycle); ε_{at} – total strain amplitude (%); a, b, c – fit parameters. Fit parameters a, b, c for LR1 and LR2, as well as peak position N_p are summarized in Table (9).

Linear approximation of the $\gamma \rightarrow \alpha'$ transformation into two linear ranges significantly simplifies further calculations while also providing an error margin. But this is not the only reason to perform linearization. Another reason

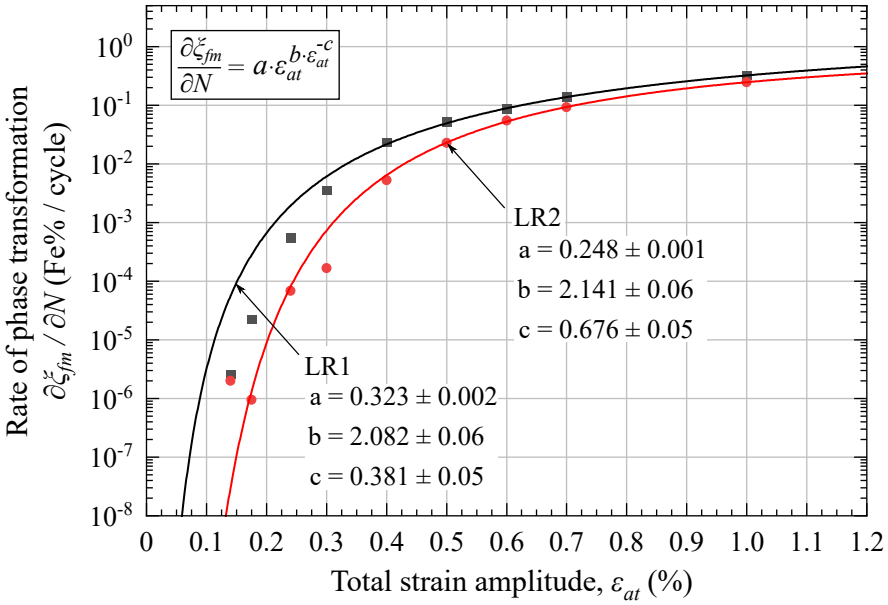

Fig. 65. Rate of phase transformation as a function of total strain amplitude at ambient temperature. LR1 signifies the highest transformation rate and LR2 – the slowest.

Table 9
Fit parameters for linear ranges LR1 and LR2, as well as the number of cycles N_p needed to reach the peak transformation rate.

Fit parameter	**LR1**	**LR2**	N_p
a	0.323 ± 0.002	0.248 ± 0.001	0.147 ± 0.007
b	2.082 ± 0.06	2.141 ± 0.06	4.454 ± 0.2
c	0.381 ± 0.05	0.676 ± 0.05	0.568 ± 0.016

for this is to make the calculations at ambient temperature compatible with calculations at elevated temperatures. Experiments showed that at temperatures above 80 °C formation of α' becomes much more linear, as demonstrated in the next section.

7.4 Influence of temperature on phase transformation kinetics

strain	strain rate	stress	temperature	α' volume
constant	variable	variable	variable	variable

In the previous section, the rate of $\gamma \rightarrow \alpha'$ transformation was mathematically described as a function of total strain amplitude. The next step towards a comprehensive evaluation of phase transformation kinetics is to see how the rate of phase transformation changes with temperature. It is generally accepted that in metastable austenitic steels $\gamma \rightarrow \alpha'$ transformation no longer occurs above M_d temperature[10] [135, 211]. Experimental determination of M_d temperature greatly depends on the sensitivity of methods used to quantify α' phase and homogeneity of the material. As we have already seen in section 7.1, M_d temperature of the 347 steel investigated in this work is definitely above 160 °C and likely to reach 240 °C. To say that M_d temperature is definitely below a certain temperature requires a more thorough investigation.

Kinetics of $\gamma \rightarrow \alpha'$ transformation near M_d temperature is not sufficiently studied due to high requirements for sensitivity to α' phase combined with the complications of the heating and repeated mechanical loading. By implementing the uniaxial magnetic balance (UMB), it was possible to measure small fractions of α' *in situ* at elevated temperatures. However, this was not quite sufficient to fully characterize the $\gamma \rightarrow \alpha'$ behavior. Spatial analysis with magnetic force imaging (MFI) showed a peculiar change in the initial α' nucleation location in the gauge length.

7.4.1 Mechanical data on isothermal fatigue tests

In this section, 9 isothermal fatigue tests were performed in the temperature range $17 < T_c < 320$ °C, where T_c is the temperature measured at the center of the fatigue specimen gauge length. Tests were performed using the TMF setup, described in section 5.3 on page 67. Strain was controlled with a sinusoidal function, with a frequency of 0.02 Hz and total strain amplitude ε_{at} = 0.51 % – parameters identical for thermo-mechanical testing. All fatigue specimens came from material Batch B, with the exception of 17 °C and 100 °C tests, which belonged to Batch A.

Fig. 66 shows the first cycle of the isothermal fatigue tests. Some intermediate temperatures are not shown to avoid cluttering the diagram. The ambient temperature test at 17 °C showed the highest stress response to the applied strain. The overall trend can be seen better in Fig. 67a, where only the first

[10] Not to be confused with M_{d30} temperature, defined as temperature at which 50 % of austenite is transformed to α' martensite when elongated by 30 %.

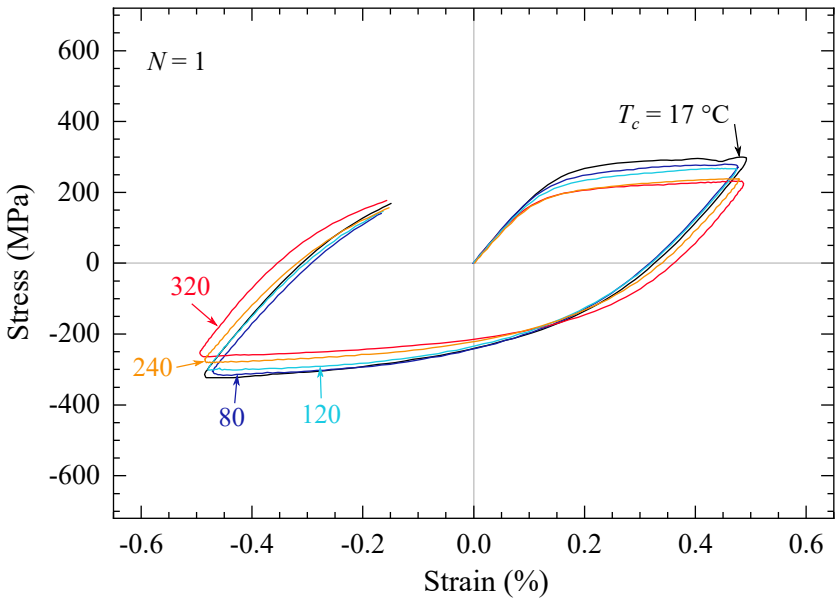

Fig. 66. Stress-strain diagram showing the first cycle of isothermal fatigue tests at various temperatures. Material: 347 Batch B.

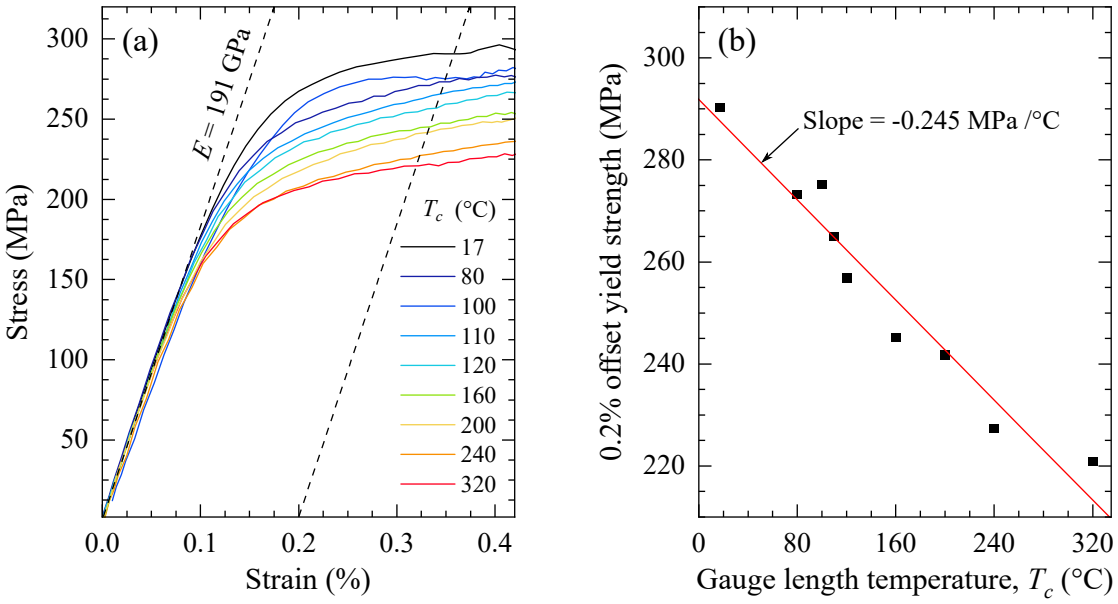

Fig. 67. Influence of the temperature on the yield strength: a) stress-strain diagram generated from the first cycle of isothermal fatigue tests; b) yield stress as a function of temperature. Yield stress is calculated as 0.2 % offset from the elastic slope. Material: 347 Batch B.

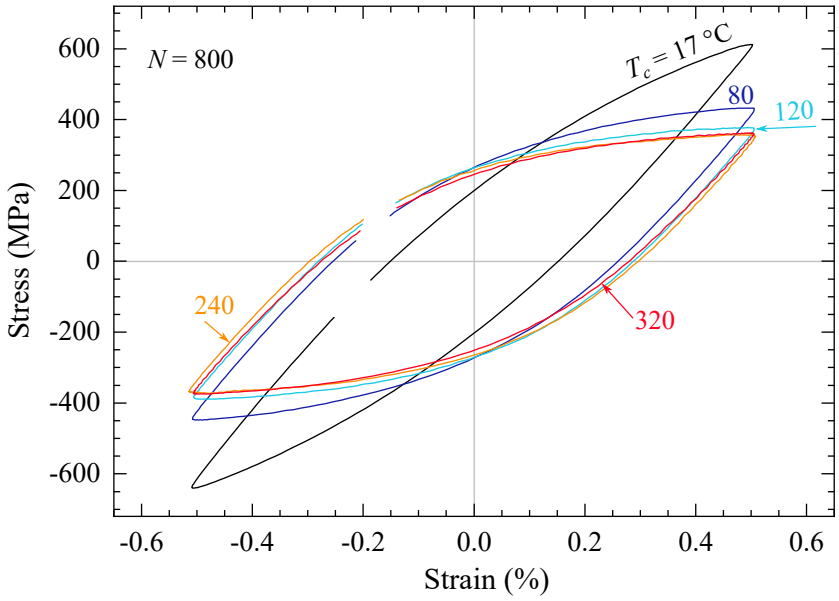

Fig. 68. Stress-strain diagram showing the 800 cycle of fatigue tests at various temperatures. Material: 347 Batch B.

quarter of the hysteresis is plotted. All 9 fatigue tests demonstrated a strong dependence of stress amplitude on temperature. From elastic strain that was measured up to 0.05 %, Young's modulus was estimated to be 191 GPa, which was in agreement with the manufacturer's specifications for this material. Elastic portion was nearly identical at all temperatures. As strain increased, a more drastic difference in stress was observed at different temperatures. Fig. 67b shows the 0.2 % offset yield strength as a function of temperature. The yield strength appeared to decrease by 0.245 MPa for one degree Celsius.

It is important to note that deformation was measured at the shafts of the fatigue specimen with calibration to 12 mm gauge length in the fully elastic region. Although in absolute terms this is not a very accurate strain measurement, the information on the stress amplitude reduction with temperature will be important for further calculations in thermo-mechanical testing.

Stress-strain hysteresis diagram at cycle number 800 at various temperatures is demonstrated in Fig. 68. After 800 cycles sufficient plastic deformation accumulated to cause strain hardening, which can be noted by increased stress amplitude. Hysteresis curves at 240 °C and 320 °C were practically indistinguishable, indicating that already at 240 °C the sum of ΔG_{mech} and ΔG_{chem} could not reach $\Delta G_{min}^{\gamma \rightarrow \alpha'}$ – minimum free energy required for the phase transformation to take place. Further explanation is provided by the evolution of the stress amplitude, shown in Fig. 69.

From Fig. 69, we can see that at the temperature of 17 °C, strain hardening occurred very quickly and reached stagnation at N= 500. At T_c = 80 °C maximum stress amplitude dropped from 650 MPa for 17 °C to 500 MPa. Stress

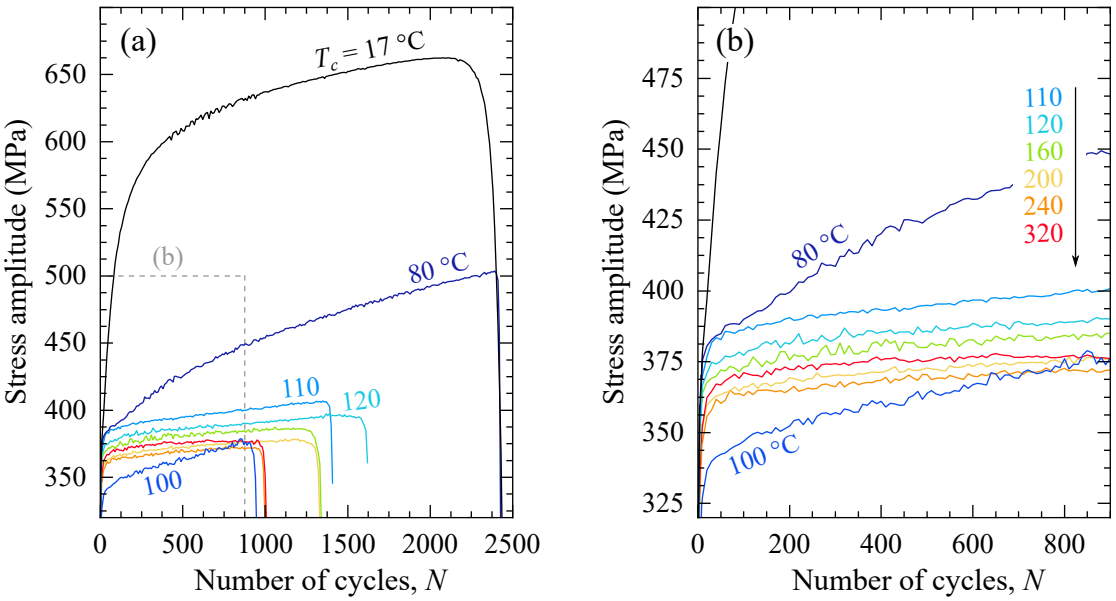

Fig. 69. Evolution of stress amplitude σ_a in isothermal constant amplitude fatigue tests with 0.51 % total strain amplitude: a) full range; b) initial range. Material: 347 Batch B.

amplitude did not exceed 400 MPa at temperatures above 120 °C. An exception is the test at 100 °C that not only showed lower stress amplitude but also fractured quicker. This could have happened because of a defect in the material or on the surface. The slope of the curve was nevertheless consistent with adjacent tests at 80 °C and 110 °C. More information on strain hardening can be extracted from magnetic measurements presented in the following section.

7.4.2 Change of $\gamma \rightarrow \alpha'$ transformation rate with temperature

Strain hardening is not an entirely reliable way to judge whether or not the phase transformation still takes place at elevated temperatures. A much more sensitive approach is to use magnetic measurements to directly measure the amount of deformation-induced martensite. For this purpose, uniaxial magnetic balance UMB-3 was implemented *in situ* during isothermal fatigue tests (see section 5.2 on page 60 for technical specifications).

Results of the magnetic measurements are presented in Fig. 70. A good correlation between the amount of deformation-induced martensite and strain hardening could be observed for all tests. The three regions, accelerated constant and decelerated, were found mostly at lower temperatures. Above 100 °C only accelerated behavior could be observed, which became mostly linear at 160 °C and above. The test at 240 °C showed only 0.05 Fe% more martensite than the 320 °C test, which showed practically zero α' formed. At temperatures above 240 °C the amount of α' formed was so little that it fell within the margin of repeatability error of UMB-3.

A linear approximation of the transformation rate was calculated similarly

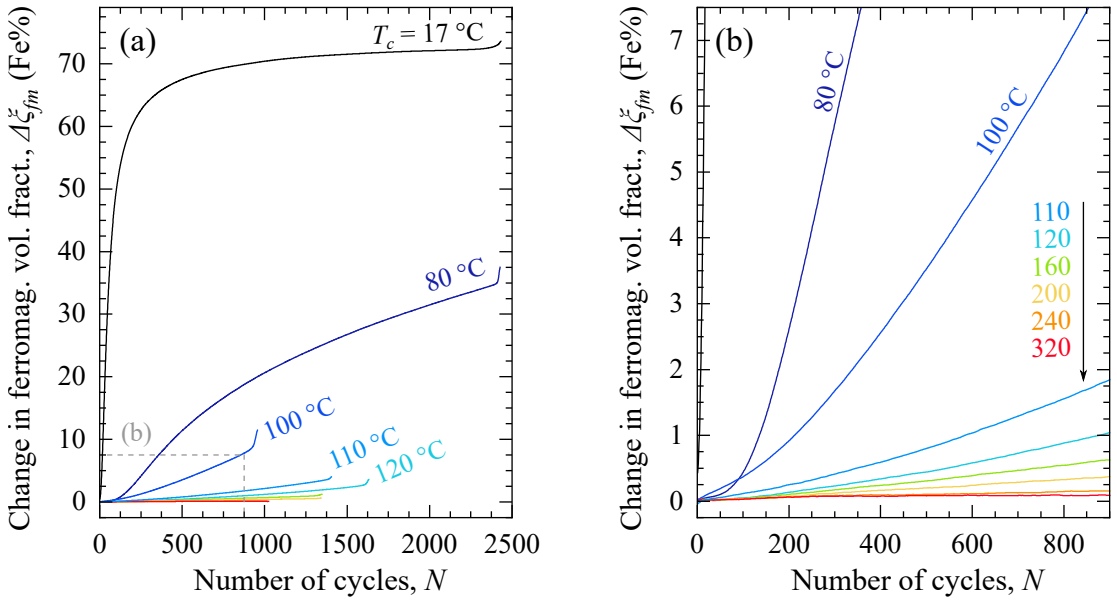

Fig. 70. Evolution of α' martensite in isothermal constant amplitude fatigue tests with 0.51 % total strain amplitude: a) full range; b) initial range. Material: 347 Batch B. Acquired with UMB-3.

to ambient temperature tests in section 7.3.2. A linear fit was applied to the transition range from accelerated to the decelerated range. Each slope was then normalized to 17 °C and plotted in Fig. 71 , with numerical values listed in Table 10. Using an empirical approach, it was found that Eq. (49) could be used to describe the rate of phase transformation as a function of temperature quite accurately:

$$\frac{\partial \xi_{fm}}{\partial N}(T_c) = k \cdot m^{T_c} \tag{49}$$

where ξ_{fm} – ferromagnetic volume fraction (Fe%); N – number of fatigue cycles; $\partial\xi_{fm}/\partial N$ – rate of $\gamma \rightarrow \alpha'$ transformation (Fe% / cycle); T_c – temperature at

Table 10
Parameters for linear approximation of the maximum rate of phase transformation (LR1) at elevated temperatures.

Temperature T_c, °C	**Linear range LR1** ξ_{fm}, Fe%	**LR1 slope** Fe%/cycle	**LR1 normalized** –
17	10.0 – 20.0	0.826	1
80	3.00 – 10.0	0.0305	0.0369
100	2.00 – 8.00	0.01066	0.0129
110	0.50 – 2.50	0.00264	0.0032
120	0.40 – 1.60	0.00163	0.00197
160	0.10 – 0.80	7.651E-4	9.26271E-4
200	0.08 – 0.50	4.1803E-4	5.0609E-4
240	0.03 – 0.10	1.4172E-4	1.71574E-4
320	0.075 – 0.09	2.6433E-5	3.20012E-5

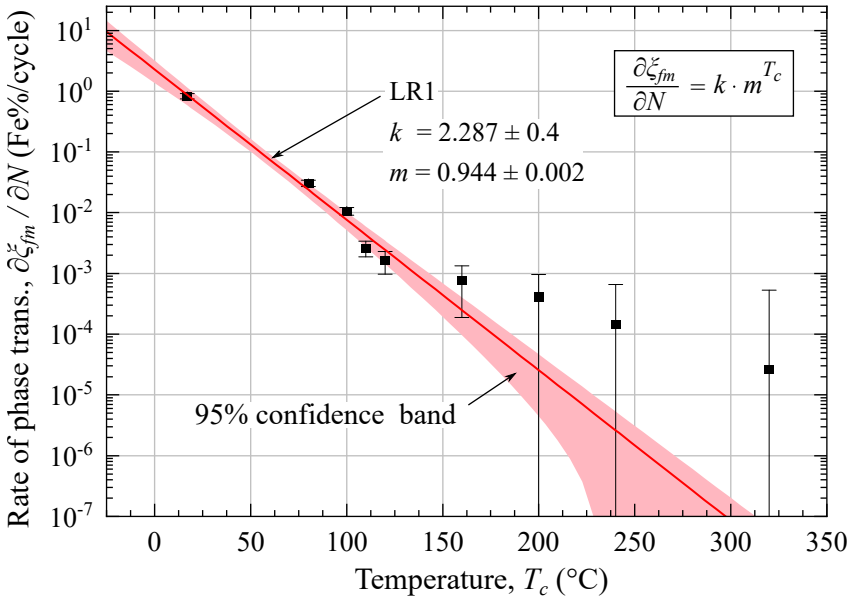

Fig. 71. Maximum rate of $\gamma \rightarrow \alpha'$ phase transformation (LR1) at constant strain amplitude ε_{at} = 0.51 % as a function of temperature. Error bars show the repeatability error of UMB-3.

the center of fatigue specimen gauge length (°C); k, m – fit parameters. For the maximum rate of phase transformation in the linear range LR1 (described in section 7.3, Fig. 64 on page 108) fit parameters were k = 2.287 ± 0.4 and m = 0.944 ± 0.002. The R^2 value of the fit was 0.93. Parameter m determines how quickly the rate of $\gamma \rightarrow \alpha'$ transformation decays with temperature. Parameter k is the proportionality coefficient that assigns numerical values.

The experimental data obtained in this section with UMB provided an integral information on the phase transformation inside of the fatigue specimen. As we have already seen in section 7.1.4 on page 93, the initial nucleation of α' inside of the fatigue specimen gauge length does not occur homogeneously. To further investigate the localization of α', magnetic force imaging was deployed and results are described in the following section.

7.4.3 Spatial and microstructural material evaluation

After constant strain amplitude tests at ε_{at} = 0.51 % presented above, fatigue specimens were cut along the rotation axis, providing a section view to the center of fatigue specimens. Electric discharge machining (EDM) was used to produce the samples with reduced mechanical deformation of the surface. All samples were then embedded in a conductive hot-mounting resin and wet ground with 320 – 1200 grit sandpaper. Grinding was followed by 6 μm, 3 μm, and 1 μm diamond suspension polishing for 10 minutes each.

Results of the MFI scans in the temperature range 17 < T_c < 160 (°C) are shown in Fig. 72. The working distance d_w was kept between 10 and 20 μm,

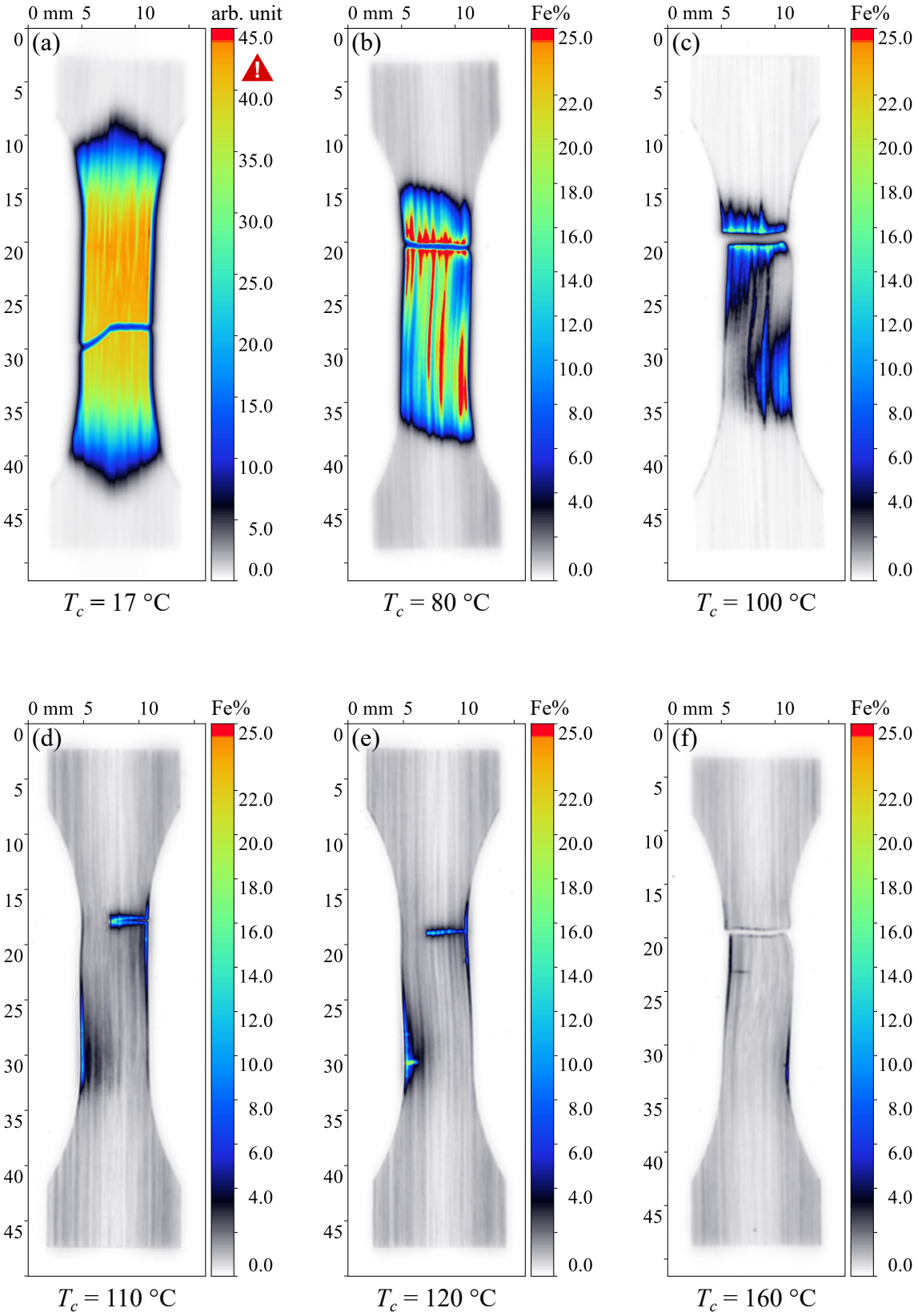

Fig. 72. Magnetic force imaging (MFI) evaluation of fatigue specimens after isothermal fatigue testing: a) T_c = 17 °C, d_w = 100 μm; b) T_c = 80 °C, d_w = 20 μm; c) T_c = 100 °C, d_w = 10 μm; d) T_c = 110 °C, d_w = 20 μm; e) T_c = 120 °C, d_w = 20 μm; f) T_c = 160 °C, d_w = 20 μm. Final surface preparation: 1 μm diamond suspension polishing. Material: 347, (a, c) – Batch A, (b, d, e, f) – Batch B.

with the exception of the fatigue test at 17 °C (a), which produced significantly more α' martensite than other tests. The working distance had to be increased to 100 μm to reduce the load on the force sensor. As the working distance increases, so does the non-linearity of the output, which also increases with Fe%. For this reason, the colormap in (a) is presented in arbitrary values. All remaining scans were calibrated to ferrite volume fraction (Fe%).

Distribution α' martensite after the isothermal test at 17 °C (Fig. 72a) was the most uniform, expanding significantly from the gauge length of the specimen to the shoulders. At 80 °C (b), a strong indication of α' forming in axial bands could be observed. The ferromagnetic volume in these bands reached 30 %, while in the troughs it was as low as 10 %. At 100 °C (c) vertical bands were present as well, but also a new trend started to appear – a stronger impact on the transition region from the gauge to the shaft. At the transition region, the ferrite content reading was 11 %, while at the center of the gauge length it was only 2.7 %.

The overall trend was a decreasing ferromagnetic content with increasing temperature, including the transition region from the shoulders to the gauge. However, the formation of α' martensite was much more persistent in the transition region. An increase in temperature could reduce the stiffness in the gauge length, which could result in more lateral movement of the specimen. In the temperature range 110 °C – 160 °C this trend continued, seemingly pushing out the phase transformation towards the surface. At 160 °C (e), for the first time, the fracture surface was less magnetic than the rest of the specimen. This is quite unusual, considering that the propagating fracture surface experiences highest deformations. The transition region reduced to the thinness below 1 mm, but still showed around 5 % ferrite content, whereas at the center it reached only 0.7 %.

The colormap full range for the remaining three tests in Fig. 73 was adjusted from 25 Fe % to 1.5 Fe %, as at these temperatures $\gamma \rightarrow \alpha'$ transformation was highly inhibited. At 200 °C (Fig. 73a) the transition region still had a noticeable increase of 1.85 % in ferromagnetic volume fraction at the very surface. At the same time, the fracture surface was completely indistinguishable from the bulk material. At even higher temperatures, 240 °C (b) and 320 °C (c), neither the fracture surface nor the transition region was more ferromagnetic than the rest of the specimen. The central part, however, appeared to have a slightly higher ferrite reading compared to the shoulders. There is no direct answer to whether or not this increase is significant due to microstructure instability and the geometrical shape of the specimen, which is discussed in greater detail in section 8.1 on page 144.

Numerical data from MFI scans is presented in Table 11. Measurements at

the center, upper and lower shoulders were taken at the rotational axis of the specimen with 3×3 mm mean average. Peak is the maximum ferrite reading in the MFI scan, excluding the fracture surface.

Further evaluation on a microscopic level was done with electron backscatter diffraction (EBSD) on the 160 °C sample. Since the sample was already embedded in conductive resin and mechanically polished for MFI investigation, the only additional preparation step for EBSD was electropolishing at the center of the gauge length with ⌀6 mm round mask for the duration of three minutes in A3 electrolyte at 35 V. At the center of the electropolished area, $0.3 \times 1.0\,\text{mm}^2$ was mapped with 300 nm step size (see Fig. 74) to evaluate the phase composition, as well as microstructure. The total fraction of bcc/bct lattice[11] was comparable with MFI measurements, considering that the area of $0.3 \times 1.0\,\text{mm}^2$ is only vaguely representative of the entire volume. Making a larger EBSD scan would require too much time for the given step size. The larger step size with a combination of lower magnification, typically required for a larger area, would have resulted in small martensitic grains being filtered out, as they would not have a good confidence index.

[11] body-centered cubic (bcc) lattice, typical for ferrite, and distorted body-centered tetragonal (bct) lattice, typical for α' martensite generally cannot be distinguished by Kikuchi lines in EBSD.

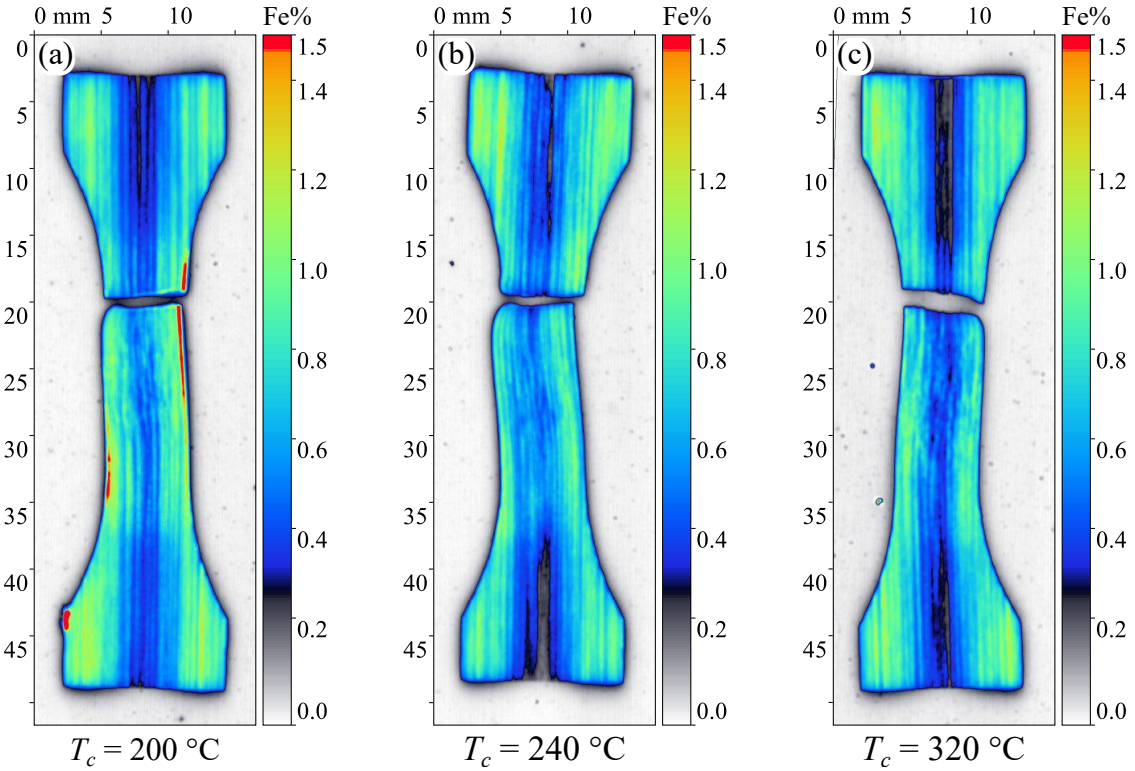

Fig. 73. Magnetic force imaging (MFI) evaluation of fatigue specimens after isothermal fatigue testing: a) T_c = 200 °C, d_w = 20 μm; b) T_c = 240 °C, d_w = 10 μm; c) T_c = 320 °C, d_w = 20 μm. Final surface preparation: 1 μm diamond suspension polishing. Material: 347 Batch B.

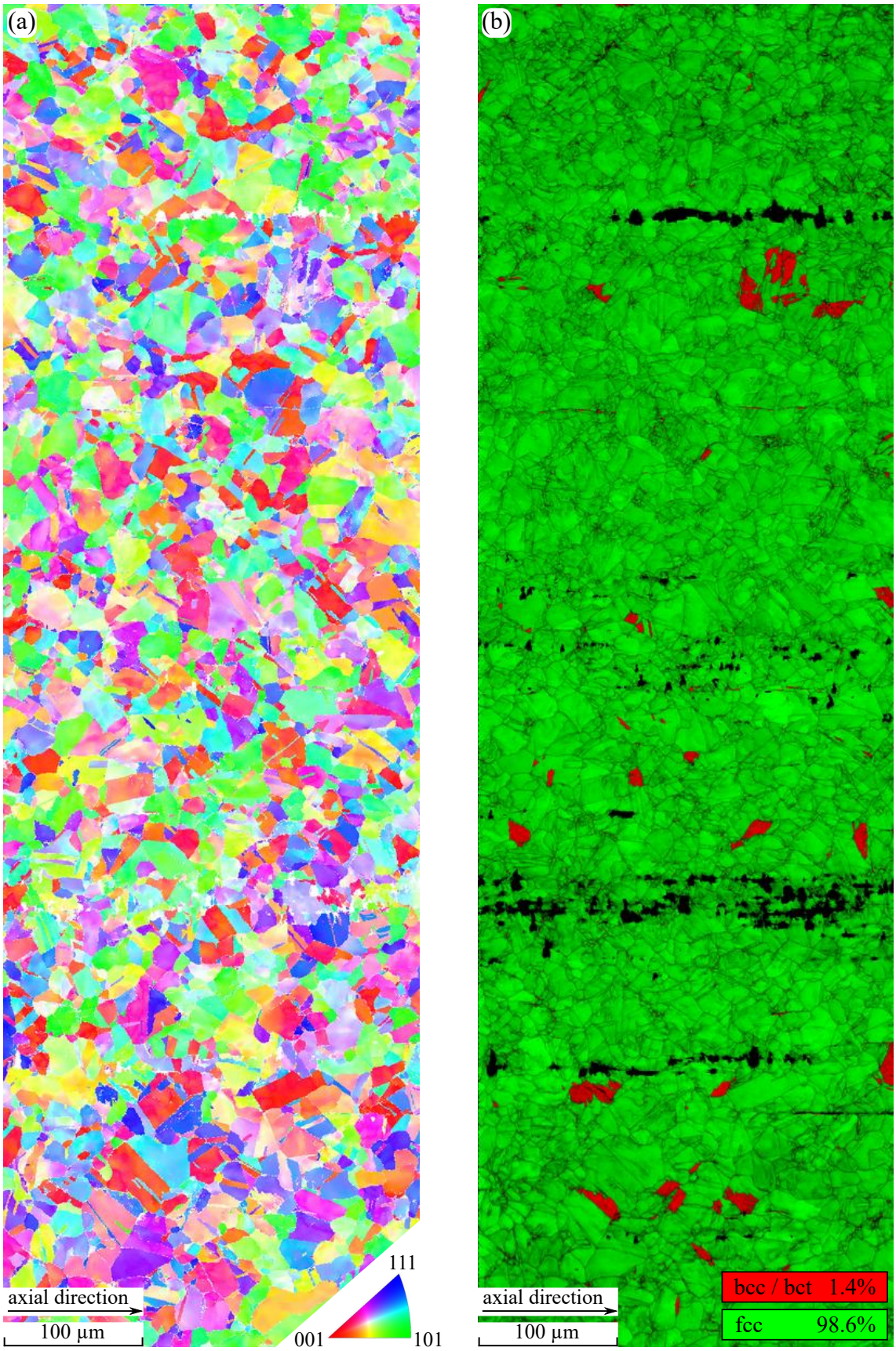

Fig. 74. Large area EBSD map at the center of the gauge length after the isothermal test at T_c = 160 °C: a) inverse pole figure; b) phase map (color) overlaid with image quality map (grayscale). Final surface preparation: 1 μm diamond suspension polishing followed by 3 minutes electropolishing.

Table 11
Ferromagnetic volume fraction for different positions on fatigue specimens after isothermal fatigue testing. The values were taken from MFI scans and averaged by 3×3 mm area.

Temperature °C	Center Fe%	Shoulder 1 Fe%	Shoulder 2 Fe%	Delta Fe%	Peak Fe%
80	18.73	0.33	0.34	18.395	35.02
100	2.91	0.12	0.15	2.775	10.96
110	1.22	0.39	0.36	0.845	11.27
120	0.95	0.40	0.37	0.565	20.61
160	0.72	0.31	0.39	0.370	5.53
200	0.48	0.38	0.32	0.130	1.85
240	0.52	0.42	0.29	0.165	1.05
320	0.43	0.31	0.35	0.100	1.01

An additional high-resolution EBSD scan with a 50 nm step size can be found in Fig. 75. From the inverse pole figure (IPF) map we can observe large deformations in austenite grains neighboring the α' grain. Despite sufficiently high resolution, no ε martensite was found. The kernel average misorientation (KAM) map (Fig. 74a) provides additional information on lattice distortions and deformation localization [212]. High KAM values are likely to reflect high dislocation density [213–215]. In this case, a high density dislocation network could be allocated with bcc / bct lattice (refer to the phase map in Fig. 74b), as well as fcc austenite. In some cases KAM bands were found to go beyond a single grain boundary.

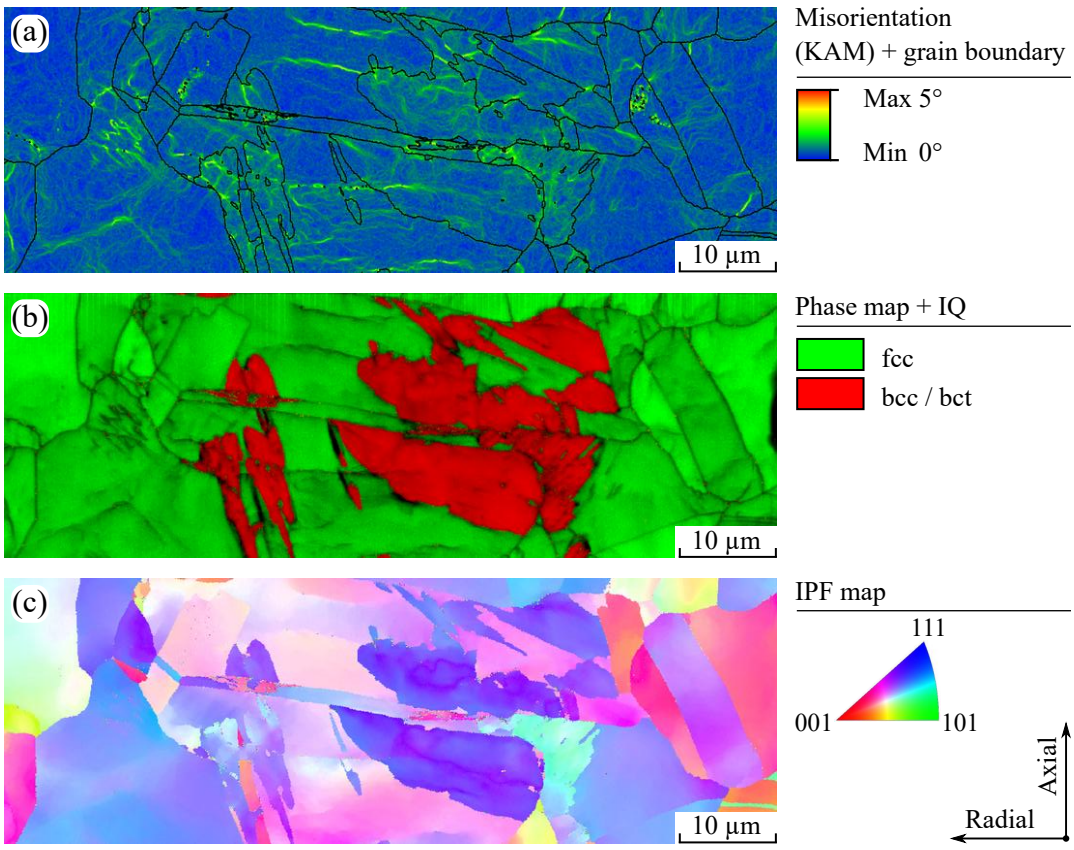

Fig. 75. High-resolution EBSD map at the center of the gauge length after the isothermal test at T_c = 160 °C: a) kernel average misorientation; b) phase map (color) overlaid with image quality map; c) inverse pole figure. Final surface preparation: 1 μm diamond suspension polishing followed by 3 minutes electropolishing.

7.5 Kinetics of thermo-mechanical $\gamma \rightarrow \alpha'$ phase transformation

strain	strain rate	stress	temperature	α' volume
variable	variable	variable	variable	variable

Previously we established the lower accumulated strain limit, how martensite morphology influences magnetic properties, the rate of phase transformation as a function of strain, as well as temperature. All these factors come into play all at once in thermo-mechanical fatigue (TMF) testing. TMF is one of the more complex material testing procedures with over eight independent parameters that should be specified for each test. The most important parameters include strain amplitude, strain rate, cooling rate, heating rate, high and low temperatures, and phase angle. Such a large number of variables gives a huge number of possible variations for a single fatigue test.

In this section, the behavior of $\gamma \rightarrow \alpha'$ transformation was tested in the span of the three temperature ranges and three strain amplitudes. The variations of phase angle were limited to 0° (in-phase, IP) and 180° (out-of-phase, OP). The formation of α' martensite was measured *in situ*, which provided information on the kinetics of phase transformation. The spatial investigation was done after the TMF tests and provided valuable insight into the localization of α' inside fatigue specimens. Finally, the microstructure was studied by means of scanning electron microscopy (SEM) and electron backscatter diffraction (EBSD).

7.5.1 Thermo-mechanical fatigue parameters

TMF tests have been performed on a servo-hydraulic fatigue testing machine with a custom-made TMF module, described in section 5.3 on page 67. The tests were performed with three degrees of freedom: strain amplitude, high temperature, and phase angle. The controlled parameters are listed in Table 12. The tests were performed at constant strain amplitude compensated for thermal strain. Strain was applied with a sinusoidal waveform, at a frequency

Table 12
Controlled parameters for TMF tests. Each unique combination of variables within one line represents one fatigue test.

High temp. T_{ch}, °C	**Low temp.** T_{cl}, °C	**Mechanical strain amplitude** ε_{am}, %			**Phase angle** θ, deg		**Total tests**
160	24	[0.42		0.62]	[0°	180°]	4
240	25	[0.42	0.51	0.62]	[0°	180°]	6
320	27	[0.42	0.51	]	[0°	180°]	4

Table 13
Heating and cooling rates for TMF tests.

High temp. T_{ch}, °C	**Avg. heat. rate** °C / s	**Max. heat. rate** °C / s	**Avg. cool. rate** °C / s	**Max. cool. rate** °C / s
160	17	18	-12	-19
240	18	21	-18	-27
320	25	29	-25	-45

of 0.02 Hz. Heating and cooling rates are listed in Table 13. To keep the heating and cooling rates reasonably similar between tests, the heating waveform had a trapezoidal function (see Fig. 76a, d). Reaching the high temperature at the center of the fatigue specimen slightly ahead of the strain amplitude and keeping it constant also allowed more time to minimize the temperature difference between the gauge length and the shoulders of the fatigue specimen.

The transition from heating to cooling was triggered at the zero crossing of the load cell signal. The advantage of this method is a fully synchronized stress and temperature, regardless of plastic strain amplitude. The disadvantage is a small phase shift between IP and OP tests. This can bee seen by comparing the peak positions in OP and IP tests in Fig. 76.

Fig. 77 and Fig. 78 help to further understand the stress-strain relationship in IP and OP tests. The figures show the hysteresis loops from different TMF tests with the same mechanical strain amplitude ε_{am} = 0.42 %. The total strain in TMF tests represents the sum of mechanical strain ε_{mech} and thermal strain ε_{therm}. Thermal strain can be subtracted from the total strain to reveal the mechanical strain. The coefficient of thermal expansion, calculated in section 5.3.2 on page 70, was used to subtract the thermal strain and plot the mechanical hysteresis in Fig. 79 and Fig. 80 for IP and OP tests, respectively.

7.5.2 TMF tests at 160 °C high temperature

The results of thermo-mechanical fatigue tests with the high temperature T_{ch} of 160 °C and the low temperature T_{cl} equal to 24 °C (as measured at the center of the fatigue specimen) are shown in Fig. 81. Kinetics of $\gamma \rightarrow \alpha'$ transformation were similar of that at ambient temperature – accelerated behavior quickly transitioned into decelerated. A significant difference was found between in-phase and out-of-phase tests. OP tests demonstrated nearly doubled transformation rates and the amount of deformation-induced martensite, compared to IP tests. This effect was much more pronounced at lower strain amplitude of 0.42 %, where the difference was almost sixfold.

Stress amplitudes in Fig. 81b were consistent with the evolution of α' fraction. OP specimens experienced the highest work hardening. Changing the

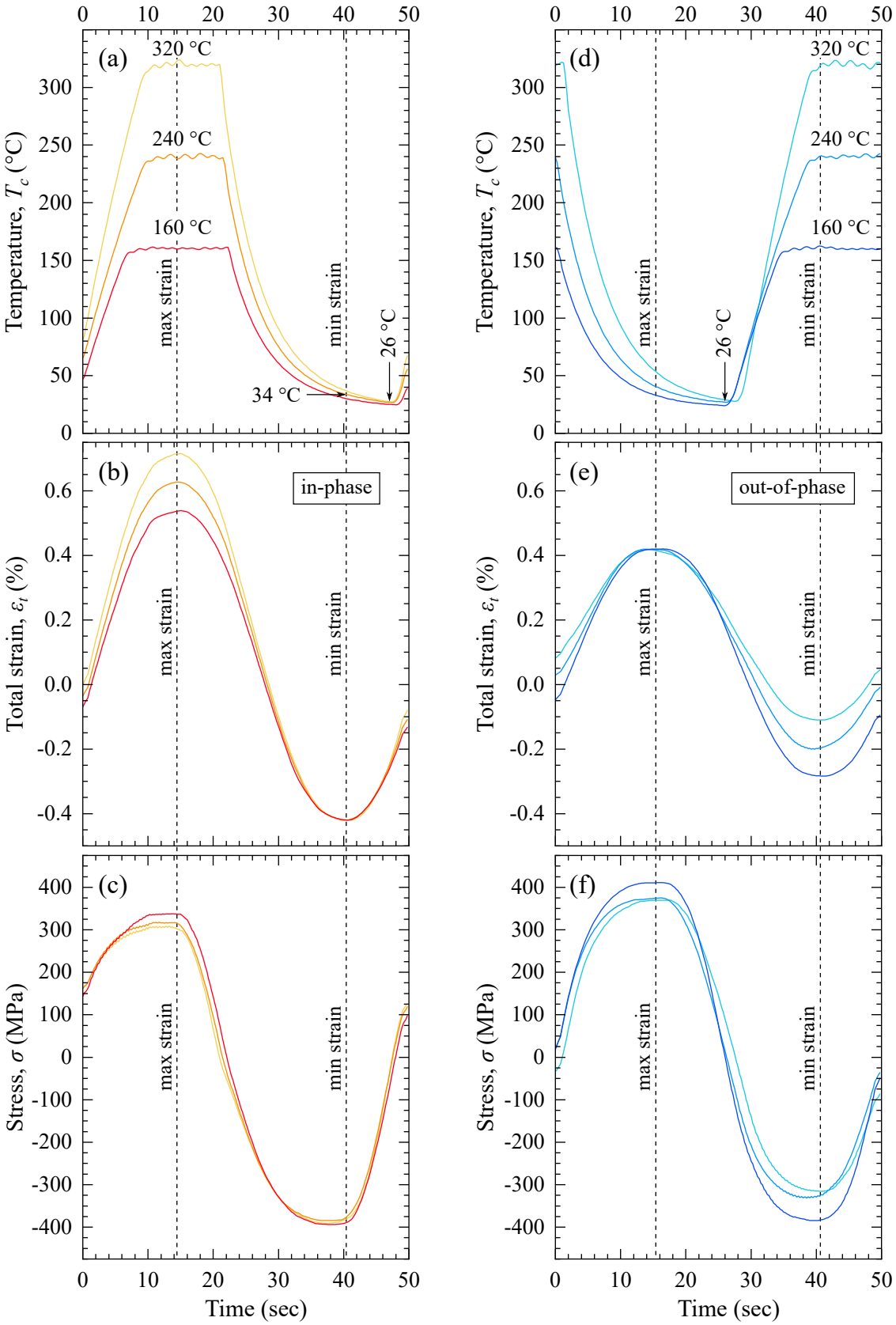

Fig. 76. One thermo-mechanical cycle at N = 800 and ε_{am} = 0.42 % for various temperatures in a time-domain format: (a, b, c) – in-phase; (d, e, f) – out-of-phase. (a, d) – temperature at the center of fatigue specimen; (b, e) – total strain, including thermal and mechanical components; (c, f) – nominal stress, as measured by the load cell.

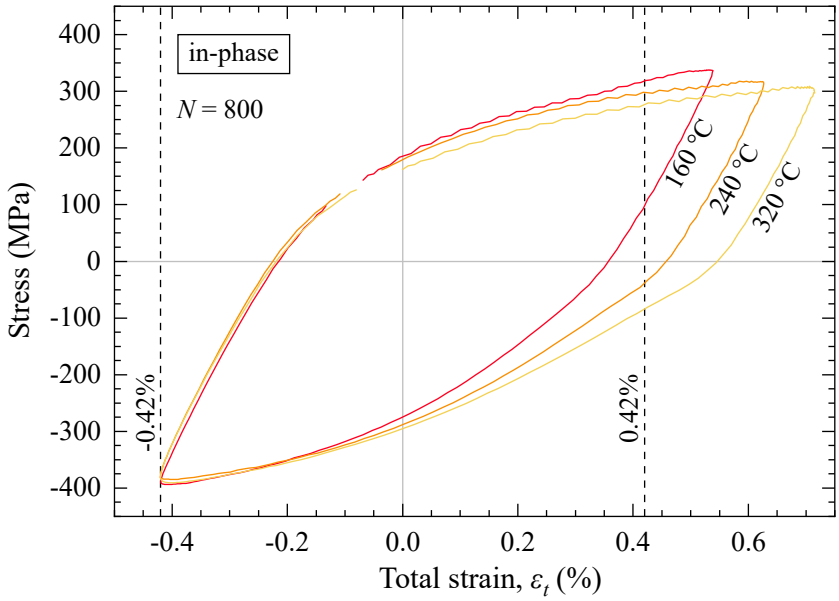

Fig. 77. In-phase total strain hysteresis at N = 800 from TMF tests with ε_{am} = 0.42 % and various high temperatures T_{ch}. Thermal expansion is not compensated here and is a part if the hysteresis.

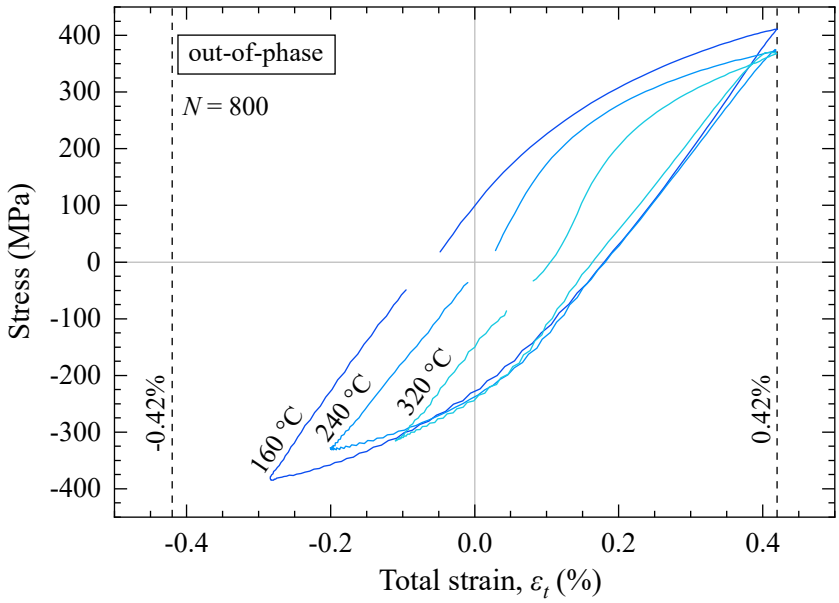

Fig. 78. Out-of-phase total strain hysteresis at N = 800 from TMF tests with ε_{am} = 0.42 % and various high temperatures T_{ch}. Thermal expansion is not compensated here and is a part if the hysteresis.

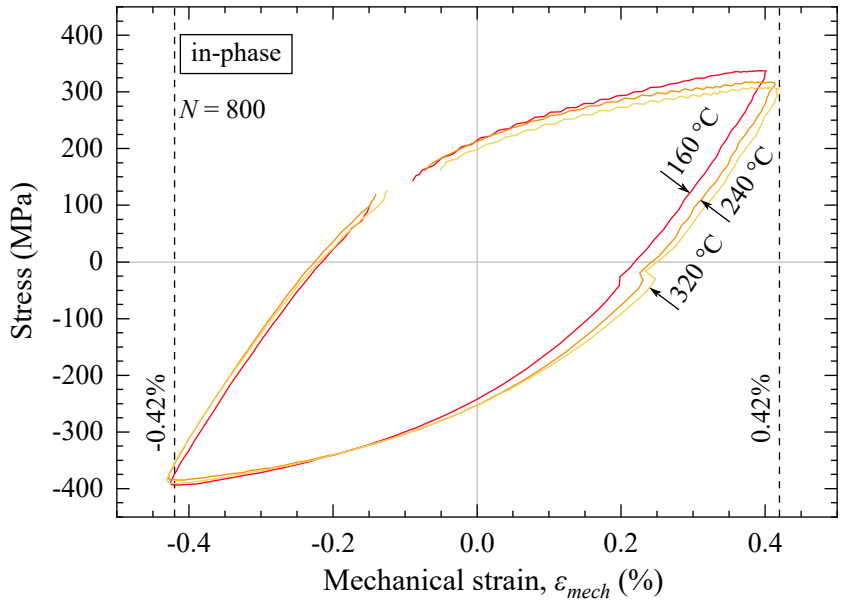

Fig. 79. In-phase mechanical strain hysteresis at N = 800 from TMF tests with ε_{am} = 0.42 % and various high temperatures T_{ch}. Thermal strain has been subtracted from mechanical strain.

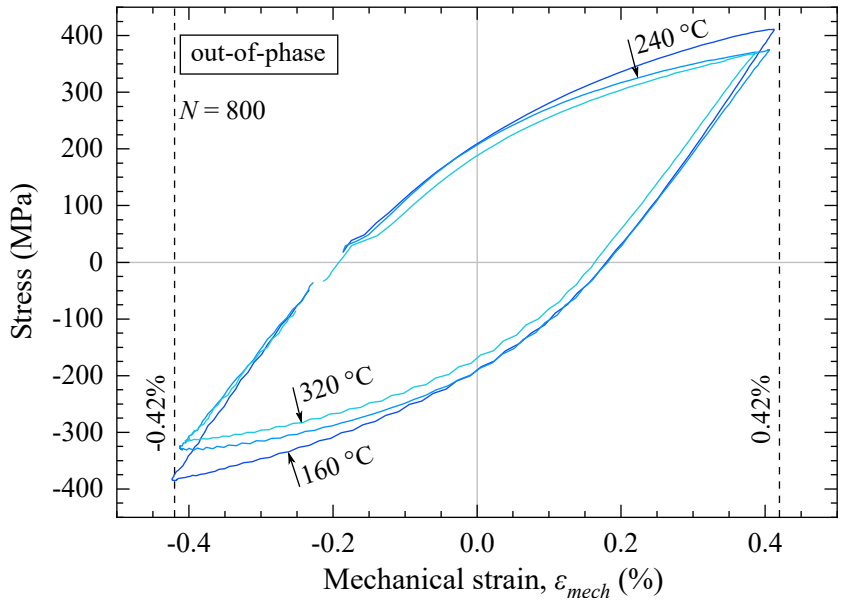

Fig. 80. Out-of-phase mechanical strain hysteresis at N = 800 from TMF tests with ε_{am} = 0.42 % and various high temperatures T_{ch}. Thermal strain has been subtracted from mechanical strain.

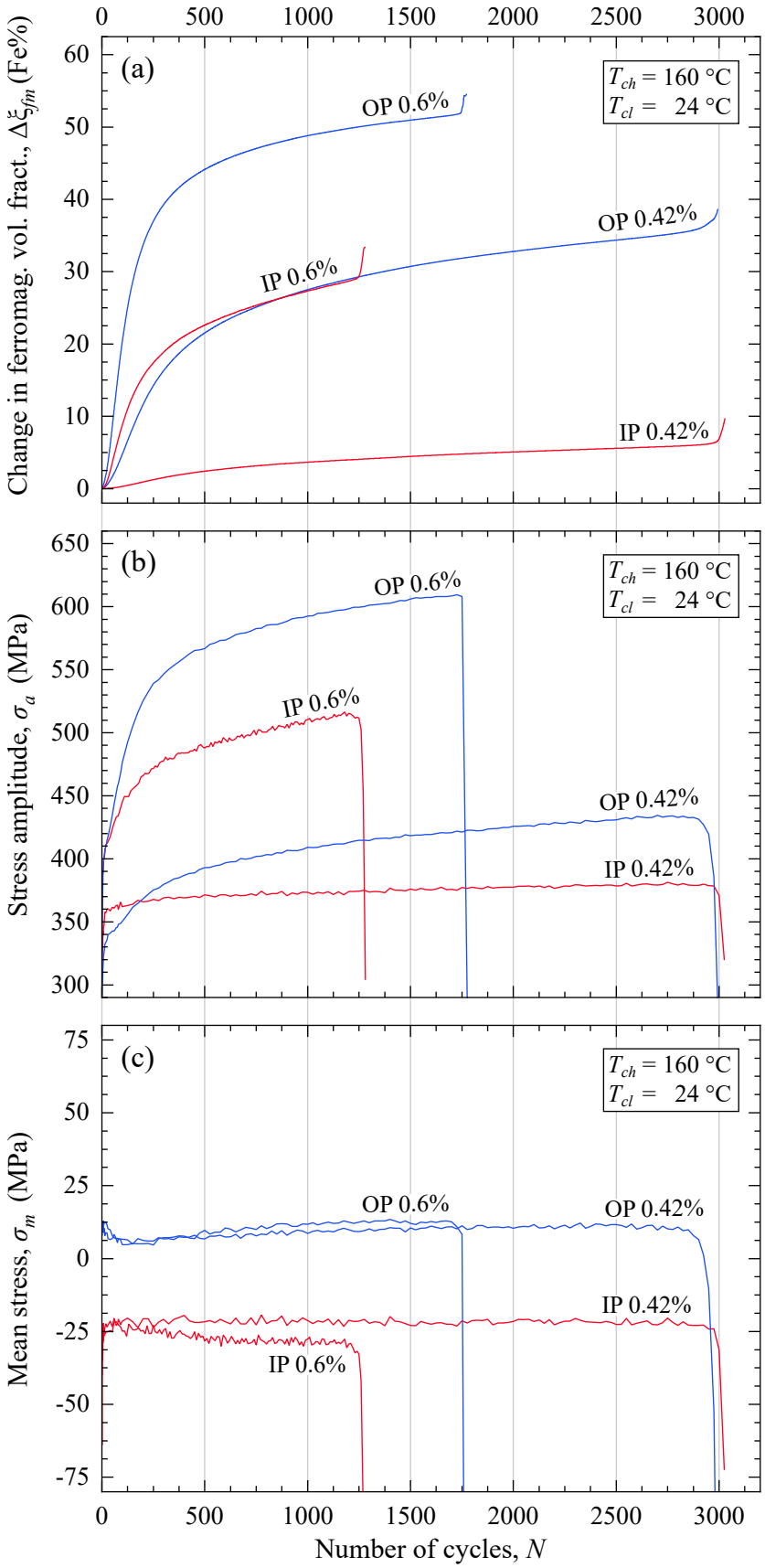

Fig. 81. *In-situ* data from constant strain amplitude thermo-mechanical fatigue tests with high temperature of 160 °C and low temperature of 24 °C: a) change in ferromagnetic volume fraction in Fe%, recorded with UMB-3; b) stress amplitude $\sigma_a = \frac{1}{2}(\sigma_{max} - \sigma_{min})$; c) mean stress $\sigma_m = \frac{1}{2}(\sigma_{max} + \sigma_{min})$.

phase from IP to OP in ε_{at} = 0.42 % test, increased the stress amplitude from 370 MPa to 435 MPa by the end of the test. For the 0.60 % tests this change was from 515 MPa to 610 MPa. Mean stress was nearly identical for different strain amplitudes, but different between IP and OP variations. For OP tests mean stress remained around 11 MPa for the whole duration of the test. In the IP test, mean stress was negative (compressive) and remained nearly constant at -25 MPa for the entire test.

After the fatigue tests were concluded, a section along the rotational axis was prepared with EDM, perpendicular to the crack propagation direction. Obtained samples were then embedded in a conductive hot-mounting resin and wet ground with 320 – 1200 grit sandpaper. Grinding was followed by 6 μm, 3 μm, and 1 μm diamond suspension polishing for 10 minutes each. Using MFI (see section 5.1) at working distance d_w = 10 μm ferromagnetic phase in the material was mapped for the sectioned samples.

The results of the MFI analysis are presented in Fig. 82 . The distribution of α' was more homogeneous in out-of-phase tests, where the axial α' bands could be easily distinguished. The amount of α' martensite at the fractured state was also higher for OP tests, which correlates with *in-situ* measurements.

In-phase tests had a tendency towards a diagonal symmetry, where more α' martensite would accumulate on the opposite sides, near the shoulder transition area. The lower part of the ε_{am} = 0.42 % IP specimen had more α' martensite than the upper part. The reason for this is likely the location of the compressed air nozzle, which was closer to the bottom of the specimen. This resulted in the cooling process happening slightly faster at the bottom and consequently slightly lower temperatures there. However, in the ε_{am} = 0.42 % OP test not only the lower part was symmetrical with the upper part, but also radial symmetry was fairly consistent.

7.5.3 TMF tests at 240 °C high temperature

The results of thermo-mechanical fatigue tests with the high temperature T_{ch} of 240 °C and the low temperature T_{cl} equal to 25 °C are presented in Fig. 83. In this temperature range three mechanical strain amplitudes ε_{am} were tested: 0.42 %, 0.51 %, and 0.6 % (see Table 12 on page 122 for more information).

At higher strain amplitudes, such as 0.6 %, the kinetics of phase transformation could still be described in terms of accelerated range and decelerated phase. However, transition to lower strain amplitudes made the $\gamma \rightarrow \alpha'$ transformation more linear. In fact, with exception of 0.6 % tests, the OP 0.51 % test was the only one showing a reduction in the rate of phase transformation. Tests performed at 0.42 % mechanical strain amplitude showed a linear

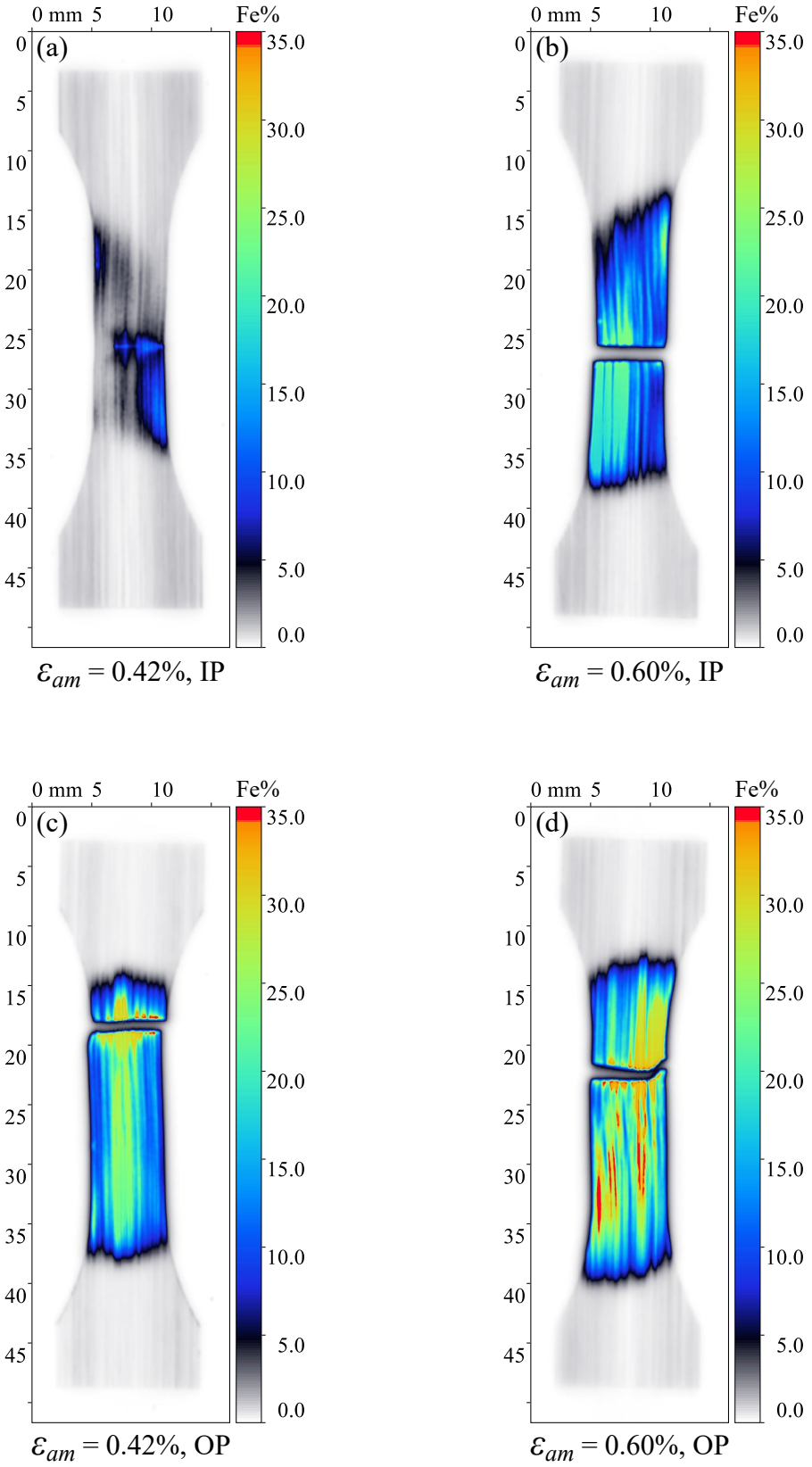

Fig. 82. MFI ferromagnetic volume density map of sectioned specimens after TMF tests at high temperature of 160 °C: a) in-phase ε_{am} = 0.42 %; b) in-phase ε_{am} = 0.60 %; c) out-of-phase ε_{am} = 0.42 %; d) out-of-phase ε_{am} = 0.60 %. d_w = 10 μm. Final surface preparation: 1 μm diamond suspension polishing.
Material: 347 (c) – Batch A, (a, b, d) – Batch B.

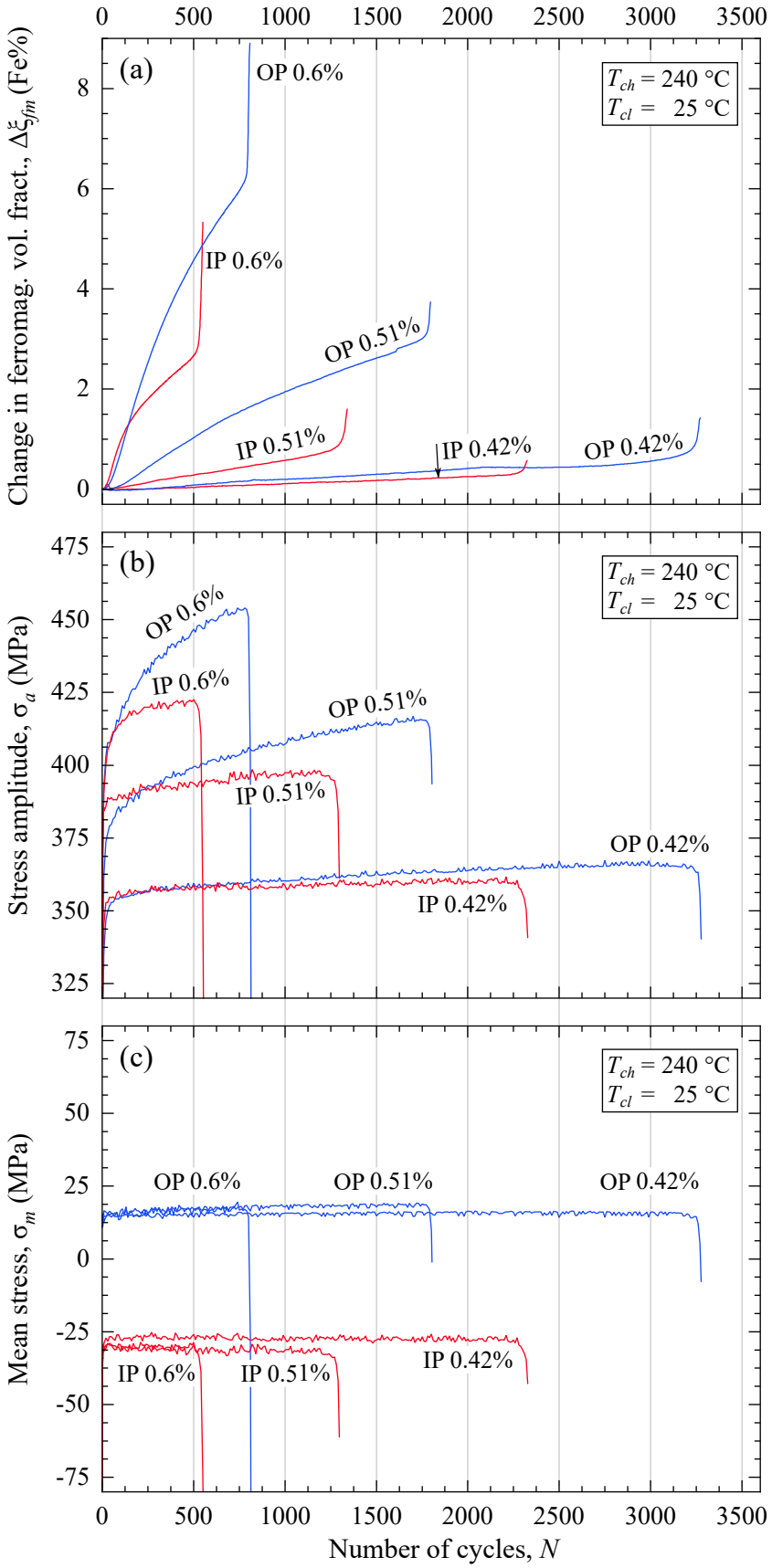

Fig. 83. *In-situ* data from constant strain amplitude thermo-mechanical fatigue tests with high temperature of 240 °C and low temperature of 25 °C: a) change in ferromagnetic volume fraction in Fe%, recorded with UMB-3; b) stress amplitude $\sigma_a = \frac{1}{2}(\sigma_{max} - \sigma_{min})$; c) mean stress $\sigma_m = \frac{1}{2}(\sigma_{max} + \sigma_{min})$. Material: 347 Batch B.

accumulation of α' martensite with the number of cycles.

The difference between IP and OP tests was less pronounced compared to the T_{ch} = 160 °C series in the previous section. The initial transformation rate (LR1) was identical for IP and OP tests at 0.6 % strain amplitude. The rate of phase transformation in the IP 0.6 % test quickly reduced after 200 cycles, while in the OP test the amount of deformation-induced martensite had doubled by 500 cycles. Similarly, the 0.51 % OP test had a double amount of α' at about 1000 cycles. TMF test with 0.42 % strain amplitude had slightly less difference between IP and OP test of about 30 %.

Cyclic hardening behavior is demonstrated by the stress amplitude in Fig. 83b. All IP tests had a slower rate of cyclic hardening compared to OP tests, similarly to the phase transformation rate in Fig. 83a. At the end of each fatigue test, the stress amplitude rapidly decreased as the crack propagation initiated. This decrease in stress amplitude also coincided with the increase in α' martensite formation due to the overall increased true stress and stress concentration at the root of the crack.

IP and OP tests could be clearly differentiated by mean stress amplitude in Fig. 83c. All IP tests had a negative (compressive) mean stress of around -27 MPa, whereas OP tests had a positive (tensile) mean stress of around 15 MPa. Mechanical strain amplitude seemed not to influence the mean stress and the variation between ε_{am} equal 0.42 %, 0.51 %, and 0.6 % were within 6 MPa. Compared to the tests at T_{ch} equal to 160 °C, mean stress increased by around 5 MPa for both IP and OP.

After the fatigue tests were concluded, a section along the rotational axis was prepared with EDM, perpendicular to the crack propagation direction. Obtained samples were then embedded in a conductive hot-mounting resin and wet ground with 320 – 1200 grit sandpaper. Grinding was followed by 6 μm, 3 μm, and 1 μm diamond suspension polishing for 10 minutes each. Using MFI at working distance d_w = 10 μm ferromagnetic phase in the material was mapped for the sectioned samples. The results are shown in Fig. 84. Unlike tests at T_{ch} equal 160 °C, at high temperature of 240 °C, α' martensite no longer formed at the center of the fatigue specimen. Instead, α' formed primarily at the transition from the gauge length to the shoulders. The lower part of the sample had more α' martensite due to the closer proximity to the compressed air nozzle and consequentially lower temperatures during the cooling cycle, typically 15 °C colder than the center. OP tests had more pronounced diagonal symmetry, where α' formed on the opposite sides of the specimen. Diagonal symmetry in IP tests was much less conspicuous.

MFI was also able to identify several non-propagating micro-cracks. For example, in Fig. 84d at a vertical position of 20 mm around a bigger propa-

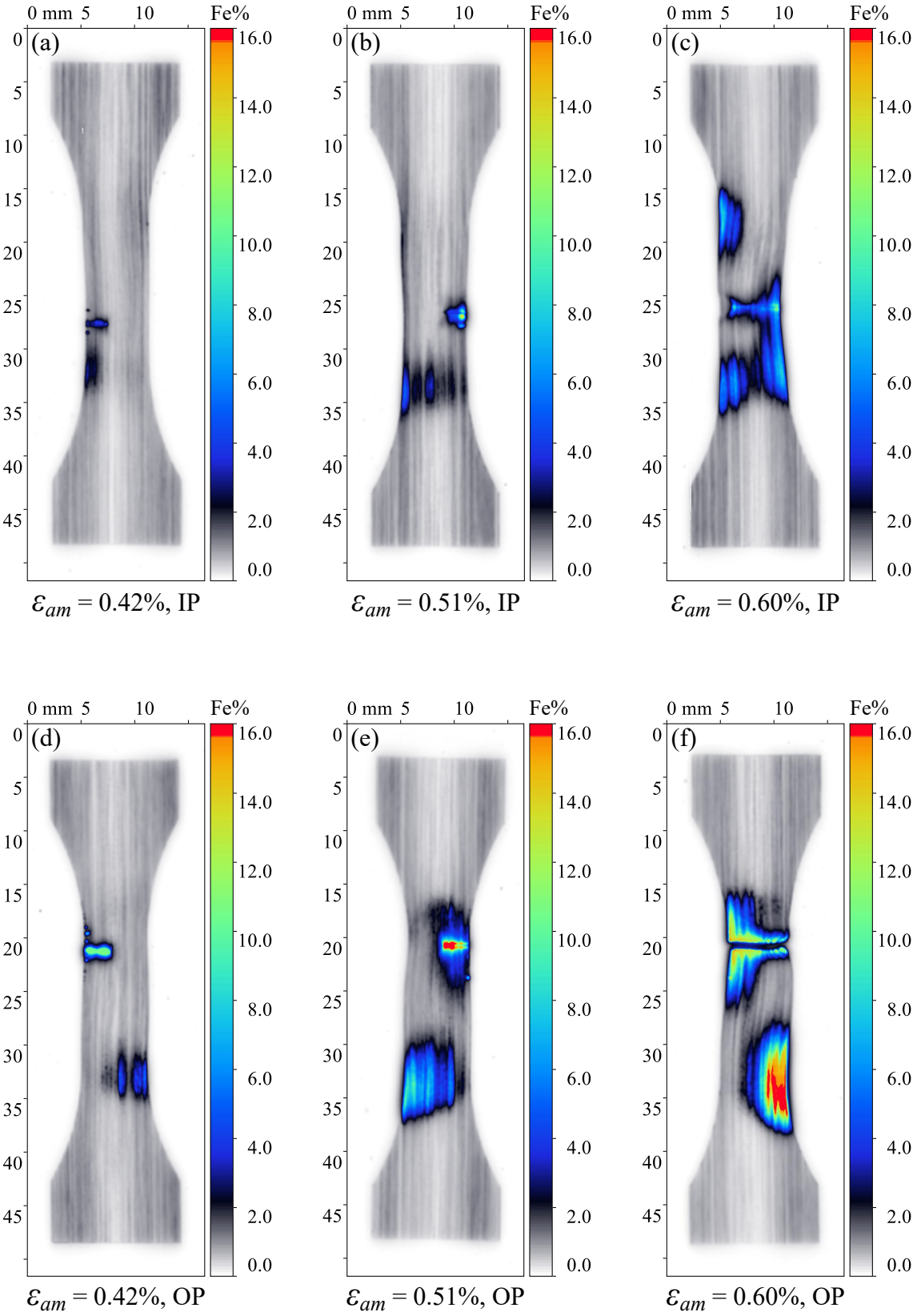

Fig. 84. MFI ferromagnetic volume density map of sectioned specimens after TMF tests at high temperature of 240 °C: a) in-phase ε_{am} = 0.42 %; b) in-phase ε_{am} = 0.51 %; c) in-phase ε_{am} = 0.60%; d) out-of-phase ε_{am} = 0.42 %; e) out-of-phase ε_{am} = 0.51 %; f) out-of-phase ε_{am} = 0.60 %. d_w = 10 μm. Final surface preparation: 1 μm diamond suspension polishing. Material: 347 Batch B.

gating crack, nine smaller non-propagating cracks could be identified as small dots. These micro-cracks advanced each time when the fatigue specimen was rapidly cooled from T_{ch} to T_{cl}. Such micro-cracks could not be easily observed with MFI at higher strain amplitudes due to the considerable amount of deformation-induced martensite.

7.5.4 TMF tests at 320 °C high temperature

Thermo-mechanical fatigue tests at high temperature T_{ch} of 320 °C were performed with two mechanical strain amplitudes ε_{am}: 0.42 % and 0.51 %. The results of *in-situ* measurements are shown in Fig. 85. The amount of deformation-induced martensite, indicated as the change in ferromagnetic volume fraction in Fig. 85a, remained below 0.2 % for both strain amplitudes, except at the very end of the test. The rapid increase in α' volume at the end correlated with a drop in stress amplitude and signified the beginning of crack propagation.

The rate of phase transformation $\partial \xi_{fm}/\partial N$ was very similar to isothermal fatigue tests at 240 °C and 320 °C. The exception is that in isothermal tests above 240 °C no additional α' martensite was formed on the fracture surface. There was an immense contrast in $\partial \xi_{fm}/\partial N$ between the 17 °C isothermal test and the T_{ch} = 320 °C TMF test. The isothermal reached 50 Fe% in just under 125 cycles at otherwise identical to TMF strain amplitude and frequency (see Fig. 70 on page 114).

Cyclic hardening behavior was only observed for 0.51 % strain amplitude. Unlike any other previously described TMF tests, IP and OP tests at ε_{am} = 0.42 % showed cyclic softening by slowly decreasing stress amplitude, as shown in Fig. 85b. Mean stresses were also clearly separated to be positive in OP tests and negative in IP, as can be seen from Fig. 85c. Compared to TMF tests with T_{ch} = 240 °C, mean stress increased by 8 MPa, resulting in 23 MPa in OP tests and -35 MPa in IP tests.

The “waves” in the UMB signal in Fig. 85a came from the change of the room temperature, where the peaks correspond to the 24-hour period fluctuation of temperature. The temperature difference between day and night was particularly high for the ε_{am} = 0.42 % tests. It is, therefore, difficult to tell whether the overall positive slope is due to the increased α' volume or a temperature change. Described further is an assessment with magnetic force imaging, which is not prone to such temperature fluctuations.

MFI analysis in Fig. 86 confirmed the *in-situ* observations of α' formed primarily at the crack propagation stage. A vertical band with lower Fe% reading at the center is typical for Batch B and could also be observed in the transverse section of the bar (see Fig. 48 on page 87). All MFI maps are oriented the

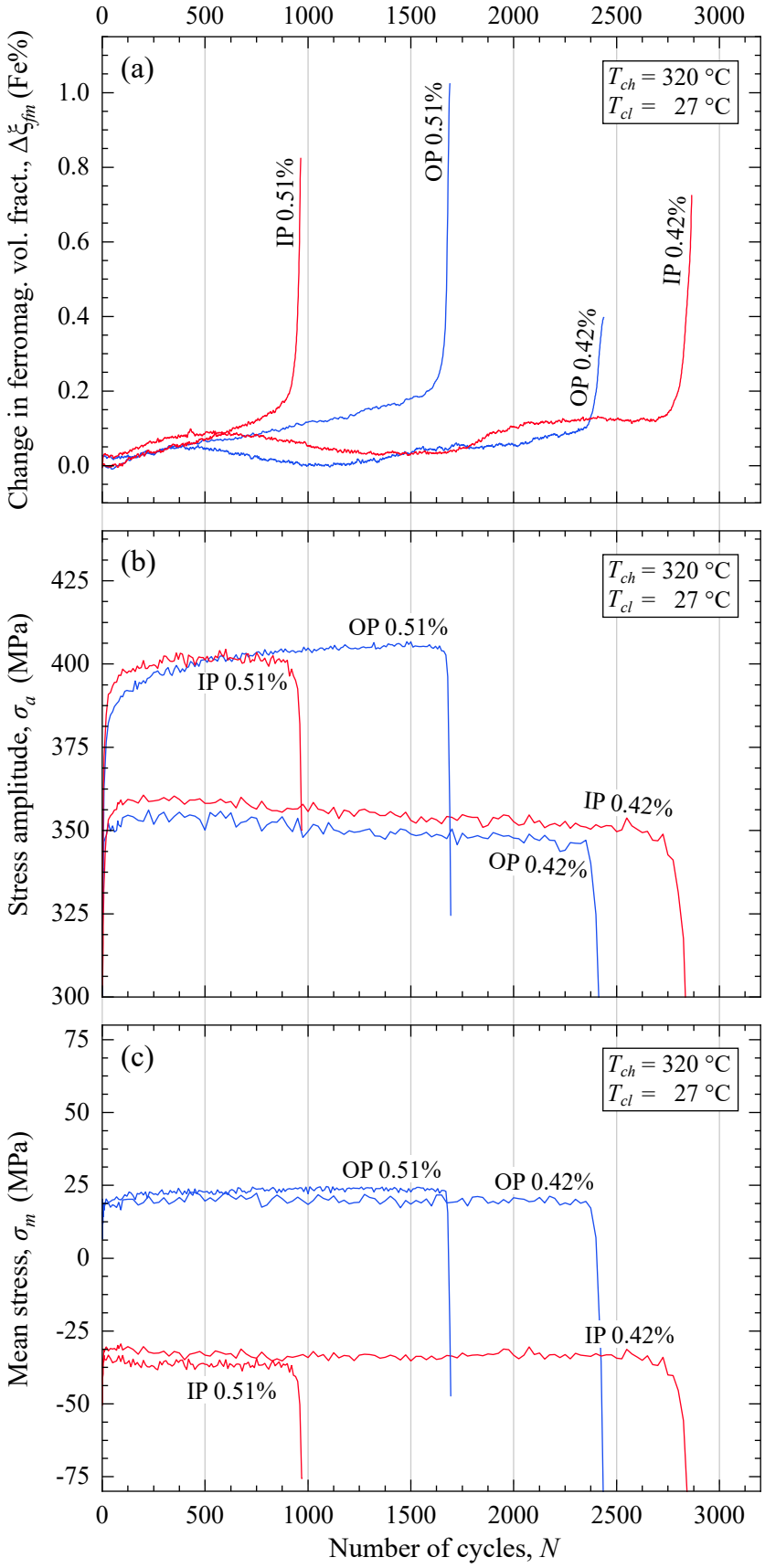

Fig. 85. *In-situ* data from constant strain amplitude thermo-mechanical fatigue tests with high temperature of 320 °C and low temperature of 27 °C: a) change in ferromagnetic volume fraction in Fe%, recorded with UMB-3; b) stress amplitude $\sigma_a = \frac{1}{2}(\sigma_{max} - \sigma_{min})$; c) mean stress $\sigma_m = \frac{1}{2}(\sigma_{max} + \sigma_{min})$. Material: 347 Batch B.

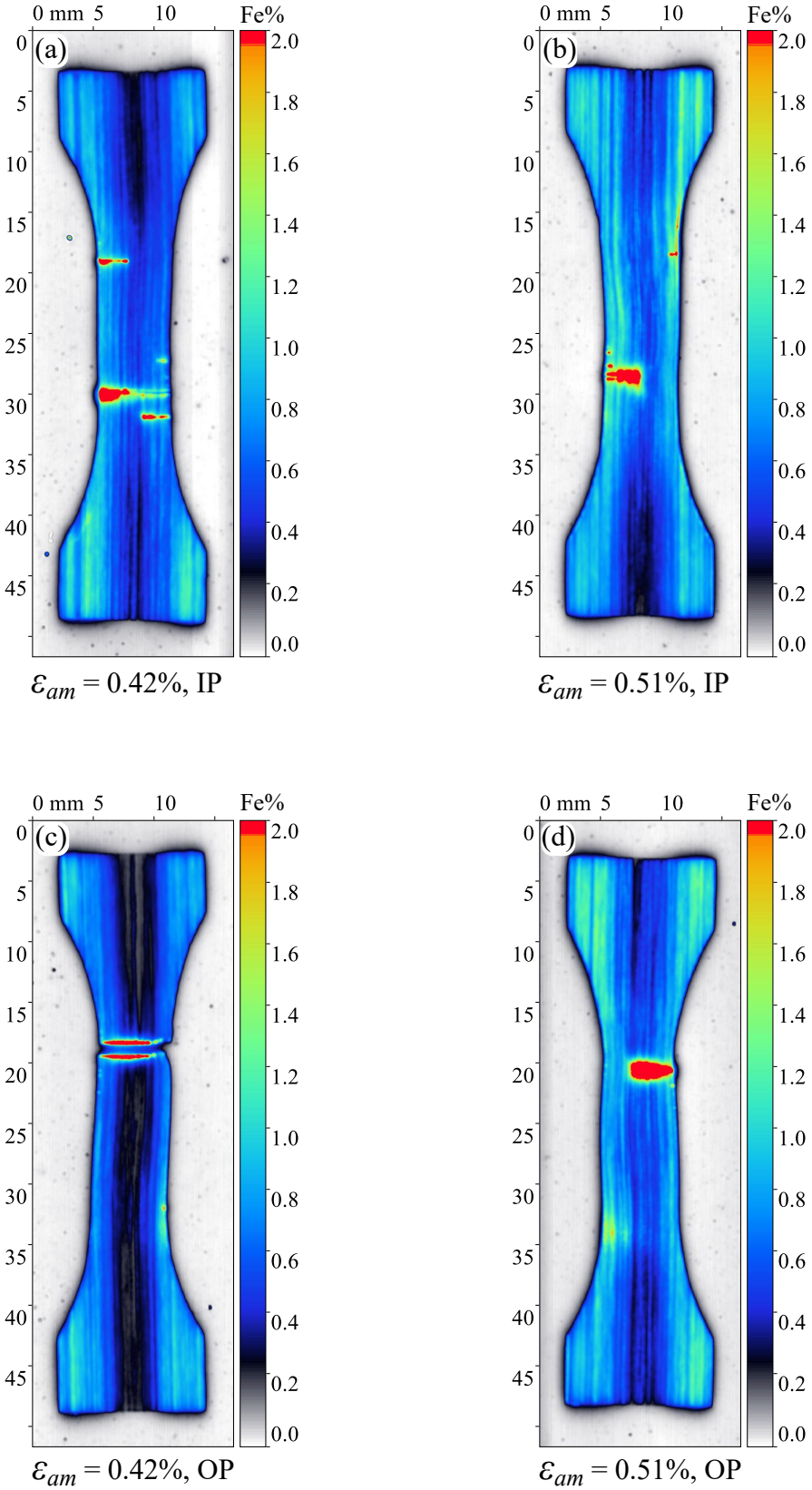

Fig. 86. MFI ferromagnetic volume density map of sectioned specimens after TMF tests at high temperature of 320 °C: a) in-phase ε_{am} = 0.42 %; b) in-phase ε_{am} = 0.51 %; c) out-of-phase ε_{am} = 0.42 %; d) out-of-phase ε_{at} = 0.51 %. d_w = 10 μm. Final surface preparation: 1 μm diamond suspension polishing. Material: 347 Batch B.

way how the fatigue specimens were mounted in the fatigue machine: the top corresponds to the upper grip and the bottom to the lower grip. Since the compressed air nozzle was located at the lower grip, the bottom of the specimen received a stronger cooling. The minimum temperature at the bottom reached 12 °C at the transition from the shaft to the gauge radius. The temperature at the center T_c at that point in time was 27 °C (designated "low temperature") and the upper part was at 37 °C. Despite this temperature gradient, no significant difference between the top and the bottom could be observed with MFI.

IP specimens failed with multiple propagating cracks, whereas OP specimens had only one large crack and several micro-cracks, which can be spotted as small dots near the specimen's outer surface. In OP tests (Fig. 86c and d), at around 33 mm vertical position there was an increase in the ferromagnetic phase without micro-cracks present in the vicinity. This indicates that the increase in ferromagnetic volume fraction, measured with UMB in Fig. 85a, corresponds primarily to the transition area between the shaft and the gauge length. Micro-cracks could also potentially appear at an early stage and contribute to the increase in the Fe% reading of UMB. There was a clear difference in the rate of phase transformation between IP and OP tests in all TMF tests. OP tests formed α' always faster, compared to IP tests. Microstructural analysis, however, did not show much difference between the two.

7.6 Mathematical extrapolation of experimental data

So far, we have observed five isolated cases where one parameter was fixed, and the response of others was studied. Each case provided information on the rate of $\gamma \rightarrow \alpha'$ transformation under various strains, temperatures, and combinations of the two. In each case, experimental data was empirically fitted with an equation, which can be merged together mathematically. The combined information is no longer purely experimental, but mathematically extrapolated to conditions that cannot be tested experimentally.

7.6.1 Isothermal fatigue

Temperature and strain amplitude data were merged together in order to fully describe the rate of phase transformation in isothermal fatigue conditions. The strain data is represented by Eq. (50) and was obtained from ambient temperature[12] tests at $T_c \approx 30\,°C$ (section 7.3). The temperature data were obtained from isothermal constant strain amplitude tests with $\varepsilon_{at} = 0.51\,\%$ in section 7.4 and represented by Eq. (51). The fit parameters for these equations are summarized in Table 14.

$$\frac{\partial \xi_{fm}}{\partial N}(\varepsilon_{at}) = a \cdot \varepsilon_{at}^{b \cdot \varepsilon_{at}^{-c}} \tag{50}$$

$$\frac{\partial \xi_{fm}}{\partial N}(T_c) = k \cdot m^{T_c} \tag{51}$$

There was a discrepancy at the intersection point of the two data sets. The isothermal fatigue test at 17 °C and 0.51 % strain amplitude had a higher rate of phase transformation than the ambient (unregulated) temperature test with a similar strain amplitude. There could be several reasons for that. Isothermal fatigue tests were performed at a much lower frequency of 0.02 Hz to be identical to TMF tests. A sinusoidal waveform was used in isothermal tests instead of triangular, meaning the peak load was sustained for a longer period of time. Finally, a different version of UMB was used to measure the α' martensite, which may also have contributed to the discrepancy. With this in mind, the

[12] Fatigue specimens were allowed to self-heat, resulting in an initial temperature spike, followed by a gradual decrease due to cyclic hardening.

Table 14
Fit parameters for isothermal fatigue test conditions. Original data represents the best fit for the experimentally measured data. Parameter *a* was normalized to temperature data.

	a	***b***	***c***	***k***	***m***
Original	0.323 ± 0.002	2.082 ± 0.06	0.381 ± 0.05	2.287 ± 0.4	0.944 ± 0.002
Corrected	2.565	2.082	0.381	–	–

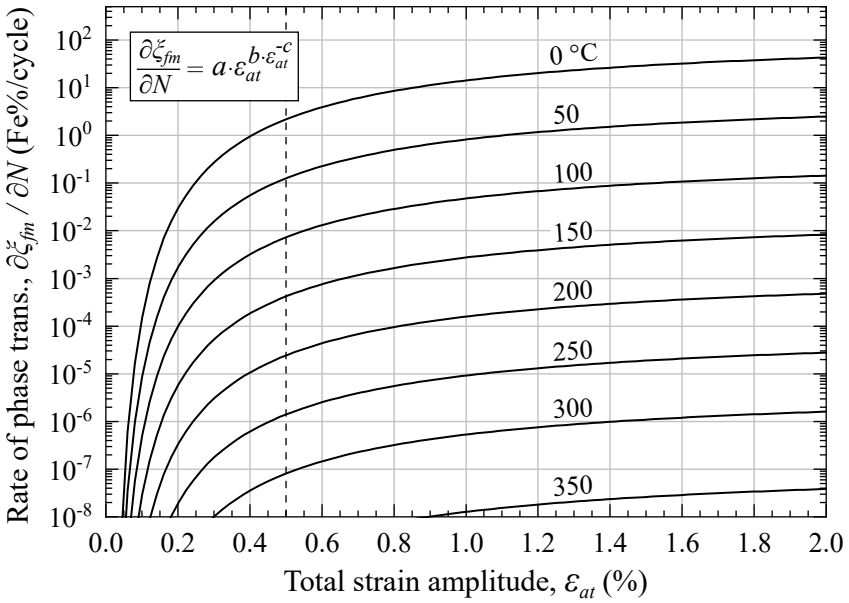

Fig. 87. Maximum rate of phase transformation (LR1) as a function of total strain amplitude, extrapolated to different temperatures.

proportionality coefficient a of all ambient temperature tests was adjusted to fit the isothermal test of similar temperature. The corrected function is plotted in Fig. 87 as strain amplitude extrapolated to different temperatures. Conversely, in Fig. 88, temperature was extrapolated to different strain amplitudes.

7.6.2 Equivalent transformation rate curve

Since equations (50) and (51) describe the same physical value, they can be written as Eq. (52), eliminating the $\partial \xi_{fm} / \partial N$ term.

$$a \cdot \varepsilon_{at}^{b \cdot \varepsilon_{at}^{-c}} = k \cdot m^{T_c} \tag{52}$$

The result is an equation for equivalent transformation rate, which can also be written explicitly as Eq. (53):

$$T_c = \frac{ln(a) + b \cdot \varepsilon_{at}^{-c} \cdot ln(\varepsilon_{at}) - ln(k)}{ln\,(m)} \tag{53}$$

The curve obtained from this equation is shown in Fig. 89. It describes the relationship between the ambient temperature and the elevated temperature phase transformation rate. The curve shows which combination of temperature and strain amplitude results in an identical phase transformation rate. To be more specific, it shows where the rate of phase transformation is equal between a given strain amplitude at ambient temperature (vertical axis) and a given temperature at a fixed strain amplitude of 0.5 % (horizontal axis).

The equivalent transformation rate curve can be used to define a phase

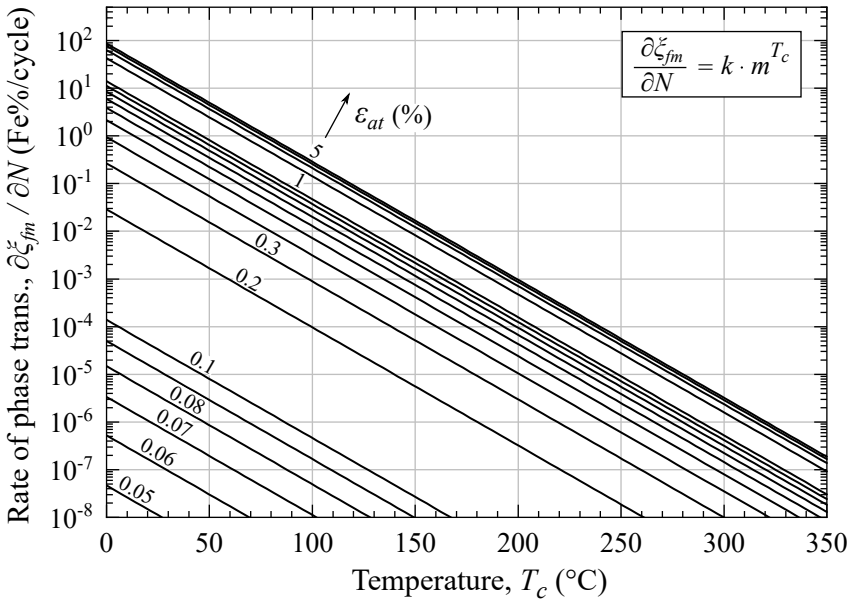

Fig. 88. Maximum rate of phase transformation (LR1) as a function of temperature, extrapolated to different strain amplitudes.

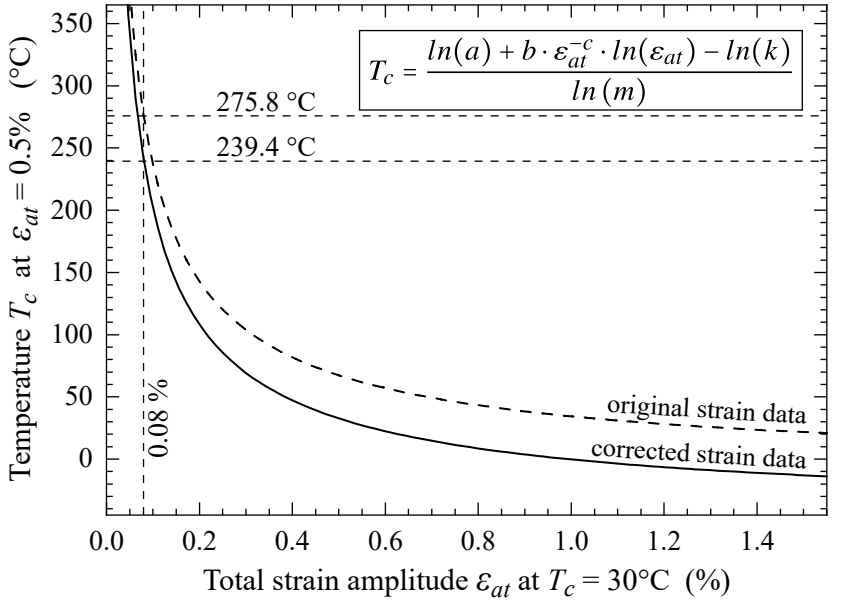

Fig. 89. Equivalent transformation rate curve. The line shows where the rate of phase transformation is equal between various strain amplitudes at ambient temperature and various temperatures at a fixed strain amplitude of 0.5 %.

transformation temperature limit for 0.5 % strain amplitude. Previously we established in section 7.1 the lowest strain amplitude required to make a change in the electrical resistance of the material, as well as to initiate $\gamma \rightarrow \alpha'$ phase transformation. At ambient temperature, ε_{at} = 0.09 % was the lowest strain amplitude at which a change in electrical resistance was found, and ε_{at} = 0.10 % was the lowest strain amplitude at which the formation of α' was detected in strain increase tests. Therefore, we can assume that the limit for the material response is slightly lower – around 0.08 %. Using Eq. (53), strain amplitude can be converted to the temperature of 239.4 °C (275.8 °C for uncorrected data). This temperature corresponds to the maximum temperature for $\gamma \rightarrow \alpha'$ phase transformation for ε_{at} = 0.5 %. This can be also confirmed by experimental data in section 7.4, where phase transformation was detected at 200 °C by both UMB and MFI, while at 240 °C detection of α' became questionable.

Alternatively, if M_d temperature is known, the strain amplitude limit for $\gamma \rightarrow \alpha'$ phase transformation at ambient temperature can be determined from the equivalent transformation rate curve. The 0.25 Fe% threshold characterization of M_d temperature, performed in Fig. 51 on page 91, indicated that 240 °C is a good candidate for it. Although the data obtained in section 7.4 showed that the $\gamma \rightarrow \alpha'$ transformation is probably still present at 240 °C but occurs at an extremely slow rate. It appears that if the strain amplitude from Eq. (52) is calculated using 240 °C temperature as an input, the result would be the same 0.08 % obtained by the electrical resistance test in Fig. 53 on page 94. This indicates that the threshold for the change in electrical resistance is closely related to the lower accumulate strain limit for $\gamma \rightarrow \alpha'$ transformation.

7.6.3 Thermo-mechanical fatigue

A considerable variety of parameters in TMF testing make it difficult for statistically significant characterization of the phase transformation process. With only two or three fatigue tests for one combination of high temperature and phase angle, only limited predictions of the phase transformation behavior could be made. To help analyze TMF data, it can be plotted together with isothermal data, such as in Fig. 90. When the high temperature T_{ch} becomes equal to the low temperature T_{cl}, TMF tests essentially become isothermal, for which a good amount of experimental data had been collected. This also means there should be an intersection point between TMF and isothermal tests at about 25 °C, which is the low temperature for all TMF tests.

The isothermal line, plotted in Fig. 90, corresponds to the experimentally obtained data for ε_{at} = 0.51 % (no extrapolation). It can be directly compared with TMF tests performed with ε_{am} = 0.51 %, plotted with filled squares. The

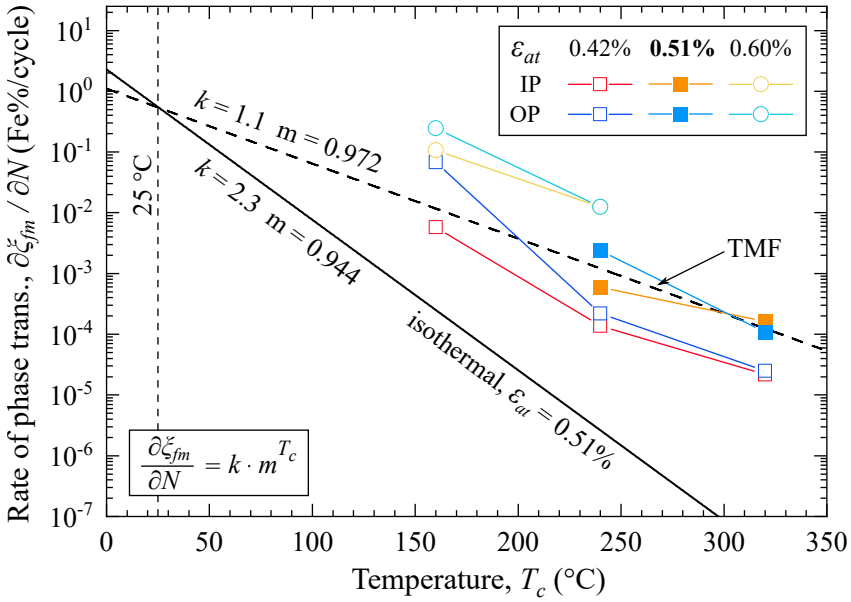

Fig. 90. Maximum rate of phase transformation (LR1) in isothermal and thermo-mechanical tests as a function of temperature.

tendency of $\partial\xi_{fm}/\partial N$ to decrease exponentially with temperature in TMF tests was found to be similar to isothermal tests and can therefore be analyzed in terms of Eq. (50). For ε_{at} = 0.51 % TMF tests, the function can be plotted through four experimental data points and the intersection with the isothermal line at 25 °C. Such a function is shown as a dashed line in Fig. 90. This line also highlights the amount of the scatter within TMF data. Although the general trend is clearly the exponential reduction in the rate of phase transformation, more tests would be needed to confirm that with sufficient statistical significance.

Part III

Discussion

"The first principle is that you must not fool yourself, and you are the easiest person to fool."

Richard Feynman

8 Reliability of Magnetic Measurements

8.1 Magnetic force imaging reliability

There are two main ways in which MFI measurements could be affected:

- Change in working distance due to insufficient sample flatness;
- Martensite induced by surface preparation.

To investigate the influence of surface flatness and the resulting change in the working distance of MFI scans, the surface topography was measured using the Mahr Perthometer PGK 120. The measured profiles are plotted together with the MFI measurements in Fig. 91–94. The dependence of the MFI signal on the working distance has already been established in section 5.1.2 on page 56, where the calibration coefficient C_{Fe} (Fe%/mV) changed linearly with the working distance. This change can be expressed as the working distance coefficient C_{wd}, which is equal to 0.1129 ± 0.0007 Fe%/(mV·μm).

The working distance was measured at the center of the MFI sample, which is the highest point due to the convex shape of the sample resulting from polishing. As the working distance d_w increases, the force in the MFI sensor decreases. Therefore, the MFI signal should be multiplied by a larger calibration coefficient C_{Fe} to obtain the same ferrite reading. In other words, the change in the working distance Δd_w should be added to the calibration coefficient C_{Fe} to become the corrected calibration coefficient $\tilde{C}_{Fe}$:

$$\tilde{C}_{Fe} = C_{Fe} + \Delta d_w \cdot C_{wd} \tag{54}$$

From Eq. (54) ferromagnetic fraction ξ_{fm} can be compensated:

$$\tilde{\xi}_{fm} = \frac{C_{Fe}}{\tilde{C}_{Fe}} \cdot \xi_{fm} \tag{55}$$

where $\tilde{\xi}_{fm}$ is the ferromagnetic volume fraction in Fe%, compensated for the change in the working distance. The results of the calculations are presented in Table 15. According to the calculations, the change in the ferrite reading due to the change in the working distance $\xi_{fm} - \tilde{\xi}_{fm}$ is one order of magnitude smaller than the observed increase $\Delta\xi_{fm}$ from the shoulders of the fatigue specimen to the center. Therefore, it is unlikely that the increase in α' martensite measured with MFI content is due to a deviation from flatness.

The effect of the flatness deviation can also be visually examined by the area around the fatigue specimen in MFI scans. This area, the gray-scale region of the MFI colormap, is the conductive hot mounting powder for SEM

Table 15
Change in MFI ferromagnetic volume fraction reading due to flatness deviation.

	Δd_w μm	ξ_{fm}, center Fe%	ξ_{fm}, shoulder Fe%	$\Delta\xi_{fm}$ Fe%	$\xi_{fm} - \tilde{\xi}_{fm}$ Fe%
ISO 320 °C (Fig. 91)	3.8	0.54	0.25	0.29	0.015
ISO 240 °C (Fig. 92)	7.43	0.48	0.30	0.18	0.027
OP 320 °C (Fig. 93)	3.27	0.23	0.20	0.03	0.006
IP 320 °C (Fig. 94)	4.48	0.44	0.23	0.21	0.016
Average	4.745	0.422	0.246	0.176	0.0159

investigations. It has a higher magnetic susceptibility than air and contains magnetic particles visible directly with MFI. Since the embedded fatigue specimen and the resin share the same surface curvature, a significant deviation in the working distance should be visually apparent from the powder surrounding the fatigue specimen. However, from what was observed, a 4 to 7 μm variation in flatness, and consequently working distance, did not have a noticeable effect on the MFI signal.

In some cases, such as in Fig. 92, the MFI sample was not perfectly parallel to the scanning plane resulting in a tilt in the measurement. After correcting the tilt in the profile (the MFI image was not corrected), we can see that the central area was the least affected by this tilt, and only the shoulders of the specimen were affected. The tilt in other MFI scans was even less significant.

Another possible reason for the apparent increase in ferromagnetic density at the center of the gauge length is the combined effect of fatigue history and sample preparation. It has been found that mechanical polishing of this material with diamond suspension produces deformation-induced martensite on the surface. After the material was subjected to low cycle fatigue at elevated temperature, a sufficient amount of plastic strain accumulated in the gauge length, but not at the shoulders. It is well known that the plastic deformation of austenite before quenching increases martensite start temperature [12]. As was explained by Cayron [12], intersection of the two shear or glide bands leads to a high stress concentration that distorts the lattice, which can lead to the reduction in the energy barrier between γ and α phases. It is, therefore, possible that the mechanical polishing would produce more martensite at the gauge length than at the shoulders of the specimen.

To study the effect of surface preparation, the fatigue specimen shown in Fig. 72f on page 116 was selected, which had already been polished with 1 μm diamond suspension. It was then electropolished for about 5 seconds and an EBSD map was taken at the center of the gauge length. 5 seconds is not quite enough to completely remove the deformed layer, but it is enough to improve

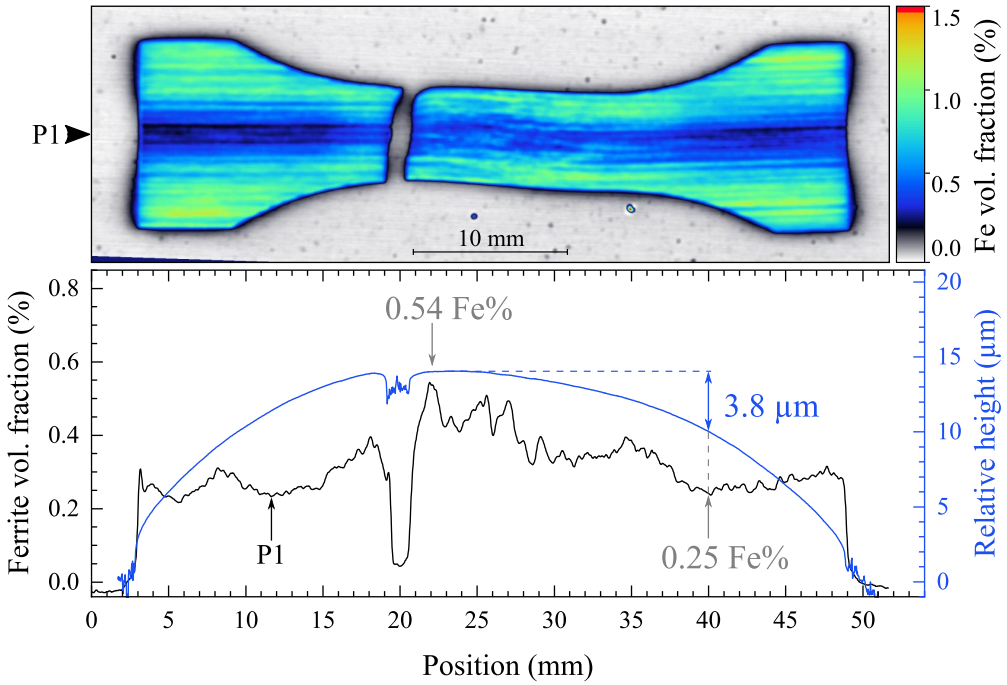

Fig. 91. MFI ferromagnetic volume density map in Fe%, after an isothermal fatigue test at 320 °C, ε_{at} = 0.51 %.

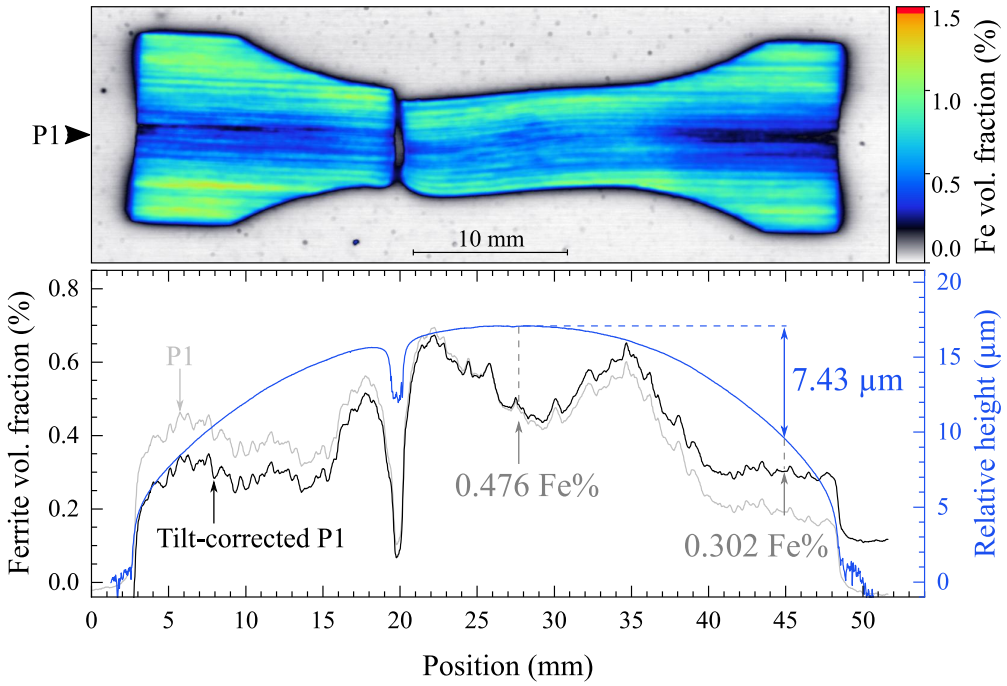

Fig. 92. MFI ferromagnetic volume density map in Fe%, after an isothermal fatigue test at 240 °C, ε_{at} = 0.51 %.

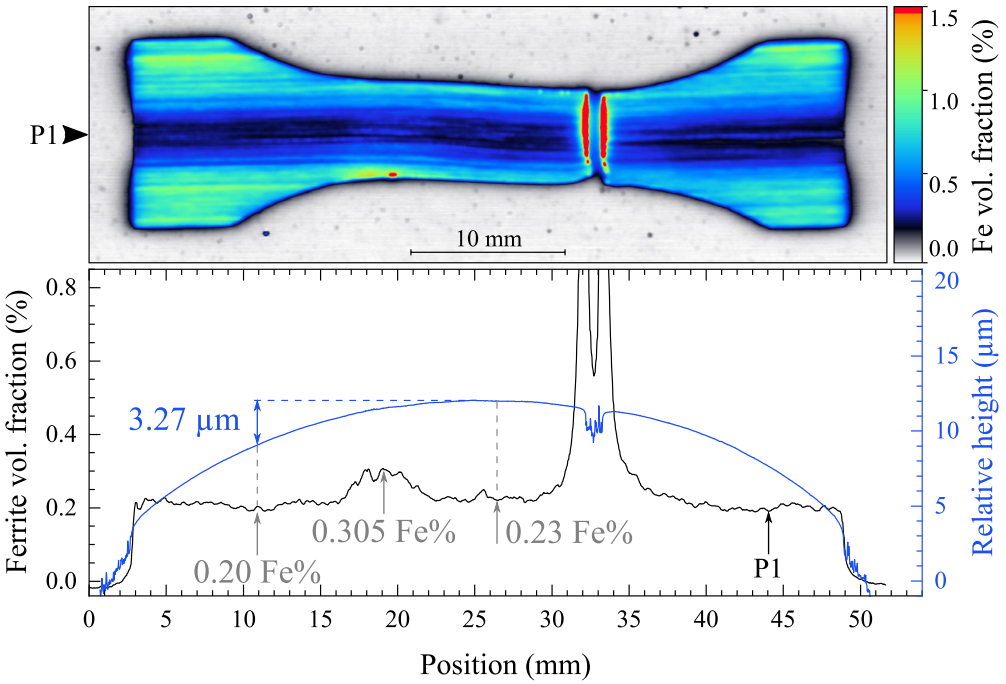

Fig. 93. MFI ferromagnetic volume density map in Fe%, after the OP TMF test at T_{ch} = 320 °C and ε_{am} = 0.42 %.

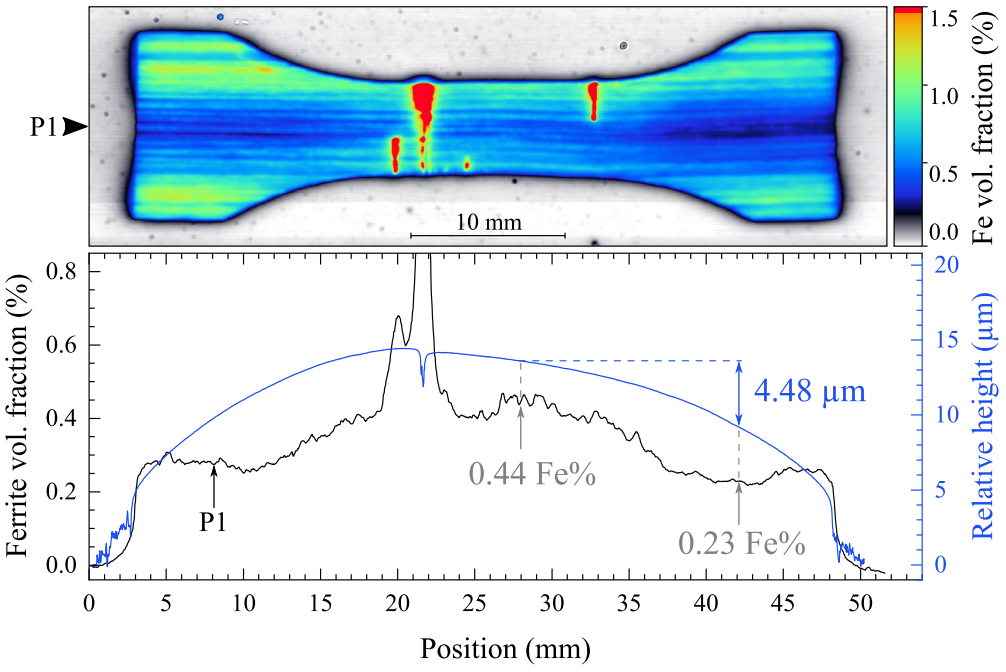

Fig. 94. MFI ferromagnetic volume density map in Fe%, after the IP TMF test at T_{ch} = 320 °C and ε_{am} = 0.42 %.

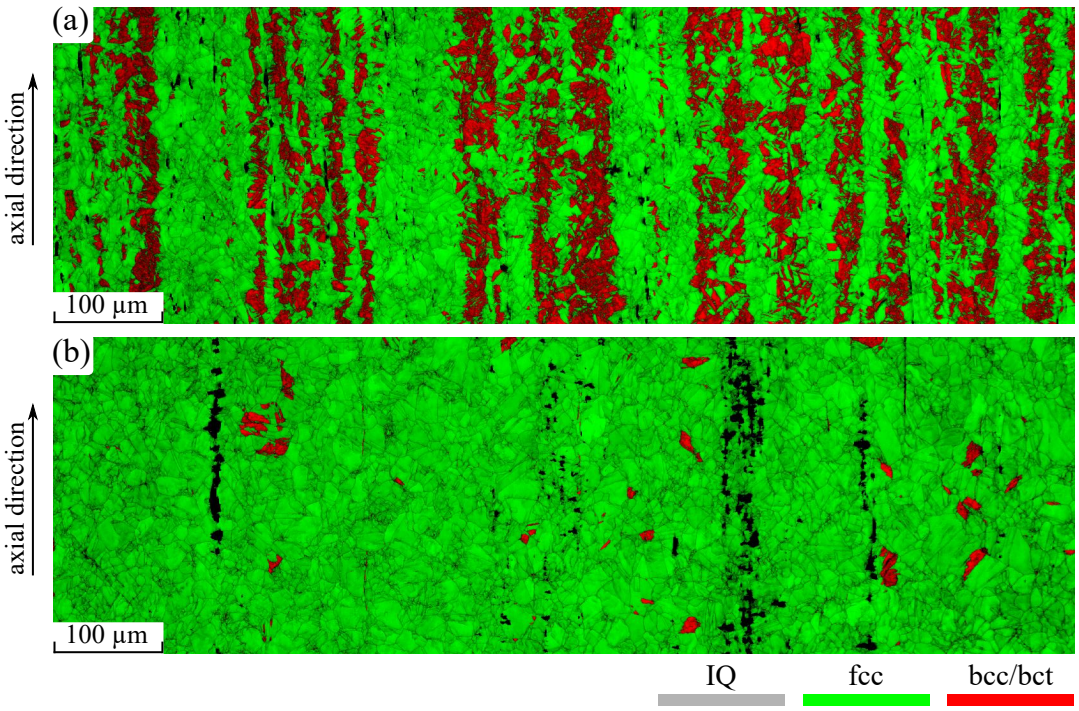

Fig. 95. EBSD phase map at the center of a longitudinal section of the fatigue specimen after isothermal fatigue test at 160 °C, ε_{at} = 0.51 %: a) after diamond suspension polishing followed by 5 seconds of electropolishing; b) after additional 200 seconds of electropolishing. Phase map (color) is overlaid with image quality (grayscale).

the EBSD pattern. The observed amount of martensite was close to 50 % (see Fig. 95a). After the sample was electropolished for additional 200 seconds, a significant reduction in martensite was observed (see Fig. 95b).

The EBSD analysis showed that the lower austenite stability after fatigue testing could be exposed by surface preparation and subsequently picked up by MFI. It is worth noting that MFI is not strongly affected by a surface layer of α' martensite. The reading of the ferrite fraction in Fig.72f is practically identical to the EBSD phase map after the extensive electropolishing in Fig. 95b, even though the MFI scan was performed on the surface shown in Fig. 95a.

8.2 Uniaxial magnetic balance reliability

Unlike the MFI measurements, the *in-situ* UMB measurements were not affected by surface preparation, as there was none. Slight lateral movement of the fatigue specimen should also not affect the UMB reading due to its design (see section 5.2). In addition, in total strain control tests there should be no significant change in specimen cross section that could effectively change the volume analyzed by the UMB. However, there were two contributions to the UMB measurements that were unrelated to the bulk Fe% reading:

- Microcrack network formation on the surface;

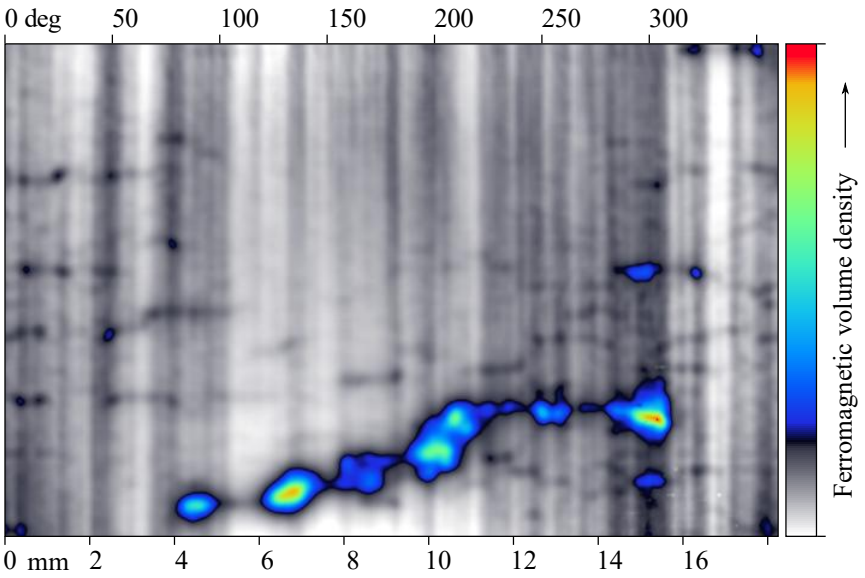

Fig. 96. 360° rotary MFI scan of the fatigue specimen after 15335 cycles IP TMF testing with $T_{ch} = 240\,°C$, $T_{cl} = 25\,°C$, $\varepsilon_{am} = 0.27\,\%$.

- Temperature drift of the UMB and the data acquisition equipment.

Repeated cooling and heating of the fatigue specimen in TMF testing inevitably leads to the formation of surface microcracks. These small cracks lead to stress concentration and act as nucleation sites for α' martensite. Since the UMB cannot distinguish between surface and volume α' martensite, it is possible that in TMF tests at $T_{ch} = 240$ and $320\,°C$ the main contribution to the MFI signal was from the microcracks on the surface. To investigate this possibility, a TMF test was performed with $T_{ch} = 240\,°C$, $T_{cl} = 25\,°C$ and $\varepsilon_{am} = 0.27\,\%$. The test was stopped by 50 % reduction in σ_{max}, which resulted in $1.53 \cdot 10^4$ cycles and a crack propagating 2 mm deep. To quantify the microcracks on the surface, a rotary MFI scan was performed on this specimen. The results are shown in Fig. 96. Due to the specifics of the material manufacturing, previously described in section 6, vertical (axial) lines are always present, even in the initial condition. All the horizontal lines in Fig. 96 correspond to the cracks on the surface. The large propagating crack can be identified at the bottom, with higher ferromagnetic content.

The UMB measurement of this test is shown in Fig. 97a. A steady increase in the UMB output was recorded that corresponds to $\Delta\xi_{fe} = 0.3$ Fe% before the crack propagation stage. The stress response showed cyclic softening in both compression and tension, as shown in Fig. 97b. The specimen was then cut in half for a planar MFI scan. The results are presented in Fig. 99, where in addition to the MFI scan, light micrographs were taken to measure the crack depth (Fig. 99c and e). Judging from the optical measurements, the most common length of small cracks was between 0.1 and 0.3 mm. The large crack was found to propagate to a depth of about 2 mm.

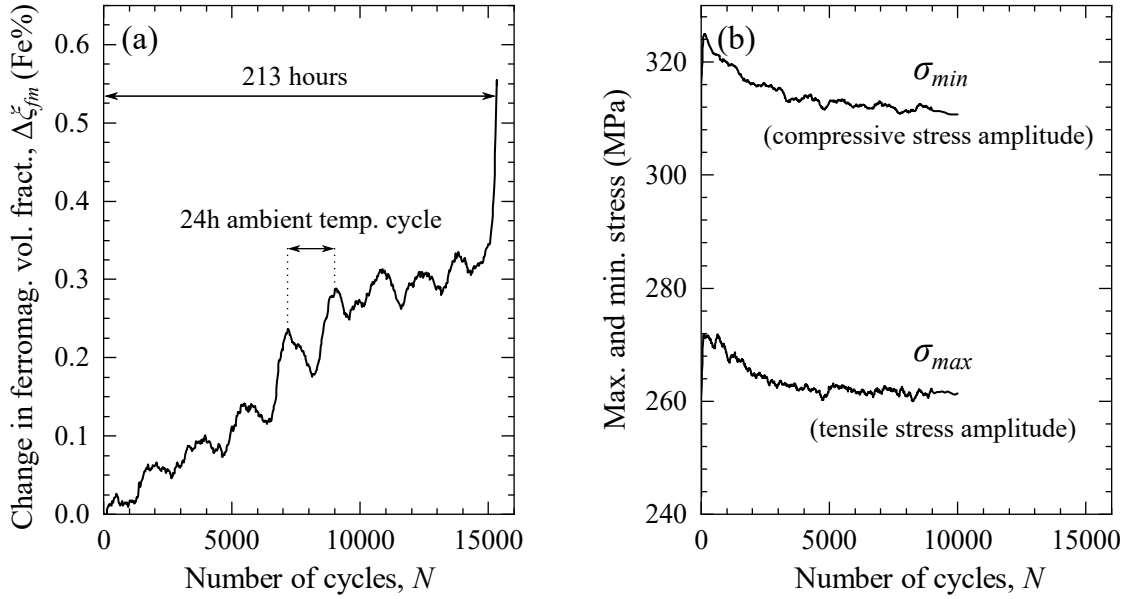

Fig. 97. In-phase TMF test with $T_{ch} = 240\,°C$, $T_{cl} = 25\,°C$ and $\varepsilon_{am} = 0.27\,\%$: a) change in ferromagnetic volume fraction measured with UMB-3; b) absolute values of maximum and minimum stress. Stress amplitude values after 10^4 cycles were lost due to a software error.

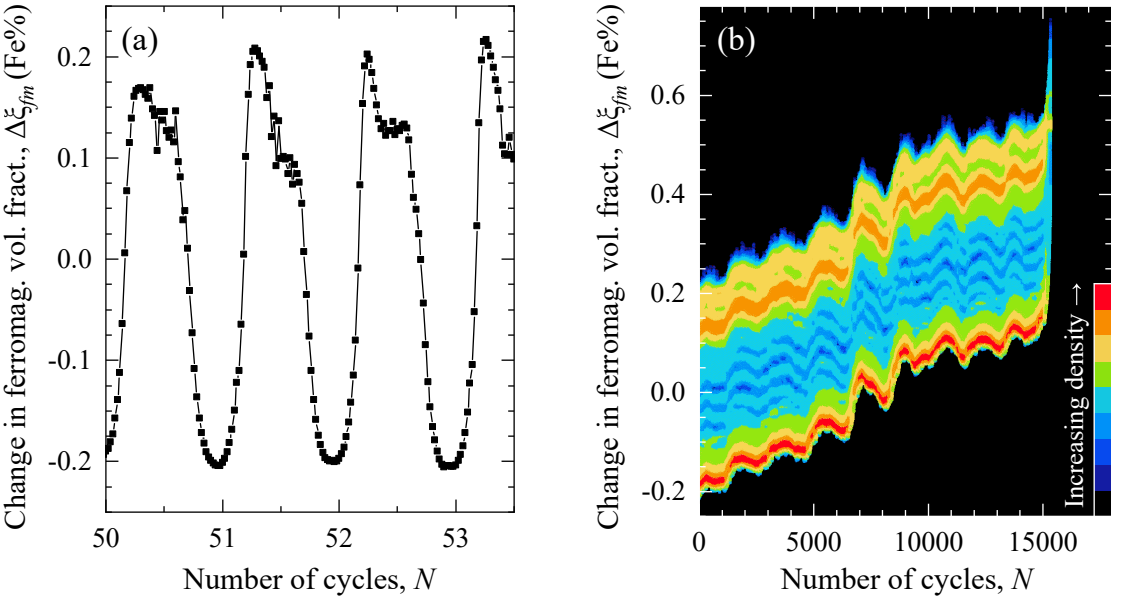

Fig. 98. The unprocessed signal from the UMB-3 *in-situ* measurement in Fig. 97a: a) individual cyclic fluctuations during TMF load; b) data point density plot for the entire test.

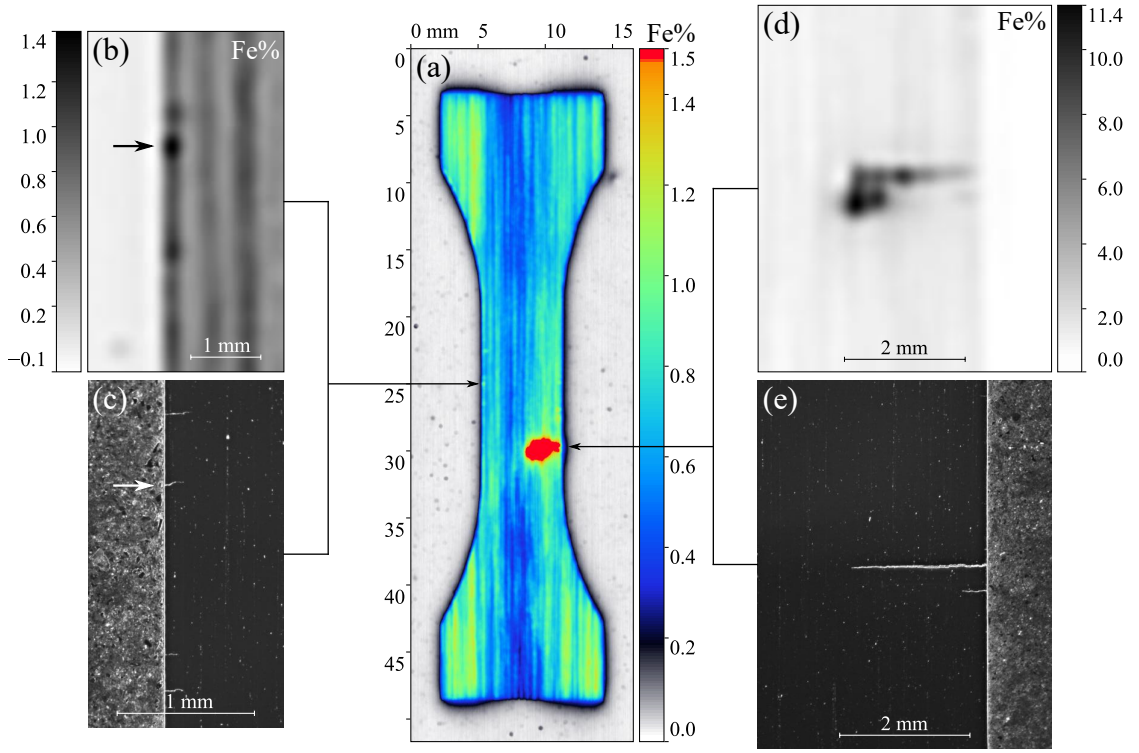

Fig. 99. Longitudinal section of the fatigue specimen shown in Fig. 96 (IP TMF test with $T_{ch} = 240\,°C$, $T_{cl} = 25\,°C$, $\varepsilon_{am} = 0.27\,\%$): a) ferromagnetic volume density map by MFI in Fe%; b) small cracks as scanned by MFI; c) light micrograph of the small cracks; d) propagating crack as imaged by MFI; e) light micrograph of the propagating crack.

From the information presented here, it can be concluded that the microcrack formation could dominate the UMB magnetic measurements in TMF tests, especially at high temperatures and low mechanical strain amplitude. While the temperature influence can be clearly identified by 24-hour cycles in the UMB signal, the overall trend did not follow the ambient temperature (see Fig. 100). Additional α' martensite formed on the surface may also explain the higher scatter in TMF tests (such as in Fig. 90 on page 141) compared to isothermal tests.

In-situ measurements with UMB-3 during TMF testing did have load-synchronous variations in the signal. These variations were then smoothed out by applying the running average to the raw signal. The unprocessed data from Fig. 97a and Fig. 100 can be found in Fig. 98. The main reason for the cyclic fluctuation of the UMB-3 signal is related to the cyclic change of temperature, magnetic field and displacement of the fatigue specimen.

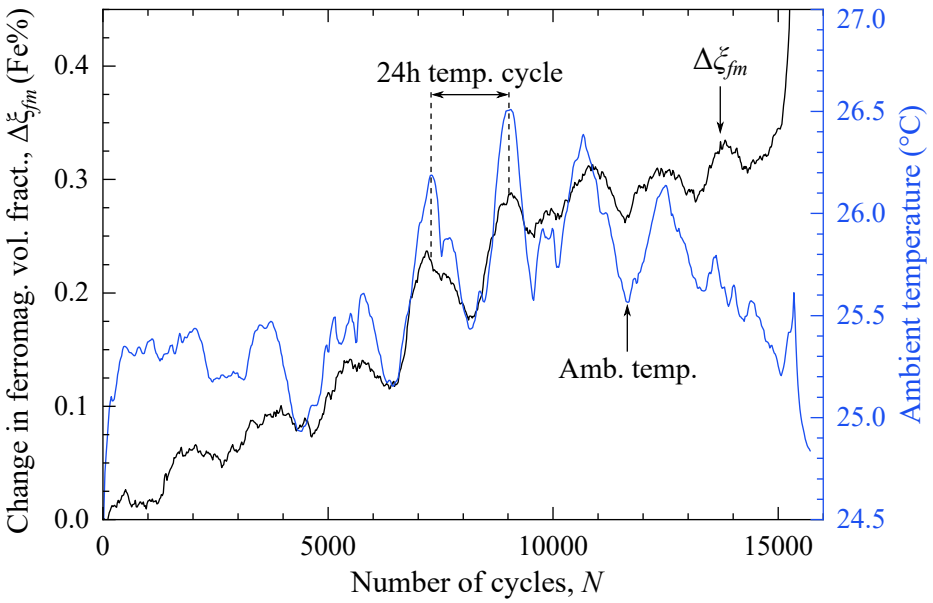

Fig. 100. Comparison of UMB output against ambient temperature during the IP TMF test with T_{ch} = 240 °C, T_{cl} = 25 °C, ε_{am} = 0.27 %.

8.3 Martensite in terms of ferrite content

Despite many EBSD and SEM measurements, it has not been possible to reliably determine the volume fraction of α' martensite that can be used as a reference for magnetic methods. The problem lies in the statistical significance of the information obtained by microscopy. The high magnification required to resolve micron-sized martensite often does not allow large areas to be examined. UMB measurements, on the other hand, cover the entire gauge volume of the fatigue specimen. The highly inhomogeneous distribution of α' martensite combined with the high probability of surface preparation induced martensite made microscopic examination problematic. Much more reliable results were achieved with δ ferrite calibration samples.

It is not uncommon to multiply the ferrite reading by about 1.7 to obtain α' martensite content [137]. However, this calibration was done for an eddy current instrument (Feritscope) and may not translate well to magnetic force measurements. EBSD investigations have shown that for a low martensite fraction (< 10 %), the ferrite readings of the MFI instrument are very comparable to the actual α' martensite fraction. Above 30 %, it is quite likely that some calibration coefficient is required. Since this work focuses mainly on small fractions of martensite, the ferrite reading can be cautiously assumed to be equal to the α' volume fraction.

9 TMF Testing Issues

9.1 Asymmetry between IP and OP thermal load

Results of thermo-mechanical tests in section 7.5 showed very consistent compressive mean stresses in out-of-phase loading, while in-phase tests always had tensile mean stresses. The reason for this behavior may be a reduction in yield strength at elevated temperatures or improper compensation for thermal expansion. To evaluate these two possibilities, the difference in σ_{max} and σ_{min} for two mechanical strain amplitudes of 0.42 % and 0.60 % can be compared in Fig. 101. As we can see, the difference between the two strain amplitudes remains very similar. Using the data in Fig. 67b on page 111, it is possible to calculate the reduction in yield strength that would occur at elevated temperatures. These data showed that the yield strength decreases by 0.245 MPa for every degree Celsius increase in temperature. Since the temperature difference between T_{ch} and T_{cl} is 215 °C, the resulting difference in yield strength can be calculated to be 53 MPa. This value is very similar to the difference in σ_{max} and σ_{min} and the difference in stress amplitudes between IP and OP tests in Fig. 101. Therefore, it is reasonable to assume that the differences observed between IP and OP tests are due to the different mechanical properties at elevated temperatures rather than improper thermal strain compensation.

The differences observed in IP and OP tests were not only in the stress amplitude. All TMF tests were programmed to switch between heating and cooling at $\sigma = 0$. The advantage of this approach is a much more symmetric stress-temperature function, such as shown in Fig. 102. The disadvantage is

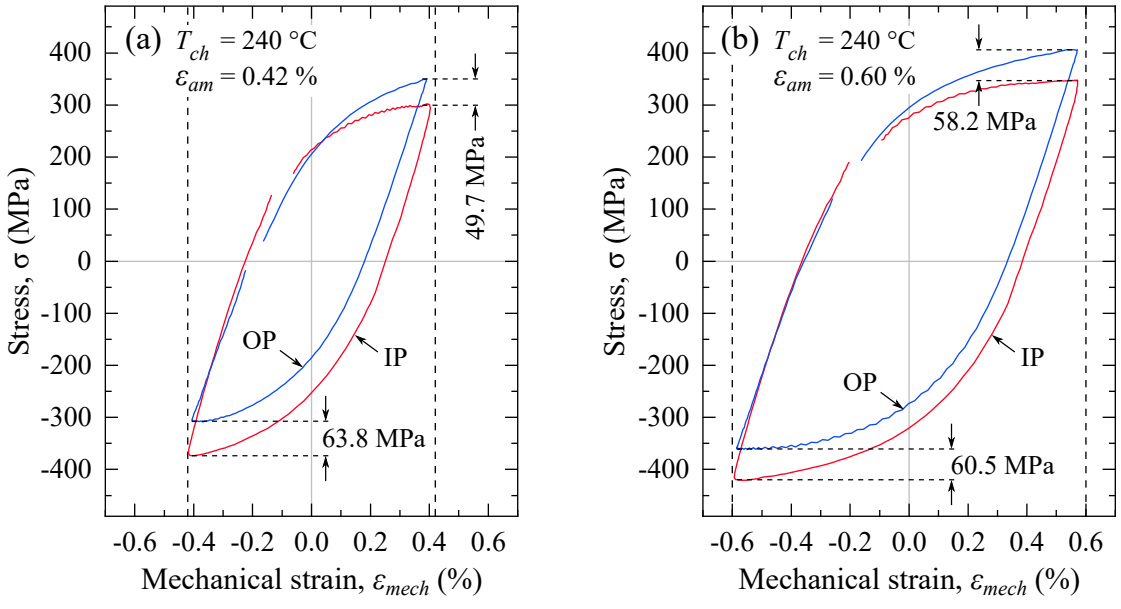

Fig. 101. Comparison of ε_{am} = 0.42 % (a) with ε_{am} = 0.60 % (b) in IP and OP TMF tests at N =10, T_{ch} = 240 °C, T_{cl} = 25 °C.

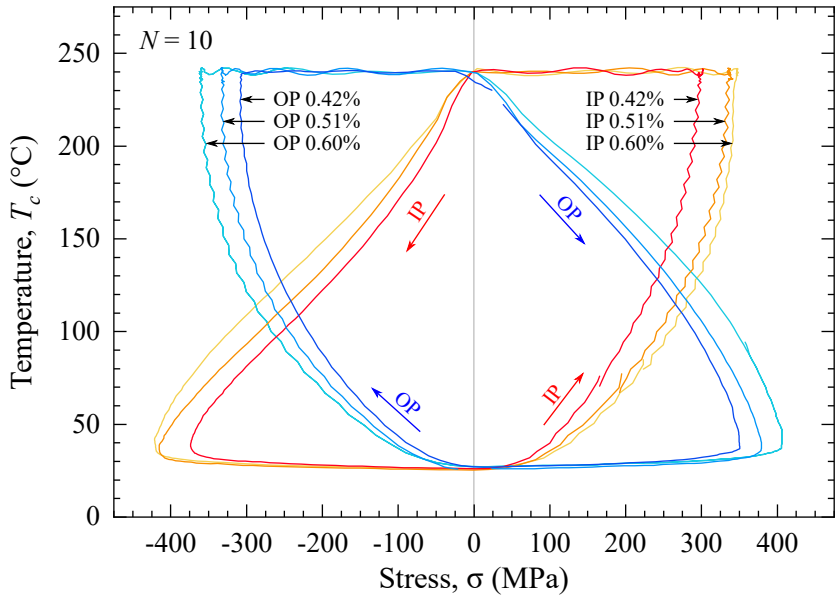

Fig. 102. Stress-temperature hystereses for various strain amplitudes, IP and OP, at $N = 10$, $T_{ch} = 240\,°C$, $T_{cl} = 25\,°C$.

a strain-amplitude-dependent phase shift between the strain and the temperature. This phenomenon can be illustrated by Fig. 103, which compares TMF tests from the same temperature range, $T_{ch} = 240\,°C$ and $T_{cl} = 25\,°C$. Since the heating in all IP tests (Fig. 103a, b, c) is triggered at the beginning of the test, there is no shift between strain and temperature. In OP tests (Fig. 103d, e, f), the heating was initiated at the end of each cycle, which resulted in a shift between temperature and strain, proportional to the plastic strain amplitude. However, thanks to the trapezoidal temperature curve, ε_{max} and ε_{min} always corresponded to the same high temperature T_{ch}. This was also true when tested at different temperatures, as shown in Fig. 76 on page 124.

9.2 Contribution of oxidation to TMF tests

When austenitic stainless steel is exposed to high enough temperatures, the affinity of chromium for carbon increases, resulting in the formation of chromium carbides $Cr_{23}C_6$ [216–218]. This process leaves less amount of chromium to suppress the oxidation of the steel. The thin layer of chromium oxide $Cr_{23}O_3$ that protects stainless steel from the environment is depleted and iron oxides (Fe_xO_y) form on the surface [219, 220]. Iron oxides can potentially be ferromagnetic and contribute to the observed kinetics of strain induced martensite. For this reason, the extent of oxidation is briefly discussed in this section.

Choi et al. [221] investigated the thickness of the oxide layer formed under isothermal fatigue conditions in air in a niobium-stabilized 316 stainless steel. They measured 0.54 μm iron oxide layer after the 800 °C test and only 0.1 μm after 600 °C test. No oxides were found below 400 °C. Oxide films

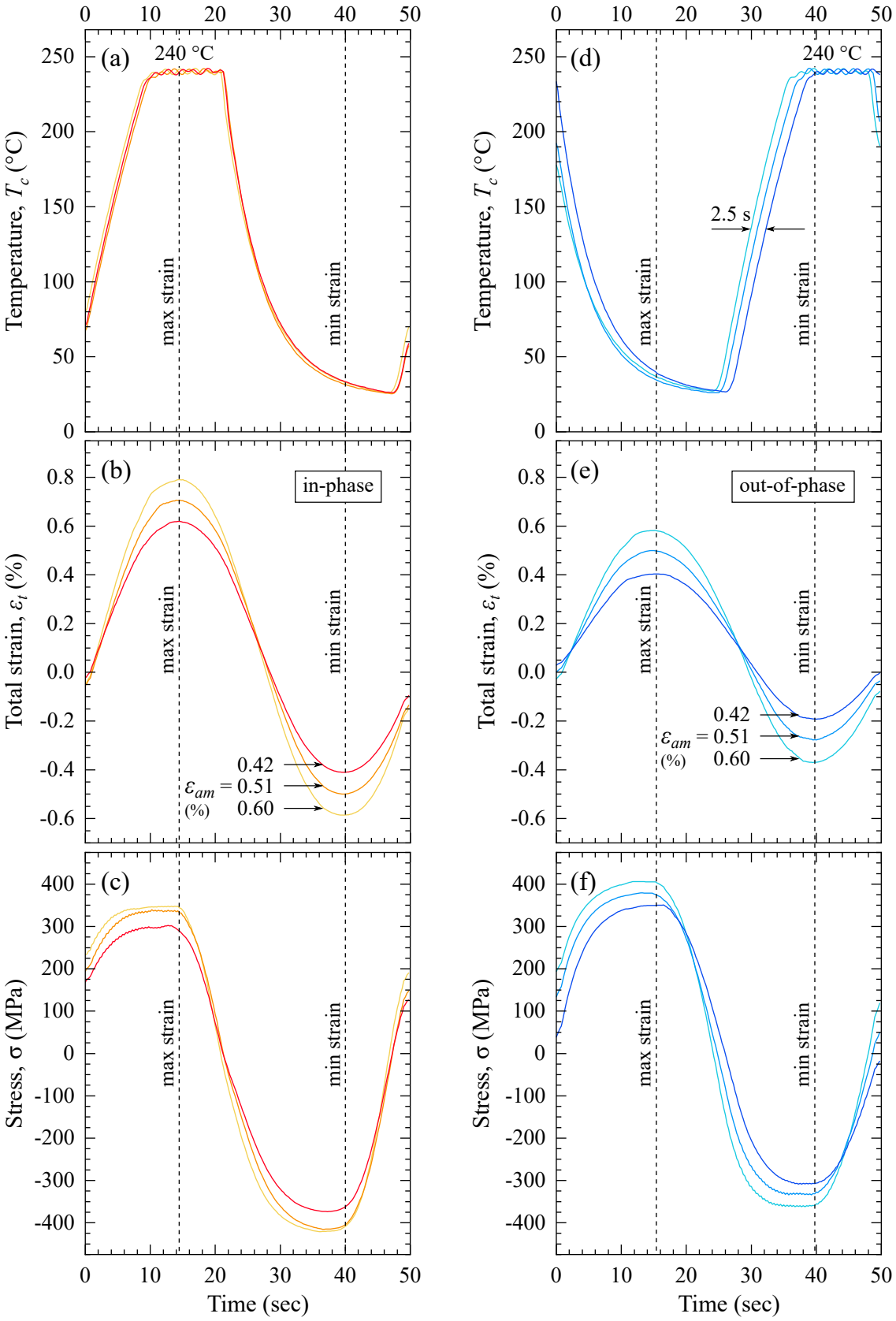

Fig. 103. One thermo-mechanical cycle at $N = 10$ and $T_{ch} = 240$ °C for different strain amplitudes in a time-domain format: (a, b, c) in-phase; (d, e, f) out-of-phase; (a, d) temperature at the center of fatigue specimen; (b, e) total strain, including thermal and mechanical components; (c, f) nominal stress, as measured by the load cell.

formed under pressurized water reactor conditions can be quite different due to the different chemistry [222].

In this work, the gauge length of the fatigue specimens was painted with a silicone based Duplicolor Supertherm paint that is heat resistant up to 800 °C. The paint was needed primarily to increase the emissivity of the surface for proper infrared temperature measurements. In addition, the paint served as a protection against oxidation. Considering that the highest temperature reached in this work did not exceed 320 °C, the effects of oxidation can be neglected. Indirect evidence for the absence of oxidation effects on magnetic measurements can also be found on the fracture surface. The exposed fracture surface in isothermal fatigue tests was ferromagnetic only at low temperatures. Above 200 °C, where oxidation is more likely, no additional ferromagnetic material was found by MFI analysis (see Fig. 73 on page 118).

9.3 Dynamic strain aging

As described by Beukel [223], the motion of a dislocation in the slip plane is generally a discontinuous process. The dislocation encounters obstacles that must be passed, possibly with thermal activation. The dislocation segment has to wait for the obstacle to be passed and, after passing, it jumps to the next obstacle at high speed. In solid solutions, diffusion of solute atoms to the dislocations can occur during this waiting time. This process is called dynamic strain aging (DSA).

DSA can be recognized by the Portevin-Le Chatelier effect, i.e., by a serrated or discontinuous stress-strain curve [224]. Such serrated stress-strain curves could be identified in many TMF tests. However, it is not trivial to estimate the influence of the two PID controllers controlling strain and temperature. Therefore, isothermal testing is more appropriate to look for the Portevin-Le Chatelier effect, as the lack of temperature variation should minimize strain control error. Fig. 104 shows stress and strain of an isothermal test performed at 320 °C. As strain approached maximum, discontinuity of the stress curve appeared to increase. These discontinuities in both tensile and compressive stresses most closely resemble serration type B [224]. This can be compared with the results from Hong et al. [225], who identified DSA for 316 stainless steel to be in the range of 250–550 °C at a strain rate of $1{\cdot}10^{-4}$. This range fits the data in Fig. 104. Microstructural observations made by Karlen et al. [226] in 316 NG steel showed the formation of cellular structure, which was the result of mutual annihilation of dislocations and the reorganization of remaining dislocations into a lower energy structure. In accordance with DSA theory, the interaction between solute atoms and dislocations limits motion of

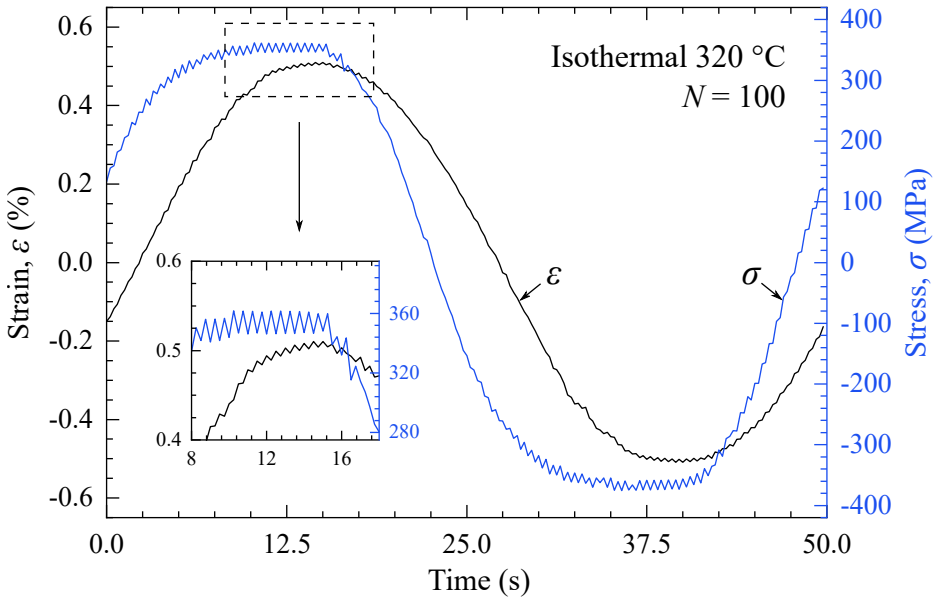

Fig. 104. Stress and strain in the isothermal fatigue test at 320 °C, $\varepsilon_{at} = 0.51\,\%$, $N = 100$, possibly showing the Portevin-Le Chatelier effect.

dislocation by pinning. This produces planar slip, which manifests as a linear microstructure [226, 227]. Such a cellular microstructure was also found in the present work (see Fig. 108 and 109).

9.4 Heating and cooling radial depths

When heating and cooling of the fatigue specimen is done too quickly, it may generate radial stresses due to uneven thermal strain. Since the heating was done by passing the low frequency 50 Hz alternating current through the specimen, it can be assumed that there was no radial temperature gradient in the heating stage. At the same time, compressed air cooling may have resulted in lower temperatures on the surface than in the center of the specimen. To investigate this possibility, a TMF test was performed at a frequency of 0.01 Hz, which is half the frequency at which TMF tests were performed in section 7.5.

From the results shown in Fig. 105, one can observe an increase in the amount of deformation-induced martensite for the 0.01 Hz test. It was previously shown in section 8.2 that TMF tests generate microcracks that can contribute to the martensite measurement. However, in the case of the 0.01 Hz test, the stress amplitude also increased, which is unlikely for the increased microcrack density. Fig. 105c shows that the low temperature remained fairly constant for the entire duration of the test with 23 °C and 26 °C for 0.01 Hz and 0.02 Hz, respectively. The temperature drop of 3 °C for the 0.01 Hz test seemingly resulted in a 20 MPa increase in stress amplitude. Most of the difference in stress amplitude came from the cold part of the cycle, as shown in Fig. 106. Therefore, it is reasonable to assume that the 3 °C difference at the

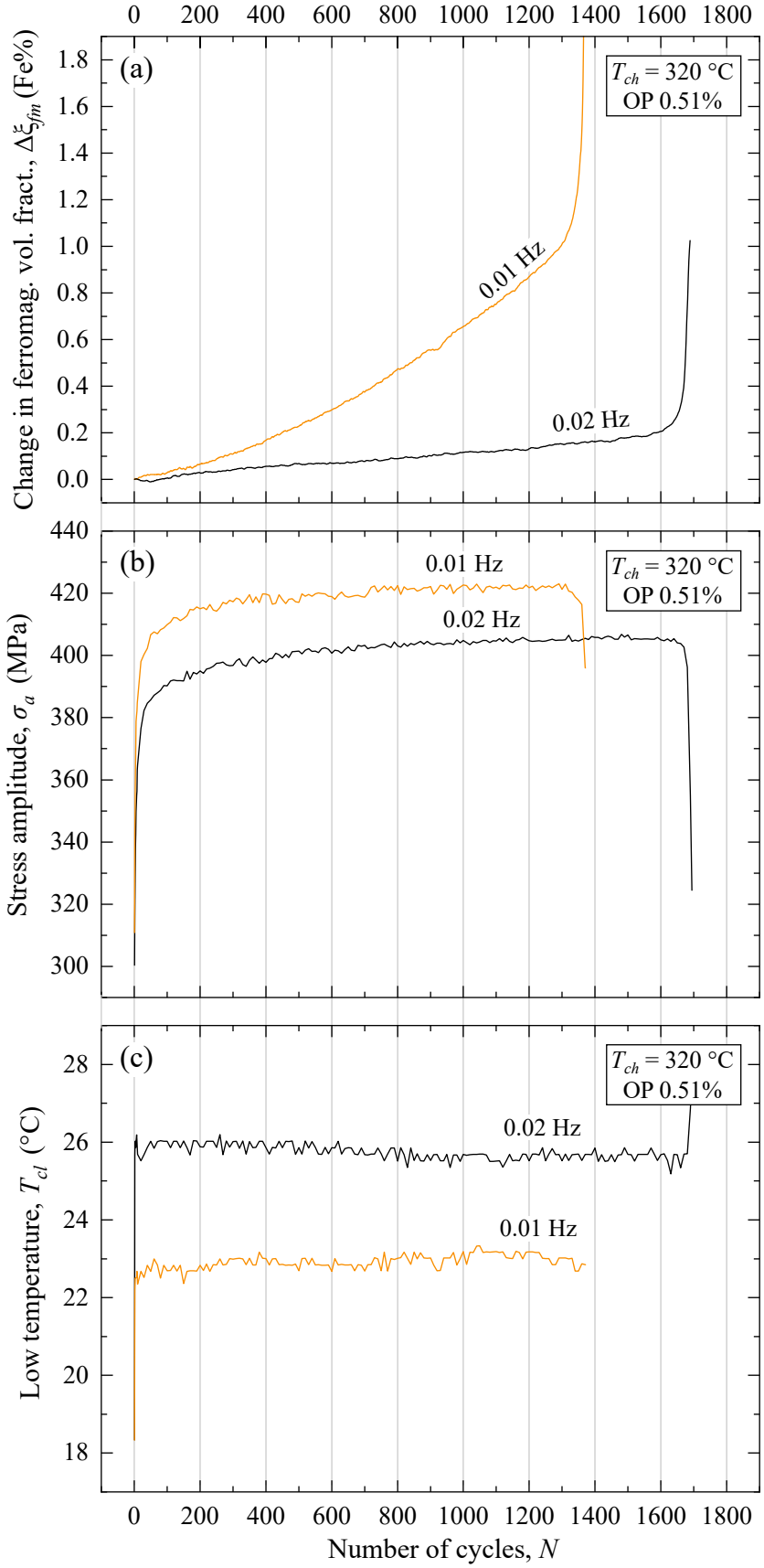

Fig. 105. Comparison of 0.01 Hz and 0.02 Hz OP TMF tests at T_{ch} = 320 °C: a) change in ferromagnetic volume fraction in Fe%, recorded with UMB-3; b) stress amplitude; c) lowest temperature at the center of the gauge length within one cycle.

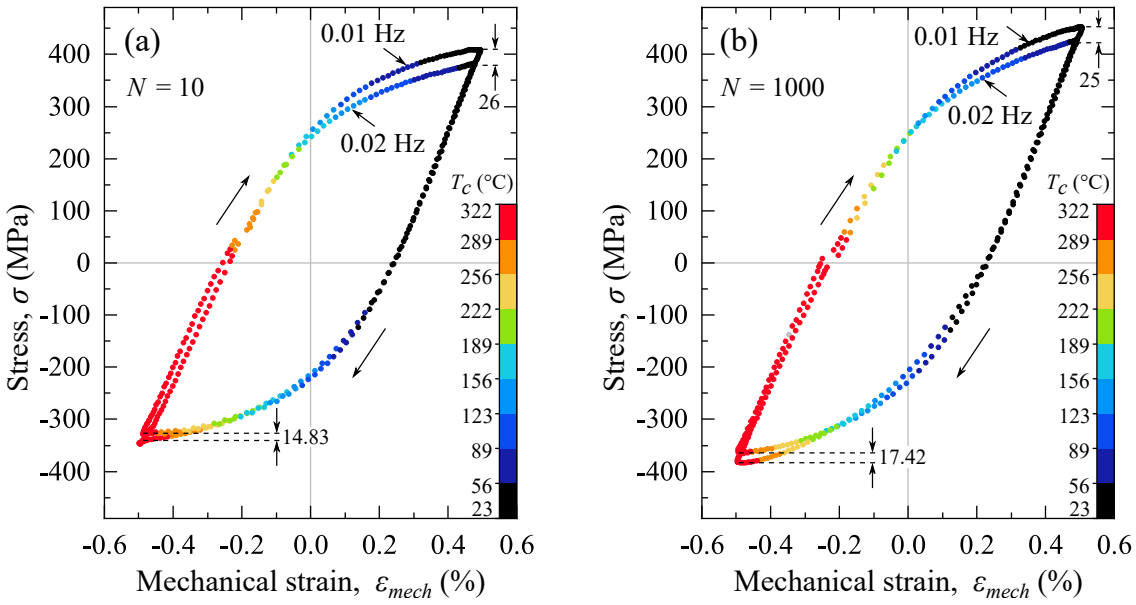

Fig. 106. Stress-strain hysteresis loop comparison of 0.01 Hz and 0.02 Hz OP TMF tests: a) at $N = 10$; b) at $N = 1000$.

center of the gauge length was accompanied by a higher temperature change at the shoulders where the extensometer blades were connected.

The temperature gradient in the axial direction is inevitable and directly proportional to the cross-section and the distance from the center. Fig. 107 shows the evolution of the temperature at the shoulders of the fatigue specimen in an OP TMF test at $N = 400$ and $T_{ch} = 320\,°C$. In the cooling cycle, the upper part of the specimen remained warmer than the center and the lower part remained colder than the center. This is due to the fact that the air nozzle was placed at the bottom of the specimen, where temperatures could drop to about 12 °C. The coldest temperature in the upper part typically remained above the ambient temperature, at around 37 °C. Despite this temperature gradient, MFI investigations in section 7.5 found no difference in α' martensite content between the upper and lower parts of the specimen.

9.5 Microstructural differences

Experimental results in section 7.5 have shown a clear difference in the rate of α' martensite formation between IP and OP TMF load. However, from the microstructural point-of-view no significant difference was found. For the comparison, two specimens that went through a TMF test with $T_{ch} = 320\,°C$, $T_{cl} = 27\,°C$, and $\varepsilon_{am} = 0.51\,\%$ were cut with EDM in the axial direction. The sample was then embedded in a conductive resin, ground, polished with diamond suspension, and finally electropolished for 3 minutes. The SEM study was performed at the center of the gauge length and is presented in Fig. 108 and 109. From backscatter SEM images (Fig. 108a and 109a), a fairly large de-

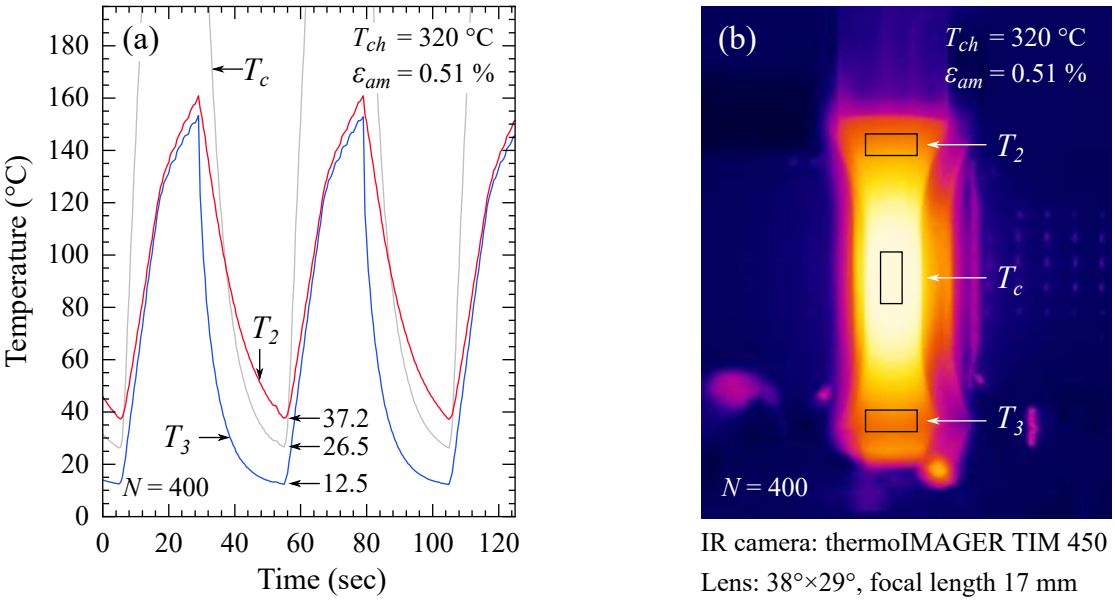

Fig. 107. Variation of temperature across the gauge length in a TMF test at $N = 400$, $T_{ch} = 320\,°C$, $T_{cl} = 27\,°C$.

formation in austenite around α' martensite could be identified in both IP and OP cases. A cellular structure could be identified after IP and OP tests by PRIAS imaging[13]. However, it appeared to be more pronounced in the IP specimen.

A TEM investigation performed by Srinivasan et al. [229] on 316 steel after 300 °C isothermal fatigue testing showed that dislocations were spaced widely in co-planar slip bands. Srinivasan pointed out that the rearrangement of dislocations into the cell configuration results in a larger mean free path for dislocations and a net decrease in dislocation density, which contributes to cyclic softening. However, in the present work, isothermal tests did not show cyclic softening at any temperatures (see Fig. 69). Similar results were presented by Nagesha et al. [230], who reported that 316L steel exhibited an initial hardening during the first 70–100 cycles, followed by a well-defined saturation that persisted until the onset of crack initiation.

Fatigue life observed in TMF tests in section 7.5 was shorter for IP load. Kumar et al. [231] pointed out that under IP TMF conditions there can be an increase in dislocation pile-up which also promoted multiple cracking, resulting in a lower fatigue life. More information on the microstructure of austenitic stainless steels under various fatigue loads can be found in other reactor safety research projects [232–242]. These projects were mainly focused on the direct fatigue life evaluation, which was not the primary objective of this work. Fatigue life results from this thesis are listed in Appendix D.

[13] Pattern Region of Interest Analysis System (PRIAS) is a method where the EBSD camera and phosphor screen are used simultaneously as both an EBSD pattern collection detector and an array of positional electron detectors. PRIAS can be used to show orientation, atomic number, and topographic contrast [228].

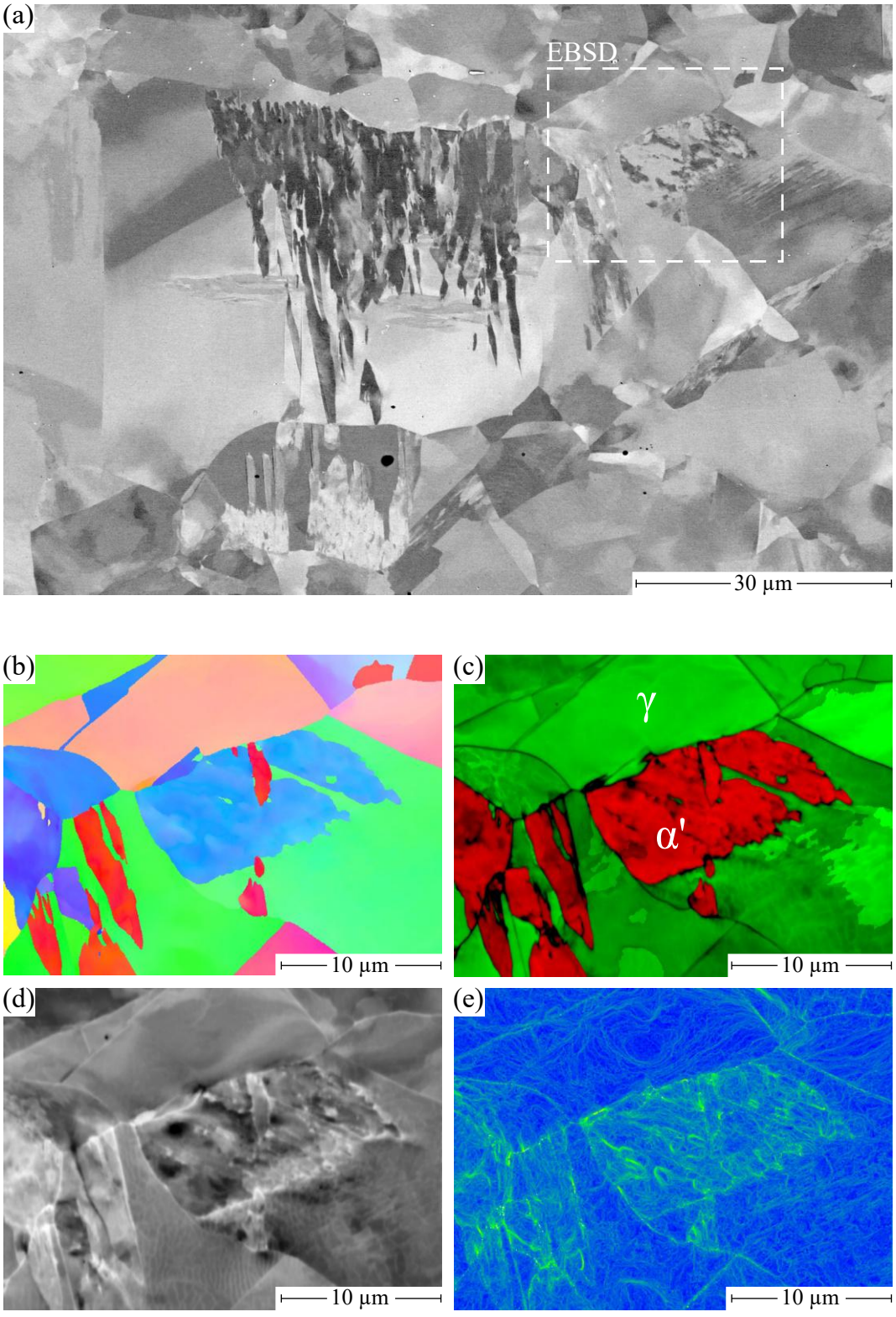

Fig. 108. Microstructure at the center of the fatigue specimen's transverse section, IP, T_{ch} = 320 °C, T_{cl} = 27 °C, ε_{am} = 0.51 %: a) backscatter SEM image; b) inverse pole figure; c) phase map (color) overlaid with image quality map (grayscale); d) Pattern Region of Interest Analysis System (PRIAS); e) kernel average misorientation. Final surface preparation: 1 μm diamond suspension polishing followed by 3 minutes electropolishing. Material: 347 Batch B.

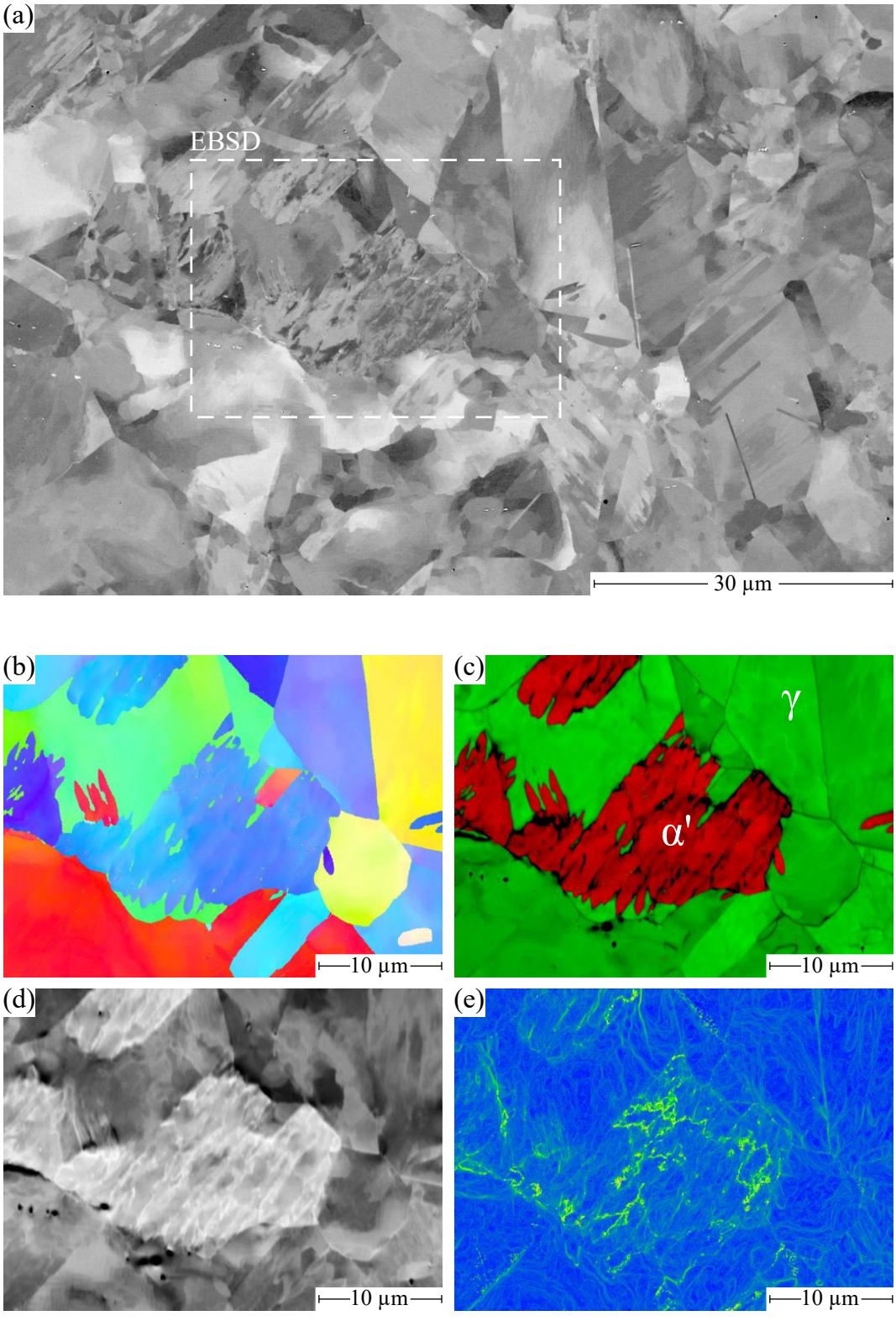

Fig. 109. Microstructure at the center of the fatigue specimen's transverse section, OP, T_{ch} = 320 °C, T_{cl} = 27 °C, ε_{am} = 0.51 %: a) backscatter SEM image; b) inverse pole figure; c) phase map (color) overlaid with image quality map (grayscale); d) Pattern Region of Interest Analysis System (PRIAS); e) kernel average misorientation. Final surface preparation: 1 μm diamond suspension polishing followed by 3 minutes electropolishing. Material: 347 Batch B.

10 Summary

METHODS

5.1 Magnetic Force Imaging (MFI) is a technique for spatially resolved characterization of magnetic susceptibility of the material. It is based on the force measurement between the material and a miniature NdFeB magnet. In austenitic stainless steel, it can visualize the distribution and density of any ferromagnetic phase, including α' martensite. The force-sensitivity is sufficient to analyze pure austenite samples. The spatial resolution was close to 0.3 mm. The output was calibrated in terms of magnetic permeability and ferrite volume fraction.

5.2 Uniaxial Magnetic Balance (UMB) is an instrument that allows for a non-contact measurement of magnetic susceptibility. It is based on the measurement of the force between two magnets balanced by a set of adjustable ferromagnetic rods. It was used for *in-situ* characterization of $\gamma \rightarrow \alpha'$ phase transformation.

5.3 Thermo-mechanical fatigue testing rig was built on the basis of a servo-hydraulic fatigue machine. The heating was realized by passing the current at 50 Hz frequency directly through the specimen. The forced cooling was done by compressed air. The temperature was measured with a pyrometer from the painted surface of the fatigue specimen.

5.4 Balanced Core Magnetometer (BCM) is a prototype handheld instrument for non-destructive testing. It measures not only the magnetic susceptibility but also the coercivity of the material. This provides additional information on the microstructural characteristics of deformation induced martensite. It is based on the measurement of the force between the electromagnet and the material. The magnetic field can be controlled with the field coil while the force response from the core is recorded. In this work, it was not used to obtain experimental results because it was designed for large objects, such as pipes, and not for fatigue specimens.

6 Material and Geometry AISI 347 (1.4550, X6CrNiNb18-10) was the material under investigation. It was produced by continuous casting to a square cross-section using an electromagnetic stirring device. The square cross-section was hot rolled into a circular cross-section and followed by treatment at 1060 °C. The resulting microstructure was ≥ 99 % austenite with variations in grain size

and chemical composition that formed longitudinal bands. Magnetic measurements showed 0.15 Fe% to 0.34 Fe% variation of ferromagnetic material within 3 mm radius from the center. At larger distance from the center, there was higher ferromagnetic volume density up to 1 Fe%.

RESULTS

7.1 Lower accumulated strain limit for phase transformation was investigated by means of *in-situ* magnetic and electrical resistance measurements. The results showed that in the scope of strain increase tests, first $\gamma \rightarrow \alpha'$ transformation at room temperature was detected at total strain amplitude of 0.10 % to 0.11 %. This initial phase transformation was initiated inside the fatigue specimen (at the center), forming a thin longitudinal α' band. If at room temperature, the strain amplitude ε_{at} of 0.12 % was sufficient to reach 0.25 Fe%, at 160 °C it was 0.17 %. Tests at 240 °C resulted in the specimen failure before 0.25 Fe% threshold could be reached. Electrical resistance measurements at room temperature detected initial drop at ε_{at} = 0.09 % that changed to an increase at ε_{at} = 0.16 %.

7.2 Martensite morphology and magnetic properties were investigated in a series of fatigue tests with different strain amplitudes. The tests were stopped when α' volume fraction reached 5 %. A much higher number of cycles was required to achieve 5 % martensite at low strain amplitude. The martensite that formed under these high-cycle fatigue (HCF) conditions had a larger portion of very fine α' martensite. Magnetic measurements with a vibrating sample magnetometer showed a much higher coercivity in the HCF regime. Fatigue tests at higher strain amplitude reached 5 % vol. fraction in low-cycle fatigue (LCF) regime. The resulting α' microstructure was more coarse with a distinct longitudinal band structure. Martensite that formed under LCF conditions accumulated primarily in one longitudinal band at the center of the specimen, whereas in the HCF regime, α' martensite was distributed more homogeneously throughout the gauge length.

7.3 Influence of strain on phase transformation kinetics was examined in a series of ambient temperature fatigue tests with a constant strain rate of 0.004 s^{-1}. Constant strain amplitude tests were in the range $0.14 \leq \varepsilon_{at} \leq 1$ (%). *In-situ* magnetic measurements revealed a clear trend between the strain amplitude and the rate of $\gamma \rightarrow \alpha'$ phase transformation. To simplify the analysis, two linear ranges were selected: LR1 represents the highest phase transformation rate at the beginning of the test and LR2 represents the slowest transformation

rate at the end of the test. The rate of phase transformation in LR1 and LR2 follows the following equation:

$$\frac{\partial \xi_{fm}}{\partial N}(\varepsilon_{at}) = a \cdot \varepsilon_{at}^{b \cdot \varepsilon_{at}^{-c}}$$

The number of cycles to reach the peak transformation rate N_p could also be expressed by a similar equation

$$\varepsilon_{at} = a \cdot N_p^{b \cdot N_p^{-c}}$$

using appropriate fit parameters a, b, and c. The difference between LR1 and LR2 was the highest at low strain amplitude and the lowest at the high strain amplitude.

7.4 Influence of temperature on phase transformation kinetics was investigated in a series of isothermal constant amplitude fatigue tests with $\varepsilon_{at} = 0.5\,\%$ in the temperature range between $17 \leq T_c \leq 320$ (°C). The maximum rate of phase transformation (LR1) fitted fairly well by an exponential function

$$\frac{\partial \xi_{fm}}{\partial N}(T_c) = k \cdot m^{T_c}$$

with appropriate fitting parameters k and m. At the temperature of 240 °C and above, the amount of deformation induced martensite dropped below what could be confidently resolved by UMB. When the 240 °C and 320 °C fatigue specimens were scanned with MFI after fatigue testing, the results showed that an additional 0.1 to 0.2 Fe% may be present at the gauge length, compared to the specimen shoulders. At 200 °C and below, there was a confident detection of α' martensite by both UMB and MFI. The distribution of α' martensite was fairly homogeneous along the gauge length at room temperate, but was pushed to the surface as the temperature increased.

7.5 Kinetics of thermo-mechanical $\gamma \rightarrow \alpha'$ phase transformation was tested under in-phase (IP) and out-of-phase (OP) thermal loads, where the low temperature T_{cl} was always the same (around 25 °C) and the high temperature T_{ch} was varied from test to test. In thermo-mechanical fatigue (TMF) tests, the rate of $\gamma \rightarrow \alpha'$ transformation was always higher than the one in isothermal tests. The largest difference in the phase transformation rate between TMF and isothermal tests was observed at lower temperatures ($T_{ch} = 160\,°C$). In TMF tests at $T_{ch} = 320\,°C$, very little α' martensite could be found in the bulk of the material. However, all microcracks and fracture surfaces were highly

ferromagnetic. This was not the case for any isothermal tests above 160 °C. The difference between IP and OP tests was the most significant at lower T_{ch} temperatures and minimal at high T_{ch} temperatures. Overall, a higher transformation rate was observed in OP tests compared to IP tests. The density of α' martensite was always minimal at the center of the gauge length. Quite often α' martensite would form diagonally, on the opposite sides of the specimen, where the diameter begins to increase.

7.6 Mathematical extrapolation of experimental data allowed to predict the kinetics of $\gamma \rightarrow \alpha'$ phase transformation in the strain-amplitude-temperature combinations that were never tested experimentally. By using the equations described in sections 7.3 and 7.4, equivalent transformation rate curve was established. It equates the rate of phase transformation between room temperature tests (constant temperature, variable strain amplitude) and elevated temperature tests (constant strain amplitude, variable temperature). Equivalent transformation rate curve can translate temperature into strain amplitude and show what the combination of strain and temperature should be to initiate phase transformation. The initial changes in the material microstructure, detected with electrical resistance measurements, occurred at ε_{at} = 0.08 %. According to the equivalent transformation rate curve, 0.08 % corresponds to 240 °C, which was also found to be the most likely candidate to be M_d temperature, above which no $\gamma \rightarrow \alpha'$ transformation should occur.

DISCUSSION

8.1 Magnetic force imaging reliability primarily depends on the constant working distance d_w and deformation-free surface preparation. The curvature of MFI samples was measured and its contribution was calculated to be negligible. Martensite induced by surface preparation, however, was detected by electron backscatter diffraction. This means that in MFI scans of 240 °C and 320 °C tests, an increase of 0.1 to 0.2 Fe% in the gauge length possibly comes from the combination of lower austenite stability after plastic deformation that was exposed by mechanical surface preparation.

8.2 Uniaxial magnetic balance reliability is influenced by formation of highly ferromagnetic microcracks on the surface in the cooling phase of TMF tests and temperature drift of the signal. It is likely that majority of UMB signal is dominated by microcracks in TMF tests with T_{ch} of 240 °C and 320 °C. The drift of the UMB signal was found to be negligible.

8.3 Martensite in terms of ferrite content was the only reliable way to calibrate magnetic instruments. Since the results of EBSD and magnetic measurements were within the margin of error, the ferrite value can be cautiously assumed to be equal to the α' volume fraction.

9.1 Asymmetry between IP and OP thermal load was detected in a form of different tensile and compressive stresses for the same mechanical strain amplitude. Using the experimentally measured reduction in yield strength as a function of temperature, the difference between IP and OP stress amplitudes was found to be very close to that expected from softening at elevated temperature.

9.2 Contribution of oxidation to TMF tests could result in an accelerated growth of microcracks and increased UMB reading of ferromagnetic volume fraction. According to the available literature, even at the highest temperature of 320 °C achieved in this work, oxidation of austenitic steel should be minimal. Moreover, all fatigue specimens were painted with a silicone based high temperature paint, which should reduce the oxidation effects even further.

9.3 Dynamic strain aging was detected by discontinuities in the stress-strain curve, also known as Portevin-Le Chatelier effect. The literature suggests that it is quite possible to occur under the given set of test conditions. However, from a purely experimental point of view, it was not possible to completely exclude the influence of the PID controllers, which adjust the strain and temperature in real time and can also produce some serrations in the stress-strain curve.

9.4 Heating and cooling radial depths were evaluated by performing a TMF test at half the frequency (0.01 Hz instead of 0.02 Hz). The low temperature T_{ch} of 0.01 Hz test was only 3 °C lower than that of 0.02 Hz. This likely indicates that 0.02 Hz provides sufficient cooling time for the bulk and surface temperatures to equalize. However, the stress amplitude was 20 MPa higher for 0.01 Hz test and the rate of phase transformation was notably higher too. The radial temperature difference due to heating is likely to be minimal.

9.5 Microstructural differences between IP and OP tests were found to be minimal, despite quite different stress response and phase transformation rate of the material. In both cases, a cellular structure was identified that is likely to be formed by dislocation pile-up.

11 Conclusions and Outlook

By implementing novel magnetic measurement techniques, such as magnetic force imaging and uniaxial magnetic balance, valuable information was obtained about the kinetics of $\gamma \rightarrow \alpha'$ phase transformation. The conditions, under which the AISI 347 was tested, were aimed to simulate the start-up and cool-down cycles of a nuclear powerplant. In the course of this work, the following questions were answered:

What are the dynamics of $\gamma \rightarrow \alpha'$ transformation at elevated temperatures in a low-cycle fatigue regime?

The results showed exponential decrease of the transformation rate by five orders of magnitude as temperature changed from ambient to 320 °C. This temperature-dependent transition from high transformation rate to low transformation rate occurred in a continuous manner. From mathematical point-of-view, the rate of transformation never reached zero as the temperature increased. The decelerated period in $\gamma \rightarrow \alpha'$ transformation was significantly delayed at elevated temperatures, resulting in specimen failure before the peak transformation rate was reached.

What is the lower accumulated strain limit for the phase transformation, below which no phase transformation should occur at a given temperature?

Below the total strain amplitude ε_{at} of 0.10 % no phase transformation was detected with magnetic methods at room temperature in low-cycle fatigue conditions. The electrical resistance measurement showed an initial increase in conductivity at 0.09 %, which changed to a decrease at 0.16 %. After analyzing the mathematical model, there appeared to be a connection between the initial increase in conductivity and M_d temperature (above which no phase transformation should occur, theoretically). It would appear that for $\varepsilon_{at} \leq 0.08$ % no phase transformation should take place at ambient temperature in the low cycle fatigue regime.

Can deformation-induced martensite morphology be different in low-cycle fatigue and high-cycle fatigue?

Experiments showed that magnetic coercivity was higher for the given volume fraction of α' martensite in high-cycle fatigue tests. After microstructural investigation it was found that large number of cycles at low strain amplitude results in a larger portion of very fine α' martensite. On the other hand, higher strain amplitude and low number of cycles resulted in coarser martensite that formed much less homogeneously compared to the low strain amplitude.

How do the magnetic properties of austenitic stainless steel change after TMF loading, similar to that of the start-stop cycle of a power-plant?

It was found that the kinetics of $\gamma \rightarrow \alpha'$ transformation under TMF cycles between ambient and elevated temperature are more similar to those of constant elevated temperature, rather than ambient. In other words, the half of the cycle at elevated temperature in TMF load has a dominant influence on the $\gamma \rightarrow \alpha'$ kinetics over the other half of the cycle at ambient temperature. This means that austenitic steel is much less ferromagnetic after TMF loading compared to the same deformation at ambient temperature.

Where does the $\gamma \rightarrow \alpha'$ transformation localize within the material at elevated temperatures and under TMF?

In both TMF and isothermal tests there was a tendency of $\gamma \rightarrow \alpha'$ transformation to follow the shear deformation. In fact, shear deformation was still able to drive $\gamma \rightarrow \alpha'$ transformation at 200 °C, even when the propagating crack could not. Those areas were identified by magnetic force imaging where the diameter of the gauge length starts to increase.

These and other questions answered in this thesis not only help to understand the fundamentals of deformation-induced phase transformation in austenitic steels, but also build a bridge to the non-destructive evaluation of thermo-mechanical damage using magnetic methods. A prototype for such evaluation, the balanced core magnetometer (BCM), was introduced in this work. First measurements with BCM showed that it can be used to estimate both magnetic coercivity and susceptibility of the material, which can be further used to evaluate α' martensite fraction and the way in which it formed.

References

[1] J. S. Park, Y. H. Choi, Application of piping failure database to nuclear safety issues in Korea, Int. J. Press. Vessel. Pip. 90-91 (2012) 56–60. doi:10.1016/j.ijpvp.2011.10.008.

[2] G. Dobmann, Fatigue monitoring by NDT of austenitic stainless steel at ambient temperature and 300C and new attempts to monitor a fracture mechanics test, Procedia Eng. 86 (2014) 384–394. doi:10.1016/j.proeng.2014.11.052.

[3] M. Lang, J. Johnson, J. Schreiber, G. Dobmann, H. J. Bassler, D. Eifler, R. Ehrlich, U. Gampe, Cyclic deformation behaviour of AISI 321 austenitic steel and its characterization by means of HTC-SQUID, Nucl. Eng. Des. 198 (2000) 185–191. doi:10.1016/S0029-5493(99)00287-3.

[4] M. Cohen, G. B. Olson, P. C. Clapp, On the classification of displacive phase transformations, in: Int. Conf. Martensitic Transform., Cambridge, USA, 1979.

[5] G. B. Olson, M. Azrin, Transformation behavior of TRIP steels, Metall. Trans. A 9 (1978) 713–721. doi:10.1007/BF02659928.

[6] J. W. Christian, G. B. Olson, M. Cohen, Classification of displacive transformations: what is a martensitic transformation?, Le J. Phys. IV 05 (1995) C8–3–C8–10. doi:10.1051/jp4:1995801.

[7] Buerger M.J., Phase Transformations in Solids, Wiley, New York, 1951.

[8] Bilby B.A., Christian J.W, The mechanisms of phase transformations in metals, Inst. Met. London (1956) 121.

[9] Carsten Müller-Bollenhagen, Verformungsinduzierte Martensitbildung bei mehrstufiger Umformung und deren Nutzung zur Optimierung der HCF- und VHCF-Eigenschaften von austenitischem Edelstahlblech, Ph.D. thesis, Universität Siegen, 2011.

[10] E. Bain, N. Dunkirk, The nature of martensite, Trans. AIME 70 (1924) 25–45.

[11] V. A. Lobodyuk, Y. Y. Meshkov, E. V. Pereloma, On tetragonality of the martensite crystal lattice in steels, Metall. Mater. Trans. A Phys. Metall. Mater. Sci. 50 (2019) 97–103. doi:10.1007/S11661-018-4999-Z.

[12] C. Cayron, One-step theory of fcc-bcc martensitic transformation, Acta Crystallogr. Sect. A Found. Crystallogr. 69 (2012) 498–509. doi:10.1107/S0108767313019016. arXiv:1211.0495v1.

[13] A. B. Greninger, A. R. Troiano, The mechanism of martensite formation, JOM 1 (1949) 590–598.

[14] G. Kurdjumow, G. Sachs, Über den Mechanismus der Stahlhärtung, Zeitschrift für Phys. 64 (1930) 325–343. doi:10.1007/BF01397346.

[15] J. M. Vallejos, C. E. Sobrero, M. Ávalos, J. W. Signorelli, J. A. Malarría, Crystallographic orientation relationships in the alpha-gamma' martensitic transformation in an Fe-Mn-Al-Ni system, J. Appl. Crystallogr. 51 (2018) 990–997. doi:10.1107/S1600576718006738.

[16] Z. Nishiyama, Strain-induced transformation in Co26Ni-8.7 Cr alloy, Sci. Rep. Tohoku Imp. Univ. 25 (1934) 94.

[17] L. Sandoval, H. M. Urbassek, P. Entel, The Bain versus Nishiyama-Wassermann path in the martensitic transformation of Fe, New J. Phys. 11 (2009). doi:10.1088/1367-2630/11/10/103027.

[18] W. Pitsch, The martensite transformation in thin foils of iron-nitrogen alloys, Philos. Mag. A J. Theor. Exp. Appl. Phys. 4 (1959) 577–584. doi:10.1080/14786435908238253.

[19] W. Pitsch, Der Orientierungszusammenhang zwischen Zementit und Ferrit im Perlit, Acta Metall. 10 (1962) 79–80. doi:10.1016/0001-6160(62)90190-6.

[20] A. J. Bogers, W. G. Burgers, Partial dislocations on the {110} planes in the B.C.C. lattice and the transition of the F.C.C. into the B.C.C. lattice, Acta Metall. 12 (1964) 255–261. doi:10.1016/0001-6160(64)90194-4.

[21] X. S. Yang, S. Sun, X. L. Wu, E. Ma, T. Y. Zhang, Dissecting the mechanism of martensitic transformation via atomic-scale observations, Sci. Rep. 4 (2014). doi:10.1038/SREP06141.

[22] M. S. Wechsler, On the theory of the formation of martensite, Trans Aime 197 (1953) 1503–1515.

[23] J. S. Bowles, J. K. Mackenzie, The crystallography of martensite transformations III. Face-centred cubic to body-centred tetragonal transformations, Acta Metall. 2 (1954) 224–234. doi:10.1016/0001-6160(54)90163-7.

[24] J. S. Bowles, J. K. Mackenzie, The crystallography of martensite transformations I, Acta Metall. 2 (1954) 129–137. doi:10.1016/0001-6160(54)90102-9.

[25] J. K. Mackenzie, J. S. Bowles, The crystallography of martensite transformations II, Acta Metall. 2 (1954) 138–147. doi:10.1016/0001-6160(54)90103-0.

[26] C. Cayron, F. Barcelo, Y. de Carlan, The mechanisms of the fcc-bcc martensitic transformation revealed by pole figures, Acta Mater. 58 (2010) 1395–1402. doi:10.1016/J.ACTAMAT.2009.10.046.

[27] J. A. Venables, The martensite transformation in stainless steel, Philos. Mag. A J. Theor. Exp. Appl. Phys. 7 (1962) 35–44. doi:10.1080/14786436208201856.

[28] P. M. Kelly, The martensite transformation in steels with low stacking fault energy, Acta Metall. 13 (1965) 635–646. doi:10.1016/0001-6160(65)90126-4.

[29] K. Shimizu, Y. Tanaka, The gamma-epsilon-alpha' Martensitic Transformations in an Fe-Mn-C Alloy, Trans. Japan Inst. Met. 19 (1978) 685–693. doi:10.2320/MATERTRANS1960.19.685.

[30] M. Humbert, B. Petit, B. Bolle, N. Gey, Analysis of the gamma-epsilon-alpha' variant selection induced by 10% plastic deformation in 304 stainless steel at -60 deg. C, Mater. Sci. Eng. A 454-455 (2007) 508–517. doi:10.1016/J.MSEA.2006.11.112.

[31] W. Fink, E. Campbell, The nature of the alloys of iron and chromium, Trans. Am. Soc. Steel Treat. 9 (1926) 717–752.

[32] N. Seljakow, J. Kurdumoff, N. Goodtzov, Tetragonal structure of carbon steel, Nature 119 (1927). doi:10.1038/119494a0.

[33] E. Öhman, Crystal structure of martensite, Nature 127 (1931) 270–272. doi:10.1038/127270b0.

[34] C. Zener, Kinetics of the decomposition of austenite, Trans. Aime 167 (1946) 550–595.

[35] A. G. Khachaturyan, Theory of phase transformations and structure of solid solutions, Nauk. Moscow (1974).

[36] T. Angel, Formation of martensite in austenitic stainless steels - Efect of deformation, temperature, and composition, J. Iron Steel Inst. 177 (1954) 165–174.

[37] O. Voehringer, E. Macherauch, Struktur und mechanische Eigenschaften von Martensit, HTM - Haerterei-Technische Mitteilungen 32 (1977) 153–168. doi:10.1515/HTM-1977-320401.

[38] G. B. Olson, M. Cohen, A mechanism for the strain-induced nucleation of martensitic transformations, J. Less Common Met. 28 (1972) 107–118. doi:10.1016/0022-5088(72)90173-7.

[39] H. Hotz, B. Kirsch, J. C. Aurich, Impact of the thermomechanical load on subsurface phase transformations during cryogenic turning of metastable austenitic steels, J. Intell. Manuf. (2020). doi:10.1007/s10845-020-01626-6.

[40] H. C. Shin, T. K. Ha, Y. W. Chang, Kinetics of deformation induced martensitic transformation in a 304 stainless steel, Scr. Mater. 45 (2001) 823–829. doi:10.1016/S1359-6462(01)01101-0.

[41] J. R. Patel, M. Cohen, Criterion for the action of applied stress in the martensitic transformation, Acta Metall. 1 (1953) 531–538. doi:10.1016/0001-6160(53)90083-2.

[42] G. F. Bolling, R. H. Richman, The plastic deformation-transformation of paramagnetic f.c.c. FeNiC alloys, Acta Metall. 18 (1970) 673–681. doi:10.1016/0001-6160(70)90097-0.

[43] G. B. Olson, M. Cohen, Kinetics of strain-induced martensitic nucleation, Metall. Trans. A 6 (1975) 791–795. doi:10.1007/BF02672301.

[44] B. He, On the factors governing austenite stability: intrinsic versus extrinsic, Materials (Basel). 13 (2020). doi:10.3390/MA13153440.

[45] C. G. Rhodes, A. W. Thompson, The composition dependence of stacking fault energy in austenitic stainless steels, Metall. Trans. A 8 (1977) 1901–1906. doi:10.1007/bf02646563.

[46] L. Kaufman, M. Cohen, Thermodynamics and kinetics of martensitic transformations, Prog. Met. Phys. 7 (1958) 165–246. doi:10.1016/0502-8205(58)90005-4.

[47] M. Izumiyama, M. Tsuchiya, Y. Imai, Effects of alloying element on supercooled A3 transformation of iron, Sci. reports Res. Institutes, Tohoku Univ. Ser. A, Physics, Chem. Metall. (1970) 105–115.

[48] C. Y. Kung, J. J. Rayment, Examination of the validity of existing empirical formulae for the calculation of Ms temperature, Met. Trans., A 13:2 (1982) 328–331. doi:10.1007/BF02643327.

[49] J. Wang, P. J. Van Der Wolk, S. Van Der Zwaag, Determination of martensite start temperature in engineering steels Part I. Empirical relations describing the effect of steel chemistry, Mater. Trans. JIM 41 (2000) 761–768. doi:10.2320/MATERTRANS1989.41.761.

[50] D. Barbier, Extension of the martensite transformation temperature relation to larger alloying elements and contents, Adv. Eng. Mater. 16 (2014) 122–127. doi:10.1002/ADEM.201300116.

[51] J. Trzaska, Calculation of critical temperatures by empirical formulae, Arch. Metall. Mater. 61 (2016) 981–986. doi:10.1515/AMM-2016-0167.

[52] G. C. Eichelmann, T. C. Hull, The effect of composition on the temperature of spontaneous transformation of austenite to martensite in 18-8 type stainless steel, Trans. Am. Soc. Met. 45 (1953) 77–104.

[53] K. W. Andrews, Empirical formulae for the calculation of some transformation temperatures., J. Iron Steel Inst. (1965) 721–727.

[54] T. Masumura, T. Tsuchiyama, S. Takaki, T. Koyano, K. Adachi, Difference between carbon and nitrogen in thermal stability of metastable 18%Cr-8%Ni austenite, Scr. Mater. 154 (2018) 8–11. doi:10.1016/J.SCRIPTAMAT.2018.05.019.

[55] R. Hossain, F. Pahlevani, V. Sahajwalla, Effect of small addition of Cr on stability of retained austenite in high carbon steel, Mater. Charact. 125 (2017) 114–122. doi:10.1016/J.MATCHAR.2017.02.001.

[56] B. Mintz, The influence of aluminium on the strength and impact properties of steel, in: Int. Con. TRIP-aided HS Ferr. Alloy., Ghent, Belgium, 2002, pp. 379–382.

[57] I. Jeong, K. M. Ryu, D. G. Lee, Y. Jung, K. Lee, J. S. Lee, D. W. Suh, Austenite morphology and resistance to hydrogen embrittlement in medium Mn transformation-induced plasticity steel, Scr. Mater. 169 (2019) 52–56. doi:10.1016/J.SCRIPTAMAT.2019.05.011.

[58] N. Al-Khirdaji, Stainless Steel Family, Technical Report, Kappa Associates International, 2022.

[59] A. García-Junceda, C. Capdevila, F. G. Caballero, C. G. de Andrés, Dependence of martensite start temperature on fine austenite grain size, Scr. Mater. 58 (2008) 134–137. doi:10.1016/J.SCRIPTAMAT.2007.09.017.

[60] H. Koohdar, M. Nili-Ahmadabadi, M. Habibi-Parsa, H. R. Jafarian, T. Bhattacharjee, N. Tsuji, On the stability of reversely formed austenite and related mechanism of transformation in an Fe-Ni-Mn martensitic steel aided by electron backscattering diffraction and atom probe tomography, Metall. Mater. Trans. A Phys. Metall. Mater. Sci. 48 (2017) 5244–5257. doi:10.1007/S11661-017-4288-2.

[61] Z. H. Cai, H. Ding, R. D. Misra, Z. Y. Ying, Austenite stability and deformation behavior in a cold-rolled transformation-induced plasticity steel with medium manganese content, Acta Mater. 84 (2015) 229–236. doi:10.1016/J.ACTAMAT.2014.10.052.

[62] S. Lee, S. J. Lee, B. C. De Cooman, Reply to comments on "Austenite stability of ultrafine-grained transformation-induced plasticity steel with Mn partitioning", Scr. Mater. 66 (2012) 832–833. doi:10.1016/J.SCRIPTAMAT.2012.02.018.

[63] E. Jimenez-Melero, N. H. van Dijk, L. Zhao, J. Sietsma, S. E. Offerman, J. P. Wright, S. van der Zwaag, Martensitic transformation of individual grains in low-alloyed TRIP steels, Scr. Mater. 56 (2007) 421–424. doi:10.1016/J.SCRIPTAMAT.2006.10.041.

[64] H. K. Bhadeshia, Some phase transformations in steels, Mater. Sci. Technol. 15 (1999) 22–29. doi:10.1179/026708399773002773.

[65] S. Chatterjee, H. S. Wang, J. R. Yang, H. K. Bhadeshia, Mechanical stabilisation of austenite, Mater. Sci. Technol. 22 (2006) 641–644. doi:10.1179/174328406X86128.

[66] M. Maalekian, E. Kozeschnik, S. Chatterjee, H. K. Bhadeshia, Mechanical stabilisation of eutectoid steel, Mater. Sci. Technol. 23 (2013) 610–612. doi:10.1179/174328407X158686.

[67] J. F. Breedis, Influence of dislocation substructure on the martensitic transformation in stainless steel, Acta Metall. 13 (1965) 239–250. doi:10.1016/0001-6160(65)90201-4.

[68] S. Kajiwara, Roles of dislocations and grain boundaries in martensite nucleation, Metall. Mater. Trans. A 17 (1986) 1693–1702. doi:10.1007/BF02817268.

[69] B. B. He, W. Xu, M. X. Huang, Increase of martensite start temperature after small deformation of austenite, Mater. Sci. Eng. A 609 (2014) 141–146. doi:10.1016/J.MSEA.2014.04.108.

[70] M. F. Ashby, The deformation of plastically non-homogeneous materials, Philos. Mag. A J. Theor. Exp. Appl. Phys. 21 (1969) 399–424. doi:10.1080/14786437008238426.

[71] K. I. Sugimoto, M. Misu, M. Kobayashi, H. Shirasawa, Effects of second phase morphology on retained austenite morphology and tensile properties in a TRIP-aided dual-phase steel sheet, ISIJ Int. 33 (1993) 775–782. doi:10.2355/ISIJINTERNATIONAL.33.775.

[72] F. G. Caballero, C. García-Mateo, J. Chao, M. J. Santofimia, C. Capdevila, C. G. De Andrés, Effects of morphology and stability of retained austenite on the ductility of TRIP-aided bainitic steels, ISIJ Int. 48 (2008) 1256–1262. doi:10.2355/ISIJINTERNATIONAL.48.1256.

[73] Q. Zhou, L. Qian, J. Tan, J. Meng, F. Zhang, Inconsistent effects of mechanical stability of retained austenite on ductility and toughness of transformation-induced plasticity steels, Mater. Sci. Eng. A 578 (2013) 370–376. doi:10.1016/J.MSEA.2013.04.096.

[74] H. S. Park, J. C. Han, N. S. Lim, C. G. Park, Nano-scale observation on the transformation behavior and mechanical stability of individual retained austenite in CMnSiAl TRIP steels, Mater. Sci. Eng. A 627 (2015) 262–269. doi:10.1016/J.MSEA.2015.01.005.

[75] S. Yan, X. Liu, T. Liang, Y. Zhao, The effects of the initial microstructure on microstructural evolution, mechanical properties and reversed austenite stability of intercritically annealed Fe-6.1Mn-1.5Si-0.12C steel, Mater. Sci. Eng. A 712 (2018) 332–340. doi:10.1016/J.MSEA.2017.11.118.

[76] P. J. Jacques, F. Delannay, J. Ladrière, On the influence of interactions between phases on the mechanical stability of retained austenite in transformation-induced plasticity multiphase steels, Metall. Mater. Trans. A Phys. Metall. Mater. Sci. 32 (2001) 2759–2768. doi:10.1007/S11661-001-1027-4.

[77] X. C. Xiong, B. Chen, M. X. Huang, J. F. Wang, L. Wang, The effect of morphology on the stability of retained austenite in a quenched and partitioned steel, Scr. Mater. 68 (2013) 321–324. doi:10.1016/J.SCRIPTAMAT.2012.11.003.

[78] I. Y. Pyshmintsev, M. De Meyer, B. C. De Cooman, R. A. Savray, V. P. Shveykin, M. Vermeulen, The influence of the stress state on the plasticity of transformation induced plasticity-aided steel, Metall. Mater. Trans. A Phys. Metall. Mater. Sci. 33 (2002) 1659–1667. doi:10.1007/S11661-002-0175-5.

[79] R. Blondé, E. Jimenez-Melero, L. Zhao, N. Schell, E. Brück, S. van der Zwaag, N. H. van Dijk, The mechanical stability of retained austenite in low-alloyed TRIP steel under shear loading, Mater. Sci. Eng. A 594 (2014) 125–134. doi:10.1016/J.MSEA.2013.11.001.

[80] M. T. Todinov, J. F. Knott, M. Strangwood, An assessment of the influence of complex stress states on martensite start temperature, Acta Mater. 44 (1996) 4909–4915. doi:10.1016/S1359-6454(96)00097-3.

[81] S. S. Hecker, M. G. Stout, K. P. Staudhammer, J. L. Smith, Effects of strain state and strain rate on deformation-induced transformation in 304 stainless steel: Part I. Magnetic measurements and mechanical behavior, Metall. Trans. A 13 (1982) 619–626. doi:10.1007/BF02644427.

[82] L. E. Murr, K. P. Staudhammer, S. S. Hecker, Effects of strain state and strain rate on deformation-induced transformation in 304 stainless steel: Part II. Microstructural study, Metall. Trans. A 13 (1982) 627–635. doi:10.1007/BF02644428.

[83] O. G. Nimaga, B. B. He, G. J. Cheng, H. W. Yen, M. X. Huang, Revealing orientation-dependent martensitic transformation in a medium Mn steel by micropillar compression, Int. J. Plast. 123 (2019) 165–177. doi:10.1016/J.IJPLAS.2019.07.016.

[84] H. Huh, S. B. Kim, J. H. Song, J. H. Lim, Dynamic tensile characteristics of TRIP-type and DP-type steel sheets for an auto-body, Int. J. Mech. Sci. 50 (2008) 918–931. doi:10.1016/J.IJMECSCI.2007.09.004.

[85] D. S. Martin, N. H. van Dijk, E. Brück, S. van der Zwaag, The isothermal martensite formation in a maraging steel: A magnetic study, Mater. Sci. Eng. A 481-482 (2008) 757–761. doi:10.1016/J.MSEA.2006.11.177.

[86] D. San Martin, N. H. van Dijk, E. Jiménez-Melero, E. Kampert, U. Zeitler, S. van der Zwaag, Real-time martensitic transformation kinetics in maraging steel under high magnetic fields, Mater. Sci. Eng. A 527 (2010) 5241–5245. doi:10.1016/J.MSEA.2010.04.085.

[87] T. Kakeshita, J. M. Nam, T. Fukuda, Kinetics of martensitic transformations in magnetic field or under hydrostatic pressure, Sci. Technol. Adv. Mater. 12 (2011). doi:10.1088/1468-6996/12/1/015004.

[88] E. Herbert, The hardening of superhardened steel by magnetism: The Lattice Resonance Hypothesis, Iron Steel Inst. 120 (1929) 569–571.

[89] V. Sadovskii, The question of the influence of magnetic field on martensitic transformation in steel, Fiz Met. Met 12 (1961) 302–304.

[90] E. Fokina, Effect of a magnetic field on the position of the martensite point in carbon steels, Fiz. Met. Metalloved. 27 (1969) 756–757.

[91] T. Kakeshita, K. Kuroiwa, K. Shimiz, T. Ikeda, A. Yamagishi, M. Date, Effect of Magnetic Fields on Athermal and Isothermal Martensitic Transformations in Fe-Ni-Mn Alloys, Mater. Trans. JIM 34 (1993) 415–422. doi:10.2320/MATERTRANS1989.34.415.

[92] K. Shimizu, T. Kakeshita, Effect of Magnetic Fields on Martensitic Transformations in Ferrous Alloys and Steels, ISIJ Int. 29 (1989) 97–116. doi:10.2355/ISIJINTERNATIONAL.29.97.

[93] T. Angel, Formation of martensite in austenitic stainless steels, J. Iron Steel Inst. 177 (1954) 165–174.

[94] D. C. Ludwigson, Plastic behaviour of metastable austenitic stainless steels, J. Iron Steel Inst. 207 (1969) 63–69.

[95] J. Burke, The kinetics of phase transformations in metals, Pergamon Press 226 (1965).

[96] O. Matsumura, Y. Sakuma, H. Takechi, Trip and its kinetic aspects in austempered 0.4 C-1.5 Si-0.8 Mn steel, Scr. Metall. 21 (1987) 1301–1306.

[97] N. Tsuchida, Y. Tomota, A micromechanic modeling for transformation induced plasticity in steels, Mater. Sci. Eng. A 285 (2000) 345–352. doi:doi.org/10.1016/S0921-5093(00)00688-2.

[98] K. I. Sugimoto, M. Kobayashi, S. I. Hashimoto, Ductility and strain-induced transformation in a high-strength transformation-induced plasticity-aided dual-phase steel, Metall. Trans. A, Phys. Metall. Mater. Sci. 23 A (1992) 3085–3091. doi:10.1007/BF02646127.

[99] I. Pychmintsev, R. Savrai, B. Cooman, O. Moriau, High strain rate behaviour of TRIP-aided automotive steels, in: Proc. Int. Conf. TRIP Aided High Strength Ferr. Alloy., Wissenschafts verlag Mainz GmbH, Aachen, Germany, 2002, pp. 299–302.

[100] W. Gerberich, G. Thomas, E. Parker, V. Zackay, Metastable austenites: decomposition and strength, in: Proc. 2nd Int. Conf. Strength Met. Alloy., ASM, Metals Park, 1970, pp. 894–899.

[101] J. R. Guimaraes, The deformation-induced martensitic reaction in polycrystalline Fe - 30.7 Ni - 0.06C, Scr. Metall. 6 (1972) 795–798. doi:10.1016/0036-9748(72)90049-X.

[102] L. Samek, E. De Moor, J. Penning, B. C. De Cooman, Influence of alloying elements on the kinetics of strain-induced martensitic nucleation in low-alloy, multiphase high-strength steels, Metall. Mater. Trans. A Phys. Metall. Mater. Sci. 37 (2006) 109–124. doi:10.1007/S11661-006-0157-0.

[103] Y. Tomita, T. Iwamoto, Constitutive modeling of trip steel and its application to the improvement of mechanical properties, Int. J. Mech. Sci. 37 (1995) 1295–1305. doi:10.1016/0020-7403(95)00039-Z.

[104] R. G. Stringfellow, D. M. Parks, G. B. Olson, A constitutive model for transformation plasticity accompanying strain-induced martensitic transformations in metastable austenitic steels, Acta Metall. Mater. 40 (1992) 1703–1716. doi:10.1016/0956-7151(92)90114-T.

[105] A. Hänsel, Nichtisothermes Werkstoffmodell für die FE-Simulation von Blechumformprozessen mit metastabilen austenitischen CrNiStählen, Ph.D. thesis, ETH Zürich, 1998. doi:https://doi.org/10.3929/ethz-a-001947695.

[106] M. Smaga, F. Walther, D. Eifler, Investigation and modelling of the plasticity-induced martensite formation in metastable austenites, Int. J. Mater. Res. 97 (2006) 1648–1655. doi:10.3139/146.101396.

[107] J. Kaleta, G. Zietek, Representation of cyclic properties of austenitic steels with plasticity-induced martensitic transformation, Fatigue Fract. Eng. Mater. Struct. 21 (1998) 955–964. doi:10.1046/J.1460-2695.1998.00086.X.

[108] U. Krupp, C. G. West, H. Duan, H.-J. Christ, Strain-induced martensite formation in metastable austenitic steels with varying carbon content, Int. J. Mater. Res. 93 (2002) 706–711. doi:10.3139/IJMR-2002-0119.

[109] M. Smaga, Experimentelle Untersuchung der Mikrostruktur sowie des Verformungs- und Umwandlungsverhaltens zyklisch beanspruchter metastabiler austenitischer Stähle, Ph.D. thesis, Technische Universität Kaiserslautern, 2005.

[110] Z. Mroz, G. Zietek, Modeling of cyclic hardening of metals coupled with martensitic transformation, Arch. Mech 59 (2007) 3–20.

[111] Y. Chen, X. Chen, B. Gao, X. Chen, K. Zhang, C. Yu, A cyclic plasticity model with martensite transformation for S30408 and its finite element implementation, Appl. Sci. 10 (2020). doi:10.3390/APP10176002.

[112] B. D. Cullity, C. D. Graham, Introduction to magnetic materials, John Wiley & Sons, Inc, 2009.

[113] R. Thompson, F. Oldfield, Environmental magnetism, Allen and Unwin Ltd, UK, 1986.

[114] H. W. Sung, C. Rudowicz, Physics behind the magnetic hysteresis loop - a survey of misconceptions in magnetism literature, J. Magn. Magn. Mater. 260 (2003) 250–260. doi:10.1016/S0304-8853(02)01339-2.

[115] C. P. Bean, J. D. Livingston, Superparamagnetism, J. Appl. Phys. 30 (1959) S120–S129. doi:10.1063/1.2185850.

[116] H. Lawton, K. H. Stewart, Magnetization curves for ferromagnetic single crystals, Proc. R. Soc. London. Ser. A. Math. Phys. Sci. 193 (1948) 72–88. doi:10.1098/RSPA.1948.0034.

[117] L. Delaey, Diffusionless Transformations, Mater. Sci. Technol. (2013). doi:10.1002/9783527603978.MST0392.

[118] B. Zwicknagl, S. Conti, M. Lenz, N. Lüthen, M. Rumpf, Geometry of martensite needles in shape memory alloys, Comptes Rendus. Math. (2020). doi:10.3929/ethz-b-000464730.

[119] E. C. Snelling, Soft Ferrites, Mullards Research Laboratories, Iliffe Books LTD, London, 1969.

[120] M. B. Stearns, Magnetostriction coefficients, Landolt-Börnstein, Condensed Matter, Volume 19A: 3d, 4d and 5d Elements, Alloys and Compounds, 1986. doi:10.1007/10311893_9.

[121] H. Hase, S. Kotake, M. Ohota, H. Kawakami, Y. Suzuki, Evaluation of fracture surface of 11/4Cr-1/2Mo steel by residual magnetization induced from inverse magnetostrictive effect, Key Eng. Mater. 340-341 (2007) 549–554. doi:10.4028/www.scientific.net/kem.340-341.549.

[122] Fischer Technology Inc., Feritscope FMP30, 2022. URL: http://www.fischer-technology.com.

[123] C. Lundin, W. Ruprecht, G. Zhou, Ferrite measurement in austenitic and duplex stainless steel castings, Technical Report, Department of materials science and engineering, University of Tennessee, 1999.

[124] V. Schoß, Dissertation, Martensitische Umwandlung und Ermüdung austenitischer Edelstähle, Ph.D. thesis, TU Freiberg, 2001.

[125] M. Smaga, F. Walther, D. Eifler, Deformation-induced martensitic transformation in metastable austenitic steels, Mater. Sci. Eng. A 483-484 (2008) 394–397. doi:10.1016/j.msea.2006.09.140.

[126] H.-J. Christ, U. Krupp, C. Mueller-Bollenhagen, I. Roth, M. Zimmerman, Effect of deformation-induced martensite on the fatigue behavior of metastable austenitic stainless steels, Proc. 12th Int. Conf. Fract. (2009).

[127] C. Müller-Bollenhagen, M. Zimmermann, H. J. Christ, Very high cycle fatigue behaviour of austenitic stainless steel and the effect of strain-induced martensite, Int. J. Fatigue 32 (2010) 936–942. doi:10.1016/j.ijfatigue.2009.05.007.

[128] F. Hahnenberger, M. Smaga, D. Eifler, Microstructural investigation of the fatigue behavior and phase transformation in metastable austenitic steels at ambient and lower temperatures, Int. J. Fatigue 69 (2014) 36–48. doi:10.1016/j.ijfatigue.2012.07.004.

[129] M. Shirdel, H. Mirzadeh, M. Parsa, Estimation of the kinetics of martensitic transformation in austenitic stainless steels by conventional and novel approaches, Mater. Sci. Eng. A 624 (2015) 256–260. doi:10.1016/j.msea.2014.11.087.

[130] A. C. Grigorescu, P. M. Hilgendorff, M. Zimmermann, C. P. Fritzen, H. J. Christ, Cyclic deformation behavior of austenitic Cr-Ni-steels in the VHCF regime: Part I Experimental study, Int. J. Fatigue 93 (2016) 250–260. doi:10.1016/j.ijfatigue.2016.05.005.

[131] M. Klein, P. Starke, D. Nowak, C. Boller, F. Walther, Separation of surface, subsurface and volume fatigue damage effects in AISI 348 steel for power plant applications, Mater. Test. 58 (2016) 601–607.

[132] M. Smaga, R. Skorupski, P. Mayer, B. Kirsch, J. C. Aurich, I. Raid, J. Seewig, J. Man, D. Eifler, T. Beck, Influence of surface morphology on fatigue behavior of metastable austenitic stainless steel AISI 347 at ambient temperature and 300 C, Procedia Struct. Integr. 5 (2017) 989–996. doi:10.1016/j.prostr.2017.07.150.

[133] J. O. Fava, F. D. Carabedo, C. C. Spinosa, M. C. Ruch, Assessment of the amount of deformation induced martensite: a calibration curve for a commercial delta-ferrite gauge, in: 12th Eur. Conf. Non-Destructive Testing, Gothenbg. 2018, June 11-15 (ECNDT 2018), 2018.

[134] V. Mazánová, M. Heczko, V. Škorík, A. Chlupová, J. Polák, T. Kruml, Microstructure and martensitic transformation in 316L austenitic steel during multiaxial low cycle fatigue at room temperature, Mater. Sci. Eng. A 767 (2019). doi:10.1016/j.msea.2019.138407.

[135] Smaga, Boemke, Daniel, Skorupski, Sorich, Beck, Fatigue Behavior of Metastable Austenitic Stainless Steels in LCF, HCF and VHCF Regimes at Ambient and Elevated Temperatures, Metals (Basel). 9 (2019) 704. doi:10.3390/met9060704.

[136] A. Putz, M. Althuber, A. Zelić, E. M. Westin, T. Willidal, N. Enzinger, Methods for the measurement of ferrite content in multipass duplex stainless steel welds, Weld. World 63 (2019) 1075–1086. doi:10.1007/s40194-019-00721-4.

[137] J. Talonen, P. Aspegren, H. Hänninen, Comparison of different methods for measuring strain induced α-martensite content in austenitic steels, Mater. Sci. Technol. 20 (2004) 1506–1512. doi:10.1179/026708304X4367.

[138] L. Zhao, N. H. Van Dijk, A. J. E. Lefering, J. Sietsma, Magnetic detection of small fractions of ferromagnetic martensite within the paramagnetic austenite matrix of TWIP steel, J. Mater. Sci. 48 (2013) 1474–1479. doi:10.1007/s10853-012-6902-4.

[139] S. Tavares, M. da Silva, J. Neto, S. Miraglia, D. Fruchart, Ferromagnetic properties of cold rolled AISI 304L steel, J. Magn. Magn. Mater. 242-245 (2002) 1391–1394. doi:10.1016/S0304-8853(01)01242-2.

[140] K. Mumtaz, S. Takahashi, J. Echigoya, Y. Kamada, L. F. Zhang, H. Kikuchi, K. Ara, M. Sato, Magnetic measurements of martensitic transformation in austenitic stainless steel after room temperature rolling, J. Mater. Sci. 39 (2004) 85–97.

[141] S. Tavares, J. Neto, M. da Silva, I. Vasconcelos, H. de Abreu, Magnetic properties and α' martensite quantification in an AISI 301LN stainless steel deformed by cold rolling, Mater. Charact. 59 (2008) 901–904. doi:10.1016/J.MATCHAR.2007.07.007.

[142] C. Kim, Nondestructive evaluation of strain-induced phase transformation and damage accumulation in austenitic stainless steel subjected to cyclic loading, Metals (Basel). 8 (2017). doi:10.3390/met8010014.

[143] F. Walther, D. Eifler, Cyclic deformation behavior of steels and light-metal alloys, Mater. Sci. Eng. A 468-470 (2007) 259–266.

[144] P. Starke, D. Eifler, C. Boller, Fatigue assessment of metallic materials beyond strain measurement, Int. J. Fatigue 82 (2016) 274–279. doi:10.1016/j.ijfatigue.2015.03.018.

[145] T. Oršulová, P. Palček, M. Roszak, M. Uhríčik, M. Smetana, J. Kúdelčík, Change of magnetic properties in austenitic stainless steels due to plastic deformation, Procedia Struct. Integr. 13 (2018) 1689–1694. doi:10.1016/J.PROSTR.2018.12.352.

[146] T. Nebel, D. Eifler, Cyclic deformation behaviour of austenitic steels at ambient and elevated temperatures, Sadhana - Acad. Proc. Eng. Sci. 28 (2003) 187–208. doi:10.1007/BF02717133.

[147] S. Foner, Versatile and sensitive vibrating sample magnetometer, Rev. Sci. Instrum. 30 (2004) 548. doi:10.1063/1.1716679.

[148] A. De Sa, L. Molyneux, A spinner magnetometer, J. Sci. Instrum. 40 (1963) 162–165. doi:10.1088/0950-7671/40/4/306.

[149] D. Dufeu, E. Eyraud, P. Lethuillier, An efficient 8 T extraction vector magnetometer with sample rotation for routine operation, Rev. Sci. Instrum. 71 (2000) 458. doi:10.1063/1.1150223.

[150] K Koyama, S Miura, H Okada, K Watanabe, Development of an extraction type magnetometer under high pressure and high magnetic fields over 200 kOe in the hybrid magnet, J. Phys. Conf. Ser. 51 (2006) 572. doi:10.1088/1742-6596/51/1/129.

[151] AGICO Corporation, KLY5 Kappabridge, 2022. URL: https://www.agico.com/text/products/kly5/kly5.php.

[152] G. Calabrese, L. Capineri, M. Granato, G. Frattini, Automated setup for magnetic hysteresis characterization based on a voltage controlled current source with 500 kHz full power bandwidth and 10 A peak-to-peak current, Rev. Sci. Instrum. 86 (2015). doi:10.1063/1.4916992.

[153] Rapiscan Systems, Satmagan 135 magnetite detector, 2019. URL: https://www.rapiscansystems.com/en/products/satmagan-135.

[154] A. W. Brewer, R. L. Moment, Techniques and standards for measuring ferrite in austenitic stainless steel welds, Weld. J. 55 (1976) 159–164.

[155] L. V. Fricke, H. N. Nguyen, B. Breidenstein, D. Zaremba, H. J. Maier, Eddy current detection of the martensitic transformation in AISI304 induced upon cryogenic cutting, Steel Res. Int. 92 (2021). doi:10.1002/SRIN.202000299.

[156] C. Cheneveau, A. C. Jolley, The magnetic balance of MM. P. Curie and C. Cheneveau, Proc. Phys. Soc. London 22 (1909) 343–359. doi:10.1088/1478-7814/22/1/325.

[157] J. M. D. Coey, Magnetism and Magnetic Materials, Cambridge University Press, 2010. doi:10.1017/CBO9780511845000.

[158] B. L. Morris, A. Wold, Faraday balance for measuring magnetic susceptibility, Rev. Sci. Instrum. 39 (1968) 1937–1941. doi:10.1063/1.1683276.

[159] D. Collinson, Methods in rock magnetism and palaeomagnetism: techniques and instrumentation, New York: Chapman & Hall, 1983.

[160] N. Krasa, D., Petersen, K., Petersen, Variable Field Translation Balance, in: Gubbins, D., Herrero-Bervera, E. Encycl. Geomagn. Paleomagn., Springer, Dordrecht, 2007. doi:10.1007/978-1-4020-4423-6_312.

[161] Magne-Gage Sales and Service Co., 2022. URL: https://www.magne-gage.com/gauges.htm.

[162] Ferrite Indicator, Severn Engineering Company, 2022. URL: https://severnengineering.com/ferrite-indicator/.

[163] D. F. Evans, A new type of magnetic balance, J. Phys. E. 7 (1974) 247–249.

[164] A. Hagermann, E. Schnepp, The modified Rankine balance: A highly efficient, low-cost method to measure low-temperature magnetic susceptibility in rock samples, Rev. Sci. Instrum. 73 (2002) 2655. doi:10.1063/1.1487897.

[165] R. S. Davis, New method to measure magnetic susceptibility, Meas. Sci. Technol. 4 (1993) 141–147. doi:10.1088/0957-0233/4/2/001.

[166] V. Lyamkin, P. Starke, C. Boller, Magnetic force imaging for spatially resolved assessment of ferromagnetic phase fraction in austenitic stainless steel, J. Magn. Magn. Mater. 497 (2019) 165973. doi:https://doi.org/10.1016/j.jmmm.2019.165973.

[167] V. Lyamkin, C. Pauly, P. Starke, F. Mücklich, C. Boller, Impact of cyclic strain on deformation-induced martensite morphology and magnetic properties of type 347 austenitic stainless steel, Mater. Today Commun. 26 (2021) 101803. doi:10.1016/j.mtcomm.2020.101803.

[168] K. Verbeken, N. Van Caenegem, D. Raabe, Identification of ϵ martensite in a Fe-based shape memory alloy by means of EBSD, Micron 40 (2009) 151–156. doi:10.1016/j.micron.2007.12.012.

[169] A. Arabi-Hashemi, Y. Guo, J. Michler, D. Casari, C. Leinenbach, X. Maeder, Stress induced martensite variants revealed by in situ high resolution electron backscatter diffraction (HR-EBSD), Mater. Des. 151 (2018) 83–88. doi:10.1016/j.matdes.2018.04.006.

[170] M. Jovicevic-Klug, P. Jovicevic-Klug, J. McCord, B. Podgornik, Investigation of microstructural attributes of steel surfaces through magneto-optical Kerr effect, J. Mater. Res. Technol. 11 (2021) 1245–1259. doi:10.1016/J.JMRT.2021.01.106.

[171] K. R. Gadelrab, G. Li, M. Chiesa, T. Souier, Local characterization of austenite and ferrite phases in duplex stainless steel using MFM and nanoindentation, J. Mater. Res. 27 (2012) 1573–1579. doi:10.1557/jmr.2012.99.

[172] Y. Xu, S. H. Zhang, M. Cheng, H. W. Song, In situ X-ray diffraction study of martensitic transformation in austenitic stainless steel during cyclic tensile loading and unloading, Scr. Mater. 67 (2012) 771–774. doi:10.1016/j.scriptamat.2012.07.021.

[173] P. Eftekharimilani, R. M. Huizenga, B. Kim, A. Bernasconi, M. J. Hermans, In-situ synchrotron X-ray diffraction studies on effects of plastic and elastic loading on bcc phase transformations of a 3rd generation 1 GPa advanced high strength steel, Metall. Mater. Trans. A Phys. Metall. Mater. Sci. 49 (2018) 78–87. doi:10.1007/S11661-017-4415-0.

[174] D. Kalkhof, M. Grosse, M. Niffenegger, H. J. Leber, Monitoring fatigue degradation in austenitic stainless steels, Fatigue Fract. Eng. Mater. Struct. 27 (2004) 595–608. doi:10.1111/j.1460-2695.2004.00784.x.

[175] K. Mumtaz, S. Takahashi, J. Echigoya, L. Zhang, Y. Kamada, M. Sato, Detection of martensite transformation in high temperature compressively deformed austenitic stainless steel by magnetic NDE technique, J. Mater. Sci. 38 (2003) 3037–3050. doi:10.1023/A:1024744307549.

[176] T. Juuti, S. Uusikallio, A. Kaijalainen, E. Heinonen, N. Tun, D. Porter, The effect of sample preparation on the microstructure of austenitic-ferritic stainless steel, Mater. Sci. Forum 879 (2017) 873–878. doi:10.4028/www.scientific.net/MSF.879.873.

[177] W. Wisniewski, C. Rüssel, An experimental viewpoint on the information depth of EBSD, Scanning 38 (2016) 164–171. doi:10.1002/sca.21251.

[178] W. Wisniewski, S. Saager, A. Böbenroth, C. Rüssel, Experimental evidence concerning the significant information depth of electron backscatter diffraction (EBSD), Ultramicroscopy 173 (2017). doi:10.1016/j.ultramic.2016.11.004.

[179] P. J. Withers, Depth capabilities of neutron and synchrotron diffraction strain measurement instruments. I. The maximum feasible path length, urn:issn:0021-8898 37 (2004) 596–606. doi:10.1107/S0021889804012737.

[180] P. J. Withers, Depth capabilities of neutron and synchrotron diffraction strain measurement instruments. II. Practical implications, J. Appl. Crystallogr. 37 (2004) 607–612. doi:10.1107/S0021889804012750.

[181] D. San Martin, P. E. J. Rivera Diaz del Castillo, E. Peekstok, S. van der Zwaag, A new etching route for revealing the austenite grain boundaries in an 11.4% Cr precipitation hardening semi-austenitic stainless steel, Mater. Charact. 58 (2007) 455–460. doi:10.1016/j.matchar.2006.06.009.

[182] G. F. Vander Voort, E. P. Manilova, Hints for imagining phases in steels, Adv. Mater. Process. (2005) 32–37.

[183] G. L. Houze, Domain-wall motion in grain-oriented silicon steel in cyclic magnetic fields, J. Appl. Phys. 38 (1967) 1089–1096. doi:10.1063/1.1709498.

[184] P. Novotný, P. Macháč, P. Sajdl, Diagnostics of austenitic steels by coercivity mapping, NDT E Int. 41 (2008) 530–533. doi:10.1016/J.NDTEINT.2008.05.003.

[185] C. P. Livitsanos, P. F. Thomson, Rapid determination of the deformation-induced martensite in metastable stainless steels, J. Mater. Sci. 12 (1977) 2209–2213.

[186] A. Miller, Y. Estrin, X. Z. Hu, Magnetic force microscopy of fatigue crack tip region in a 316L austenitic stainless steel, Scr. Mater. 47 (2002) 441–446.

[187] G. Shaw, R. B. G. Kramer, N. Dempsey, K. Hasselbach, N. M. Dempsey, A Scanning Hall Probe Microscope for high resolution, large area, variable height Magnetic Field Imaging, Rev. Sci. Instrum. 87 (2016). doi:10.1063/1.4967235.

[188] J. J. Sáenz, N. García, J. C. Slonczewski, Theory of magnetic imaging by force microscopy, Appl. Phys. Lett. 53 (1988) 1449–1451. doi:10.1063/1.99965.

[189] S. S. Hecker, M. G. Stout, K. P. Staudhammer, J. L. Smith, Effects of strain state and strain rate on deformation-induced transformation in 304 stainless steel: Part I. Magnetic measurements and mechanical behavior, Metall. Trans. A 13 (1982) 619–626. doi:10.1007/BF02644427.

[190] M. Niffenegger, H. J. Leber, Sensitivity of the magnetization curves of different austenitic stainless tube and pipe steels to mechanical fatigue, J. Nucl. Mater. 377 (2008) 325–330. doi:10.1016/j.jnucmat.2008.03.007.

[191] Robert C. Weast, CRC handbook of chemistry and physics, Chemical Rubber Publishing Company, Boca Raton, 1990.

[192] Danieli Rotelec, Electromagnetic stirring and induction heating systems, Technical Report, France, 2005.

[193] D. Kotecki, T. Siewert, Constitution diagram for stainless steel weld metals: a modification of the WRC-1988 diagram, Weld. Res. Suppl. (1992) 171–178.

[194] P. Starke, F. Walther, D. Eifler, Fatigue assessment and fatigue life calculation of quenched and tempered SAE 4140 steel based on stress-strain hysteresis, temperature and electrical resistance measurements, Fatigue Fract. Eng. Mater. Struct. 30 (2007) 1044–1051. doi:10.1111/j.1460-2695.2007.01174.x.

[195] J. Mai, L. Peng, Z. Lin, X. Lai, Experimental study of electrical resistivity and flow stress of stainless steel 316L in electroplastic deformation, Mater. Sci. Eng. A 528 (2011) 3539–3544. doi:10.1016/j.msea.2011.01.058.

[196] M. A. Omari, I. Sevostianov, Estimation of changes in the mechanical properties of stainless steel subjected to fatigue loading via electrical resistance monitoring, Int. J. Eng. Sci. 65 (2013) 40–48. doi:10.1016/j.ijengsci.2013.02.006.

[197] P. Starke, F. Walther, Model-based correlation between the electrical resistance and the dislocation structure of the fatigue-loaded ICE-railway wheel steel R7, Mater. Test. 57 (2015). doi:10.3139/120.110681.

[198] H. Knobbe, P. Starke, S. Herenu, H. J. Christ, D. Eifler, Cyclic deformation behaviour, microstructural evolution and fatigue life of duplex steel AISI 329 LN, Int. J. Fatigue 80 (2015) 81–89. doi:10.1016/j.ijfatigue.2015.05.002.

[199] T. Nebel, Verformungsverhalten und Mikrostruktur zyklisch beanspruchter metastabiler austenitischer Stahle, Ph.D. thesis, Techn. Univ. Kaiserslautern, 2002.

[200] G. P. Hatch, R. E. Stelter, Magnetic design considerations for devices and particles used for biological high-gradient magnetic separation (HGMS) systems, J. Magn. Magn. Mater. 225 (2001) 262–276. doi:10.1016/S0304-8853(00)01250-6.

[201] M. Amitava, P. K. De, D. K. Bhattacharya, P. K. Srivastava, D. C. Jiles, Ferromagnetic properties of deformation-induced martensite transformation in AISI 304 stainless steel, Metall. Mater. Trans. A 35A (2004) 599–605. doi:10.1007/s11661-004-0371-6.

[202] A. Das, Magnetic properties of cyclically deformed austenite, J. Magn. Magn. Mater. 361 (2014) 232–242. doi:10.1016/J.JMMM.2014.02.006.

[203] J. Manjanna, S. Kobayashi, Y. Kamada, S. Takahashi, H. Kikuchi, Martensitic transformation in SUS 316LN austenitic stainless steel at RT, J. Mater. Sci. 43 (2008) 2659–2665. doi:10.1007/s10853-008-2494-4.

[204] J. Keisler, O. K. Chopra, W. J. Shack, Fatigue strain-life behavior of carbon and low-alloy steels, austenitic stainless steels, and alloy 600 in LWR environments, Argonne National Laboratory, 1995.

[205] K. H. Herter, X. Schuler, T. Weißenberg, Fatigue behaviour and crack growth of ferritic steel under environmental conditions, in: 38th MPA-Seminar Oct. 1 2, 2012 Stuttgart, 2012.

[206] X. Schuler, K. H. Herter, J. Rudolph, Derivation of design fatigue curves for austenitic stainless steel grades 1.4541 and 1.4550 within the German nuclear safety standard KTA 3201.2, in: 2013 ASME Press. Vessel. Pip. Div. Conf., 2013.

[207] K. Mumtaz, S. Takahashi, J. Echigoya, L. Zhang, Y. Kamada, M. Sato, Temperature dependence of martensitic transformation in austenitic stainless steel, J. Mater. Sci. Lett. 22 (2003) 423–427. doi:10.1023/A:1022999309138.

[208] S. Gangopadhyay, G. C. Hadjipanayis, B. Dale, C. M. Sorensen, K. J. Klabunde, V. Papaefthymiou, A. Kostikas, Magnetic properties of ultrafine iron particles, Phys. Rev. B 45 (1992) 9778–9787. doi:10.1103/PhysRevB.45.9778.

[209] Q. Li, C. W. Kartikowati, S. Horie, T. Ogi, T. Iwaki, K. Okuyama, Correlation between particle size/domain structure and magnetic properties of highly crystalline Fe3O4 nanoparticles, Sci. Rep. 7 (2017). doi:10.1038/s41598-017-09897-5.

[210] X. M. Zhang, E. Gautier, A. Simon, Orientation relationships of deformation-induced martensite in FeNiC alloys, Acta Metall. 37 (1989) 487–497. doi:10.1016/0001-6160(89)90232-0.

[211] D. T. Llewellyn, Work hardening effects in austenitic stainless steels, Mater. Sci. Technol. 13 (1997) 389–400. doi:10.1179/MST.1997.13.5.389.

[212] L. Saraf, Kernel Average Misorientation Confidence Index Correlation from FIB Sliced Ni-Fe-Cr alloy Surface, Microsc. Microanal. 17 (2011) 424–425. doi:10.1017/s1431927611002996.

[213] L. Kubin, A. Mortensen, Geometrically necessary dislocations and strain-gradient plasticity: a few critical issues, Scr. Mater. 48 (2003) 119–125. doi:10.1016/S1359-6462(02)00335-4.

[214] R. Hossain, F. Pahlevani, M. Z. Quadir, V. Sahajwalla, Stability of retained austenite in high carbon steel under compressive stress: An investigation from macro to nano scale, Sci. Rep. 6 (2016). doi:10.1038/srep34958.

[215] C. peng Liu, R. ming Ren, D. yi Liu, X. juan Zhao, C. huan Chen, An EBSD Investigation on the Evolution of the Surface Microstructure of D2 Wheel Steel During Rolling Contact Fatigue, Tribol. Lett. 68 (2020). doi:10.1007/s11249-020-1277-1.

[216] R. Nishimura, I. Musalam, Y. Maeda, The effect of sensitizing temperature on stress corrosion cracking of type 316 austenitic stainless steel in hydrochloric acid solution, Corros. Sci. 44 (2002) 1343–1360. doi:10.1016/S0010-938X(01)00117-2.

[217] L. Toth, F. Haraszti, T. Kovacs, Heat treatment effect for stainless steel corrosion, Eur. J. Mater. Sci. Eng. 3 (2018) 38–42.

[218] H. He, W. Tian, J. Li, K. Shi, M. Sun, J. Li, Failure analysis and finite element simulation on service conditions of SUS304 stainless steel, J. Mater. Eng. Perform. 30 (2021) 5987–5999. doi:10.1007/S11665-021-05744-X.

[219] A. Kartaman, E. Nurlaily, A. S. D. Putri, J. C. Sihotang, N. A. Kundari, Corrosion analysis of post-heat treatment and post-weld SS316 with electrokinetic reactivation and cyclic polarization method, J. Phys. Conf. Ser. 1436 (2020) 012104. doi:10.1088/1742-6596/1436/1/012104.

[220] J. Wang, B. Meng, J. Lu, Y. Zhou, D. Yang, Q. Wang, M. Chen, F. Wang, Studies on the oxidation behavior and Microstructural evolution of two Nb-modified HR3C austenitic steels under pure water vapor at 650 deg C, Materials (Basel). 13 (2020). doi:10.3390/MA13235447.

[221] W. K. Choi, S. Ha, J. C. Kim, J. C. Park, A. Gong, T. W. Kim, Oxidation damage evolution in low-cycle fatigue life of niobium-stabilized austenitic stainless steel, Materials (Basel). 15 (2022). doi:10.3390/MA15124073.

[222] H. C. Wu, B. Yang, S. L. Wang, M. X. Zhang, Effect of oxidation behavior on the corrosion fatigue crack initiation and propagation of 316LN austenitic stainless steel in high temperature water, Mater. Sci. Eng. A 633 (2015) 176–183. doi:10.1016/j.msea.2015.03.026.

[223] A. Beukel, Theory of the effect of dynamic strain aging on mechanical properties, Phys. status solidi 30 (1975) 197–206. doi:10.1002/PSSA.2210300120.

[224] J. M. Robinson, M. P. Shaw, Microstructural and mechanical influences on dynamic strain aging phenomena, Int. Mater. Rev. 39 (1994) 113–122. doi:10.1179/IMR.1994.39.3.113.

[225] S. G. Hong, S. B. Lee, Mechanism of dynamic strain aging and characterization of its effect on the low-cycle fatigue behavior in type 316L stainless steel, J. Nucl. Mater. 340 (2005) 307–314. doi:10.1016/j.jnucmat.2004.12.012.

[226] W. Karlsen, M. Ivanchenko, U. Ehrnstén, Y. Yagodzinskyy, H. Hänninen, Microstructural manifestation of dynamic strain aging in AISI 316 stainless steel, J. Nucl. Mater. 395 (2009) 156–161. doi:10.1016/j.jnucmat.2009.10.047.

[227] K. Peng, K. Qian, W. Chen, Effect of dynamic strain aging on high temperature properties of austenitic stainless steel, Mater. Sci. Eng. A 379 (2004) 372–377. doi:10.1016/j.msea.2004.03.004.

[228] M. Nowell, PRIAS Imaging - New approaches to visualizing microstructure, 2014. URL: https://edaxblog.com/2014/02/25/prias-imaging-new-approaches-to-visualizing-microstructure/.

[229] V. S. Srinivasan, R. Sandhya, K. Bhanu Sankara Rao, S. L. Mannan, K. S. Raghavan, Effects of temperature on the low cycle fatigue behaviour of nitrogen alloyed type 316L stainless steel, Int. J. Fatigue 13 (1991) 471–478. doi:10.1016/0142-1123(91)90482-E.

[230] A. Nagesha, R. Kannan, P. Parameswaran, R. Sandhya, K. B. S. Rao, V. Singh, A comparative study of isothermal and thermomechanical fatigue on type 316L(N) austenitic stainless steel, Mater. Sci. Eng. A 527 (2010) 5969–5975. doi:10.1016/j.msea.2010.05.082.

[231] T. S. Kumar, S. D. Yadav, A. Nagesha, R. Kannan, G. V. Reddy, Isothermal and thermomechanical fatigue behaviour of type 316LN austenitic stainless steel base metal and weld joint, Mater. Sci. Eng. A 772 (2020) 138627. doi:10.1016/j.msea.2019.138627.

[232] H. L. M. Niffenegger, M. Grosse, D. Kalkhof, M. M. A.Vincent, L. Pasco, Material characterization of fatigue specimens made from metastable austenitic stainless steel, Technical Report, Paul Scherrer Institut, Villigen Switzerland, 2003.

[233] H. Seifert, S. Ritter, H. Leber, Environmentally-assisted cracking in austenitic light water reactor structural materials. Final report of the KORA-I project, Technical Report 09, Paul Scherrer Institute, 2009.

[234] M. Ramesh, H. J. Leber, K. G. Janssens, M. Diener, R. Spolenak, Thermomechanical and isothermal fatigue behavior of 347 and 316L austenitic stainless tube and pipe steels, Int. J. Fatigue 33 (2011) 683–691. doi:10.1016/j.ijfatigue.2010.11.005.

[235] I. Virkkunen, Thermal fatigue of austenitic and duplex stainless steels, Acta Polytech. Scand. Mech. Eng. Ser. 115 (2001).

[236] E. A. Soppa, C. Kohler, E. Roos, Fatigue mechanisms in an austenitic steel under cyclic loading: Experiments and atomistic simulations, Mater. Sci. Eng. A 597 (2014) 128–138. doi:10.1016/j.msea.2013.12.036.

[237] J. Fingerhuth, I. Varfolomeev, S. Moroz, S. Eckmann, H. Oesterlin, D. Siegele, Joint project: Assessment of fatigue strength under consideration of cyclic softening and hardening processes. Subproject: 1501395A Numerical investigation, Technical Report, Fraunhofer IWM Freiburg, 2013.

[238] A. Sorich, M. Smaga, D. Eifler, Estimation of the fatigue limit due to cyclic hardening and softening processes Subproject: 1501395B Experimental investigations, Technical Report, Lehrstuhl für Werkstoffkunde WKK - Technische Universität Kaiserslautern, 2014.

[239] R. Acosta, K. Heckmann, J. Sievers, T. Schopf, T. Bill, P. Starke, K. Donnerbauer, L. Lücker, F. Walther, C. Boller, Microstructure-based lifetime assessment of austenitic steel AISI 347 in view of fatigue, environmental conditions and NDT, Appl. Sci. 11 (2021) 11214. doi:10.3390/APP112311214.

[240] B. Reicherter, X. Schuler, K.-H. Herter, Reactor safety research project No. 1501296 Proof of fatigue strength of ferritic and austenitic nuclear components, Technical Report, Materialprüfungsanstalt (MPA) Universität Stuttgart, 2009.

[241] T. Schopf, T. Daniel, M. Smaga, Reactor safety research project No. 1501548 Investigations of the fatigue behavior of austenitic materials and their welds for RPV and reactor internals in the HCF and VHCF regime, Technical Report, MPA Universität Stuttgart, WKK Universität Kaiserslautern, Framatome GmbH, 2020.

[242] R. Acosta, P. Starke, C. Boller, L. Lücker, A. Schmiedt-Kalenborn, F. Walther, T. Schopf, L. Stumpfrock, K. Heckmann, J. Sievers, Reactor safety research project No. 1501528 Microstructure based determination of the maximum operation time of materials and components in nuclear technology considering damage due to corrosion fatigue, Technical Report, Saarland University, TU Dortmund, MPA Stuttgart, GRS, 2020.

A. Technical Drawings

A.1 Heat Shield

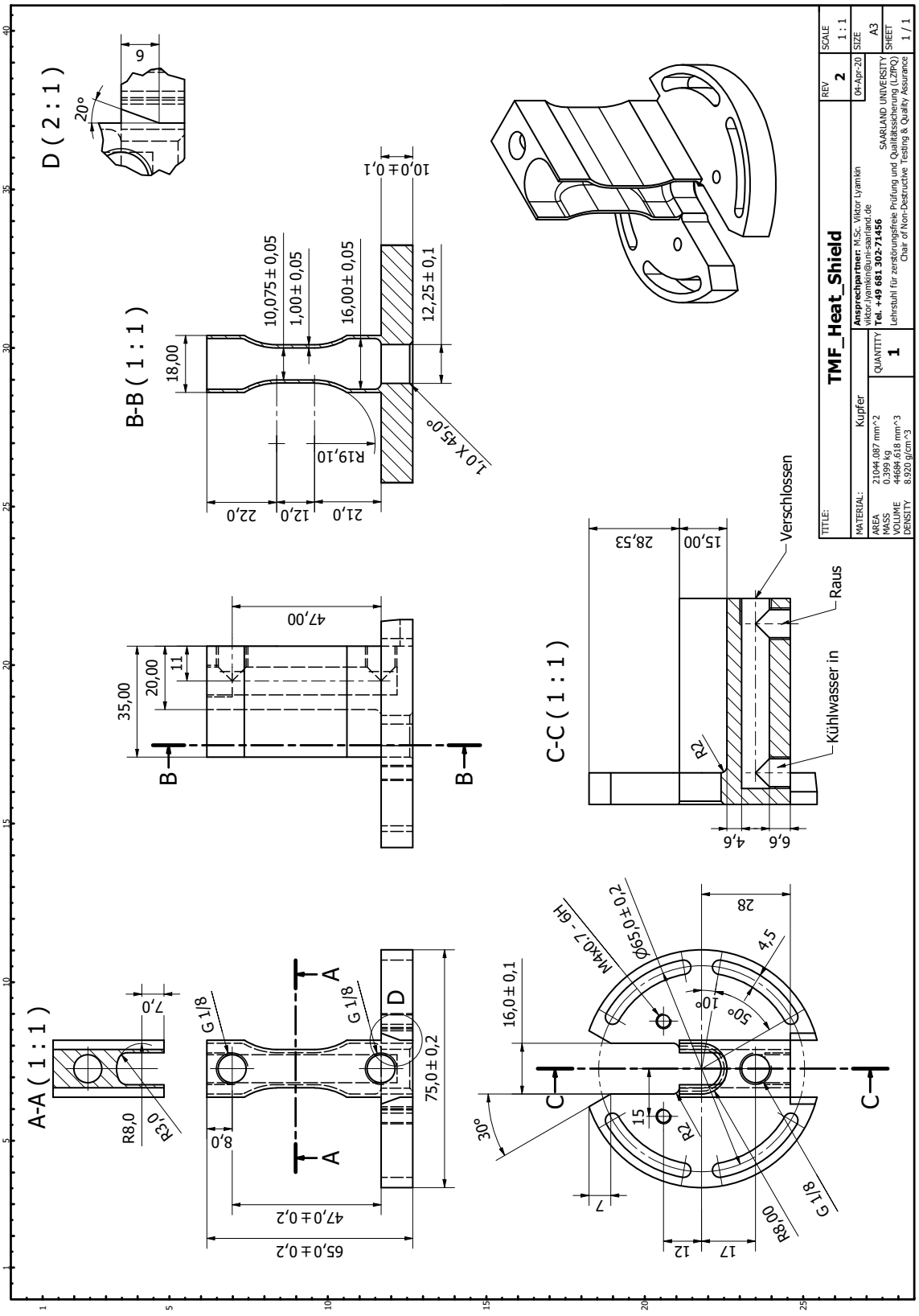

A.2 Current Injection Clamp

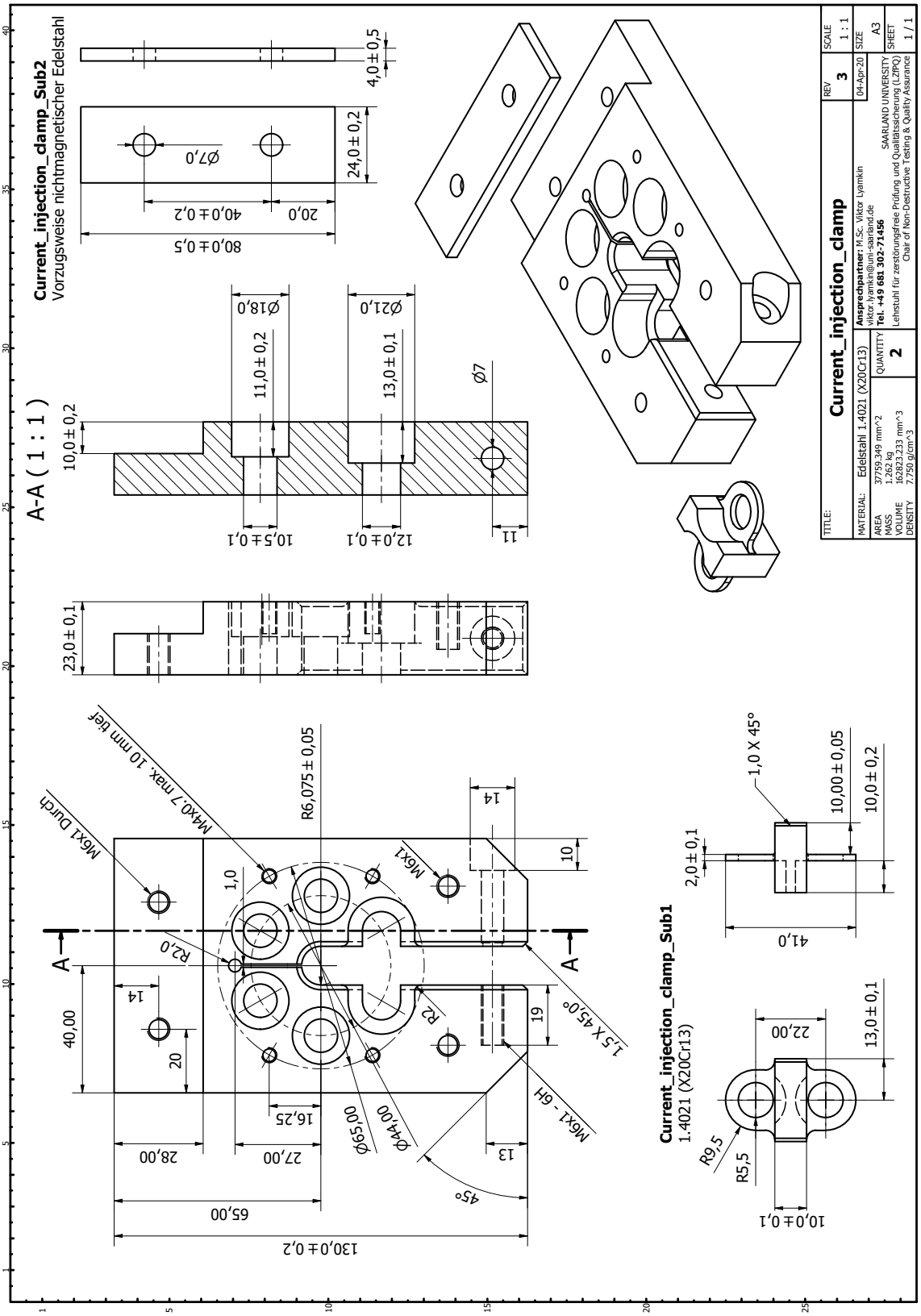

A.3 Compressed Air Nozzle

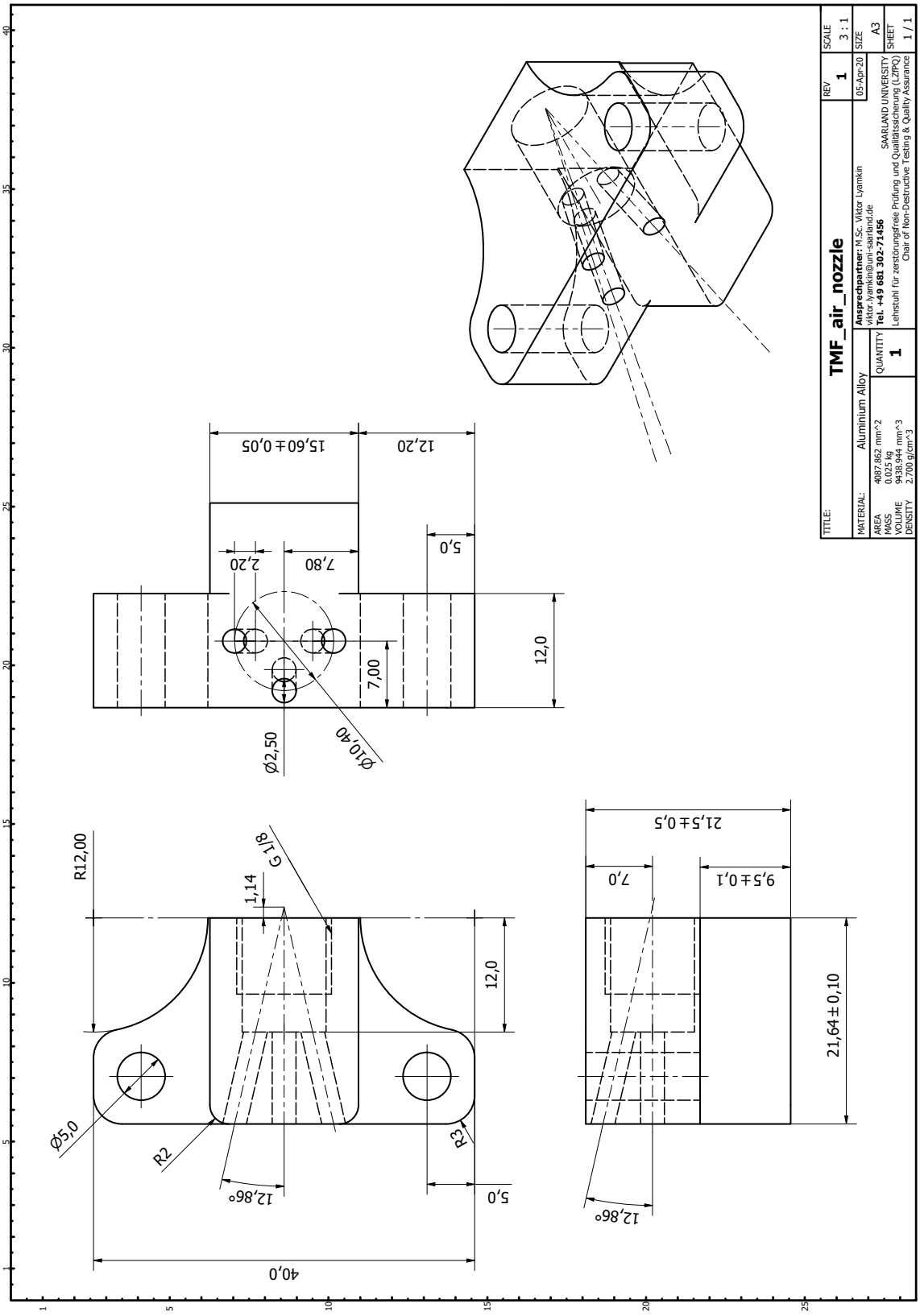

A.4 Extensometer Blade

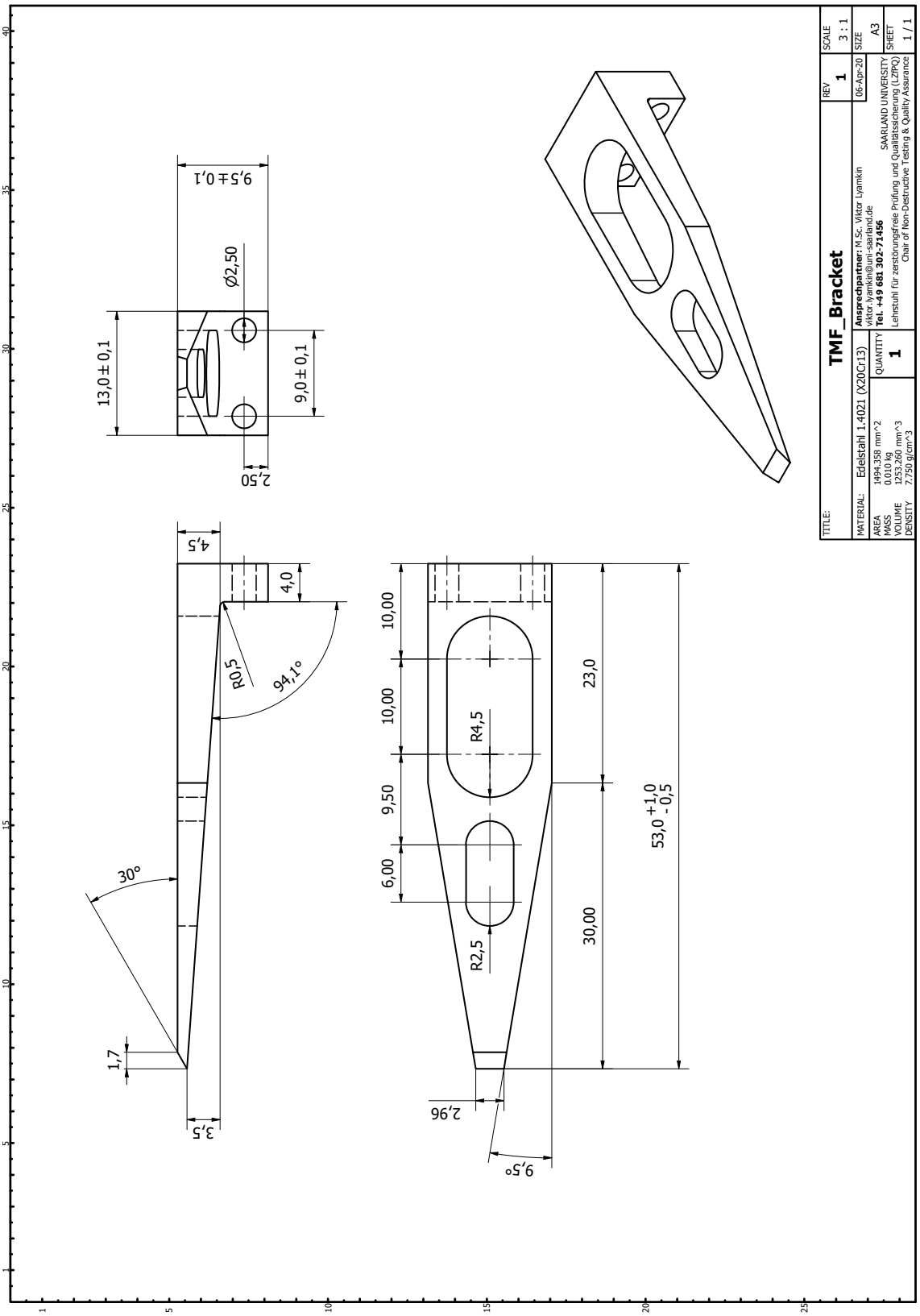

B. Patent disclosure statement

(19) Deutsches Patent- und Markenamt

(10) **DE 10 2019 126 891 A1** 2021.04.08

(12) **Offenlegungsschrift**

(21) Aktenzeichen: **10 2019 126 891.5**
(22) Anmeldetag: **07.10.2019**
(43) Offenlegungstag: **08.04.2021**

(51) Int Cl.: ***G01R 33/12*** (2006.01)
G01N 27/72 (2006.01)

(71) Anmelder:
Universität des Saarlandes, 66123 Saarbrücken, DE

(74) Vertreter:
Zeiner, Johannes, Dipl.-Ing. Dr.-Ing., 66115 Saarbrücken, DE

(72) Erfinder:
Lyamkin, Viktor, 66125 Saarbrücken, DE; Boller, Christian, Prof. Dr., 83727 Schliersee, DE

(56) Ermittelter Stand der Technik:

DE	**102 44 834**	**B3**
US	**3 431 489**	**A**

Müller, M., Güntherodt, H-J.: A pendulum balance for high temperature magnetic susceptiblilty measurements. In: Journal of Physics E. Scientific Instruments, Volume 14, Nr. 4, 1981, S. 453 – 456.

Rechercheantrag gemäß § 43 PatG ist gestellt.

Die folgenden Angaben sind den vom Anmelder eingereichten Unterlagen entnommen.

(54) Bezeichnung: **Vorrichtung und Verfahren zur zerstörungsfreien Bestimmung von Eigenschaften eines Materials, insbesondere zur Bestimmung eines Schädigungsgrades des Materials, eines Ferritanteils und/oder einer magnetischen Suszeptibilität**

(57) Zusammenfassung: Die Erfindung betrifft eine Vorrichtung (1; 1a) sowie ein Verfahren zur zerstörungsfreien Bestimmung von Eigenschaften eines Materials (7; 7a), insbesondere zur Bestimmung eines Schädigungsgrades des Materials, eines Ferritanteils und/oder einer magnetischen Suszeptibilität, die mindestens einen bewegbaren, aus einem magnetischen oder magnetisierbaren Material gebildeten Messkopf (4; 9, 10) sowie ein mit diesem gekoppeltes Messmittel (5; 5a) aufweist, durch das eine auf den mindestens einen Messkopf (4; 9, 10) wirkende Kraft und/oder dessen Bewegung während einer Bestimmung der Eigenschaften des Materials erfasst werden kann. Zweckmäßigerweise ist mindestens ein Ausgleichsmagnet (2; 12, 13) vorgesehen ist, der mit dem mindestens einen Messkopf (4; 9, 10) zur Einstellung eines Gleichgewichtszustandes, in dem sich auf den mindestens einen Messkopf wirkende Kräfte in einem Gleichgewicht befinden, magnetisch wechselwirkt. Vorteilhaft wird eine eine besonders empfindliche Vorrichtung ausgebildet, die insbesondere zur Bestimmung von Eigenschaften von austenitischen, rostfreien Stählen besonders gut geeignet ist.

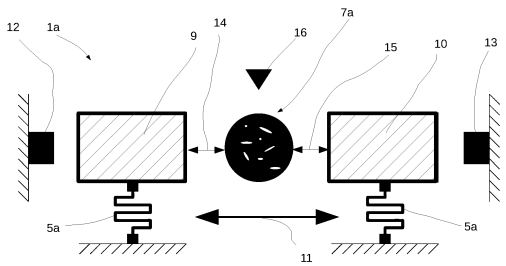

C. Fracture surfaces (1/2)

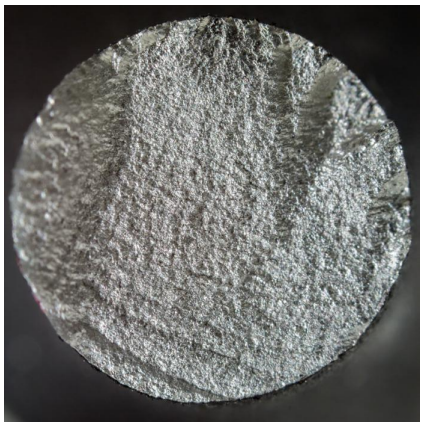

T_c=80 °C, ε_{at}=0.51%, N_f=2431
Isothermal, ref. to Fig. 72b.

T_c=100 °C, ε_{at}=0.51%, N_f=959
Isothermal, ref. to Fig. 72c.

T_c=160 °C, ε_{at}=0.51%, N_f=1352
Isothermal, ref. to Fig. 72f.

T_c=200 °C, ε_{at}=0.51%, N_f=1344
Isothermal, ref. to Fig. 73a.

T_c=240 °C, ε_{at}=0.51%, N_f=1013
Isothermal, ref. to Fig. 73b.

T_c=320 °C, ε_{at}=0.51%, N_f=1021
Isothermal, ref. to Fig. 73c.

T_{ch}=160 °C, ε_{am}=0.60%, N_f=1288
IP - TMF, ref. to Fig. 82b.

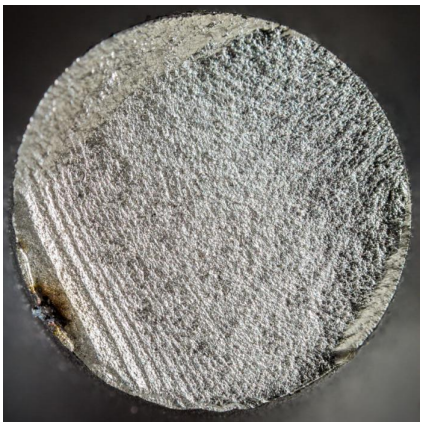

T_{ch}=160 °C, ε_{am}=0.42%, N_f=3001
OP - TMF, ref. to Fig. 82c.

C. Fracture surfaces (2/2)

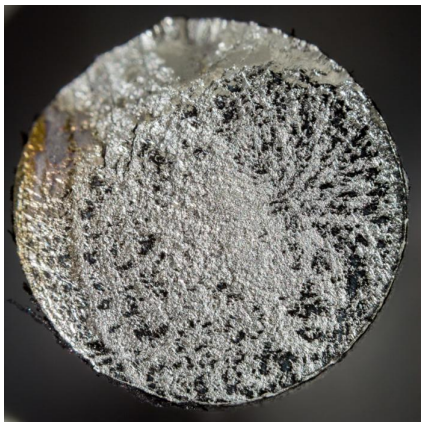

T_{ch}=160 °C, ε_{am}=60%, N_f=1781
OP - TMF, ref. to Fig. 82d.

T_{ch}=240 °C, ε_{am}=60%, N_f=817
OP - TMF, ref. to Fig. 84f.

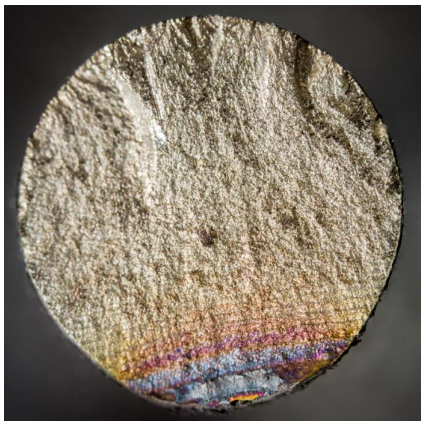

T_{ch}=320 °C, ε_{am}=0.42%, N_f=2451
OP - TMF, ref. to Fig. 86c

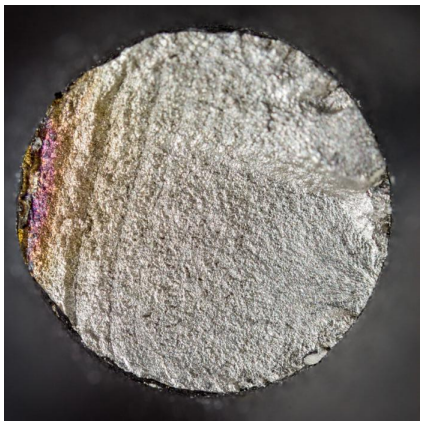

T_{ch}=240 °C, ε_{am}=0.51%, N_f=1745
OP - TMF

T_{ch}=320 °C, ε_{am}=0.51%, N_f=1936
OP - TMF

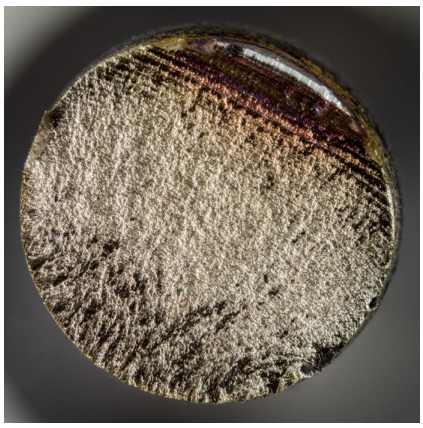

T_{ch} = 320 °C, ε_{am}=0.42%, N_f=1135
OP - TMF

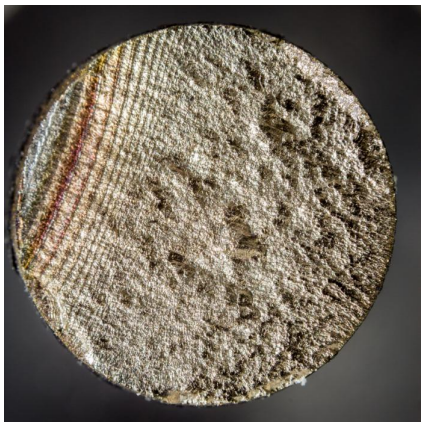

T_{ch}=320 °C, ε_{am}=0.27%, N_f=2462
IP - TMF (no therm. strain comp.)

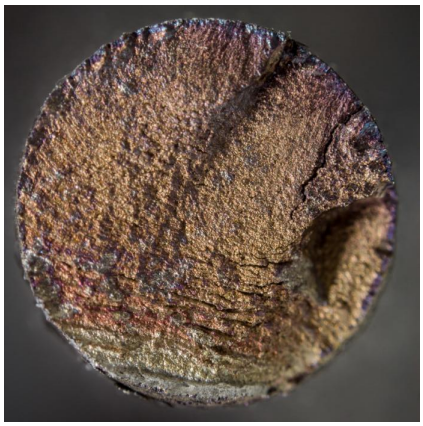

T_{ch}=450 °C, ε_{am}=0.27%, N_f=1048
IP - TMF (no therm. strain comp.)

D. Fatigue tests and number of cycles to failure

D.1 Constant amplitude tests, ambient temperature

i	Sp. No	Control mode	*R*	Load function	Amplitude	Number of cycles
1	1.16	Strain	-1	Sine, 5 Hz	0.175 %	500 000 [c]
2	2.12	Strain	-1	Sine, 5 Hz	0.175 %	10 000 [c]
3	1.24	Strain	-1	Sine, 5 Hz	0.175 %	100 000 [c]
4	3.18	Strain	-1	Sine, 5 Hz	0.175 %	90 000 [c]
5	1.23	Strain	-1	Sine, 5 Hz	0.175 %	215 000 [c]
6	2.28	Strain	-1	Sine, 5 Hz	0.175 %	1 800 000 [c]
7	3.28	Stress	-1	Sine, 5 Hz	230 MPa	10 000 [c]
8	3.13	Strain	-1	Sine, 5 Hz	0.165 %	2 100 000 [c]
9	3.8	Strain	-1	Sine, 5 Hz	0.220 %	29 370 [c]
10	1.1	Strain	-1	Trapezoid	0.500 %	134 [c]
11	1.15	Strain	-1	Triangle, 0.004 s^{-1}	0.160 %	257 324 [c]
12	3.21	Strain	-1	Triangle, 0.004 s^{-1}	0.500 %	4 380 [a]
13	3.11	Strain	-1	Triangle, 0.004 s^{-1}	0.140 %	365 622 [c]
14	3.28	Strain	-1	Triangle, 0.004 s^{-1}	0.190 %	310 400 [c]
15	3.27	Strain	-1	Triangle, 0.004 s^{-1}	0.280 %	32 500 [a]
16	3.2	Strain	-1	Triangle, 0.004 s^{-1}	0.240 %	68 700 [a]
17	3.1	Strain	-1	Triangle, 0.004 s^{-1}	0.300 %	39 500 [a]
18	3.22	Strain	-1	Triangle, 0.004 s^{-1}	0.400 %	9 500 [a]
19	1.26	Strain	-1	Triangle, 0.004 s^{-1}	0.700 %	930 [a]
20	1.20	Strain	-1	Triangle, 0.004 s^{-1}	0.600 %	1 605 [a]
22	3.31	Strain	-1	5 Hz – 15 Hz sine	0.165 %	20 000 000 [c]
23	1.29	Strain	-1	5 Hz – 10 Hz sine	0.195 %	6 144 102 [c]
24	1.9	Strain	-1	Triangle, 0.004 s^{-1}	1.000 %	390 [a]
25	1.31	Strain	-1	Triangle, 1 Hz	0.220 %	130 000 [a]
26	1.14	Strain	-1	Triangle, 2 Hz	0.203 %	100 000 [a]
27	1.11	Strain	-1	Triangle, 1 Hz	0.203 %	230 000 [a]
28	1.4	Strain	-1	Triangle, 0.004 s^{-1}	0.185 %	1 212 811 [c]

D.2 Constant amplitude tests, isothermal

Parameters according to section 7.4 on page 110.

i	Sp. No	Temperature	*R*	Load function	Strain amplitude	Cycles to failure
1	2.22	17 °C	-1	Sine, 0.02 Hz	0.51 %	2 468 [a]
2	ZB12	80 °C	-1	Sine, 0.02 Hz	0.51 %	2 431 [a]
3	1.27	100 °C	-1	Sine, 0.02 Hz	0.51 %	959 [a]
4	ZB15	110 °C	-1	Sine, 0.02 Hz	0.51 %	1 407 [b]
5	ZB13	120 °C	-1	Sine, 0.02 Hz	0.51 %	1 630 [b]
6	ZB14	160 °C	-1	Sine, 0.02 Hz	0.51 %	1 352 [a]
7	ZB17	200 °C	-1	Sine, 0.02 Hz	0.51 %	1 344 [a]
8	ZB18	240 °C	-1	Sine, 0.02 Hz	0.51 %	1 013 [a]
9	ZB16	320 °C	-1	Sine, 0.02 Hz	0.51 %	1 021 [a]
10	1.1	320 °C	-1	Sine, 0.02 Hz	0.51 %	922 [a]

a. Fully raptured specimen

b. Tensile stress amplitude reduced by 50 %

c. No failure of the specimen (run-out or interrupted)

D.3 Thermo-mechanical fatigue tests

Parameters according to section 7.5 on page 122.

i	Sp. No	High temp.	Low temp.	Phase	Mech. strain amplitude	Cycles to failure
1	ZA09	160 °C	24 °C	IP	0.42 %	3 036 [b]
2	ZA06	160 °C	24 °C	IP	0.60 %	1 288 [a]
3	2.23	160 °C	24 °C	OP	0.42 %	3 001 [a]
4	ZA07	160 °C	24 °C	OP	0.60 %	1 781 [a]
5	ZB04	240 °C	25 °C	IP	0.27 %	15 335 [b]
6	ZB06	240 °C	25 °C	IP	0.42 %	2 328 [b]
7	ZB05	240 °C	25 °C	OP	0.42 %	3 277 [b]
8	ZB09	240 °C	25 °C	IP	0.51 %	1 323 [b]
9	ZB10	240 °C	25 °C	OP	0.51 %	1 804 [b]
10	ZA04	240 °C	25 °C	IP	0.60 %	558 [b]
11	ZA05	240 °C	25 °C	OP	0.60 %	817 [a]
12	ZA11	320 °C	27 °C	IP	0.42 %	2 872 [b]
13	ZA08	320 °C	27 °C	OP	0.42 %	2 451 [a]
14	ZB19	320 °C	27 °C	IP	0.51 %	971 [b]
15	ZB08	320 °C	27 °C	OP	0.51 %	1 694 [b]

D.4 Strain increase tests, ambient temperature

Initial strain amplitude: 0.05 %

i	Sp. No	*R*	Amp. increase per step (%)	Step time (min)	Strain rate (s^{-1})	Step count	Max. stress	Sp. Failure
1	2.27	-1	0.05	90	0.002	13	668 MPa	No
2	2.19	-1	0.04	90	0.005	13	672 MPa	Yes
3	3.5	-1	0.05	30	0.004	17	721 MPa	Yes
4	3.6	-1	0.05	120	0.004	11	615 MPa	Yes
5	3.7	-1	0.01	120	0.004	24	338 MPa	No
6	3.9	-1	0.01	120	0.004	31	436 MPa	Yes

D.5 Strain increase tests, isothermal

Parameters according to Table 7 on page 89:
Step time: 120 min;
Initial strain amplitude: 0.05 %
Amplitude increase per step: 0.01 %;
Strain rate: 0.004 s^{-1};
Waveform: triangle;

i	Sp. No	Temperature	*R*	Step count	Max. stress	Sp. Failure
1	2.23	17 °C	-1	34	557 MPa	No
2	1.10	80 °C	-1	31	458 MPa	Yes
3	3.30	110 °C	-1	26	326 MPa	Yes
4	3.24	120 °C	-1	25	319 MPa	Yes
5	1.7	160 °C	-1	21	253 MPa	Yes
6	3.3	240 °C	-1	19	221 MPa	Yes

a. Fully raptured specimen
b. Tensile stress amplitude reduced by 50 %
c. No failure of the specimen (run-out or interrupted)

E. Units for magnetic properties

Quantity	Symbol	Gaussian & cgs emu [a]	Conversion factor, C [b]	SI & rationalized mks [c]
Magnetic flux density, magnetic induction	B	gauss (G) [d]	10^{-4}	tesla (T), Wb/m^2
Magnetic flux	Φ	maxwell (Mx), G·cm^2	10^{-8}	weber (Wb), volt second (V·s)
Magnetic potential difference, magnetomotive force	U, F	gilbert (Gb)	$10/4\pi$	ampere (A)
Magnetic field strength, magnetizing force	H	oersted (Oe), [e] Gb/cm	$10^3/4\pi$	A/m [f]
(Volume) magnetization [g]	M	emu/cm^3 [h]	10^3	A/m
(Volume) magnetization	$4\pi M$	G	$10^3/4\pi$	A/m
Magnetic polarization, intensity of magnetization	J, I	emu/cm^3	$4\pi \cdot 10^{-4}$	T, Wb/m^2 [i]
(Mass) magnetization	σ, M	emu/g	1 $4\pi \cdot 10^{-7}$	A·m^2/kg Wb·m/kg
Magnetic moment	m	emu, erg/G	10^{-3}	A·m^2, joule per tesla (J/T)
Magnetic dipole moment	j	emu, erg/G	$4\pi \cdot 10^{-10}$	Wb·m [i]
(Volume) susceptibility	χ, κ	dimensionless, emu/cm^3	4π $(4\pi)^2 \cdot 10^{-7}$	dimensionless henry per meter (H/m), Wb/(A·m)
(Mass) susceptibility	χ_ρ, κ_ρ	cm^3/g, emu/g	$4\pi \cdot 10^{-3}$ $(4\pi)^2 \cdot 10^{-10}$	m^3/kg H·m^2/kg
(Molar) susceptibility	χ_{mol}, κ_{mol}	cm^3/mol, emu/mol	$4\pi \cdot 10^{-6}$ $(4\pi)^2 \cdot 10^{-13}$	m^3/mol H·m^2/mol
Permeability	μ	dimensionless	$4\pi \cdot 10^{-7}$	H/m, Wb/(A·m)
Relative permeability [j]	μ_r	not defined		dimensionless
(Volume) energy density, energy product [k]	W	erg/cm^3	10^{-1}	J/m^3
Demagnetization factor	D, N	dimensionless	$1/4\pi$	dimensionless

a. Gaussian units and cgs emu are the same for magnetic properties. The defining relation is $B = H + 4\pi M$.
b. Multiply a number in Gaussian units by C to convert it to SI (e.g., 1 G $\cdot$ 10^{-4}T/G = 10^{-4} T).
c. SI (*Systeme International d'Unites*). Where two conversion factors are given, the upper one is recognized under, or consistent with SI and is based on the definition $B = \mu_0(H + M)$, where $\mu_0 = 4\pi \cdot 10^{-7}$ H/m. The lower one is not recognized under SI and is based on the definition $B = \mu_0 H + J$, where the symbol I is often used in place of J.
d. 1 gauss = 10^5 gamma (γ).
e. Both oersted and gauss are expressed as cm$^{-1/2}$·g$^{1/2}$·s^{-1} in terms of base units.
f. A/m was often expressed as "ampere-turn per meter" when used for magnetic field strength.
g. Magnetic moment per unit volume.
h. The designation "emu" is not a unit.
i. Recognized under SI, even though based on the definition $B = \mu_0 H + J$. See footnote c.
j. $\mu_r = \mu/\mu_0 = 1 + \chi$, all in SI. μ_r is equal to Gaussian μ.
k. $B \cdot H$ and $\mu_0 M \cdot H$ have SI units J/m^3; $M \cdot H$ and $B \cdot H/4\pi$ have Gaussian units erg/cm^3.

[R. B. Goldfarb and F. R. Fickett, U.S. Department of Commerce, National Bureau of Standards, Boulder, Colorado 80303, March 1985]